Aeroacoustic modeling of a LOX/CH4 rocket engine for high-frequency combustion instability prediction analyses

Luca Trotta

Delft University of Technology

TU Delft

DLR Deutsches Zentrum für Luft- und Raumfahrt
German Aerospace Center

Aeroacoustic modeling of a LOX/CH4 rocket engine for high-frequency combustion instability prediction analyses

by

Luca Trotta

Student Number: 4557085

Supervisor at the sending academic institution:
Ir. B.T.C. Zandbergen

Supervisor at the receiving research institution:
Dr. W. Armbruster

Academic Institution:
Delft University of Technology,
Aerospace Engineering faculty,
Kluyverweg 1, 2629 HS Delft, the Netherlands

Hosting Institute:
Deutsches Zentrum für Luft- und Raumfahrt (DLR),
Institute of Space Propulsion,
Im Langen Grund, 74239 Hardthausen, Germany

Thesis Period at DLR:
02/05/2022 - 30/11/2022

Greenlight Approval:
11 January 2023

Thesis Defense Date:
23 February 2023

Cover page: Airbus Safran Launchers' technology demonstrator of a LOX/CH_4 engine firing in Lampoldshausen [1]

TUDelft DLR

Preface

This report represents the work that was performed at the Space Propulsion Institute of the German Aerospace Center (DLR) as part of my thesis to obtain a Master of Science degree in the Space Engineering Master of the Aerospace Engineering faculty of the Delft University of Technology. The thesis was performed within the combustion dynamics group of DLR´s Space Propulsion Institute in Lampoldshausen and deals with assessing the performance of an Aeroacoustic solver to model the acoustic eigenmodes of a LOX/CH_4 rocket combustor, to improve the reliability of high-frequency combustion instability analyses.

This document is aimed at a technical audience having knowledge of thermal rocket propulsion and fluid dynamics. Firstly, this report was written to illustrate the work performed during the thesis to the thesis committee of TU Delft and the research community dealing with thermoacoustic instabilities in liquid rocket engines. Secondly, its purpose is to document the work for DLR. Hence, it describes the performed test cases to be reproducible by their researchers, and it summarizes the outcome of the analyses. Based on it, recommendations for future steps are drawn to support DLR in achieving its future goal of predicting and preventing high-frequency combustion instabilities in liquid rocket engines.

Thirdly, this report is also written taking into consideration students and hopes to illustrate how active and exciting this research field is, and how major of a technical risk combustion instabilities still represent nowadays during new engine development programs. For TU Delft students that are interested in performing their thesis on this topic, it is recommended to have at least followed the following courses beforehand: AE4S01 Thermal Rocket Propulsion, AE4261 Internal Flows, AE4202 CFD for Aerospace Engineers, AE4262 Combustion for Propulsion and Power Technologies. Furthermore, the course AE4260A Fundamental of Aeroacoustics is seen as a great plus.

Lastly, I am extremely grateful for all the people that have accompanied me on this journey. I would like to thank my DLR supervisor, Dr. Wolfgang Armbruster, for his support in helping me understand the intricate topic of combustion instabilities and for his feedback backed up by his experience in the field. My TU Delft supervisor, Ir. Barry Zandbergen, for his elaborate and critical feedback to improve the value of the work done. Ir. Federica Tonti, for her help related to numerical simulations and assistance in solving technical issues. Dr. Justin Hardi for making the internship and thesis at DLR become reality, and, finally, to my family, my girlfriend, and my friends for their continuous support.

Luca Trotta
Lampoldshausen, February 2023

Contents

List of Tables

List of Figures

List of Symbols and Abbreviations

Symbols

Symbol	Definition	S.I. Unit
A	Surface area	[m^2]
A_{fc}	Power Spectral Density amplitude about the central frequency fc	[bar^2/Hz]
A_p	First integration coefficent of the acoustic Fourier transfer	[-]
A_s	Integration coefficent of the entropy Fourier transfer	[-]
A_Ω	Integration coefficent of the vorticity Fourier transfer	[-]
A^+	Amplitude of right-moving (incident) wave	[Pa or m/s]
A^-	Amplitude of left-moving (reflecting) wave	[Pa or m/s]
B	Coefficient of asymmetry of the asymmetric Lorentzian profile	[-]
B_p	Second integration coefficent of the acoustic Fourier transfer	[-]
c	Speed of sound	[m/s]
C_p	Constant pressure specific heat	[J/kg K]
C_v	Constant volume specific heat	[J/kg K]
D	Diameter	[m]
D_h	Hydraulic diameter	[m]
d_c	Face-plate diameter	[m]
e	Specific energy	[J/kg]
e	Wall roughness	[m]
f	Frequency	[Hz]
f_c	Central frequency chosen for curve-fitting	[Hz]
f	Friction coefficient	[-]
F	External forces source term	[N]
F_p	Fourier Transform	[-]
F_t	Thrust force	[N]
F_{visc}	Viscous forces per unit mass	$[\frac{N}{kg}]$
h	Mesh size	[m]
He	Helmholtz number	[-]
i	Imaginary unit	[-]
I	Acoustic Intensity	[W/m^2]
I	Identity matrix	[-]
J	Momentum flux ratio	[-]
k	Wave number	[1/m]
k	Thermal conductivity	[W/mK]
k_l	Correction factor for longitudinal modes	[-]
k_t	Correction factor for transverse modes	[-]
K	Flame stretch term	[1/s]

Symbol	Definition	S.I. Unit
L_i	Damping loss *i*	[-]
L	Length	[m]
M, Ma	Mach number	[-]
M	Mass source term	[kg]
$\dot{m}_b$	Mass burning rate	[kg/s]
$\dot{m}$	Mass flow	[kg/s]
$\mathcal{O}()$	Order of the numerical scheme	[-]
n	Crocco's interaction index	[-]
$n_{elements}$	Number of mesh elements per wavelength	[-]
p	Static pressure	[Pa]
p	Discretization order	[-]
Pe	Peclet number	[-]
P_W	Wetted perimeter	[m]
PSD_{AL}	Asymmetric Lorentzian profile's Power Spectral Density	[bar^2/Hz]
PSD_F	Fano profile's Power Spectral Density	[bar^2/Hz]
PSD_L	Lorentzian profile's Power Spectral Density	[bar^2/Hz]
$\dot{Q}$, $\dot{q}$	Heat release rate	[W/m^2]
Q	Heat source term	[J]
q_f	Coefficient of asymmetry of the Fano profile	[-]
R	Universal gas constant (8.314462)	$[\frac{J}{K \cdot mol}]$
R	Reflection coefficient	[-]
R^2	Coefficient of determination	[-]
R_a	Divergence radius	[m]
R_u	Throat radius	[m]
Re	Reynolds number	[-]
$Re(\square)$	Real number of $\square$	[-]
Str	Strouhal number	[-]
S_c	Mass source term	$[\frac{kg}{m^3 \cdot s}]$
S_e	Energy source term	[W/m^3], [Pa/s]
S_m	Momentum source term	[N/m^3], [m/s^2]
S_b	Flame speed	[m/s]
$\mathbf{S}_\mathbf{u}^{v,s,\nabla p_0=0}$	Momentum source term	[m/s^2]
T	Temperature	[K]
t	Time	[s]
$\mathbf{u}$	Velocity vector	[m/s]
u	x-velocity	[m/s]
v	y-velocity	[m/s]
w	z-velocity	[m/s]
W_{fc}	Width at half maximum of the peak at frequency fc	[1/s]
$\mathbf{X}$	Body forces per unit mass	$[\frac{N}{kg}]$
Y	Mass fraction	[-]
Y	Acoustic admittance	$[\frac{kg}{Pam^3}]$
Z	Impedance	$[\frac{Pa \cdot s}{m}]$
Z_c	Characteristic impedance	$[\frac{Pa \cdot s}{m}]$
z	Specific impedance	[-]
$\alpha_{m,n}$	Coefficient for Bessel function's roots $J(\pi\alpha_{m,n})$	[-]
α_p	Coefficient of thermal expansion	[1/K]
β_T	Isothermal compressibility	[1/Pa]

Symbol	Definition	S.I. Unit
γ	Specific heat ratio	[-]
δ	Kronecker unit delta	[-]
δ	Mapping diffusion coefficient	[-]
ϵ	Absolute percentage error	[-]
θ_i	Incidence angle	[rad]
ν	Damping rate	[1/s]
ν_{dif}	Diffusion coefficient	[m^2/s]
ρ	Density	[kg/m^3]
Π	Dissipation function	[kg/m^2 s]
Φ	Dummy variable	[-]
σ, τ	Friction-related stress tensor	[N/m^2]
τ	Crocco's Time-lag	[s]
μ	Dynamic viscosity	[Pa s]
μ_λ, μ_B	Bulk viscosity	[Pa s]
ω	Frequency	[rad/s]
Ω	Vorticity	[1/s]

Abbreviations

Abbreviation	Definition
1D	One-dimensional
3D	Three-dimensional
APE	Acoustic Perturbation Equations
ARPACK	Arnoldi Package
AY	Academic Year
BPT	Bleed Pressure valve Turbine
BPV	Bleed Pressure Valve
BKD	Brennkammer D (Combustion Chamber D)
BKH	Brennkammer H (Combustion Chamber H)
BKL	Brennkammer LUMEN (Combustion Chamber LUMEN)
B.C.	Boundary condition(s)
CAA	Computational Aeroacoustic
CARA	DLR high-performance-computing cluster
CEA	Chemical Equilibrium with Applications
CFD	Computational Fluid Dynamic
CNES	Centre national d'études spatiales
CNRS	Centre national de la recherche scientifique
CPU	Central Processing Unit
CVRC	Continuosly Variable Resonance Combustor
DES	Detached Eddy Simulation
DLR	Deutsches Zentrum für Luft- und Raumfahrt (German Aerospace Center)
DMD	Dynamic Mode Decomposition
DNS	Direct Numerical Simulation
DYN	Dynamic pressure sensor in the combustion chamber

Abbreviation	Definition
FCV	Fuel Control Valve
FDF	Flame Describing Function
FEA	Finite Element Analysis
FEM	Finite Element Method
FFM	Fuel Flowmeter
FFT	Fast Fourier Transform
FTF	Flame Transfer Function
GLS	Galerkin Least-Squares
GMRES	Generalized minimal residual method
GTS	Gradient Suppression Stabilization
Hydrolox	Engine using liquid Oxygen (LOX) and liquid Hydrogen (LH_2) as propellant
IDE	Integrated Development Environment
iCHE	Inhomogenous Convective Helmholtz Equation
IGN	Igniter
IMFT	Institut de Mécanique des Fluides de Toulouse
INJ	Injector
L1	Fist longitudinal mode
L2	Second longitudinal mode
LEE	Linearized Euler Equations
LES	Large Eddy Simulation
LH_2	Liquid Hydrogen
LNG	Liquid Natural Gas
LNS	Linearized Navier-Stokes
LOM	Low-Order Modeling
LOX	Liquid Oxygen
LUMEN	Liquid Upper-Stage Demonstrator Engine
MCC	Main combustion chamber
MEA	Mean Absolute Error
Methalox	Engine using Methane (CH_4) and Liquid Oxygen (LOX) as propellants
MFV	Main Fuel Valve
MMH	Monomethylhydrazine
MOV	Main Oxidizer Valve
MSc	Master of Science/Master
MUMPS	Multifrontal Massively Parallel sparse direct Solver
N.A.	Not Available
NASA	National Aeronautics and Space Administration
NEM	Nozzle Extension
NIST	National Institute of Standards and Technology
nLEE	Nonlinear Linearized Euler Equations
NTO	Dinitrogen Tetroxide
OCV	Oxidizer Control Valve
OFM	Oxidizer Flowmeter

Abbreviation	Definition
ONERA	Office National d'Etudes et de Recherches Aérospatiales
PARDISO	Parallel Direct Sparse Solver
PCCIR	Pressure sensor in the combustion chamber
PCCIRDYN	Dynamic pressure sensor in the combustion chamber
PDE	Partial Differential Equation
Ph.D.	Doctor of philosophy
PM	Optical sensor
PSD	Power Spectral Density
R1	First radial mode
RAM	Random Access Memory
RANS	Reynolds Averaged Navier Stokes
RCV	Regenerative-cooling Control Valve
REST	Rocket Engine Stability Initiative
RASPy	Data-processing Python library of DLR
RPA	Rocket Propulsion Analysis software
ROF	Ratio Oxidizer-to-Fuel
RO	Research Objective
RQ	Research Question
SciPy	Python's scientific computing library
SD	Standard Deviation
sFEM	Stabilized Finite Element Method
SRK	Soave-Redlich-Kwong gas model
SST	Shear-Stress-Transport
SUPG	Streamline Upwind Petrov-Galerkin
STL	Sensitive Time-Lag
T1	First tangential mode
T2	Second tangential mode
T1L1	First longitudinal and first tangential combined mode
TIR	Temperature sensor of the injector
TFV	Turbine Fuel Valve
TOV	Turbine Oxidizer Valve
TU Delft	Technische Universiteit Delft (Delft University of Technology)
TUM	Technische Universität München
UDMH	Unsymmetrical dimethylhydrazine
URANS	Unsteady Reynolds Averaged Navier Stokes
ULA	United Launch Alliance
v.	Software version
XCV	Extinguisher Control Valve

Superscripts

$'$	Fluctuation
$''$	Second-order Fluctuation
$\widehat{\ }$	Complex number
$\overline{\square}$	Average quantity of $\square$
A	Area averaged quantity
M	Mass flow averaged quantity
p	Pressure taken as reference disturbance

Subscripts

$\underline{\underline{\square}}$	Tensor of $\square$
0	Background flow property
ν	Damping rate related
c	Chamber property
CFD	Required CFD input
cz	Combustion zone
f	frequency related
$F, fuel, CH4$	Fuel
i	Incident to the boundary
in	Inner dimension or inlet
LNS	Wanted LNS output
m	Radial mode shape number
max	Maximum quantity
n	Tangential mode shape number
O, ox, LOX	Oxidizer
out	Outer dimension or outlet
q	Longitudinal mode shape number
t	Total quantity
$turb$	Turbopump
x	x-direction component
y	y-direction component
z	z-direction component

Abstract

High-frequency combustion instabilities represent the main technical risk faced by design engineers when developing new chemical rocket propulsion systems. Such instabilities are driven by the coupling between the flames' heat release rate and the combustion chamber's acoustic field. As such, they can only be assessed during detailed design phases, making design iterations costly. Despite constant efforts being invested in developing numerical tools for their analysis, their reliable prediction remains a major issue. Furthermore, with the advent of the New Space industry, a need to cost-effectively analyze the stability of Hydrocarbon-based systems is stressed.

As a result, this work contributes towards the development of a reliable numerical framework to predict the onset of high-frequency combustion instabilities in liquid rocket engines by ameliorating their acoustic modeling. More specifically, the performance of a novel Linearized Navier-Stokes (LNS) solver in COMSOL is benchmarked against its established Helmholtz solver and validated against the data of two hot-fires of DLR's LOX/CH4 LUMEN engine. Following a step-wise increase in modeling complexity and by investigating how the background flow description influences the results, sub-5 % eigenfrequency errors were obtained. The results also showed that the moving background flow in rocket engines significantly reduces the eigenfrequencies, and that its influence can be accounted for by prescribing varying flow properties to the acoustic solvers. Besides achieving the most accurate eigenfrequency results for a LOX/CH_4 system, a more representative velocity disturbance distribution is also attained with the LNS simulation, allowing future studies to better account for the influence of velocity fluctuations on the heat release rate driving the instabilities.

1 Introduction

The aim of this document is to improve the currently available numerical capabilities that the space industry has for predicting high-frequency combustion instabilities in liquid rocket engines by proposing the use of a novel and practical aeroacoustic solver. More specifically, since these types of instabilities are driven by the feedback between the combustion chamber's acoustic and the unsteady heat release rate from the flames, the extent to which accurate acoustic results can be obtained using this novel solver is investigated. To start, the relevance of the research is described in Section 1.1, where the severe consequences associated with encountering high-frequency combustion instabilities during the development of new bi-propellant rocket engines are explained. These instabilities not only represent the main technical risk during such phases but are also inherent to these systems. On top of that, based on the complexity of the problem, nowadays there is still a lack of a reliable and satisfactory prediction tool, which leads to a ceaseless need for improving the current numerical prediction standards.

The work presented in this report was performed with the Space Propulsion Institute of the German Aerospace Center (DLR), which provided the resources required for performing this research. Furthermore, this document also works toward DLR's need to develop an accurate fully-numerical tool to predict and investigate high-frequency combustion instabilities in their liquid rocket engines. Next to framing the need for the research in Section 1.1, the aim of the study and its constraints are delineated in Section 1.2, where the outline of the report is also included.

1.1 Research relevance

Fifty-three years have passed since the Saturn V rocket, propelled by Rocketdyne's vigorous F-1 engines, successfully launched the Apollo 11 crew into history by sending the first humans to the moon on July 16, 1969. Considering the great leaps of progress made by the space industry in the past few decades alone, one would expect that the main technical risks encountered during the Apollo program, which are at the heart of the vehicles used to enable space exploration, would have already long been solved. Yet, there is still a field that poses a significant challenge to engineers faced with the development of new bi-propellant rocket engines, namely combustion instabilities.

Combustion instabilities occur due to the coupling between the processes inside a propulsion system that ultimately lead the combustor to experience pressure oscillations larger than 5% of the mean chamber pressure [2–4]. Given the underlying mechanisms triggering the instabilities, the latter are often classified based on the frequency at which the oscillations occur, and a distinction is made between low-frequency, intermediate-frequency, and high-frequency instabilities, with the latter being the most damaging to the engine [2]. The presence of combustion instabilities does not only present a performance risk for the mission in which the engine is to be used, but also a cost and schedule risk for the overall engine development program. In the worst case, combustion instabilities could lead to pressure oscillations in the chamber peaking up to twice the mean pressure, and heat transfer rates increasing up to 2 to 10 times the nominal ones, which would lead to a rapid structural failure of the engine, sometimes occurring within one second of operation [2]. Even if the engine does not directly fail due to the consequences of the instabilities, in addition to impacting its lifetime, the presence of unstable combustion dynamics can also negatively affect the structural integrity of the payload. This is due to the engine inducing longitudinal low-frequency vibrations on the surrounding construction around the same frequency range of the natural frequencies of the vehicle's structure [3].

Nowadays, to investigate the presence of dangerous instabilities within the engine´s intended operational regime, the industry still significantly relies on sub-scale [5, 6] or full-scale [7–10] propulsion system tests. This is in part due to the shortcomings in fully understanding the coupling mechanisms that drive the instabilities, leading to unreliable numerical prediction analyses [11]. This need for assessing the engine´s stability accurately via testing, or lack of a suitable prediction method thereof, leads to additional capital expenditures due to the cost associated with testing high-pressure bi-propellant combustion systems (often using cryogenic media) under representative operating conditions [5, 7, 11–14]. Furthermore, instability-related issues often arise at a late development phase of the engine, with most of the detailed design of the system already completed [11]. This means that a considerable amount of the overall development cost has already been committed, and iterating the design to solve the problem at such a stage would require a significant added cost. The tediousness of this iterative process and the significant contribution it can have on the overall development time of the engine, are best described by a quote from ULA´s CEO and president Tory Bruno, who, during a 2017 interview about the development status of Blue Origin´s BE-4 engine, said [15]:

> *"It's not unusual, by the way, to have some instability when you develop a new engine [...], but I have been in situations where you tried the tried and true things, then nothing works, and nine months later you're still stuck"*

This shows that combustion instabilities, besides representing a major technical risk, can also have a major influence on the program's cost and schedule risks. Looking back, a well-known example of an engine development program afflicted by severe combustion instabilities was that of the F-1 engine, where, during the early 60s, the challenges to face became so critical and difficult to solve that for fear of threatening the success of the American Moon program, NASA and Rocketdyne began *Project Fist*, a Combustion Stability program aimed at resolving the issues arising from the instabilities. The program carefully investigated the tests in which unstable behaviors were observed [16, 17], during which, for example, pressure overshoots of 50% and burn-through of the injector plate would occur [16]. For illustration, Figure 1.1a shows the integral version of the F-1´s injector plate, while Figure 1.1b shows the same component after high-frequency combustion instabilities severely damaged its faceplate during a test run. Finally, by the end of the engine´s development, 3200 full-scale hot-fire tests were performed to fix the F-1's instability issues [18], with an associated estimated cost of billions of dollars [11].

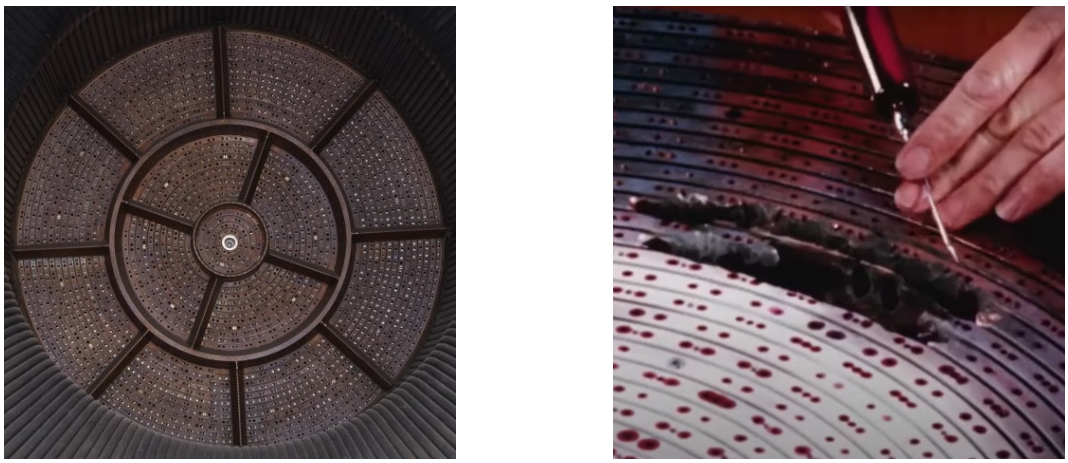

(a) Intact injector plate of the F-1 Engine [19] **(b)** Damaged F-1 injector faceplate [20]

Figure 1.1: F-1 injector faceplate before and after being damaged by a high-frequency instability

These days, the occurrence of combustion instabilities is kept more secretive by the industry. Troubles associated with such phenomena are often hidden since they are difficult problems to solve, with no general rule on how to tackle them, which will bring negative attention to a company. Thus, while being

a problem that any engine designer has to face when developing a new system from scratch, due to the lack of published data it is unclear how many of today´s modern engines have encountered serious combustion instabilities during their development. Of the few documented cases, the LE-8 LOX/LNG engine, developed by the Japanese Space Agency (JAXA) in collaboration with IHI Corporation [10], and the LE-9 LOX/LH_2 engine, developed as the first stage engine for the H3 launch vehicle by Mitsubishi Heavy Industries Ltd. and JAXA [9], are examples of contemporary engines that suffered from unstable combustion dynamics. Looking at the European sector, in 1980 an Ariane 1 launcher's mission failed due to one of its Viking engines (at that time powered by the propellant combination NTO/UDMH) experiencing combustion instabilities [21]. After this episode, in the European scene, combustion instabilities issues appeared again during testing of the Aestus engine in 1998 (running on NTO/MMH), leading to the creation of the European REST program (Rocket Engine Stability initiative) by the CNES, ONERA, DLR, and CNRS [21]. Nowadays, the European joint research program REST incorporates new industry partners and research institutions with the aim to develop methods to predict high-frequency combustion instabilities [22]. In addition, looking at more contemporary engines, mitigation strategies used to get rid of unstable behaviors can also be seen in ArianeGroup´s Vulcain LOX/LH_2 engine, due to the presence of damping devices in the chamber aimed at removing an undesired instability mode, as shown in Figure 1.2 for a cut-out of its combustion chamber, where so-called Helmholtz resonators are visible.

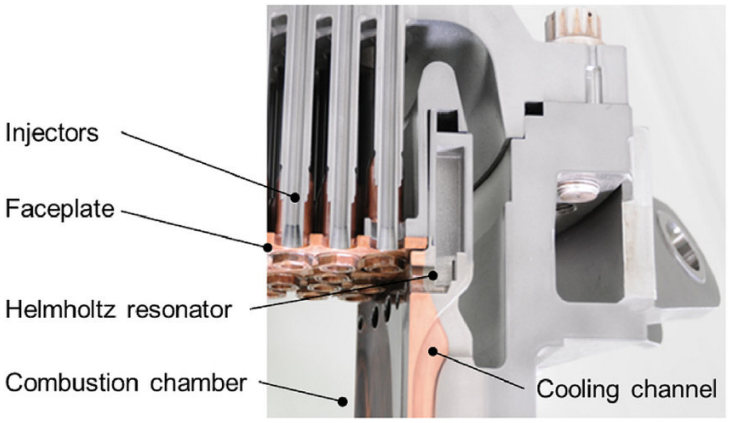

Figure 1.2: Helmholtz resonators visible in the combustion chamber of the Vulcan engine, taken from Armbruster et al. [6]

Therefore, even if companies do not always make it public, unstable combustion dynamics still affect today´s industry despite the many years of advancements in this field since the Apollo era [7, 23]. To investigate the reason why combustion instabilities occur and to find methodologies to mitigate them, the research community, just like the industry, heavily relies on running hot-fire tests to gather experimental evidence [5, 11, 12, 24–28], which requires expensive dedicated equipment to be used. Furthermore, to allow to experiment with high-pressure propulsion systems safely in a laboratory environment often involves scaling down the engine of interest [11]. The latter causes the physics inside the experimental engine to be modified when compared to the full-scale engine. For instance, a consequence of scaling down the system could be the reduction in its power density, which makes the engine less prone to high-frequency instabilities, and could lead to some oscillation modes not being triggered during experiments [11]. Even if a combustor is scaled down with representative power densities, the difference in chamber dimensions will inherently lead to large changes in the resonance frequency of the combustion chamber, creating uncertainty about whether the full-scale system will be stable or not.

Hence, to support the experimental investigations performed by the research community and to provide the industry with a cost-effective way to predict the presence of any instabilities in their systems, there is a need to develop reliable numerical tools to simulate the onset of combustion instabilities in full-scale bi-propellant rocket engines. On top of that, as a result of the ongoing privatization of the space sector, companies are emerging in the launch service segment aiming to develop new launch vehicles to try to

profit from the increasing demand to send payloads to space in a cost-effective way. As a consequence, new liquid rocket engines are being developed at the moment around the world by agile businesses that might not have the time nor money to perform exhaustive qualification tests for their propulsion systems, and for which fully-numerical tools to assess the combustion dynamics of their engine can be desirable. Additionally, these modern liquid rocket engines favor the use of Hydrocarbon-based and Liquid Oxygen (LOX) propellants over the high-performance LOX/Hydrogen propellant combination (used extensively in the past) since they generally allow for cheaper systems to be designed, and are easier to handle [12]. This further emphasizes the need for reliable combustion instability prediction tools since this new alternative propellant combination can not take advantage of the abundant experience that was gained in the past for LOX/LH_2 systems and the respective design mitigation strategies that were devised against severe combustion instabilities [29]. Moreover, another current trend supporting the demand for numerical prediction tools is the decrease of safety margins during design to optimize for a higher system efficiency [30], since the latter would impose a lower boundary on the maximum acceptable pressure oscillation and wall heat transfer generated by the instabilities.

Given the importance that combustion instabilities play in the development of liquid rocket engines, and the need for numerical means to investigate them, this report adds to the body of knowledge targeting to improve the reliability of numerical tools that predict the onset of combustion instabilities in liquid rocket engines.

1.2 Research aim and report structure

The research work presented in this report was performed at the Space Propulsion Institute of the German Aerospace Center (DLR) in Lampoldshausen as part of a Master's thesis in Space Engineering at the TU Delft. As such, to add to the body of research related to the prediction of combustion instabilities in liquid rocket engines, while meeting the time requirement for the thesis, the research had to be focused and boundaries set, which are described hereafter. Starting with what type of instability to study, due to high-frequency instabilities being the most harmful for the operation of the engine, it was decided to limit the research activities to them. High-frequency instabilities are driven by the coupling of the chamber acoustic with the combustion process, and thus, the work was focused on analyzing the combustion chamber only. This means that the instabilities of the overall propulsion system are not considered here and the influences of disturbances occurring far upstream of the chamber are neglected.

Secondly, from the previously outlined need for a reliable numerical approach to predict instabilities, the research proposes the use of an innovative acoustic solver to tackle the shortcomings of similar state-of-the-art solvers and to improve the representation of the acoustic field in the combustor. Furthermore, based on the New Space industry favoring Hydrocarbon-based systems, a LOX/CH_4 engine is examined for the present work. For this, DLR required their Liquid Upper-Stage Demonstrator Engine (LUMEN) to be analyzed. Besides being pertinent for the current worldwide space industry, performing the analyses for LUMEN allows validation data to be retrieved from two hot-fire runs made available by DLR. The choice of the acoustic solver researched in this report study stemmed from the output of a study that surveyed the literature to provide an overview of the different methods used by both the industry and the research community to predict combustion instabilities. From the latter, three classes of approaches were identified, namely Low-Order Modeling (LOM), Acoustic-based methods, and CFD-based methods. From these, Acoustic-based methods were found to be the most practical for an industrial setting and are here considered in this report. The inputs and outputs of the Acoustic-based approaches were further investigated to understand what are the key parameters that drive the correct prediction of combustion instabilities. This boiled down to three aspects: an accurate estimation of the acoustic eigenfrequencies of the combustor, an accurate prediction of the associated damping rates, and an appropriate representation of the heat release rate (also known as the source term) in the function of the flow disturbances encountered in the chamber. From a time-management point of view, all of these aspects could not be analyzed by a

single MSc thesis without already possessing a modeling framework at the start of the research activities. As such, also on the basis of DLR's requirements, the heat release rate source term was omitted from the analyses. The focus was directed primarily to the accurate estimation of the eigenfrequencies, and secondly to assess how the natural damping rates would compare to the real damping rates of the system. Aiming to improve the evaluation of the eigenfrequencies and damping rates from literature, a Linearized Navier-Stokes (LNS) solver is used in this work, which is also benchmarked against the established Helmholtz solver. In contrast to its aeroacoustic counterpart, the Linearized Euler Equations (LEE) solver, namely the most accurate Acoustic-based solver used in literature, LNS offers the inclusion of viscous effects in the analysis and is more numerically stable, thus requiring less stabilization diffusion to be added to the equations. Furthermore, this solver is also available in the software *COMSOL Multiphysics*, which not only represents the most widely used software for Acoustic-based combustion instability analyses in the space propulsion sector [17, 31–34] but is also required to be used by DLR.

The following report is structured as follows. Firstly, a review of the literature dealing with the prediction and modeling of thermoacoustic instabilities in high-power density propulsion systems is provided in Chapter 2. In this chapter, an overview of the acoustic theory needed to gain physical insight into the simulations' results, is provided, and an outline of the available approaches to predict combustion instabilities is described. From this, a detailed look at the previously-mentioned Acoustic-based approaches follows. Chapter 2 summarizes the literature study that preceded this work and is concluded by a comprehensive overview of the eigenfrequency and damping rate accuracies from the literature.

Following is Chapter 3, where, based on the output of the literature survey from Chapter 2, the plan for the research is explained. Here, based on the research gap identified from the literature, the research questions and the research objective for the report are formulated. The chapter is then finalized with an outline of the methodology used in the thesis and a plan for performing the simulations.

Next, with a clear view of the methodology, Chapter 4 presents the various simulation test cases and their respective setups and results. Following from the content of Chapter 3, these are divided into three main categories: Chemical Equilibrium flow, state-of-the-art flow description, and detailed three-dimensional flow description. This subdivision is based on the layers of simplifications that are commonly used in the research community to model the background flow when using acoustic-based prediction methods. The state-of-the-art description refers to slicing the CFD results along the axial direction of the combustor, and at each location taking the cross-sectional average of the field of interest, so to obtain a 1D radially-averaged profile. An improvement of this is then proposed by taking the whole three-dimensional CFD results and mapping them to the computational domain to be used by the simulation of interest.

After obtaining the results of the numerical analyses, aimed at improving the current acoustic modeling standard for thermoacoustic instability analyses, a discussion of the results is provided in Chapter 5. Here, firstly the data of two of LUMEN's hot-fire test runs (for which high-frequency pressure sensors' data was available) is analyzed, and the necessary acoustic information regarding the eigenfrequencies and associated damping rates are extracted for validation purposes. Finally, the numerical results are compared to the obtained experimental results, and hypotheses for the observed difference in the results are formulated.

Finally, the report is concluded in Chapter 6, where also recommendations for future work are laid down. These are formulated to not only improve the results of the current study but also to outline the next steps that need to be tackled to build up the simulation tool to predict the onset of instabilities, which represents DLR's goal to be achieved in the upcoming years.

2 Background

In this chapter, the theoretical background for the work performed during the thesis, and a literature survey concerning the prediction methods of combustion instability, are laid down. High-frequency combustion instabilities are the most harmful to the engine, and given the importance that the acoustic field plays in generating this kind of instabilities, the first part of this chapter, Section 2.2, describes some fundamental concepts of waves occurring inside enclosed passages (also known as guided waves). For the application of interest, the latter section concentrates on acoustic waves propagating inside a cylinder, so to illustrate fundamental physical behaviors that will later be useful to analyze the simulations' results. Furthermore, Section 2.2 will also describe the various canonical fluid dynamic fluctuations to better understand how numerical solvers differ from each other based on their assumptions.

With the theoretical background set, the second part of this chapter provides a review of the literature on predicting combustion instabilities. Firstly, in Section 2.3, a general overview of the different prediction strategies is given. As a second step, within the approaches identified in Section 2.3, a closer look at acoustic-based methods used in this report is taken in Section 2.4. As will become clear from Section 2.3, such hybrid methods are sought after due to their practicality and accuracy, and were chosen to be investigated in this report because not only do they represent the state-of-the-art of combustion instability modeling but also because room for improvement was identified. From these, the Linearized Navier-Stokes (LNS) solver was chosen as the method to be researched in the current work because it has the potential for improving the accuracy of the acoustic modeling of rocket combustors, which lies at the heart of modern stability prediction tools.

2.1 High-frequency combustion instabilities

Before introducing numerical methods to predict the onset of high-frequency combustion instabilities, firstly, a description of the physical mechanism driving this instability is here provided. Even though a detailed understanding of the fundamental mechanisms that drive different types of instabilities is nowadays still lacking [11], a common classification exists among the research community regarding what the different types of combustion instabilities and their most likely excitation mechanisms are [2, 3, 7]. To start, a combustion process is considered stable if the magnitudes of the pressure oscillations' amplitudes in the combustion chamber are under 5% of the nominal chamber pressure. If pressure amplitudes above the 5% threshold are recorded but their occurrence is random, then the combustion process is defined as a *rough combustion* [2]. Finally, for consistent pressure oscillations above 5% of the chamber pressure, the combustion is deemed unstable. Based on its damping characteristics, the system in which the instability occurs can be further classified as an *Amplificator*, if the disturbance causing the instability propagates downstream in the combustion chamber and is eventually washed away, or as a *Resonator*, if the disturbance propagates everywhere and is not dissipated, leading to a self-sustained instability [35]. Once an unstable combustion process has been identified, it can be categorized into one of three types of instabilities, namely low-frequency, intermediate-frequency, or high-frequency instability.

Also known as *Screaming*, *Screeching*, and *Squealing*, high-frequency instabilities typically occur at frequencies above 1000 [Hz]. The main mechanism driving this instability is the coupling between the heat release rate of the flames and the acoustic field of the combustor, hence why they also go by the name of thermoacoustic instabilities or intrinsic instabilities. The latter stems from the fact that the acoustic field is an inherent feature of the combustor that can not be removed [2, 3]. Even though frequency classifications are a commonly used rule of thumb to assess what type of instability occurs in a given

engine, it should be noted that for very large chambers, thermoacoustic instabilities can also occur below the 1000 [Hz] mark [16]. Compared to the other types of instabilities, for the same pressure amplitude, thermoacoustic instabilities contain the largest energy content primarily due to the higher frequencies at which they occur. This becomes visible when expressing the energy transported by a three-dimensional wave traveling through an elastic medium in terms of the amplitude and the frequency, which shows that the energy content is proportional to the squared of the former and the squared of the latter [36]. Additionally, high-frequency instabilities are often encountered when developing new liquid (and solid) rocket engines [2], and while they can couple with the feed system, on their own, they occur only inside the combustion chamber.

As will be explained in Section 2.2, an enclosed geometry such as a cylindrical combustion chamber has distinct acoustic eigenmodes arising. Given that the acoustic field is characterized by an oscillatory pressure disturbance propagating as a wave, and since most rocket combustors can be deemed as acoustically compact systems having little damping [37], these waves reflect at walls with negligible acoustic losses. While propagating in the chamber, if a pressure oscillation attains its maximum amplitude at a point where combustion is happening, then the thermal energy of the latter can be converted into acoustic energy, leading to an increase in the magnitude of the pressure wave's amplitude. This is known as the Rayleigh Criterion [17, 38], which mathematically can be expressed as in Equation 2.1.

$$\int_V \int_{t_s} p'(x,t)Q'(x,t)dtdv \geq \int_V \int_{t_s} \sum_i L_i(x,t)dtdv \tag{2.1}$$

The Rayleigh Criterion is the driving mechanism for high-frequency combustion instabilities [29, 34, 35, 39, 40], and states that in a given volume (V) for a studied time (t_s), a combustion chamber is unstable if the unsteady heat release rate from the flame and the acoustic pressure disturbance (respectively $Q'(x,t)$ and $p'(x,t)$) are periodically larger than the damping losses of the system ($L_i(x,t)$). This can be understood as well from the fact that once energy has been added from the flame to the acoustic wave, after the wave has propagated in the chamber and returns to the same location where the combustion released heat, given the larger pressure amplitude that the wave now has, if the latter is in phase with the heat release rate of the flame, even more energy is added into the acoustic field. After the acoustic wave has traveled back to the combustion region, the latter will experience a higher pressure than the mean chamber pressure leading to an even greater heat release rate of the flame and creating a closed feedback loop with the acoustic field. For the sake of simplicity, for the remainder of the report, high-frequency combustion instabilities will only be referred to as combustion instabilities, a simplistic denomination that is often used in literature [35].

2.2 Flow perturbations and acoustic theory

In this section, a closer look is taken at the nature of the acoustic field inside cylindrically shaped thermoacoustic systems, such as rocket engines. Firstly, a summary of the canonical modes, i.e. naturally arising fundamental modes, occurring when fluid is perturbed by small-amplitude disturbances, is provided in Section 2.2.1. Here, the link between pressure disturbance and acoustics is made, and it is discussed how the different canonical modes can couple with each other. Then, by isolating the acoustic propagation from the other two canonical modes, namely entropy and vorticity disturbances, in Section 2.2.2, the homogeneous wave equation is solved to obtain the acoustic eigenmodes inside a cylindrical geometry. Finally, with an understanding of how the pressure disturbance tends to propagate inside cylindrical geometries, Section 2.2.3 concludes the section by discussing how flow effects need to be accounted for in rocket propulsion applications for accurate acoustic modeling.

2.2.1 Flow perturbations

Acoustic waves are compression waves that travel through a medium via pressure oscillations. The latter cause regions of compression and rarefaction that are then transferred to the nearby molecules of the

medium and that are eventually picked up by our eardrums and perceived as sound. Therefore, in a fluid medium, acoustic waves propagate due to unsteady pressure disturbances. If a fluid is perturbed, the pressure disturbance that causes sound is not necessarily the only one that gets generated. Disturbances in temperature, velocity, density, vorticity, and entropy are also propagated. These effects are already included in the compressible formulation of the governing equation of fluid flow, that is the Navier-Stokes equations, but can not be identified in the equations since they fall under the mean flow variables. To visualize the different disturbances it is useful to make use of linear propagation theory and to linearize the governing equations about small perturbations.

To start, the Navier-Stokes equations are considered, with the Continuity, Momentum, and Energy equations given by Equation 2.2, Equation 2.3, Equation 2.4, respectively. Here, the use of Delfs [41] formulation is made, where **M** is the source term for the mass, **F** is the source term for external forces acting on the fluid and **Q** is the heat source term. Furthermore e_t, given by $e_t = e + \frac{1}{2}\mathbf{u}^2$, is the total specific energy, and τ, given by $\underline{\underline{\tau}} = \mu_\lambda(\nabla \cdot \vec{\mu})\underline{\underline{\delta}} + 2\mu\underline{\underline{S}}$, is the viscous stress tensor, with μ indicating the dynamic viscosity, and μ_γ the second viscosity or bulk viscosity. In addition, k represents the thermal conductivity, $\underline{\underline{\delta}}$ the Kronecker unit delta, and $\underline{\underline{S}}$ the tensor of the strain rate, determined via $\underline{\underline{S}} = \frac{1}{2}\left[\nabla\vec{u} + (\nabla\vec{u})^T\right]$.

$$\frac{\partial \rho}{\partial t} + \nabla \cdot (\rho \mathbf{u}) = M \tag{2.2}$$

$$\frac{\partial \rho \mathbf{u}}{\partial t} + \nabla \cdot (\rho \mathbf{u}\mathbf{u}) + \nabla p = \nabla \cdot \underline{\underline{\tau}} + \mathbf{F} + M\mathbf{u} \tag{2.3}$$

$$\frac{\partial \rho e_t}{\partial t} + \nabla \cdot (\rho e_t \mathbf{u}) + \nabla \cdot (p\mathbf{u}) = \nabla \cdot (k\nabla T) + \nabla \cdot (\underline{\underline{\tau}}\mathbf{u}) + \mathbf{Q} + \mathbf{F} \cdot \mathbf{u} + M e_t \tag{2.4}$$

Assuming canonical disturbances to be small-amplitude perturbations that are superimposed over the mean flow, Equation 2.5, Equation 2.6 and Equation 2.7 can be used to describe the perturbations about the background flow variables by decomposing the variables into their mean steady-state value (indicated by the subscript $\langle 0 \rangle$), and into small, unsteady disturbances (denoted using the superscript $\langle' \rangle$). This assumption can be justified by taking acoustic pressure as an example. The threshold of pain for the human ear lies around an acoustic pressure amplitude of 200 [Pa] [42]. While pressures in liquid rocket combustion chambers can easily range from 30 to 80 [bar] for research combustors [5, 43, 44], and up to pressures of 200 to 300 [bar] for high-performance main stage engines [45, 46]. Thus, by representing less than 0.5% of the standard sea level atmospheric pressure, even if high values are considered for the amplitude of the acoustic pressure, this is still several orders of magnitude smaller than the chamber pressure of liquid rocket engines, and therefore its amplitude can be considered much smaller than that of rocket engines' mean flows. This also makes it acceptable to neglect higher order fluctuation terms in Equation 2.5, Equation 2.6 and Equation 2.7. While this linearized approach can be used at the onset of instability, where the amplitudes of the oscillation can still be considered small compared to the mean operating point of the engine, as will be explained later at the end of this subsection, it can not be used to model the whole development of the instability, where amplitudes of the order of magnitude of the operating pressure are reached.

$$p(\mathbf{x}, t) = p_0(\mathbf{x}) + p'(\mathbf{x}, t) \tag{2.5}$$

$$\rho(\mathbf{x}, t) = \rho_0(\mathbf{x}) + \rho'(\mathbf{x}, t) \tag{2.6}$$

$$\mathbf{u}(\mathbf{x}, t) = \mathbf{u_0}(\mathbf{x}) + \mathbf{u}'(\mathbf{x}, t) \tag{2.7}$$

Substituting Equation 2.5, Equation 2.6 and Equation 2.7 into Equation 2.2, Equation 2.3 and Equation 2.4, and expanding the equations about the first order perturbation, leads a set of linearized fluid dynamic equations known as the *Linearized Navier-Stokes* (LNS) equations. These are given by Equation 2.8 for the Continuity equation, by Equation 2.9 for the Momentum equation, and by Equation 2.10 for the Energy equation.

$$\frac{\partial \rho'}{\partial t} + \nabla \cdot \left(\rho_0 \mathbf{u}' + \rho' \mathbf{u}_0\right) = M \tag{2.8}$$

$$\rho_0 \left(\frac{\partial \mathbf{u}'}{\partial t} + \left(\mathbf{u}' \cdot \nabla\right) \mathbf{u}_0 + \left(\mathbf{u}_0 \cdot \nabla\right) \mathbf{u}' \right) + \rho' \left(\mathbf{u}_0 \cdot \nabla\right) \mathbf{u}_0 = \nabla \cdot \sigma + \mathbf{F} - \mathbf{u}_0 M \tag{2.9}$$

$$\begin{aligned} &\rho_0 C_\mathrm{p} \left(\frac{\partial T'}{\partial t} + \left(\mathbf{u}' \cdot \nabla\right) T_0 + \left(\mathbf{u}_0 \cdot \nabla\right) T' \right) + \rho C_\mathrm{p} \left(\mathbf{u}_0 \cdot \nabla\right) T_0 \\ &- \alpha_\mathrm{p} T_0 \left(\frac{\partial p'}{\partial t} + \left(\mathbf{u}' \cdot \nabla\right) p_0 + \left(\mathbf{u}_0 \cdot \nabla\right) p' \right) - \alpha_\mathrm{p} T' \left(\mathbf{u}_0 \cdot \nabla\right) p_0 = \nabla \cdot \left(\mathrm{k} \nabla T'\right) + \Phi + Q \end{aligned} \tag{2.10}$$

As will be motivated in the next chapter, the software *COMSOL Multiphysics* is used for the subsequent research activities to run the required simulations. For this reason, in the above equations, COMSOL's formulation has been used. Here, the viscous stress tensor has been renamed from τ (as used in the previously shown Navier-Stokes equations) to σ. Also, the bulk viscosity has been renamed from μ_λ to μ_B, and α_P represents the coefficient of thermal expansion and β_T is the isothermal compressibility. The equations can be further transformed from the time domain into the frequency domain by assuming the disturbances to be harmonically oscillating, and thus being able to use Fourier transform reformulation as given by Equation 2.11 for the pressure, where F_p represents its Fourier transform.

$$p'(\mathbf{x}, t) = F_p(\mathbf{x}, \omega) e^{-i\omega t} \tag{2.11}$$

Referring to the work of Lieuwen [40], the canonical disturbances can then be derived from the above-shown LNS equations. To simplify the analysis, Lieuwen further assumes the flow to be inviscid, one-dimensional, non-reactive, isentropic, calorically perfect, and with negligible molecular transport. After transforming the simplified equation in the frequency domain, and after manipulating them into an eigenfunction form, a solution for the complex pressure, density, and velocity fluctuations can be obtained. This can be further expanded to account for the fluctuation of vorticity and entropy as well, leading to the solution of the simplified equations given by Equation 2.12. A detailed derivation was omitted since it was considered to be outside the scope of this report, and for that, the interested reader is referred to the work of Lieuwen [40].

$$\begin{bmatrix} \hat{p}'(x) \\ \hat{\rho}'(x) \\ \hat{T}'(x) \\ \hat{u_x}'(x) \\ \hat{u_y}'(x) \\ \hat{s}'(x) \\ \hat{\Omega}'(x) \end{bmatrix} = \begin{bmatrix} 1 & 1 & 0 & 0 \\ \frac{1}{c_0^2} & \frac{1}{c_0^2} & 1 & 0 \\ \frac{\gamma-1}{\gamma p_0} T_0 & \frac{\gamma-1}{\gamma p_0} T_0 & -\frac{T_0}{\rho_0} & 0 \\ \frac{1}{\rho_0 c_0} & -\frac{1}{\rho_0 c_0} & 0 & 0 \\ 0 & 0 & 0 & 1 \\ 0 & 0 & \frac{\gamma R}{(\gamma-1)\rho_0} & 0 \\ 0 & 0 & 0 & \frac{i\omega}{u_{x,0}} \end{bmatrix} \begin{bmatrix} A_p e^{\frac{i\omega x}{c_0 + u_{x,0}}} \\ B_p e^{\frac{i\omega x}{c_0 - u_{x,0}}} \\ A_s e^{\frac{i\omega x}{u_{x,0}}} \\ A_\Omega e^{\frac{i\omega x}{u_{x,0}}} \end{bmatrix} \tag{2.12}$$

From the solution, the oscillations in flow variables are expressed in function of three canonical modes, namely acoustic, vortical, and entropy disturbances. From such analysis, it becomes clear which flow variables' oscillations are due to which canonical mode. Firstly, from Equation 2.12, it can be seen that the acoustic disturbance influences pressure, density, temperature, and velocity fluctuations, since the first two terms of the right-most column vector of Equation 2.12 represent the acoustic fluctuations [40]. While the entropy mode influences the temperature and density oscillations, the vortical mode only affects the velocity variations [40]. This shows that on one hand the acoustic and vortical modes affect the fluid motions, and on the other hand the acoustic and entropy modes influence the thermodynamic state of the flow and that overall the acoustic mode plays a central role in affecting all the oscillations. In addition, the solution presented by Lieuwen also shows the acoustic wave propagating both upstream and downstream at the speed of sound (corrected by the flow velocity), while the entropy and vortical modes are advected from regions of high concentrations to regions of low concentrations at the characteristic speed of the flow.

Canonical mode coupling

While from Equation 2.12 it can be seen that the three canonical modes propagate independently from each other, these can couple as a result of boundary conditions, flow non-uniformities, and non-linearities, for which a short description of each is presented below. While non-linearities can not be accounted for by the linearized governing equations presented above, boundary conditions are always present for a well-posed problem and large flow non-uniformities occur inside a rocket combustor, especially across the flame region. To account for the coupling due to these two effects, an appropriate numerical approach will have to be used (such as solving the LNS equations).

Firstly, the coupling between the canonical modes always occurs due to given boundary conditions. At boundaries, such as a wall, the total fluctuation must be prescribed, which following the previous discussion, always involves more than one mode. Taking the wall boundary condition as an example, this can impose a constraint on the velocity and temperature fluctuations. For the total velocity fluctuation, which will couple the acoustic and vortical modes, a zero normal velocity fluctuation component at the boundary or a no-slip wall (zero overall velocity fluctuation at the boundary) can be described. The null normal velocity condition will require an incident acoustic wave to be reflected at the wall at an angle equivalent to the incidence angle. While the no-slip condition, further requires the tangent velocity to be zero as well. This necessitates the vortical mode to excite a velocity oscillation that can cancel out the acoustic velocity term at the wall. The latter can be visualized in Figure 2.1 and corresponds to a transfer of energy (loss) from the acoustic mode to the vortical one. Similarly, temperature oscillations can also be described at the wall, with the choice between an adiabatic wall and an isothermal wall, both coupling the acoustic mode with the entropy mode.

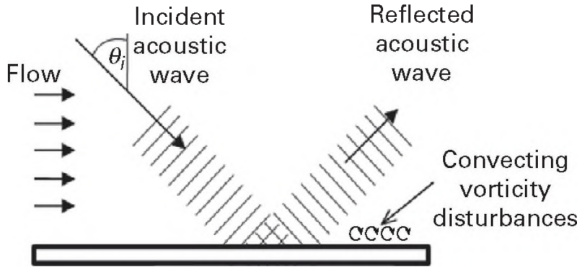

Figure 2.1: Acoustic and vortical mode coupling due to a no-slip wall boundary condition. Taken from Lieuwen [40]

Secondly, mode coupling can also occur due to flow non-uniformities. This is visible if the equation for the rate of variation of the vorticity is considered, and in it, the equations describing the variables' variations about the mean flow variables are substituted (i.e. equations of the form of Equation 2.5), resulting in Equation 2.13 [40]. From the latter equation it becomes clear that if the background flow is rotational, that is $\Omega_0 \neq 0$, velocity gradients will excite vortical fluctuations over time. Also, vorticity perturbations are excited if the background flow and the oscillatory disturbances are baroclinic (i.e. gradients of pressure and density are not aligned). Similarly, in zones where entropy disturbances are accelerated, such as the nozzle, so-called acoustic-entropy waves are generated, where acoustic fluctuations are excited [47].

$$\frac{D_0\Omega'}{Dt} = -\mathbf{u}' \cdot \nabla\Omega_0 + \Omega_0 \cdot \nabla\mathbf{u}' + \Omega' \cdot \nabla\mathbf{u}_0 - \Omega_0\nabla \cdot \mathbf{u}' - \Omega'\nabla \cdot \mathbf{u}_0 + \frac{\nabla\rho' \times \nabla p_0}{\rho_0^2} + \frac{\nabla\rho_0 \times \nabla p'}{\rho_0^2} \quad (2.13)$$

Lastly, the coupling of acoustic, entropy, and vortical modes can also arise due to non-linearities in the equations. The analysis here presented accounted only for first-order fluctuating terms, but if the equations are expanded to include higher-order terms, then the interaction between the canonical modes will take place directly in the governing equations even in the absence of flow non-uniformities [40]. As described by Lieuwen, if second-order terms are included, these will grow proportional to the square of

the amplitude of the oscillations and should be included when nonlinear regimes of instability need to be analyzed, or if the amplitude of the disturbance is large, for example, if the pressure fluctuation has the same order of magnitude as the chamber pressure.

An illustratory example of this is given in Figure 2.2, where the development of the pressure oscillation of a combustion instability is considered over time. The various stages of an instability's evolution depict that it first starts growing linearly before starting to resonate and growing exponentially, leading up to the so-called overshoot region [35]. Here, the exact maximum amplitude reached depends on various factors, with the first one being if the engine is structurally able to sustain the loads. If the engine does not fail, dynamic combustion effects such as flame quenching can halt the combustion, or, given the high oscillating pressure amplitudes reached, non-linear effects can lead to a redistribution of energy to other combustion instability modes [40]. If the combustion chamber can endure the overshoot zone, the limit-cycle region is reached. Here, non-linear effects lead to constant amplitude oscillations.

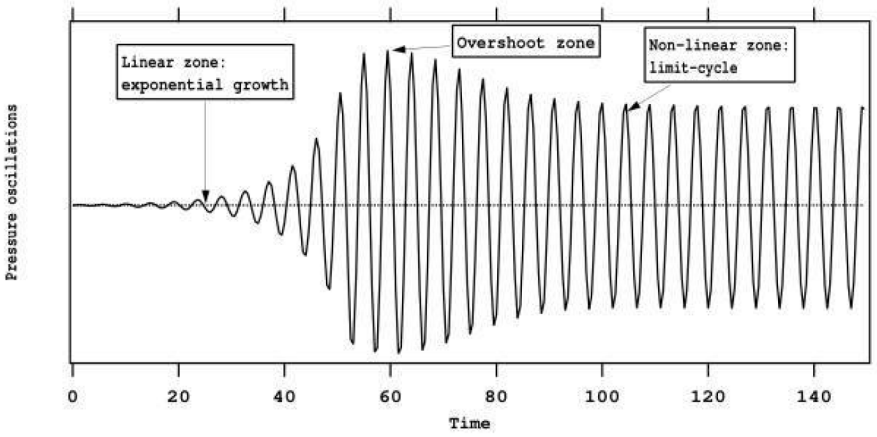

Figure 2.2: Temporal development of combustion instability. Taken from Poinsot & Veynante [35]

To model the behavior of the overshoot and limit-cycle regimes, the linearized governing equations need to be expanded to include non-linear effects (i.e. to include higher-order fluctuation terms). To get to a point where these instability regions can be accurately predicted, first a reliable prediction of the onset of the instability is needed. Since a tool to do so is still missing nowadays [11, 12], it is deemed more critical to be able to predict whether an instability occurs than to be able to model its effects after it has occurred. Therefore, given the simplifications that can be applied to predicting the onset of combustion instabilities, only the linearized set of governing equations will be considered for the remainder of this report. For a derivation and investigation of the non-linear set of governing equations, the interested reader is referred to the work of Portillo et al. [48], Krediet et al. [49] and Nayfeh [50]. As explained later in Section 3.2.3, by formulating the linearized equations in the frequency domain, the eigenfrequencies, the damping rates, and the spatial distributions of the wave of considered parameters (called the mode shapes) can directly be obtained as the output of the analysis. Whether a given mode is stable or not can directly be analyzed by the damping rate, where positive values indicate stable cases that are dampen out, while negative values represent growth rates of unstable modes. If excessively large pressure amplitudes are returned by the linearized analysis, to the level of requiring design changes to be implemented, then these are expected to occur around the overshoot region of Figure 2.2, which is governed by exponential growth for which the small-amplitude assumption of the linearized equations breaks down. Hence, even though high-amplitude regions can not be accurately modeled by a linearized approach, this can still be used to assess if the pressure amplitudes that are solved for are of the same order of magnitude as the chamber pressure. If that is the case, then, to know if instabilities can be sustained or not by the system, a non-linear simulation will have to be performed.

2.2.2 Wave equation

Previously, the Rayleigh Criterion introduced the fundamental coupling mechanism that is driving high-frequency combustion instabilities. It stated that the combustion process can transfer energy into the acoustic field via its heat release rate, leading to larger pressure fluctuations in the chamber. Section 2.2.1 then followed and presented that various canonical disturbance modes for fluids exist. After linearizing the governing equations about small amplitude disturbances, and simplifying the equations to allow for a closed-form solution to be found, Equation 2.12 revealed that three natural disturbance modes exist, namely acoustic, entropy, and vortical modes. Equation 2.12 also showed that pressure fluctuations are associated with the acoustic mode and that they can be influenced by vortical and entropy modes only due to boundary condition coupling and flow non-uniformities coupling. Therefore, given that acoustics represents the main canonical mode influencing the pressure fluctuations, in this subsection, the governing equations are simplified to only model the effect of the acoustic field, and to present how the pressure fluctuations tend to propagate inside a cylindrical geometry.

Beginning with the Navier-Stokes equations given by Equation 2.2, Equation 2.3 and Equation 2.4, the same approach of decomposing the flow variables into their mean background flow component and their oscillatory part, as done previously to derive the LNS equations, is used. To derive the wave equation, the flow is further assumed to be inviscid, isentropic, non-reactive, and quiescent (i.e. M=0), so to simplify the analysis. Given the latter assumptions, the isentropic relation can be used to link the pressure to the density. Next, taking the time derivative of the simplified continuity equation, subtracting the divergence of the momentum equation from it, and using the isentropic relation, leads to the homogenous wave equation describing the propagation of the pressure oscillations. This is given by Equation 2.14.

$$\frac{1}{c_0^2}\frac{\partial (p')^2}{\partial t^2} - \nabla^2 p' = 0 \tag{2.14}$$

The above equation describes the propagation of acoustic waves in space and time. By assuming the wave to be harmonically oscillating, the complex pressure representation, as given by Equation 2.15, can be used to decouple the temporal dimensions from the spatial one, by converting the equation in the frequency domain. The resulting equation goes by the name of the homogeneous Helmholtz equation and is reported in Equation 2.16. In the two equations below, ω is the oscillation frequency in radian per second, and k, given by $k = \frac{\omega}{c_0} = 2\pi\frac{f}{c_0}$, is the wavenumber.

$$p'(x,t) = Re\left(\widehat{p}(x)e^{-i\omega t}\right) \tag{2.15}$$

$$\nabla^2\widehat{p} + k^2\widehat{p} = 0 \tag{2.16}$$

Acoustic boundary conditions

To solve the above Helmholtz equation, two boundary conditions have to be applied and it is useful to describe them directly in terms of the pressure oscillation. For that, three boundary conditions that are often used to constrain acoustic problems are briefly introduced below. Albeit also imposing a constraint on the velocity fluctuation, for the sake of simplicity, for the remainder of this report these conditions will be referred to as acoustic boundary conditions. Firstly, the Admittance (Y) is introduced, which can be seen as the amount of energy that passes through a system's boundary [24]. The Admittance for a standing wave is given by Equation 2.17, while for a traveling wave by Equation 2.18. In the latter, A^+ and A^- respectively indicate the amplitude of the wave incident to the boundary considered, and the amplitude of the wave reflected from it.

$$Y = \rho_0 c_0 \frac{\mathbf{n}\cdot u'}{p'} \tag{2.17}$$

$$Y = \frac{A^+e^{-ikx} + A^-e^{ikx}}{A^+e^{-ikx} - A^-e^{ikx}} \tag{2.18}$$

Secondly, the Admittance can also be linked to the so-called Reflection coefficient (R), via Equation 2.19. The Reflection coefficient, contrary to the Admittance, indicates the amount of energy that is not transmitted through a boundary and is thus reflected. As for the Admittance, also the Reflection coefficient makes use of the amplitudes of the waves leaving/reflected from the boundary, and hence, a reference orientation has to be defined.

$$R = -\frac{1-Y}{1+Y} = \frac{A^+}{A^-} \tag{2.19}$$

The third acoustic boundary condition here presented is the Impedance (Z), which has the advantage, over the two conditions introduced before, that it can be described independently of the chosen reference axis' orientation. A distinction is made between Impedance and Characteristic Impedance (Z_c), the two given by Equation 2.20 and Equation 2.21, respectively. In the following report, the notation utilized by Poinsot [35] is used to define the Impedance, and depending on the author, the exact definition of the latter can vary. For instance, Lieuwen [40] defines the Impedance simply as the ratio of the pressure fluctuation over the velocity fluctuation.

$$Z = \frac{1}{\rho_0 \cdot c_0}\frac{p'}{u'} \tag{2.20}$$

$$Z_c = \rho_0 \cdot c_0 \tag{2.21}$$

Furthermore, the Impedance can also be linked to the Reflection coefficient and the Admittance, via Equation 2.22

$$R = -\frac{1-Y}{1+Y} = \frac{Z+1}{Z-1} \tag{2.22}$$

For a correct description of the acoustic field inside a rocket combustion chamber, being able to accurately represent the inlet boundary conditions of the injector elements and the outlet boundary of the nozzle is crucial. In practice, they are either determined via complex formulations or derived from experiments [51, 52]. For the nozzle boundary condition, it was standard practice in the past to determine the Admittance or the Impedance via semi-empirical equations [53–58]. While nowadays, ISO standards are available to evaluate this for cylindrical geometries [59, 60]. Despite a large number of literature available to estimate the acoustic boundary condition of choked nozzles, determining the acoustic boundary conditions of the injector is more difficult and less researched [24, 32]. An approach, used especially during an early analysis of combustion instabilities, is to use idealized acoustic boundary conditions for the nozzle throat and the injector elements to represent their principal effects [11, 17]. An overview of these idealized conditions is shown in Figure 2.3, where an "Open" condition (also known as *Sound Soft* [17]) specifies no resistance to the wave propagation across a boundary and hence leads Z=0. Conversely, a "Closed" condition (known as well by the name of *Sound Hard* [17]) fully obstructs the passage of a wave through the boundary and results in Z=∞.

Description	Scenario	Condition	Impedance	Reflection Coefficient
Infinite Inlet	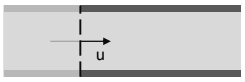	Non-reflecting	Z = - 1	R = 0
Infinite Outlet		Non-reflecting	Z = 1	R = ∞
Constant Pressure	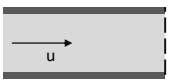	Non-reflecting (Open) $p' = 0$	Z = 0	R = - 1
Wall	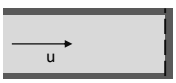	Reflecting (Closed) $u' = 0$	Z = ∞	R = 1
Choked Flow		Reflecting $u' = 0$	Z = ∞	R = 1

Figure 2.3: Summary of ideal boundary conditions for guided waves. Taken from Trotta [61]

Acoustic eigenmodes

With the acoustic boundary conditions presented, a solution of the Helmholtz equation (Equation 2.16) can be solved for. The case of a cylinder with a uniform cross-section and no background flow is here considered. This very simplified case allows finding an analytical solution for the frequencies at which pressure fluctuations tend to oscillate in a geometry similar to a rocket combustion chamber. By making use of the cylindrical coordinates (r, θ, x), the eigenfrequency solution for a Closed-Closed or Open-Open cylinder is given by Equation 2.23 [35]. In the equation, D is the cylinder's diameter, L its length, and m, n, q indicate the chamber's acoustic eigenmodes, with q referring to the longitudinal mode, n to the tangential mode and m to the radial mode. The latter two are transverse modes, meaning that their oscillation happens within the cross-sectional plane of the cylinder. Furthermore, $\alpha_{m,n}$ is the solution of the Bessel function $J(\pi\alpha_{m,n}) = 0$, for which several values are tabulated in Table 2.1. Equation 2.23 shows that three main modes are naturally excited in a cylindrical geometry, and a combination of them can also take place.

$$f_{m,n,q} = \frac{c_0}{2}\sqrt{\left(\frac{\alpha_{m,n}}{\frac{D}{2}}\right)^2 + \left(\frac{q}{L}\right)^2} \tag{2.23}$$

Table 2.1: Values of the $\alpha_{m,n}$ coefficient leading to the roots of the Bessel function $J(\pi\alpha_{m,n})$

$\alpha_{m,n}$	**m = 0**	**m = 1**	**m = 2**	**m = 3**	**m = 4**
n = 0	0.000	1.220	2.333	3.238	4.241
n = 1	0.586	1.697	2.717	3.726	4.731
n = 2	0.972	2.135	3.173	4.192	5.204
n = 3	1.337	2.551	3.612	4.643	5.662
n = 4	1.693	2.995	4.037	5.082	6.110

As an illustration, Figure 2.4 presents how within a given cross-section of the cylinder, the transverse modes oscillate. Of the high-frequency instability modes, the tangential ones are considered to be the most damaging [2]. To complement this, Figure 2.5 shows the pressure eigenmodes for a cylinder with both ends acoustically closed, for the first two longitudinal modes, the first two tangential modes, the first radial mode, and the combination of the latter transverse modes with the two longitudinal modes. These modes were obtained by solving the homogeneous Helmholtz equation in COMSOL Multiphysics. Taking the example of the longitudinal modes, these can be distinguished by analyzing their wavelength knowing that it is given by $\lambda = \frac{2L}{n}$, where n=1, 2, 3, etc, for standing waves in a pipe with both ends closed, where, n represents the various harmonics and L is the length of the pipe. Similarly, for a pipe with one end closed and the other open, the relationship for the wavelength follows $\lambda = \frac{4L}{n}$, this time with n=1, 3, 5, etc. Taking the example of the first tangential (i.e. T1) mode, firstly, for the commonly used geometries of rocket combustion chambers, it arises at a higher frequency than the first longitudinal (i.e. L1) mode (hence associated with a higher energy content), but not at as high frequency as higher tangential modes or radial modes (possibly resonating with the feed system). Secondly, as explained in more detail in the next subsection, in practical combustors transverse modes have their pressure oscillation concentrated at the injector plate. Given the velocity oscillation that they induce along the radial direction of the engine, they greatly influence the flame structure and can increase by several factors the heat transfer to the chamber wall [2, 40]. Furthermore, at the injector plate, the pressure oscillation caused by these modes can result in boundary layer thinning [2], further increasing the heat flux from the gases to the wall.

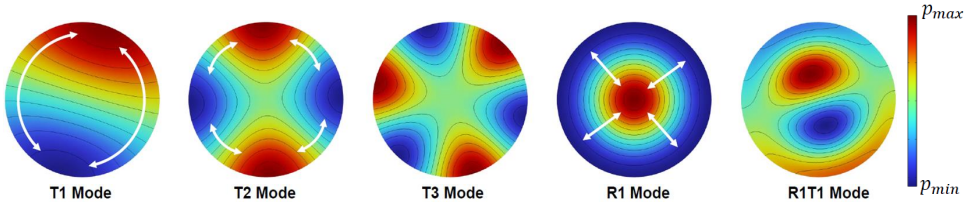

Figure 2.4: Pressure fluctuations of the transverse eigenmodes for a guided wave inside a cylindrical geometry in a quiescent flow. Taken from Trotta [61]

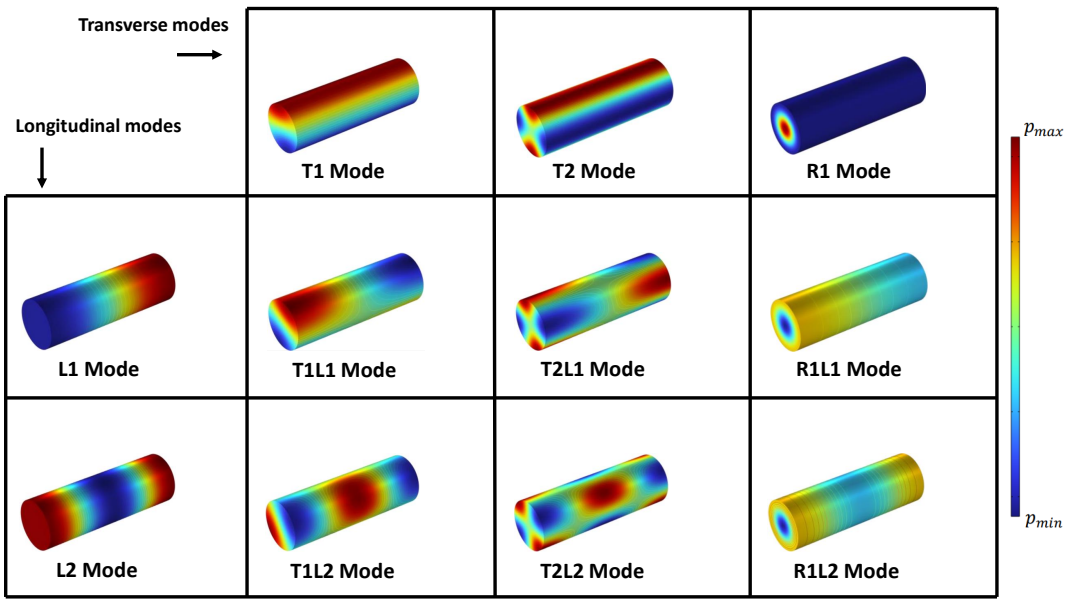

Figure 2.5: Acoustic eigenmodes (pressure fluctuations) for a guided wave inside a cylindrical geometry in a quiescent flow

2.2.3 Flow effects

The previous subsection presented how pressure fluctuations propagate in a cylinder in the absence of a moving background flow. This can further be extended to account for the influence that background flow gradients have on the acoustic field. A region of high gradients in a rocket engine is known to be the nozzle, where the combustion gases get accelerated from the Mach number at the end of the combustion chamber (which can attain values up to 0.4 [2]) to sonic conditions at the throat, where the assumption of quiescent flow is not valid. Besides the gradients associated with accelerating the flow, the combustion region inside a chamber is also the source of large gradients. Its effects on the speed of sound are shown in Figure 2.6, where the axial variation of the speed of sound for DLR's LOX/LH_2 BKD combustor is depicted [43]. The curves in the figure, all retrieved from CFD fields, indicate different operating conditions. The axial variation was computed by slicing the CFD results along the longitudinal direction of the combustion chamber, and at each slice taking the area average.

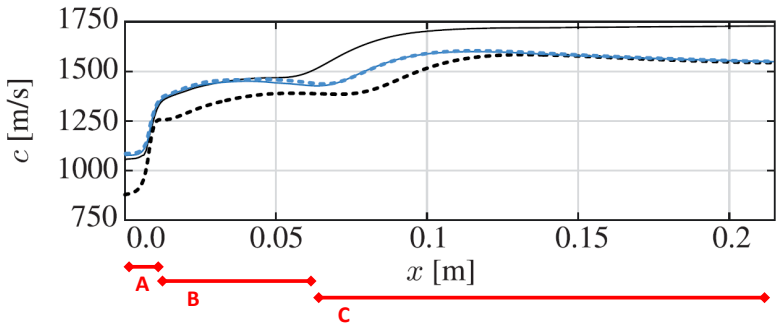

Figure 2.6: Longitudinal variation of the radial-averaged speed of sound of the BKD combustor, for different simulation runs. Taken from Trotta [61], and originating from Schulze & Sattelmayer [43]

From Figure 2.6, three regions of large speed of sound variation are visible. These were arbitrarily noted as regions A, B, and C for clarity. In region A the cryogenic propellants are injected, while in region B combustion occurs at the periphery of the LOX core [43]. Finally, once most of the combustion process has been completed, the second plateau of region C is reached. Overall, large gradients over small distances are created in the background flow by the combustion process, and it is expected that the acoustic field would be majorly influenced by this too. Even though a closed-form solution for the

non-homogenous Helmholtz equation accounting for flow gradients can not be obtained, Gröning presents a derivation to obtain the analytical solution of the Helmholtz equation with the presence of a uniform background flow field [62], with the solution provided by Equation 2.24.

$$f_{mnq} = \frac{c_0}{2}\sqrt{\left(\frac{\alpha_{nm}}{\frac{D}{2}}\right)^2\left(1-M_0^2\right)+\left(\frac{q}{L}\right)^2\left(1-M_0^2\right)^2} \tag{2.24}$$

The above equation shows that the higher the Mach number of the background flow, the lower the eigenfrequency of a given mode becomes. Furthermore, Equation 2.24 also shows that the presence of a moving background field lowers a longitudinal mode more than a transverse one since the former has a $(1-M_0^2)$ dependency on the Mach number, while the latter only $\sqrt{(1-M_0^2)}$. Regarding how the mode shapes are influenced by an increasing Mach number, in his work, Gröning also provides the modes shapes for the pressure, computed at M=0 and M=0.2. These are shown for the T1 mode in Figure 2.7, and display that the higher the Mach number, the more transverse modes get focused on the inlet face of the cylindrical geometry considered.

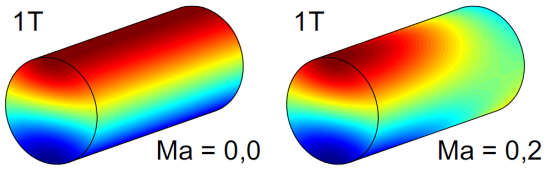

Figure 2.7: Comparison of the T1 eigenmode for Mach M=0 and M=0.2. Taken from Gröning [62]

On top of reducing the eigenfrequencies of the system and modifying its mode shapes, the presence of a moving background flow also affects its acoustic losses. In a quiescent flow inside a cylinder, if a reflection coefficient of one is used on all of its boundaries, all of the acoustic waves get reflected and its energy is retained. This does not hold anymore with the presence of a moving flow. Even if a unity reflection coefficient is again considered, a portion of the energy gets lost through the outlet boundary due to the convecting effect of the background flow. This can be demonstrated by analyzing the time-averaged acoustic intensity flux crossing the outlet boundary and the intensity flux of an incident wave crossing this boundary directly [40]. Taking the ratio of the former (I_{avg}) over the latter (I_i) simplifies to Equation 2.25. Considering the previously mentioned reflection coefficient of one, it can be seen that even if a Mach number as low as 0.1 is taken, over time, only 33% of the initial incident flux remains in the system.

$$\frac{I_{avg}}{I_i} = \frac{(1+M)^2-|R|^2(1-M)^2}{(1+M)^2} \tag{2.25}$$

2.3 Stability prediction techniques

The previous section introduced the conceptual basis needed to understand how acoustic waves behave inside a rocket combustor, and what aspects of high-frequency instabilities can be modeled using linearized perturbation theory. With the theoretical foundation set, the following section provides an overview of the numerical methods that are available to model combustion instabilities in liquid rocket engines. They are classified based on three main categories distinguished by their main features, these being: CFD-based models, low-order models, and acoustic-based models, respectively summarized in Section 2.3.1, Section 2.3.2 and Section 2.3.3. Based on these summaries, the acoustic-based models were chosen as the preferred modeling approach given their trade-off between modeling complexity and computational cost.

A general overview of the methods that can be used to model combustion stability is provided in Figure 2.8. This expands upon the classification given by Beinke in his Ph.D. thesis [17] and classifies the different

models into one of three categories, namely low-order models (LOM), Acoustic-based models, and CFD-based models. In Figure 2.8, these three families of modeling approaches are arranged based on their associated computational cost (on the abscissa) and modeling simplifications (on the ordinate). As a reference, on the same graph, experiments are also plotted. These can not only be used on their own as a way to assess combustion stability but their results can also be utilized as input for the previously mentioned numerical methods, as visible through the dotted grey lines which link the output of one method to the input of another. The two inputs that the numerical methods used to predict combustion instabilities require are the flow properties inside the combustion chamber, and, depending on the method considered, the transfer function describing the response of the flame under given conditions. Note, that while not plotted in Figure 2.8, the flow properties can also be computed via other approaches, for example via Chemical Equilibrium with Applications (CEA). It should also be pointed out that in Figure 2.8, the classification of the methods (i.e. fidelity versus cost) is not to scale, meaning that the relative distance between methods does not provide information, for example, about how much more expensive a given method is with respect to another one.

What primarily distinguishes the three prediction methodologies presented in Figure 2.8 is how the combustor acoustics is modeled concerning the reactive flow inside the combustor (here simply named as the flow field), for which two approaches can be devised. These two approaches divide the prediction models into those that solve the flow field and the acoustic simultaneously (i.e. falling within the CFD-based method), and those that decouple the acoustic from the flow field, solving for the former assuming small-amplitude disturbances and employing linearized perturbation theory (i.e. falling under the LOM or Acoustic-based methods). Within the latter group, a further distinction can be made based on whether the chosen method solves for the linearized governing equations only in one dimension and sets up a network of transfer functions to describe the system (i.e. LOM), or solves the linearized equations in two or three dimensions accounting for the realistic geometry of the system (i.e. Acoustic-based methods). It should be noted that while a clear distinction exists between CFD-based methods and the other two approaches, the difference between the Acoustic-based methods and LOM is more cloudy, with the latter that can be seen as a ”sub-method” of the former, for which a network of the transfer function can be set similar to the ones used in control theory. The three approaches that can be applied to predict combustion instabilities in propulsive systems are described hereafter.

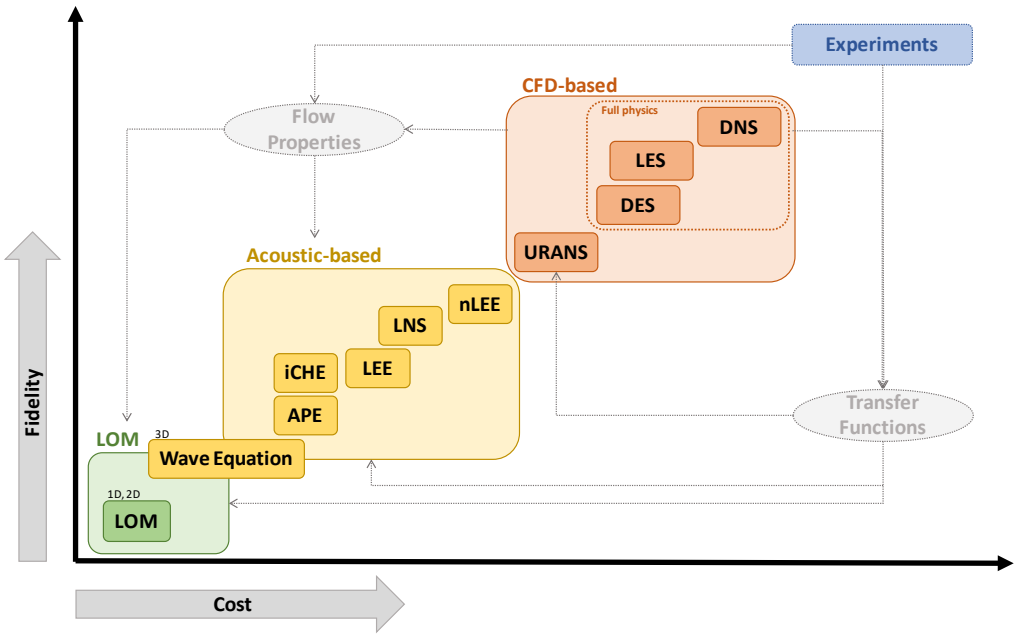

Figure 2.8: Overview of numerical high-frequency combustion instability prediction methods. Taken from Trotta [61], and originally adapted from Beinke [17]

2.3.1 CFD-based models

The first class of methods considered corresponds to the CFD-based models, which represent the most computationally expensive family, albeit being the one with the least modeling assumptions (e.g. simplifications of the physics). For the CFD-based approach, the full set of compressible, reactive Navier-Stokes equations is solved in a transient manner to simulate both the acoustic and fluid dynamics at once. This family of methods is further subdivided depending on how the turbulence is modeled based on the standard Computational Fluid Dynamic (CFD) practices. The main drawback of the CFD-based approaches is the excessive computational cost that originates from having to solve simultaneously different physical phenomena that occur at largely different lengths and time scales, namely the acoustic and fluid fields. To illustrate this, the example of DLR's LOX/LH_2 BKD combustor is again used here.

Taking the T1 mode as a reference, the first tangential acoustic mode for the BKD engine takes place with a period of around $\sim 10^{-4}$ [s], which compared to the reaction time of high-pressure hydrolox systems ($\sim 10^{-9}$ [s]) is five orders of magnitudes slower [43]. This shows that in a rocket combustor, by solving the acoustic and flow fields simultaneously, the required time-step of the transient simulation is imposed by the combustion dynamics. Furthermore, a similar story occurs for the necessary minimum mesh size, which is also imposed by the flow field's physics and is much smaller than what would otherwise be needed by the acoustic alone. For the case of the BKD running with 60 [bar] chamber pressure and having an 80 [mm] chamber diameter, a Kolmogorov length scale for the smallest scale turbulent eddies of circa 1 [μm] is predicted to occur in the vicinity of the injector plate [63]. This is again five orders of magnitudes smaller than the characteristic length scale of the acoustic, which using a conservative value of 1250 [m/s] from Figure 2.6 for the speed of sound in the chamber, has a T1-mode wavelength of around 12.5 [cm]. The example of the BKD shows that due to the combustion and turbulent flow field, an overly fine computational domain (in space and time) is imposed on the resolution of the acoustic as well. This leads to a very long run-time for the simulation, which, since it will be solved in the time domain for the flow field, will further require to be post-processed if the acoustic eigenfrequencies of the chamber need to be retrieved. The large cost associated with running CFD-based simulations makes this type of method impractical for an industrial setting in which iterations of the system's design can still occur [17]. The previous discussion on CFD-based methods assumed the main goal of this approach to be to solve the flow field and the acoustic at once, while CFD analysis can also be used in an open loop with the hybrid approaches presented by Acoustic-based methods. Here, a transient CFD simulation is run to extract how the heat release rate of the flame would change depending on the disturbance analyzed, which will then be used as the source term for an acoustic simulation to simulate the close-loop feedback driving high-frequency instabilities, or a steady-state solution can be used to describe the background flow field for the acoustic simulation [14, 29, 30, 33, 34, 43, 64–67].

2.3.2 Low-order models

On the opposite side to the CFD-based approach, low-order methods (LOM) can be found on the cost versus modeling assumption spectrum. These, together with the acoustic-based methods, assume the disturbances to be imposed over the flow field (i.e. the background flow) and model the feedback between flame response and the pressure fluctuations via a transfer function that is seen as a source term in the resulting governing equations. LOM achieves a lower cost compared to Acoustic-based methods by further assuming uniform flow and often only considering one-dimensional flow as well [68]. In addition, LOM also uses geometries for which analytical solutions of the wave equation can be found [35]. This greatly simplifies complex geometries and allows a propulsion system to be broken down into simpler geometrical components, creating a network thereof that is linked at its interfaces by transfer matrices [35]. For example, the latter was used to predict the stability of azimuthal modes of an annular gas turbine's combustion chamber, where segments were added at each burner and a network built with the chamber (modeled as a circular segment with a 1D propagating wave) with flame transfer functions [68].

With a LOM approach, systems with complex features or with repeating sections operating in parallel (e.g. coaxial injection elements) can be simplified into a closed-loop system, and control theory approaches can be used to analyze its dynamics [69]. LOM can also be used to derive acoustic boundary conditions at the interface between components, for instance between the injector ports and the combustion chamber [70]. While these methods can predict effects occurring at low Mach number inside geometries with one dimension considerably larger than the others, for example in orifices to predict whistling [71, 72], when considering rocket combustors, Section 2.2.2 showed that acoustic waves propagate both longitudinally and transversely. This requires the three-dimensional representation of the chamber to be used, especially if flame regions are considered. For that, the wave equation, also known as the Helmholtz equation in the frequency domain, is seen in this report as the transition between LOM and Acoustic-based approaches, with its three-dimensional representation falling within the latter group.

2.3.3 Acoustic-based models

The last family of approaches that can be employed to study combustion instabilities is one of the Acoustic-based models. These relax the assumptions made on the flow field and geometry by LOM, allowing for a more accurate representation of the physics, while still decoupling the acoustic from the flow field's computation, hence leading to significantly lower costs than CFD-based methods [29]. In the aeroacoustic community, these approaches also go by the name of hybrid CFD/CAA methods, where a CFD analysis is used in what is called the *near-field* to compute the acoustic fluctuations originating from a fluid dynamic source, and are then propagated using a Computational Aeroacoustic (CAA) simulation to a required *far-field* [41]. For the application of interest, the fluid properties for the CAA simulation can be described via the output of a steady-state CFD simulation of the whole field inside the combustion chamber up to the sonic throat of the nozzle. Furthermore, from a transient CFD simulation of one or more flames, the flame response to a provided fluctuation can be obtained and used as the source term of the CAA analysis [11, 34]. The latter could also be experimentally obtained [73], or, for simple cases, analytically [74–76].

Within the acoustic-based approaches, various methods exist, as is visible from Figure 2.8, which in this report are classified into two sub-categories. On one hand, there are pressure acoustic methods, such as the Wave Equation and the Inhomogeneous Convective Helmholtz Equation (iCHE), where entropy and vortical disturbances are omitted, and only the acoustic canonical perturbations are considered. On the other hand, there are aeroacoustic methods, for example, the Acoustic Perturbation Equations (APE), the Linearized Euler Equations (LEE), and the Linearized Navier-Stokes (LNS) equations, where the influence of entropy and vortical modes are not neglected. The latter sub-category has two main advantages. Firstly, when considering their formulation in the frequency domain, their eigenvalue solution also returns the damping rates in addition to the eigenfrequencies. Secondly, aeroacoustic solvers such as the Linearized Euler Equations (LEE) or the Linearized Navier-Stokes (LNS) equations, since they still retain the formulation of the original governing equations (they are not transformed into a wave equation) and can account for the variation that the background flow has on the acoustic field, they automatically derive the correct acoustic boundary condition at the sonic throat of the nozzle. Because they employ the separation of acoustic and fluid dynamic scales, Acoustic-based methods are highly efficient numerical means that since 2009 have been representing the preferred numerical strategies in the rocket propulsion community to predict combustion instabilities [14, 29, 30, 33, 34, 43, 64–67].

2.4 Approaches used in this report

From the stability prediction techniques previously presented, in this report, the analytical solution to the wave equation is used from the LOM approaches, and the Helmholtz solver and LNS solver are used from the Acoustic-based methods. The reason for choosing the analytical solution and Helmholtz solver in addition to the LNS solver (the main one to be investigated) is explained in more detail in Section 3.2.2. To summarize, the reason relates to the modeling approach chosen where the complexity of

the simulations is gradually increased to verify intermediate results and gain confidence in the modeling approach. Furthermore, benchmarking LNS' performance against simplified and established methods also allows for assessing whether in early design phases, the complexity brought forward by LNS is necessary, or if accurate-enough results can be achieved via computationally cheaper means.

Based on the theory presented in the first half of this chapter, and with an overview of how the various prediction techniques differ from each other, the analytical solution, the Helmholtz equation, and the Linearized Navier-Stokes equations are presented respectively in Section 2.4.1, Section 2.4.2 and Section 2.4.3. For the analytical solution, the case of the so-called corrected analytical solution is described in Section 2.4.1, since the standard formulation accounting for a uniform background flow was already introduced in Section 2.2. For the interested reader, additional information on some of the other Acoustic-based approaches from Figure 2.8, can be found in Appendix A.

2.4.1 Corrected analytical solution

Starting with the corrected analytical solution, this represents a low-cost method to compute the eigenfrequency of modes of interest. The standard analytical solution, accounting for the influence of a moving flow on the frequency results, was introduced in Equation 2.24. The corrected analytical approach makes use of the analytical solution of the Helmholtz equation for cylindrical geometries (similar to Equation 2.24) and corrects it for the axial speed of sound distributions in the chamber. The equation used by this approach, firstly introduced by Hardi et al. [77], is reported in Equation 2.26 below, where k_l and k_t represent the correction factors for longitudinal modes and transverse modes, respectively. While common ranges for the correction coefficients for hydrolox systems are found to be in the range $0.9<k_l<0.95$ and $0.8<k_t<0.88$, typical ranges for methalox engines are unknown [77]. The coefficients k_l and k_t are denoted as the longitudinal and the transverse correction factors. As can be seen from Equation 2.26 the former affects oscillatory modes that are composed of longitudinal modes, while the latter for the ones having a transverse mode. These coefficients are computed via Equation 2.27, for the longitudinal one, and Equation 2.28, for the transverse one. The longitudinal coefficient accounts for the average speed of sound in the chamber, while the transverse one takes into consideration only the average speed of sound in the combustion zone since in the presence of a moving background flow this is where they are mostly focused (as shown in Figure 2.7). Both are normalized by the maximum speed of sound in the chamber, leading to a coefficient close to 1 for chambers having negligible variations in the speed of sound.

$$f = \frac{c_0}{2}\sqrt{\left(\frac{\alpha_{mn}}{\frac{D}{2}}\right)^2 \left(1 - M_0^2\right) k_t^2 + \left(\frac{q}{L}\right)^2 \left(1 - M_0^2\right)^2 k_l^2} \tag{2.26}$$

$$k_l = \frac{\bar{c}}{c_{max}} \tag{2.27}$$

$$k_t = \frac{\bar{c_{cz}}}{c_{max}} \tag{2.28}$$

2.4.2 Helmholtz equation

Two of the main shortcomings of the corrected analytical solution are the lack of information regarding mode shape distributions and the assumption of a cylindrical geometry. An improvement from the analytical solution can be seen in the Helmholtz equation, which is able to tackle the two mentioned drawbacks. The Helmholtz equation was presented for its homogeneous formulation in the absence of a background flow in Section 2.2.2 by Equation 2.16. Its time-domain formulation, denominated simply as the wave equation, is given by Equation 2.14. The Helmholtz equation, by formulating the continuity and momentum equations into a wave equation, represents the computationally cheapest numerical method of the Acoustic-based approaches thanks to its elliptical expression that can be solved effectively by Garelkin Finite Element Methods (FEM) [78]. By neglecting the presence of a background flow, the homogeneous and non-convective Helmholtz equation can be used in cases where a combustion

chamber operates at very low Mach numbers. This is the case for gas turbines, where the Helmholtz solver, with the addition of a heat release source term, was used to predict the onset of combustion instabilities [79, 80]. For rocket engines, where chamber Mach numbers around 0.3 and 0.4 can be attained in the chamber [2] and where the nozzle plays a critical role for the combustor acoustics [40], neglecting the presence of a background flow leads to large errors, up to 90 % for the eigenfrequencies [81].

The homogeneous non-convective Helmholtz equation can be expanded to account for the presence of a homogeneous background flow if the assumption of a quiescent flow, made in Section 2.2.2, is relaxed (i.e. $\mathbf{u}_0 \neq 0$). Doing so leads to a homogeneous convective Helmholtz equation, given by Equation 2.29 in the time domain and by Equation 2.30 in the frequency domain [37]. This convective Helmholtz equation can be made further extended to account for the influence of flow gradients on the acoustic field and the interaction of the other two canonical modes with the acoustic one. This more complex version of the Helmholtz equation is called the inhomogeneous convective Helmholtz equation (iCHE) and was first derived by Heilmann & Sattelmayer [37] in 2022. Albeit more detailed than its homogenous version, challenges were faced by the authors to describe all necessary boundary conditions. More information on the iCHE approach can be found in Appendix A.

$$\frac{\partial^2 p'}{\partial t^2} + 2\mathbf{u}_0 \cdot \nabla \frac{\partial p'}{\partial t} + \mathbf{u}_0 \cdot \nabla \left(\mathbf{u}_0 \cdot \nabla p' \right) - c_0^2 \nabla^2 p' = 0 \tag{2.29}$$

$$\omega^2 \hat{p} - 2\mathrm{i}\omega \mathbf{u_0} \cdot \nabla \hat{p} - \mathbf{u_0} \cdot \nabla (\mathbf{u_0} \cdot \nabla \hat{p}) + c_0^2 \nabla^2 \hat{p} = 0 \tag{2.30}$$

An example of the homogeneous Helmholtz equation being applied for rocket propulsion applications can be found in the work of Watanabe et al. [9]. Here, by adding the heat release source term for the closed feedback loop of thermoacoustic instabilities, the authors predict the instabilities of the Japanese LE-9 engine for a new injector geometry. Unfortunately, the authors quantify neither the accuracy of the acoustic simulation nor whether a reliable instability prediction could be obtained. An approach that is sometimes used when utilizing a Helmholtz solver to predict combustion instabilities in rocket engines, is to derive the acoustic boundary conditions from experimental results. In the case of Watanabe et al., the admittance of the injectors was obtained from experimental data, and the heat release rate gotten from optical data of a subscale experiment [9].

2.4.3 Linearized Navier-Stokes (LNS) equations

The main question to be answered by the report relates to the Linearized Navier-Stokes (LNS) solver, which is here described. Looking at the overview from Figure 2.8, the Acoustic-based methods can be divided into two sub-categories, namely, pressure acoustic techniques and aeroacoustic approaches. All variations of the Helmholtz equation, where the governing equations are reformulated into a single wave equation, fall under the former category, while methods of the like of the Linearized Euler Equations (LEE) and LNS full under the aeroacoustic approaches. The governing equations of LNS were previously presented in Equation 2.8, Equation 2.9, and Equation 2.10. What differentiates LNS from the other aeroacoustic methods from Figure 2.8, which are described in detail in Appendix A, is the inclusion of viscous effects. This is expected to be beneficial for a more accurate prediction of the acoustic properties inside an engine since fewer assumptions on the physics are made. Furthermore, the presence of a ”natural” viscosity in the equations has a positive effects on the numerical stability of the simulation. While improvements over LEE are expected with LNS, no literature could be found where an LNS solver was used to perform numerical analyses for combustion stability applied to rocket engines. The only similar application was found in the work of Hofmeister et al. [82], where the authors study the acoustic damping rates of a gas turbine research combustor via a LEE solver, and just briefly mention (without providing any further detail) that they compared the LEE results to an LNS simulation to study how viscous effects would influence their calculated damping rate. Even though the analytical equation, the homogeneous non-convective Helmholtz equation, and the LNS equations are used in this report, the interested reader can obtain more details on the other Acoustic-based methods presented in Figure 2.8, in

Appendix A. A summary of the advantages and disadvantages of each linearized Acoustic-based method from Figure 2.8 and the analytical solution are given below in Table 2.2.

Table 2.2: Advantages and disadvantages of linearized Acoustic-based methods and analytical solutions

	Advantages	Disadvantages
Analytical solution	+ Results obtained instantly + Limited design input required	- Geometry oversimplification - Constant properties
Corrected analytical solution	+ Results obtained instantly + Accounts for properties variation along the chamber	- Geometry oversimplification - Requires knowledge about speed of sound variation
Helmholtz	+ Computationally cheap + Easy to solve without dedicated solver + Robust	- Neglects interaction between canonical modes - Neglects viscous effects - Homogenous background flow - Damping rate not a direct output
iCHE	+ Cheapest method accounting for flow gradients and interaction between canonical modes + Throat impedance obtained directly by the solver	- Equation unclosed if all convective terms are included - Difficult to specify a physically-meaningful velocity oscillation's B.C.
APE	+ No stabilization needed compared to other aeroacoustic methods + Varying background flow accounted for in the equations + Throat impedance obtained directly by the solver	- Neglects viscous effects - Neglects interaction between canonical modes
LEE	+ Interaction between canonical modes + Varying background flow accounted for in the equations + Throat impedance obtained directly by the solver	- Neglects viscous effects - Stability issues
LNS	+ Interaction between canonical modes + Varying background flow accounted for in the equations + Throat impedance obtained directly by the solver + Accounts for viscous effects	- Most expensive linear aeroacoustic method

Over the past decade, modern Acoustic-based approaches to predict combustion instability in aerospace propulsion systems have favored the use of the LEE solver over other approaches [29, 30, 33, 43, 64, 83–85]. Although the Helmholtz equation is still being used for the same purpose [9, 17], LEE has mainly been adopted by the research team of the University of Munich. In general, Acoustic-based methods have the advantage over CFD-based methods of being more computationally efficient, and, as will be seen in Section 2.6, are able to achieve the same (if not better) accuracies for the eigenfrequencies. Within Acoustic-based methods, aeroacoustic solvers, such as LEE, represent a trade-off between higher fidelity and computational cost. Given the difficulties still faced nowadays in reliably predicting combustion instabilities in liquid rocket engines, besides how the source term is accounted for, a higher degree of fidelity than LEE is required to allow for more accurate acoustic results. For this reason, LNS was chosen as the solver to be investigated in this report, since it is able to account for viscous effects, expected to better represent the losses of the system while being inherently more stable to solve for than LEE.

2.5 Representing the source term

In the preceding part of this section, some linearized Acoustic-based solvers were introduced. Even though the equations presented allowed for the inclusion of the flame response (i.e. the heat release rate that would close the feedback loop with the acoustic wave propagation inside the combustor), a description of how to compute it was omitted. Hence, a brief discussion on how to go about modeling the flame response to given flow fluctuations is presented in this section.

On the right-hand side of the inhomogeneous equations presented earlier, the term involving the heat release rate $\dot{q}'$ (in the time domain) or $\hat{\dot{q}}$ (in the frequency domain) refers to the heat source term of the

flame. The latter couples with the acoustic field during a high-frequency combustion instability, and the most widely used method to determine it is to set up a reduced order method for it based on data extracted from a transient CFD analysis. For this, two types of functions for the acoustic source term can be derived, namely: a Flame Transfer Function (FTF) and a Flame Describing Function (FDF) [34]. Both represent a response function that outputs a given fluctuation in the flame's heat release rate based on an input fluctuation from the canonical disturbances. For the common shear coaxial injectors encountered in liquid rocket engines, the formulation of the flame transfer functions is often based on input fluctuations of only pressure, for the simplest case, only velocity, or a combination of the two [14, 29, 30, 33–35, 43, 64–67, 85]. What input flow fluctuation greatly influences the unsteady heat release of the flame depends on the type of flame encountered and on the methodology used by the author. While transfer functions based on pressure fluctuations, and pressure plus velocity fluctuations are the most common for the application of interest of this report, extensions of this are also possible, for example, to account for the fluctuations in injected propellant mass. For a comprehensive explanation of how fluctuating flow properties influence the flame's heat release rate, the interested reader is pointed Lieuwen's work [40].

About the FTF, this is a linear function of given input fluctuations. If only the pressure fluctuations are considered to drive the flame's heat release rate, then from a provided transient CFD solution, to derive the FTF, the fluctuating pressure and heat release rate need to be extracted, and a Dynamic Mode Decomposition (DMD) or Bandpass filter used to obtain the frequency content associated to those fluctuations. Then, as a function of the frequency and spatial location, a magnitude, and phase for the heat release rate can be obtained [34]. The FTF can also be expanded to account for the non-linearities associated with using the amplitude of the fluctuations as input as well. In this case, the latter would correspond to an FDF.

One of the simplest yet widely used flame responses that are used in literature is Crocco & Cheng's n-τ model [86], which is given by Equation 2.31. Here, the heat release fluctuation is expressed in terms of the average heat release rate, and as a linear function of the pressure oscillation. In the model, n is called the interaction index, while τ is known as the time delay. The former is dimensionless and can be seen as a gain of how strongly the heat release is coupled with the considered fluctuation of interest, here given by the pressure fluctuation. On the other hand, the time delay indicates the time of the vaporization process, which, given the assumption of negligible atomization time of this approach, corresponds to the time between the injection of the propellants and the start of combustion.

$$\dot{q}' = \bar{\dot{q}} n \left[p'(t) - p'(t-\tau) \right] \tag{2.31}$$

In order to predict combustion instabilities with acoustic modeling tools, it is necessary to add the flame response as a source term into the model for an accurate prediction of the damping rates [33]. However, for the conditions of liquid propellant rocket engines, measuring or calculating FTFs is a large challenge on its own and is currently under investigation by several international research groups [14, 29, 30, 33–35, 43, 66, 85]. Therefore, it was decided that this study will focus purely on the acoustics side of thermoacoustic instabilities. The main motivation behind this decision is that first, the acoustics of liquid propellant rocket engine combustion chambers need to be accurately modeled before the complexity can be increased with FTF in the next steps toward reliable stability predictions. In other words, the accurate modeling of the combustion chamber acoustics is an important first step in stability predictions, which needs to be mastered before the flame response is included in the modeling.

2.6 Current instability prediction standards for liquid rocket engines

In this section, the background chapter on the literature related to modeling high-frequency combustion instabilities in a liquid rocket engine is concluded. Here, an overview of what the present combustion instability prediction standards are is provided, and the accuracies of methods presented hereafter are summarized for convenience in Table 2.3. The frequency at which instability occurs and its associated damping rate, are chosen as the two metrics to assess the accuracy of the methods. Firstly, the frequency

was chosen because it is the first parameter that is checked during the development of an engine to assess whether thermoacoustic instabilities coupled with the feed system could occur (the natural frequencies of the modes of the latter two are compared to check if they match). Also, if the mode frequency is inaccurate, an incorrect heat release rate response from the flame would be obtained. Secondly, the damping rate was chosen as metric as well because it drives whether or not an accurate amplitude of the flow fluctuations will be obtained by the analysis since it represents the acoustic energy loss in the system.

To start, it should be noted that from the references previously presented in this chapter, two trends could be seen. Firstly, more often than not, when a given method is used to study the onset of combustion instabilities in liquid rocket engines, the author reports the numerical results and concludes that the method can be used in practice for investigating the stability of real engines. Only occasionally are the errors in their analysis quantified by validating their simulation tool against experimental data. This leads to uncertainty about the accuracy of the results obtained by the author. Secondly, of the few results for which an error can be quantified, most of the test cases deal with LOX/LH_2 systems, and a lack of numerical tools validated against Hydrocarbon-based engines was found. Due to the slower chemical kinetics, LOX/CH_4 flames travel deeper into the combustor than for LOX/LH_2 systems, leading to a smaller volume of the combustor being composed of mixed combustion products. This causes the speed of sound gradients to cross over a larger length of the chamber, possibly requiring a different method to account for the background flow than done for hydrolox systems to achieve results of the same accuracy.

LOM approach

To provide an overview of the accuracy of various combustion instability prediction methods, firstly, the LOM approach of Kobayashi et al. is introduced [87]. In their work, the authors account for the acoustic source term by extending Crocco's theorem following the method of Hutt & Rocker [88], where oscillations in the mass flow of the injected propellants and the fluctuation of the mass flow of the burned gases are included as a transfer function in the closed feedback loop with the acoustic. For them, the authors both modeled the acoustic via the analytical solution of a cylinder (corrected for the nozzle length, as described by Natanzon [89]), as well as using an acoustic solver from the commercial software ACTRAN. For the test case used by Kobayashi et al., namely NASA's 82 injector elements LOX/CH_4 research combustor [90], the authors are able to estimate the T1's frequency with an accuracy of 7.5% (using the 1D analytical acoustic solution for a cylinder corrected via Natanzon's method [89]) and 9.85% (using the 3D numerical ACTRAN solution for the acoustic) when compared to experimental data. Contrary to the eigenfrequency, the authors mention that further investigations are needed to understand the discrepancy of the amplitude of instability compared to experimental results. Exact quantification of the error for the amplitude of the instability could not be obtained given that the authors do not make it explicit in their paper, nor do they provide units nor an explanation of what they consider as the amplitude of the instability (e.g. power spectral density, the magnitude of the pressure oscillation, etc.), meaning that a comparison with the experimental data of the combustor, reported in NASA's technical report [90], could not be derived. As a recommendation to improve the results, the authors suggest expanding the transfer functions to account for a phase relationship and to further improve the acoustic response of the chamber.

Acoustic-based approach

Next to LOM, acoustic-based methods were previously seen to represent the physics of the acoustic field using fewer assumptions while being able to model complex 3D geometries. For such approaches, more data on the accuracy of combustion stability simulations are available, which are described hereafter. Starting with the paper of Selle et al. [33], an international cooperation between Purdue University, the Technical University of Munich, ONERA, IMFT, and CNRS, the authors used a LEE solver using Crocco's n-τ flame response function to model the combustion instability of a single coaxial injector using Methane as fuel and a mixture of 90 % Hydrogen Peroxide and 10% water as the oxidizer. This led

to errors around 10% for the eigenfrequencies, and errors between 35.0% and 68.1% for the damping rates depending on the length of the oxidizer post used. In this work, the errors are presented for the L2 mode since this was found to be the one most amplified by the presence of the combustion process and hence investigated in the paper. Further validated acoustic-based methods applied to liquid rocket combustors can be found in the publications of Schulze & Sattelmayer [29, 43], and in Beinke's Ph.D. thesis [17]. About the analyses performed by Schulze & Sattelmayer, firstly, the authors analyze a generic experimental combustor filled with air using the LEE solver with an FTF flame response. For such study, the authors obtain for the T1 mode, frequencies errors below 2.6% and damping rate errors below 16% [29]. In their second analysis, the same authors investigate DLR's BKD research combustor (running on LOX/H_2) and using the same LEE solver with FTF, they obtain, depending on the test run considered, frequency errors below 2.6% for the T1 mode (validation data for the damping rates are not reported). In the latter publication, for the four test runs considered, Schulze & Sattelmayer are able to correctly predict the stability of the engine [43]. Albeit promising, in his Ph.D. thesis, Chemnitz tried to replicate the results for the BKD while additionally expanding the FTF source term, and showed that the correct prediction of the unstable T1 mode varied significantly depending on how the flame response is modeled [85].

Regarding the work from Beinke [17], the author used DLR's BKH combustor as a test case. The BKH combustor uses LOX/H_2 as the propellant and has a peculiar rectangular-shaped combustion chamber, which easily allows triggering a T1 mode in the combustor [91]. For illustration, a graphical representation of the BKH combustor is shown in Figure 2.9.

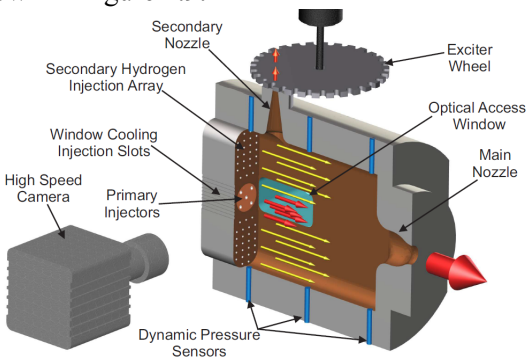

Figure 2.9: Illustration of the cut-out of the BKH combustor. Taken from Beinke [17]

This combustor, due to the large area expansion between the injector and combustion chamber, is characterized by a very low Mach number of 0.04 in the chamber [92]. With the addition of the short length of its combustion zone [17], the convective effects of the background flow marginally affect the prediction of the chamber's eigenmodes, as can be understood from Equation 2.24. This explains how Beinke, solving the Helmholtz equation in COMSOL Multiphysics with the absence of a flame response, was able to attain errors for the frequencies of BKH's L1, T1L1, and T1 modes of 0.7%, 2.1% and 2.4%, respectively. Other Helmholtz results are provided by Urbano et al. [93], where an LES simulation was run for the whole BKD combustor, including the complete nozzle and its 42 injector elements and domes, and the speed of sound field time-averaged and used as input for the Helmholtz run. The simulation returned the frequency of the T1 and R1 modes of the chamber with an error between 1% and 6.2% for the former (depending on the hot-fire run compared to), and of 6.3% for the latter.

CFD-based approach

Moving to CFD-based methods, the use of LES or hybrid LES methods is often employed. Given the large computational cost associated with running such simulations, most of the analyses focus on a single injector element or on simplified combustors. For example, this is the case for Purdue's CVRC combustor (the same combustor investigated by Selle et al. [33]) which possesses a single injector. The analysis from Selle et al. [33] also introduces the results of an LES simulation, which is able to attain errors for the L2

mode's frequency of 14.7% and 17.7%. KangKang et al. [94], investigating the same CVRC combustor and using a hybrid RANS/LES solver, achieved an error below 7.2% for the L1 eigenfrequency, and an error below 19.2% for its damping rate. A study on this combustor was also performed by Hasti & Ranjan [95] and Srinivasan, Ranjan & Menon [96]. Via an LES simulation, the former obtained frequency errors around 6.7% for the first longitudinal modes, and amplitude errors ranging from 70.9% (for the L1 mode) to 88.9% (for the L3 mode), While the latter, using Methane instead of Hydrogen as fuel, through an LES simulation obtained frequency errors of around 18% for the first two dominant modes and amplitude errors of 36%. Additionally, frequency errors for an LES approach were also reported by Urbano et al. [93], where the BKD engine was again studied, achieving 2.8% and 4.3% error for the T1 mode and of 4.4% for the R1 mode. Besides that, the authors were able to correctly represent physical phenomena as observed during experiments [93].

To summarize, for LOX/H2 rocket engines, there is more heritage and with the current state-of-the-art of Acoustic-based and CFD-based methods, frequency errors below 5% are attainable. However, for engines using Methane as fuel there is less experience, and, based on the results of Table 2.3, the international research showed that predicting resonance frequencies for hydrocarbon rocket engines seems to be more challenging even when using the current state-of-the-art models, delivering frequency errors between 7.1% and 18%.

Table 2.3: Overview of the frequency and damping rate accuracy of modern combustion instability prediction standards for liquid rocket engines

Authors	Propellant	Operating Pressure	Mode	Approach	Eigenfrequency Error	Damping Rate Error
Kobayashi et al. [87]	LOX / CH_4	133.0 [bar] / 147.0 [bar]	T1	Analytical solution (Natanzon) + Hutt & Rocker STL	$\epsilon_f \leq 7.5\%$ / 10.0%	N.A.
Selle et al. [33]	90%H_2O_2, 10% H_2O / CH_4	13.4 [bar]	L2	LEE + Crocco n-τ STL	$7.1\% \leq \epsilon_f \leq 11.1\%$	$35.1\% \leq \epsilon_\nu \leq 68.1\%$
Schulze & Sattelmayer [29]	Air	1.9 [bar]	T1	LEE + FTF	$\epsilon_f \leq 2.5\%$	$\epsilon_\nu \leq 48.5\%$
Schulze & Sattelmayer [43]	LOX / H_2	70.0 [bar] / 80.2 [bar]	T1	LEE + FTF	$0.7\% \leq \epsilon_f \leq 2.8\%$	N.A.
Beinke [17]	LOX / H_2	60.0 [bar]	L1, T1, T1L1	Helmholtz	L1 ϵ_f = 0.7 % T1 ϵ_f = 2.1 % T1L1 ϵ_f = 2.4 %	N.A.
Urbano et al. [93]	LOX / H_2	66.3 [bar] / 74.5[bar]	T1, R1	Helmholtz	T1 ϵ_f = 1.0% / 6.2% R1 ϵ_f = 6.3 %	N.A.
Selle et al. [33]	90%H_2O_2, 10% H_2O / CH_4	13.4 [bar]	L2	LES	$\epsilon_f \leq 17.7\%$	N.A.
KangKang et al. [94]	90%H_2O_2, 10% H_2O / CH_4	15.8 [bar]	L2	LES/RANS	ϵ_f = 7.2%	$\epsilon_\nu = 19.2\%$
Urbano et al. [93]	LOX / H_2	66.3 [bar] / 74.5[bar]	T1, R1	LES	T1 ϵ_f = 2.8 % / 4.3% R1 ϵ_f = 4.4 %	N.A.
Hasti & Ranjan [95]	42% O_2, 58% H_2O / H_2	13.4 [bar]	L1, L2, L3	LES	L1 ϵ_f = 6.9 % L2 ϵ_f = 6.7 % L3 ϵ_f = 6.6 %	N.A.
Srinivasan et al. [96]	42% O_2, 58% H_2O / CH_4	13.4 [bar]	L1, L1, L2	LES	L1 $\epsilon_f \approx$ 18.0 %	N.A.

3 Methodology

In this chapter, the research questions to be answered in this report are formulated and the approach to be followed to answer them is framed. To do so, Section 3.1 starts by summarizing the output of the literature survey on the combustion instability prediction capabilities presented in the previous chapter, and identifies two research gaps that should be tackled to obtain more reliable stability predictions for liquid rocket engines. Of the two research gaps, given the time-constrained thesis, only one of them, namely the one related to improving the acoustic modeling of rocket combustors, could be investigated in the framework of this study. Hence, research questions for it are formulated in Section 3.1, and from that, a research objective is derived. Based on the research questions and objective, Section 3.2 follows, where the chapter is concluded by describing the approach used by the author to answer the latter questions.

3.1 Research Plan

While examining the available numerical prediction tools in Chapter 2, the latter ended by providing an overview of the errors achieved by current numerical tools. In general, to predict an instability, the coupling between the acoustic field in a combustion chamber and the exciting heat release rate from the flame has to be modeled. As a physical result of the coupling, one or more natural propagation modes of the acoustic field resonate, leading to large amplitude pressure fluctuations. Unstable modes are identified by the frequency at which they occur and by the amplitude they attain (e.g. amplitude of the pressure fluctuation, intensity, power spectral density, etc.). For small-amplitude fluctuations (e.g. in the linear-growth regime of an instability) non-linear effects are negligible, and an instability will resonate at the acoustic natural frequencies of the chamber, for which the presence of a flame response can be neglected. This can be seen in the work of Selle et al. [33], where the peaks of the impulse spectra were obtained at the same frequency for two different LEE simulations, one accounting for the heat release source term and one neglecting the flame response altogether. Acoustic eigenfrequencies of the combustor can be used to identify the various (potentially) unstable modes, and are the first parameter that is checked during early design phases to see whether feed system coupled instabilities occur [77]. Thus, eigenfrequencies are the first parameter that needs to be accurately retrieved by any numerical tool that aims to predict combustion instabilities.

Next to the frequency, the maximum pressure oscillation found for the various modes is also of interest since one could learn whether the instability can be sustained by the engine without needing a system redesign or not. Firstly, it must be noted that if a linearized method is used to predict the instability, and if the analysis returns a pressure oscillation with an amplitude of the same order of magnitude as the chamber pressure, then the analysis should be extended to account for the non-linear effects associated with such large amplitude oscillations. Secondly, it is worth mentioning that to this day, no information exists in the literature that defines what can be considered as an acceptable margin for the pressure fluctuations of an unstable mode. Hence it is the engine designer's task to critically assess what pressure amplitude falls within the chosen safety margin. Concerning the amplitude of the fluctuating parameters, what drives their correct prediction is an accurate estimation of the damping rate. The latter can also be used as the metric of assessing whether a given fluctuating mode becomes unstable without having to control if the pressure oscillations attain amplitudes higher than 5% of the mean chamber pressure. An unstable mode can be discerned when its damping rate becomes negative, hence leading to an exponential rise of the amplitudes [31]. Therefore, given the role they play in correctly predicting fluctuating properties amplitudes, and because they can indicate if an acoustic mode is stable or not, damping rates are seen as the second fundamental parameter that needs to be accurately modeled for a reliable prediction of thermoacoustic instabilities.

Looking at the comparison of the performance of advanced LOM, Acoustic-based methods, and CFD-based models given in Table 2.3, it can be seen that their accuracies for the eigenfrequencies are not far apart. For the damping rates, direct comparisons with experimental data are more scarce to find, but from what is reported in Table 2.3 CFD-based methods seem to have the potential of providing lower errors. To improve LOM analyses, either a more complex flame response is considered (note that the results presented by Kobayashi et al. [87] already consider a more intricate response than those of the Acoustic-based methods shown in Table 2.3), or its acoustic modeling is improved. If the latter is chosen, then an acoustic-based method is considered. If changes related to the flame response are not considered, then the results presented in Table 2.3 for the Acoustic-based methods can be improved in two ways, both dealing with how the acoustic field of the combustor is modeled. Considering that CFD-based methods provide similar frequency errors than acoustic-based methods while requiring far more computational resources than the latter, for the research activities for which this report was written, it was chosen to ameliorate the accuracy of numerical stability prediction tool by focusing on improving the eigenfrequency predictions of Acoustic-based methods, and examining how the damping rate estimations are altered as a result. Due to the time requirement of the thesis, flame responses were chosen to be disregarded in the present study, with the rationale that implementing them represents the next step in the research activities for which the improvements that are considered in this report for the acoustic modeling, have to first be shown to work.

As a result, by also considering the constraints imposed by DLR (the receiving institution at which the thesis was performed), the following report aims to improve the acoustic modeling of a LOX/CH_4 liquid rocket combustor, by validating the eigenfrequencies and damping rates results of a novel aeroacoustic approach that at the moment of writing was not found to have been tested for rocket propulsion applications. The requirements set by DLR for the thesis are described later in Section 3.2.1, while the model under consideration is the previously mentioned LNS. This aims at improving the results by accounting for viscous effects since the Acoustic-based methods presented in Table 2.3 all assume inviscid flow. Furthermore, as mentioned in Section 2.4.3, LNS also has the advantage of being an inherently more stable solver than LEE due to the presence of natural dissipation in the equations. For the test case of a gas turbine's combustor, Hofmeister et al. [82] estimate the viscous effects to account for around 8.2% to 9.9% of LEE's damping rate, and conclude that viscous losses have little influence. Contrarily to Hofmeister et al, Tamanampudi et al. [34], while predicting the stability of Purdue's CVRC rocket combustor via a nonlinear LEE solver, state that viscous effects should be examined in future studies to assess their influence on the prediction.

In addition to LNS representing a novel acoustic solver for rocket propulsion application, the inclusion of a detailed three-dimensional flow field to characterize the background flow for aeroacoustic simulations for properties other than the speed of sound was also found to never have been published in the literature. The current modern approach to account for the background flow during a linearized acoustic simulation of a rocket combustor constitutes taking the results of a three-dimensional steady-state CFD simulation, slicing the latter flow field along the longitudinal axis of the combustor, and taking the area-average of the resulting cross-sectional slices to derive a one-dimensional radially-averaged flow field description that is then used as input for the aeroacoustic simulation [29, 33, 43, 97]. While this approach leads to a smooth variation of the background flow, it completely neglects the flow gradients occurring within the cross-sectional plane of the engine. This approach ignores how the various flame structures of the many coaxial injectors found in representative rocket combustion chambers affect the acoustic eigenmodes. The only analysis where the radial stratification of the background flow has been investigated for properties other than the speed of sound and applied to aeroacoustic solvers, is provided by Chemnitz & Sattelmayer [98]. In their work, the authors study how accounting for the flow's radial stratification affects the eigenfrequency and damping rates results for a 2D LEE simulation of DLR's BKD combustor. The authors greatly approximate the radially-varying flow inside the combustor by deriving it from a 1D

profile obtained via radially averaging a steady-state CFD solution (as mentioned earlier). Furthermore, the variation of flow properties across a flame structure was assumed to follow a cosine distribution, and radially stratified flow was only accounted for in the combustion region, with the rest of the chamber following the 1D profile description. Nevertheless, even though a 2D simulation was performed with smooth gradients in flow properties in the combustion zone along the radial direction, the authors show that the presence of the stratified flow mainly influences the damping rates and the distribution of the acoustic modes. By accounting for two flame structures, deviations below 1% and 10% were observed respectively for the eigenfrequencies and damping rates, and large influences on the distribution of mode shapes were seen. As a recommendation for future work, the authors suggest investigating the effect that the number of flames has on these results. In their work, only two flames were accounted for in a 2D axis-symmetric analysis, and from their idealized cosine fitting approach, the authors retrieved clean speed of sound profiles for the flame based on a single-flame CFD result. This leads the speed of sound profiles of the two flames to be symmetric to the centerline of their respective injector elements, and neglects flame-to-flame interaction [11].

Since Acoustic-based combustion stability prediction analyses use the output of an acoustic simulation as input for a flame transfer function to retrieve its heat release rate fluctuation, acting as a source term for the acoustics, besides eigenfrequencies and damping rates, obtaining an accurate spatial distribution for the mode shapes is also of importance. In this report, pressure mode fluctuations are mainly assessed since these allow a straightforward verification of the eigenmodes of interest, as seen from Figure 2.5. In reality, apart from pressure fluctuations, the mode shapes for the velocity, temperature, and density can also be returned by the solver, which in turn can be used as input parameters for the transfer functions and influence its output.

What can be considered a valid flame transfer function to accurately model the stability of a rocket engine is still a very active field of research. At the moment of writing, the most widely used input parameters for the transfer function in rocket engines using coaxial shear injectors (using Acoustic-based methods) are to use pressure fluctuations, velocity fluctuations, or a combination of both [14, 29, 30, 33, 34, 43, 64–67]. Yet, even if propulsive systems other than methalox are considered, a negligible body of literature has focused on tackling a detailed description of such fluctuations for Acoustic-based methods. By using radially averaged profiles as input, the cross-wind variations of flow properties are neglected. This leads to acoustic simulation being conducted for constant background flow properties within the given cross-section of the engines and hence impeding the simulation to return radially varying flow fluctuations distributions for parameters other than the acoustic pressure. Accounting for a detailed background flow also enables an accurate description of the flame structures and their low-temperature LOX core which are expected to improve the accuracy of the LNS simulation by reducing the frequencies of its modes (LOX core is characterized by a low speed of sound). Therefore, the effects of including the complete three-dimensional CFD field as input for the acoustic simulation will also be investigated in this report. For the identified opportunities, aimed at improving the modeling accuracy of acoustic-based methods (even though in the absence of a flame response), the research questions presented hereafter were formulated to guide the research work [61].

Research questions

To ameliorate the acoustic modeling of rocket combustor, three research questions to be answered in the following report were formulated. These are reported together with the rationale behind them in **RQ.1**, **RQ.2** and **RQ.3** below. When necessary, suq-questions were added to aid to answer the main question. These are named in the following way: **RQ.X.S.Y**, where **X** identifies the number of the research question under which they fall, **S** indicates the sub-question and **Y** refers to the number of the sub-question considered.

- **RQ.1**:***To what extent can COMSOL Multphysics' LNS solver return physical results for the acoustic field inside a cryogenic bi-propellant rocket combustor in the presence of a background flow?***

Rationale: Given that this is the first time a detailed LNS analysis is performed for cryogenic liquid rocket propulsion applications, it is unknown whether physical results can be obtained using the commercial software COMSOL (e.g. will the simulation converge?). As will be explained in Section 3.2.1, the use of COMSOL Multiphysics is a requirement imposed by the receiving institution, namely DLR. Back in 2016, when trying to characterize the performance of a LEE solver in predicting the eigenmodes of the BKH combustor, COMSOL failed to return physical results when including the presence of a background flow, with only spurious solutions found by the simulation [92]. Hence, the first step towards improving the acoustic modeling of rocket combustors via an LNS simulation in COMSOL is to first make sure that the latter is robust enough for the application of interest, which includes solving the acoustic field with the presence of large flow gradients occurring over small distances (e.g. due to combustion using cryogenic media).

- **RQ.2**: ***To what extent can sub-5% frequency errors be obtained with COMSOL Multiphysics' LNS solver when simulating the acoustic modes of a LOX/CH4 rocket combustor for combustion stability prediction applications?***

- **RQ.2.S.1**: *How does the performance of LNS compare to solvers used by the industry?*
- **RQ.2.S.2**: *How does the method chosen to describe the background flow affect the accuracy of the eigenfrequencies and respective damping rates?*
- **RQ.2.S.3**: *What modeling requirements are necessary to accurately model the chamber's eigenfrequencies versus the damping rates?*

Rationale: Once LNS has been verified to return the results as expected, the accuracy with which it does has to be investigated. The primary aim is to accurately simulate the eigenfrequency of the combustor and to do so, absolute errors below 5% are wished-for to rank the LNS simulation amongst the most accurate methods found in literature, as shown in Table 2.3. It must be said that in the latter, all sub-5% errors were attained for hydrolox systems, and no validated Acoustic-based results could be found for methalox engines.

-**RQ.3**: ***How accurately can damping rates be retrieved from a COMSOL Multiphysics' LNS simulation accounting for background flow variations?***

-**RQ.3.S.1**: *How does including the detailed CFD field as input for the LNS' background flow influence the accuracy of the damping rates?*
-**RQ.3.S.2**: *To what extent can the damping rate errors found in literature be replicated with an LNS simulation without accounting for the flame response?*

Rationale: Finally, besides the mode frequencies, it is desired to validate the LNS simulation for the obtained damping rates as well. Damping rate errors were found to be scarcely reported in the literature, and given that the LNS analysis conducted for the thesis will neglect the presence of a flame response, the same accuracy as for the eigenfrequencies is not expected to be obtained, given that depending on the phase and on the frequency of the heat release rate of the flame, the latter can greatly amplify or attenuate acoustic modes. At the same time, while errors below 19.2% (i.e. the best estimate given in Table 2.3) are not expected to be attained, due to the little validated data available, the LNS analysis will also be used to understand what errors for the damping rates can be achieved using an advanced Acoustic-based method while neglecting the flame response.

Research objective

From the previous research questions, the research objective for the thesis was formulated and is stated below. A 5% accuracy was chosen for the eigenfrequency based on the errors reported in Table 2.3 for

the most advanced Acoustic-based approaches, which make use of a LEE solver. Given that LNS can account for viscous effects, errors similar to the ones obtained for LEE are expected to be attainable. However, it should be noted that none of the results reported for LEE in Table 2.3 were achieved for a methalox engine, and the very accurate frequencies (i.e. with an error below 3%) were only obtained for hydrolox systems. Applying the LEE solver to an engine utilizing Methane as fuel, from Table 2.3, led already more than double the error for the frequency predictions.

- **RO.1** ***To provide a sub-5% error prediction of the acoustic eigenmodes' frequencies in a representative LOX/CH4 rocket combustor and to assess the predicted damping rates of such eigenmodes, by analyzing the accuracy of COMSOL's LNS solver and using DLR's LUMEN demonstrator engine as test-case to validate the results***

Regarding the experimental results used to validate the simulations, these will be taken from two hot-fire test runs of DLR's Liquid Upperstage Demonstrator Engine (LUMEN), and throughout the report, the latter will be used as a test case for the simulations. More information on the LUMEN engine can be found in the subsequent section.

3.2 Modeling approach

Following the research questions, a modeling approach designed to answer them is here described. Firstly, in Section 3.2.1 the collaboration with DLR's Space Propulsion Institute in Lampoldshausen is elucidated. The thesis was written with DLR, which in addition to providing test data and input for the acoustic simulations from their LUMEN project, also required the use of the software COMSOL Multiphysics for the research activities here presented. After describing DLR's requirements for the thesis, Section 3.2.2 follows, where the methods chosen to compare LNS' results against approaches used by the industry are stated. With a clear idea of the simulation methods to be used, a short explanation for why throughout the thesis it was chosen to run all the simulations in the frequency domain rather than in the more intuitive time domain is provided in Table 3.3. Finally, the section is concluded in Section 3.2.4 by detailing the simulation approach to be followed to investigate the effect on the results including a detailed description of the background flow with LNS. For this, simulation stages were set up with a step-wise increase in modeling complexity so to increase the modeling confidence and to assess how the inclusion of different parameters influences the results.

3.2.1 Collaboration with the German Aerospace Center (DLR)

As previously mentioned in this report, the current study was performed at DLR's Space Propulsion Institute in Lampoldshausen. This collaboration not only allowed the author to perform the simulation for a representative LOX/CH_4 rocket engine and to validate the results against experimental data, but also permitted DLR to obtain a thorough understanding of what Acoustic-based solver would best simulate the acoustic eigenmodes in their combustors and to gain experience using aeroacoustic solvers, both in the framework of combustion instability studies. For that, the commercial software COMSOL Multiphysics was required to be used for the present study, which is a widely used software in the rocket propulsion community to predict combustion instabilities via Acoustic-based methods [17, 29, 33, 34, 43, 99]. For DLR's Space Propulsion Institute the following thesis represents the initial step towards their goal of building a robust and reliable numerical tool to predict the onset of combustion instabilities in their bi-propellant combustors.

Before this thesis, the institute used a LOM approach during the design phases of their combustors to estimate whether injection-coupled thermoacoustic instabilities would occur in their systems [77] and to identify acoustic modes from experimental results [39]. Another method employed by the Space Propulsion Institute of DLR to predict the frequency of the acoustic modes while being able to retrieve their mode shapes, is to use COMSOL's Helmholtz solver. As shown in Table 2.3, with this method Beinke [17] was able to retrieve the L1, T1, and T1L1 frequencies with an error below 2.5% for the

BKH hydrolox engine. As described in Section 2.6, this particular type of combustor is characterized by a chamber Mach number of 0.04, for which the assumptions made by the Helmholtz equation are applicable. Therefore, with this thesis, DLR aims to obtain a generally-applicable aeroacoustic solver that can attain better errors than the ones found in the literature.

The Liquid Upper-Stage Demonstrator Engine: LUMEN

DLR's LUMEN engine represents the test case considered in this report, for which raw experiment data from two of its hot fires is made available for validation purposes. The LUMEN project was started by DLR in 2017 to intensify its experience in testing rocket engines at a system level, while allowing to develop a bread-board engine in the 25 [kN] thrust range to test components in representative conditions for a LOX/LNG upper-stage engines, in line with the current European LOX/LNG engine developments [100]. Once finalized, LUMEN will use an expander bleed cycle with two separate (parallel) turbopumps for the oxidizer and fuel side and will be regeneratively cooled, with the heat pickup starting at the nozzle exit. A schematic representation of its architecture is shown in Figure 3.1, while its nominal operating conditions are reported in Table 3.1. In this table, p_c indicates the static chamber pressure, ROF is the oxidizer-to-fuel-ratio, $\dot{m}$ represents the mass flow, T is the static temperature at the inlet of an injector dome, Δp specifies the pump pressure rise and F_t is the nominal sea-level thrust. Additionally, subscripts LOX and CH_4 distinguish the parameters for the oxidizer and fuel, respectively. To get a better feeling of the system's layout, the interested reader is re-directed to the following informative video: *DLR's technology demonstrator LUMEN* [101].

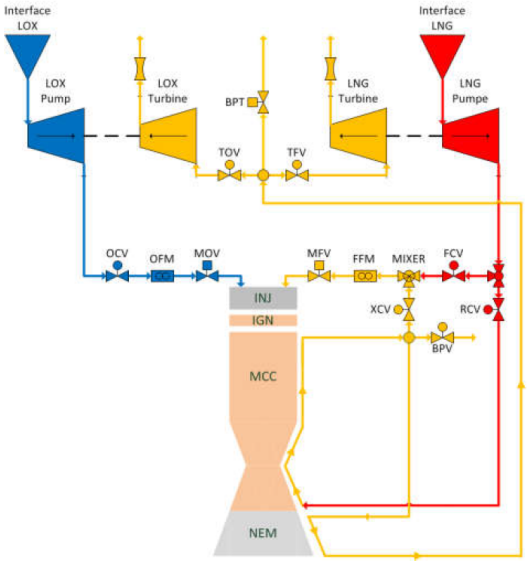

Figure 3.1: LUMEN system architecture. Taken from Deenken et al. [100]

Table 3.1: Nominal operating conditions of LUMEN

Parameter	Value
p_c	60 [bar]
ROF	3.4 [-]
$\dot{m}_{LOX}$	5.85 [kg/s]
$\dot{m}_{CH4}$	1.75 [kg/s]
T_{LOX}	98 [K]
T_{CH4}	215 [K]
$\Delta p_{turbo,LOX}$	85 [bar]
$\Delta p_{turbo,CH4}$	100 [bar]
F_t	25 [kN]

About its combustion chamber design, LUMEN has a chamber diameter and chamber length of 80 [mm] and 262.8 [mm], respectively, and uses 42 shear-coaxial injector elements. The chamber length corresponds to the size of the cylindrical section of the combustor in the absence of an instrumentation ring. This ring connects the faceplate to the chamber (adding around 16 [mm] of length) and is used during experiments to attach measurement devices at the start of the chamber. Additionally, the size of the converging part of the nozzle (i.e. from the end of the cylindrical chamber to the nozzle throat) is 60 [mm], and the ratio of the cross-sectional area of the chamber to the throat area is 2.3 [-]. Furthermore, while planning to be using a laser plasma igniter, allowing up to four re-ignitions, the current version of the system uses a simple torch igniter. A cut-out view of the LUMEN combustion chamber as used during early test campaigns is shown in Figure 3.2. Similarly, an illustration of LUMEN's injector is provided by Figure 3.3. For the latter, the volume occupied by the fluid is shown. For example, this means that for the view showing the close-up of an injector element, the un-filled region between the LOX core and outer CH_4 sleeve is in reality a solid wall. The injector of LUMEN is additively manufactured, the walls

of the LOX injector are made out of stainless steel while the outer walls of the CH_4 injector are made out of a copper alloy. The inner walls of the CH_4 injector, since they interface with the LOX section, they are also made out of stainless steel. In addition to Figure 3.3, a 2D cut-out of the injector is shown Figure 3.4, where the nomenclature used throughout this report to denote various elements of the injector is given. Regarding the inlet locations where the propellants are injected into their respective domes, it should be noted that while the CH_4 is injected along the whole outer surface of its dome, the LOX is injected only at discrete protrusions, as can be seen at the end of its dome in Figure 3.3.

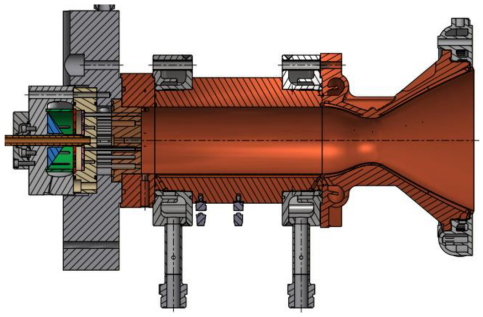

Figure 3.2: Cut-out view of the battleship version of the LUMEN combustor. Taken from Hardi et al. [44]

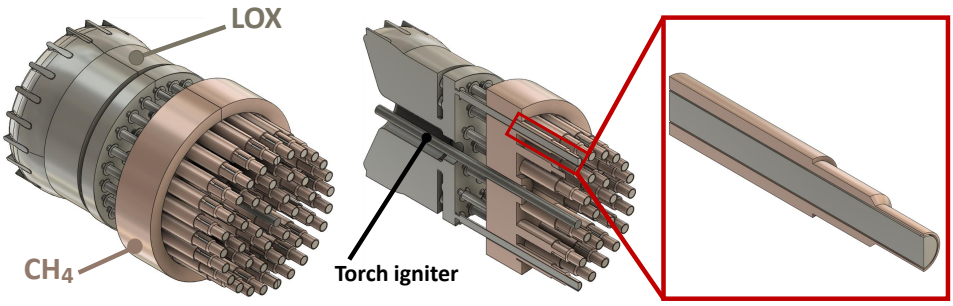

Figure 3.3: Views of LUMEN's injector

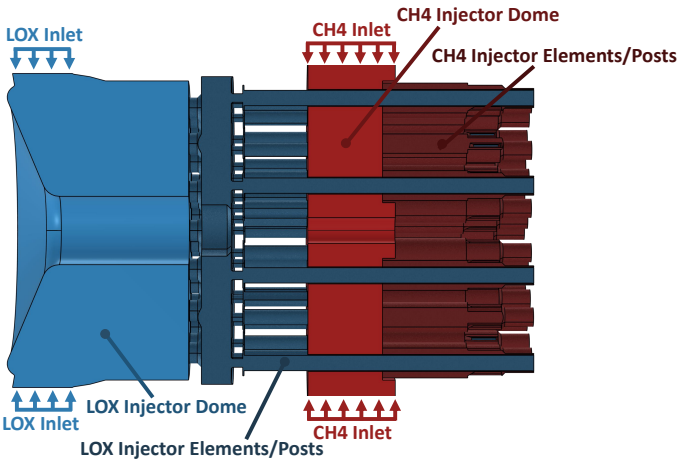

Figure 3.4: Cut-out of the LUMEN injector showing its various elements

LUMEN CFD simulation

In addition to using the data from hot-fire runs of two early LUMEN test campaigns, a detailed reactive CFD solution of the LUMEN combustor is also made available by DLR for the thesis. Albeit unpublished at the time of writing of this report, this CFD simulation was performed for design purposes related to the

length of the chamber needed for cooling. The CFD simulation of LUMEN's combustion chamber was performed in 2021 by DLR's Ph.D. researcher Schneider. More specifically, the analysis was conducted within the framework of assessing that enough enthalpy could be extracted by LUMEN's chamber cooling system to drive its turbines [77], and was performed alongside calorimetric test campaigns. The results presented in this report regarding the CFD analysis have not been published to the moment of writing, and hence are treated as confidential. The physical domain, together with the numerical mesh used for the CFD, is shown in Figure 3.5. While an overview of the set-up of the RANS CFD simulation performed by Schneider, and used as input for the research activities here presented, is summarized in Table 3.2. DLR's CFD code TAU, used for the LUMEN CFD analysis, has already been validated in the past for a number of reactive flow simulations inside cryogenic bi-propellant rocket engines [17, 102, 103].

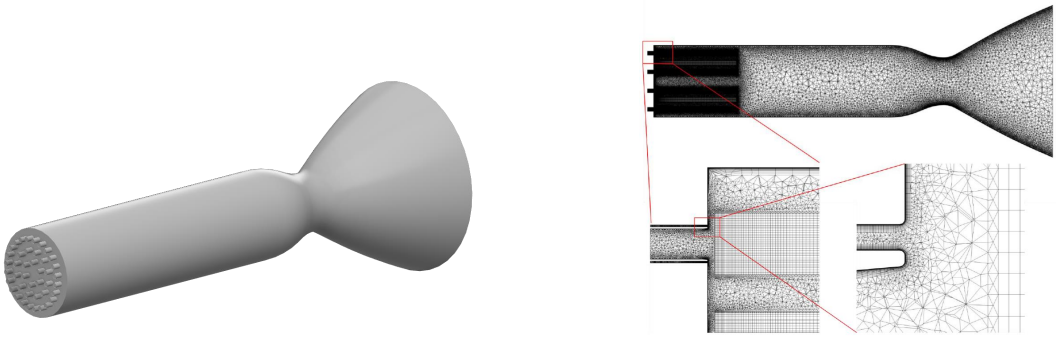

(a) Volume of the LUMEN's combustor used for the CFD analysis **(b)** Mesh used for LUMEN's combustion chamber CFD analysis

Figure 3.5: Inner chamber's volume and mesh used for the LUMEN CFD

Table 3.2: LUMEN CFD set-up used

Conditions	CFD Set-up
Study type	RANS, steady-state
Domain	3D
Turbulence model	Menter k-ω SST
Inlet condition	Propellant's mass flux and static temperature
Outlet condition	Nozzle exit pressure
Chamber and nozzle wall condition	1D heat transfer + prescribed cooling fluid's temperature distribution
Injectors' wall condition	Adiabatic
Spatial scheme	2^{nd} order MAPs + Upwind
Temporal scheme	2^{nd} order explicit 3-stage Runge-Kutta
Combustion model	TAU's flamelet model
Reaction mechanism	Zhukov-Kwong
Real gas model	Soave-Redlich-Kwong (SRK)
Mesh size	$27 \cdot 10^6$
Domain volume	$2.83 \cdot 10^{-3}$ [m^3]
Mesh type	Hybrid mesh
Maximum y$^+$	9.5
Computational resource	DLR's CARA cluster (1280 CPUs)

Since the CFD simulation for the LUMEN combustion chamber was performed parallel to a calorimetric test campaign to characterize the heat transfer at its chamber wall, the CFD results were validated against the experimental results of the latter campaign. The comparison with experimental data that was performed by Schneider, showed a maximum absolute error for the pressure in the combustor below around 4.5 %. Furthermore, errors below 10 % were obtained for the heat flux in the chamber, except at around a distance of 73 [mm] from the face-plate, where an error of around 58 % was obtained. As an illustration, the speed of sound, obtained from the CFD analysis, for the LUMEN engine is shown in Figure 3.6. Given the confidential nature of the unpublished CFD results that are here presented, in this report, the

values of the colormap are only given for the speed of sound field since this variable is mostly used for acoustic analysis only. The exact values for other fields (e.g. the density) are kept confidential so to allow DLR to publish literature about the CFD results in the future.

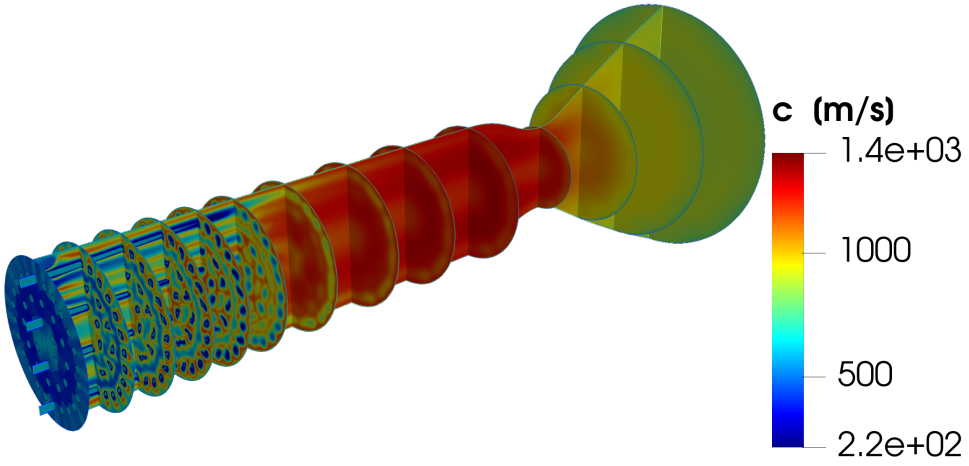

Figure 3.6: LUMEN CFD Speed of sound result

3.2.2 Benchmarking the Linearized Navier-Stokes (LNS) solver

Looking at the research questions **RQ.1** and **RQ.2**, benchmarking the LNS simulation against other validated approaches will help to verify the simulation and to assess whether the errors obtained with LNS are due to the chosen method, or are inherent to the studied problem (e.g. if wrong CFD results are used to represent the background flow). Therefore, in this report, the LNS results will be compared to the results obtained via two other methods. Firstly, the simplest case of the analytical result of the Helmholtz equation is used. This allows to verify that the mode shapes calculated with LNS are obtained in the expected ballpark as specified by a commonly used LOM model. For this, the solution of the homogeneous convective Helmholtz equation given in Equation 2.24 is used together with the corrected approach suggested by Hardi et al. [77] (reported in Equation 2.26). Using the corrected analytical equation will also help DLR to obtain further data points for the correction coefficients of methalox engines.

Secondly, to account also for the nozzle geometry and the feed system part leading to the injector elements, the second method, in addition to the analytical solution for a cylinder, will be to use COMSOL's Helmholtz solver. In addition to the analytical solution, this method will also allow us to verify the mode shapes of the LNS simulation. At the moment when this research was performed, COMSOL's Helmholtz solver was the standard way with which the Space Propulsion Institute of DLR would numerically retrieve mode shape information from their combustors. Hence, comparing its results with LNS will allow a direct assessment of what improvements LNS could bring to DLR. Moreover, given its assumption about uniform flow and neglection of convective flow effects, the Helmholtz approach is also used during early engine development phases by the industry since it allows for a better prediction of acoustic modes than the analytical solution while not needing a steady-state CFD simulation to describe the background flow in detail. Thus, benchmarking LNS' performance with the Helmholtz solver also allows the industry to understand whether the advantages that the former brings are worth the increase in computational cost compared to the latter.

3.2.3 Time domain versus frequency domain studies

With a clear view of the different means that will be used in this report to predict the acoustic field inside the LUMEN combustor, a brief motivation is here presented to explain why all the subsequent simulations in this report will only be performed in the frequency domain. The present discussion is based on the

overview provided by Schulze & Sattelmayer [29] and a summary of the comparison between the time domain and the frequency domain is here reported in Table 3.3.

Table 3.3: Comparison of the traits characterizing a LEE simulation solved in the frequency-domain versus the time-domain as illustrated by Schulze & Sattelmayer [29]. Taken from Trotta [61].

Frequency Domain (i ω)	**Time Domain ($\frac{\partial}{\partial t}$)**
Eigenvalue problem formulated $\rightarrow$ Arnoldi algorithms	Temporal evolution of primary variables solved $\rightarrow$ Runge-Kutta time stepping
(+) Fast computation in $\sim$ minutes	(-) Long computation time $\sim$ hours
(?) Numerical damping not investigated	(+) Low numerical damping
(+) Easy to implement acoustic boundary conditions	
(+) Damping rate is directly computed, since it is part of the complex eigenfrequency	(-) Post-processing of results needed to derive the damping rate
(-) Only applicable for linear propagations	(+) Can be extended for non-linear propagation

For the case of a linearized solver solving the simulation in the frequency domain represents a more computationally efficient way to retrieve eigenfrequencies and damping rates information for a combustor. Given that it allows reformulating the equations into an eigenvalue problem, a more efficient algorithm can be exploited to retrieve the desired parameters in the frequency domain. Conveniently, the desired frequency and damping rate information are directly returned as the solution of the problem, while if a time domain study is performed, these would have to be post-processed from the time variation of the pressure fluctuation (as would be done from experimental data).

3.2.4 Design of simulation strategy

In Chapter 4, the setup and results of the acoustic simulations are reported. For that, the structure of the chapter is based on the simulation strategy that was followed throughout the research activities to allow for a step-wise increase in modeling complexity and to assess variations in the results at each major modeling stage. This subsection describes the approach that was followed to run the simulations and therefore concludes the current methodology chapter.

The modeling steps taken are based on how the background flow is modeled in the considered analysis. The first step removes the need of a CFD analysis as input, and uses only constant flow properties inside the chamber. To do so, chemical equilibrium analysis is used, employing the software *RPA* to retrieve the properties of the combustion gases. This is comparable to using CEA values since the chemical library from RPA is based on the thermodynamic database from NASA Glenn [104]. In this modeling phase, the analytical solution given by Equation 2.24 and a Helmholtz simulation in COMSOL is computed. This represents the baseline to verify the results that will be obtained with LNS, which will provide an answer to research question **RQ.1**. The use of the analytical solution of the Helmholtz equation for a cylindrical geometry with CEA values is used in early design phases to check that the chosen length of the combustion chamber does not have natural modes that are too close in frequency to the ones of its feed system [77]. If the natural frequencies of the chamber are close to the ones of the feedsystem, then feed-system coupled high-frequency combustion instabilities could occur. Furthermore, even though in the previous chapter it was seen that the Helmholtz equation can be expanded to account for the flame response and be used for predictive analyses, in its homogenous form this equation allows it to be readily solved without the need for specialized software. This allows the Helmholtz equations to be used during preliminary design phases as well while accounting for complex geometries and thus representing an improvement over the analytical solution. Besides that, while the analytical solution can be used to verify the frequency of the LNS simulation, the Helmholtz equation is additionally needed to verify the shape of the acoustic mode of the latter.

The second modeling step indicates the current standard in the rocket propulsion literature to account for the background flow field in the acoustic simulation, namely to radially average a steady-state RANS simulation of the combustor and derive 1D variations of the flow variables along the axis of the engine. Here, the LNS simulation following the modern standard to account for the background flow is performed. Since due to the inclusion of varying flow properties the frequency results of the LNS are expected to vary considerably from the ones obtained with the analytical solution using CEA values, the corrected version of the analytical solution from Hardi et al. [77] is also computed within this modeling step. Furthermore, the Helmholtz simulation from the previous step is here also revised to account for changing input flow parameters in the chamber. Following this increase in modeling complexity, partial answers to sub-questions such as **RQ.2.S.2** and **RQ.2.S.3** can already be obtained by the end of this intermediate study.

The last step aims to improve the state-of-the-art standard for the background flow modeling by mapping the whole detailed 3D CFD solutions directly as input for the LNS simulation. With this advancement, an answer for **RQ.3.S.1** can be obtained. Finally, a comparison of the simulation results with experimental data is required to obtain a final answer for **RQ.2** and **RQ.3**. For this, the test data of two LUMEN hot-fire campaigns (i.e. BKL-CALO20 02run2 and 02run6), occurring at the same operating conditions as simulated by the CFD analysis, are analyzed. From the data, eigenfrequency and damping rates information are extracted, allowing the error of the simulations to be determined.

4 Acoustic Modeling

Based on the structure devised in Section 3.2.4, the following chapter will present the set-up of the simulations and calculations performed to answer the research questions previously presented in Section 3.1. Even though in this chapter the results obtained by the analyses are shown, a thorough description of the results will be presented in Chapter 5, where the experimental data of LUMEN will be processed and the numerical results validated. Initially, during the thesis, simulations leading up to the LNS case with radially averaged CFD field were performed for the LUMEN chamber set-up studied by Schneider during its CFD investigation (presented in Section 3.2.1). When comparing the results with experimental data it was discovered that the length of the combustion chamber studied by Schneider was slightly smaller than the one used during the experiments, thus altering the accuracy of the longitudinal modes. As will be explained later in more detail in Section 4.2.1, the flow properties within the end of the chamber section (before the nozzle contraption) were projected for the missing 15.4 [mm] of the simulated chamber. Given the short distance and the region to be extracted having already reached a plateau in flow properties' variations, having to "lengthen" the simulated chamber was deemed to only marginally affect the results. More details on this are provided in Section 4.2.1. What is worth noting for the reader, is that the results presented hereafter (up to Section 4.3) are all reported for the lengthened chamber geometry and that the initial "shorter" chamber results are reported for reference purposes in Appendix B.

This chapter is divided into three parts, based on how the background flow is modeled. Firstly, Section 4.1 assumes a constant and homogenous background flow field across the whole combustor and takes the flow properties from CEA, thus not making use of Schneider's LUMEN CFD analysis as input. This represents the most simplified analysis that can be performed and by comparing its results with more complex analyses, the influence of the background flow description can be studied. Following, in Section 4.2 a further step is taken, accounting for the background flow variations and the current state-of-the-art approach of radial averaging a steady-state CFD field and using the resulting 1D profile as input is described. While in Section 4.1 only an analytical solution of the wave equation and the Helmholtz solver are computed, in Section 4.2 the analysis for LNS is added. In addition, the latter section also updates the results obtained in Section 4.1 to account for the presence of a varying flow field in the chamber. Even though longitudinal modes, which are characterized by the acoustic pressure oscillating along the axial direction of the chamber, will be influenced at each section of the combustor by the average speed of sound attained (hence expected to be accurately modeled using a radial averaged background flow description), it is unknown how transverse modes will be influenced by averaging the speed of sound in their propagation plane. Given the 42 flame regions inside the LUMEN chamber, a transverse oscillation has to propagate across extremely different regions of the speed of sound over very small distances, possibly leading to large accuracy changes in predicting such modes depending on how the background flow is modeled. Therefore, to assess how a detailed three-dimensional description of background flow influences the prediction of the acoustic modes of a rocket combustor, the last step taken in this chapter is to run the LNS simulation using the exact CFD results of the LUMEN combustion chamber as input. This is done in Section 4.3, where this chapter is concluded.

4.1 Chemical Equilibrium Flow

The first modeling step taken in this report assumes chemical equilibrium and constant flow properties in the combustor. To derive the CEA properties of the combustion products inside the chamber, the software Rocket Propulsion Analysis (RPA) is used. The reference operating conditions used for the RPA calculation are summarized in Table 4.1 and are the ones that were used as input for the LUMEN

CFD analysis for which experimental data is available. The values of Table 4.1 were retrieved from the test run that the CFD analysis of Schneider used for validation. As such, the pressure and temperature of the propellants were measured in their respective injector domes, the mass flows prior to entering the injectors, and the chamber pressure just downstream of the faceplate. While Table 4.1 corresponds to the average quantities obtained during experiments, the parameters reported earlier in Table 3.1 represent LUMEN's nominal design values.

Table 4.1: Reference operating condition used for LUMEN's CFD analysis

Parameter	p_c	ROF	$\dot{m}_{CH4}$	$\dot{m}_{LOX}$	T_{CH4}	T_{LOX}	p_{CH4}	p_{LOX}
Value	63.7 [bar]	3.4 [-]	1.7 [kg/s]	5.9 [kg/s]	201.0 [K]	115.5 [K]	71.0 [bar]	69.8 [bar]

As will be seen later in Section 4.2, since RPA's thermal conductivity at different sections of the combustor will be used in further modeling stages, for the RPA study, information about the nozzle is required in addition to the information contained in Table 4.1. For that, besides the contraction area ratio presented in the previous chapter, an expansion ratio of 1.1537 [-] was obtained from LUMEN's CAD file. This value does not correspond to the expansion provided by the divergent nozzle shown in Figure 3.5a, but to the expansion ratio provided by the latter nozzle cut at 10 [mm] post throat. While geometrical simplifications of the LUMEN engine are discussed in more detail in Section 4.1.2, the reason for cutting the nozzle 10 [mm] after the throat is twofold. Firstly, due to the hyperbolic nature of the wave equation, acoustic disturbances do not travel upstream in a supersonic medium, and hence for the acoustic analysis of a rocket engine, the section post sonic throat is irrelevant for the analysis. Secondly, albeit not important, a small part of the supersonic nozzle is nevertheless included to make sure that the sonic line is properly represented in aeroacoustic analyses for the chosen solver to derive its own acoustic boundary condition at the throat.

The resulting CEA values relevant for this section are given in Table 4.2. The exact input and output values from RPA are given for completeness in Appendix C. Additionally, given the need from the Helmholtz solver to use the injectors' speed of sound and density as well, CoolProp was used to compute the latter parameters [105], and their values are provided in Table 4.3. The CoolProp results were obtained for the conditions specified in Table 4.1.

Table 4.2: CEA values for the combustion products for the LUMEN combustor

	$\mathbf{M}_0$	$\mathbf{c}_0$	ρ_0
Combustion products	0.27 [-]	1245.7 [m/s]	4.6 [kg/m3]

Table 4.3: CoolProp speed of sound and density values for the fuel and oxidizer injectors

	$\mathbf{c}_0$	ρ_0
CH_4	388.0 [m/s]	216.9 [kg/m3]
LOX	739.4 [m/s]	1028.6 [kg/m3]

4.1.1 Analytical solution

With the CEA results obtained (Table 4.2), the analytical equations can be solved. The results of the latter are tabulated in Table 4.4 for a number of modes. Throughout this report seven eigenmodes will be computed, where each of the natural propagating directions is represented. This not only provides more information for the comparison with experimental results but also leads to more data to be gathered than in literature, where authors focus only on predicting one or a few modes. In Table 4.4, Equation 2.24 is used as the analytical solution. For this, solutions are computed for two cases: for only the cylindrical combustion chamber and for the case of assuming both the combustion chamber and the nozzle contraption to be cylindrical. In addition, the variation proposed by Natanzon [89], which is sometimes used with LOM approaches [87], was also added. Here, the same analytical solution as before is considered, and the characteristic length of the engine is changed. For that, depending on how acoustically compact the nozzle can be assumed, either a half or a third of the overall converging nozzle length is added to the

length of the cylindrical chamber. Given that all these variations in the analytical approach only vary the considered length, all methods reported in Table 4.4 led the same frequencies for purely transverse modes. For an overview of the various mode shapes, the reader is referred back to Figure 2.5.

Table 4.4: Analytical solutions of the convective Helmholtz equation for a cylindrical geometry with various lengths

	Analytical Solution (without nozzle) L = 278.2 [mm]	**Natanzon-1/3 L = 298.2 [mm]**	**Natanzon-1/2 L = 308.2 [mm]**	**Analytical Solution (with nozzle) L = 338.2 [mm]**
L1	2078 [Hz]	1938 [Hz]	1875 [Hz]	1709 [Hz]
L2	4155 [Hz]	3877 [Hz]	3751 [Hz]	3418 [Hz]
T1	8790 [Hz]	8790 [Hz]	8790 [Hz]	8790 [Hz]
T1L1	9032 [Hz]	9001 [Hz]	8988 [Hz]	8955 [Hz]
T2	14580 [Hz]	14580 [Hz]	14580 [Hz]	14580 [Hz]
R1	18300 [Hz]	18300 [Hz]	18300 [Hz]	18300 [Hz]

4.1.2 Geometrical simplifications

In addition to the above-mentioned analytical solution, a Helmholtz simulation for the complex geometry of the LUMEN combustor using CEA values is performed. The geometrical simplifications made for this Helmholtz case are the same that will be used in the next section to run the LNS simulation and are here described. These were driven by what aspects of the combustion chamber and injectors have to be included for the LNS analysis. Thus, the geometry is simplified in light of what is important for LNS, and the resulting simplified geometry is used for the sake of consistency for all simulations.

The complete inner volume (occupied by the fluids), used for the analyses presented hereafter, of LUMEN's injectors and of its combustor is shown in Figure 4.1. To start, as mentioned earlier, the diverging section of the nozzle is cut 10 [mm] downstream of the throat. While this is done for the LNS solver to properly determine (from the background flow) where the supersonic flow regime starts, for the Helmholtz simulations, the 10 [mm] cut downstream of the throat is not performed. This is due to the solver dealing with the homogeneous wave equation that does not use background flow velocity information as input, and thus, for the Helmholtz simulations the nozzle is cut exactly at the throat.

In addition to cutting the diverging section of the nozzle, LUMEN's injector was also simplified. On one hand, as can be learned from Schulze & Sattelmayer [29] the inclusion of the domes of the injectors is necessary to adequately model the damping properties of the system, since not including such features led to a reduction of the damping rates by a factor of 20. On the other hand, in studies investigating the resonant modes of the injector [43, 77], it can be seen that its resonance modes occur most strongly in its posts and are quickly dissipated in its first dome (upstream of the chamber). Hence, while a proper representation of the injectors is important to aim to accurately model the acoustic damping rates of the combustor, the modeling of the whole feed system is seen as unnecessary for the acoustic analysis of the combustor. For this reason, the section of LUMEN's feed system modeled was chosen to end at the first domes of the LOX and CH_4 injectors. Further simplifications made to the injectors include removing the edge fillet interface between the injectors' posts and the combustion chamber, and neglecting the presence of the torch igniter since steady-state conditions of LUMEN are considered.

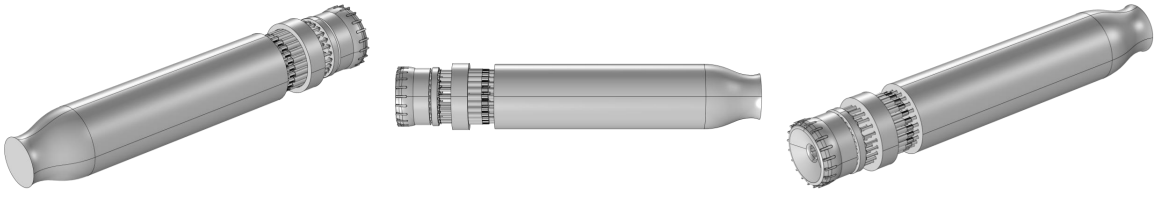

Figure 4.1: Simplified geometry for the LUMEN combustion chamber and injectors

4.1.3 Helmholtz with constant properties

With the geometrical simplifications explained, the set-up and results of the first Helmholtz simulation presented in this report are described hereafter. As explained in the previous subsection, the only difference between the geometry used by the Helmholtz solver (and used as a reference for the analytical equations as well) and the LNS simulation is that the former is cut directly at the throat, while the latter includes for the first 10 [mm] of the supersonic section of the nozzle. The Helmholtz simulations that are presented in this report make use of the same meshing strategy as LNS, and more details on the meshing approach used can be found in Section 4.2.5. A detailed (cross-sectional) view of the mesh used for the Helmholtz simulations is given in Figure 4.2. Given the lack of symmetry of the injector pattern, all simulations had to be carried out in the full three-dimensional domain. The resulting mesh for the Helmholtz runs presented herein consists of $2.13 \cdot 10^6$ unstructured elements with an average element quality of 0.64 (a value of 1 represents a perfectly regular tetrahedron). Given the requirement posed by DLR, all simulations (meshing included) were performed with the FEA software COMSOL Multiphysics 6.0.

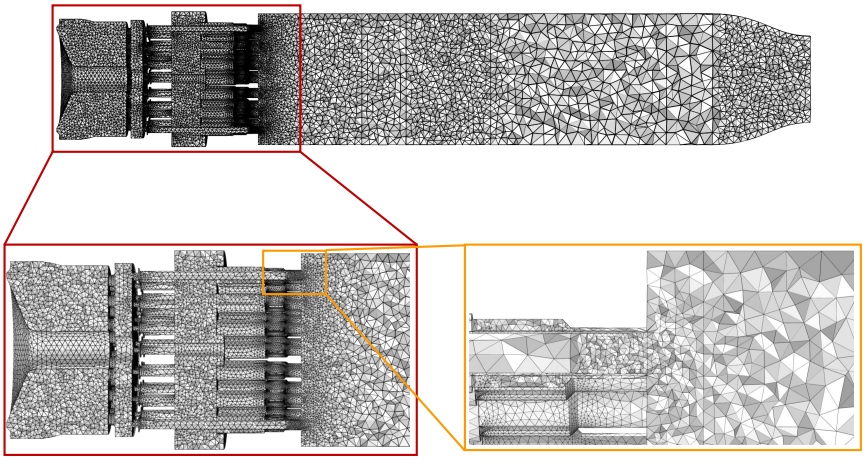

Figure 4.2: Cross-sectional view of the mesh used for the Helmholtz simulations

Regarding the boundary conditions, a fully reflecting condition ($Z=\infty$) was described at the nozzle throat where the geometry was cut. As can be seen from Figure 2.3, this condition is equivalent to treating the nozzle throat as a wall, and therefore the sound hard wall boundary condition was applied to the latter as well as to all solid walls of the geometry. The surfaces on which the wall condition was applied can be visualized in Figure 4.3a and Figure 4.3b. In such figures, the highlighted surfaces in light blue indicate where the boundary was set, while grey areas show where this does not apply. On top of that, conditions for the pressure fluctuations at the inlets of the injectors were also imposed. For those locations, the pressure of the field was assumed to be equal to the background flow pressure, that is no pressure fluctuations occurred. This translates to a non-reflecting boundary condition ($Z=0$), and the surfaces on which this was applied can be visualized in Figure 4.4a (for the LOX injector's inlet) and in Figure 4.4b (for the Methane injector's inlet).

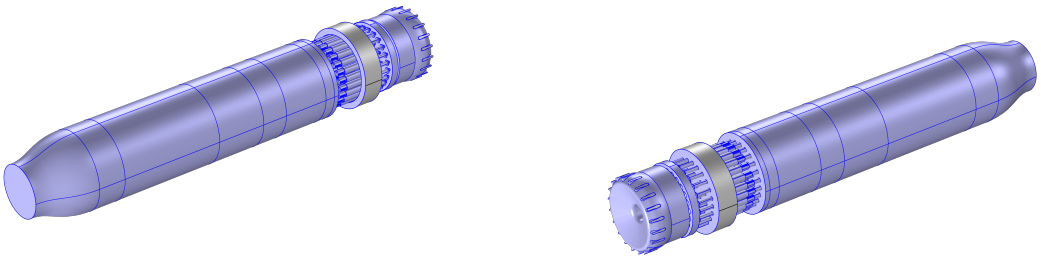

(a) Sound hard boundary condition at the wall of the chamber and injectors, plus nozzle throat

(b) Sound hard condition at the wall of the chamber and injectors

Figure 4.3: Sound hard boundary conditions used for the Helmholtz simulations

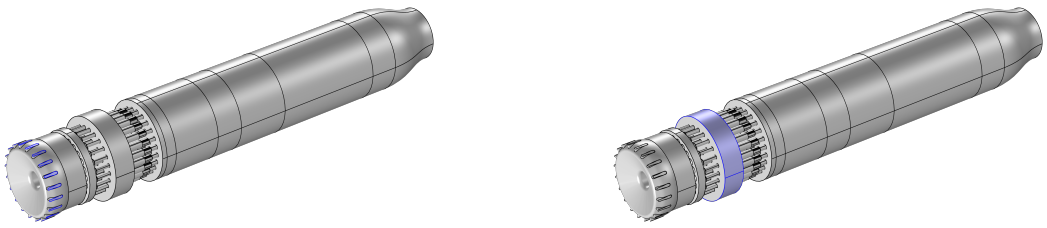

(a) LOX inlet condition **(b)** CH_4 inlet condition

Figure 4.4: Sound soft boundary conditions used for the Helmholtz simulations

The discretization used throughout this report involves linear elements. A quadratic Lagrange discretization was also tested for the Helmholtz simulations, and led to the same results as for linear elements. This showed that with the mesh presented, the results were independent of the employed discretization. Similarly, also the eigenfrequency solver is not varied across simulations, and consistent use is made of the ARPACK method with the MUMPS solver. The latter is a direct solver that albeit requiring more RAM than other available solvers in COMSOL (e.g. PARDISO), is more robust [17]. Moreover, as the convergence criterion for the simulations, the default value of 1E-6 was used for the relative error of the eigenfrequencies. Lastly, before the simulation could be run, a search method for the eigenfrequencies had to be set. From previous analyses [92], it was found that the most reliable way to retrieve the intended eigenmodes was to set up a manual search where the simulation would be solved around a given range of frequencies and the frequencies closest (in absolute magnitude) to the prescribed search locations, returned. To make this approach applicable for engines where it is unknown where the various acoustic modes are located frequency-wise, use is here made of the analytical solutions, and their search iterated. For example, if a given mode is to be solved, the search in COMSOL would be centered firstly around the analytical solution for that mode, with a parametric sweep applied for adding a few additional frequencies to search around that value in case the analytical results are too far from the simulation's prediction. As the complexity and fidelity of the simulations increase, prior simplified runs can be used as starting point for the eigenfrequency search, leading to a search strategy converging on the intended mode. Overall, more manual iterations for the frequency search were needed for this Helmholtz simulation (to capture the intended mode in the solution) than for the subsequent LNS simulation, with the reason being that the previously introduced analytical results lead to large errors in the predicted frequencies, hence providing a starting point for the search that is further away from the solution of the Helmholtz simulation than the solution of the LNS simulation is from the latter. Running the Helmholtz simulation using constant CEA properties for the background flow in the LUMEN combustor led to the eigenfrequency results presented in Table 4.5, and the corresponding mode shapes as shown in Figure 4.5 and Figure 4.6 for the combustion chamber. Given that a quiescent flow is here considered and that the majority of the chamber has a cylindrical shape, as expected, the mode shapes are in accordance with the ones for a pure cylinder that were shown earlier in Chapter 2.

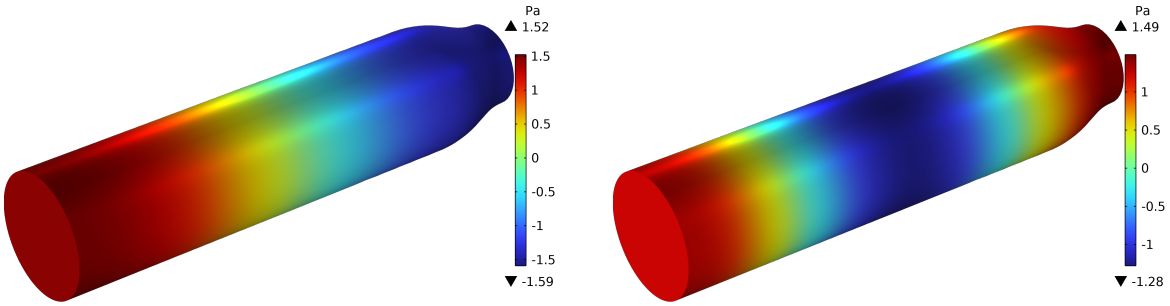

(a) L1 mode (1934 [Hz]) **(b)** L2 mode (3846 [Hz])

Figure 4.5: Longitudinal mode shape results obtained from the Helmholtz simulation using constant CEA values

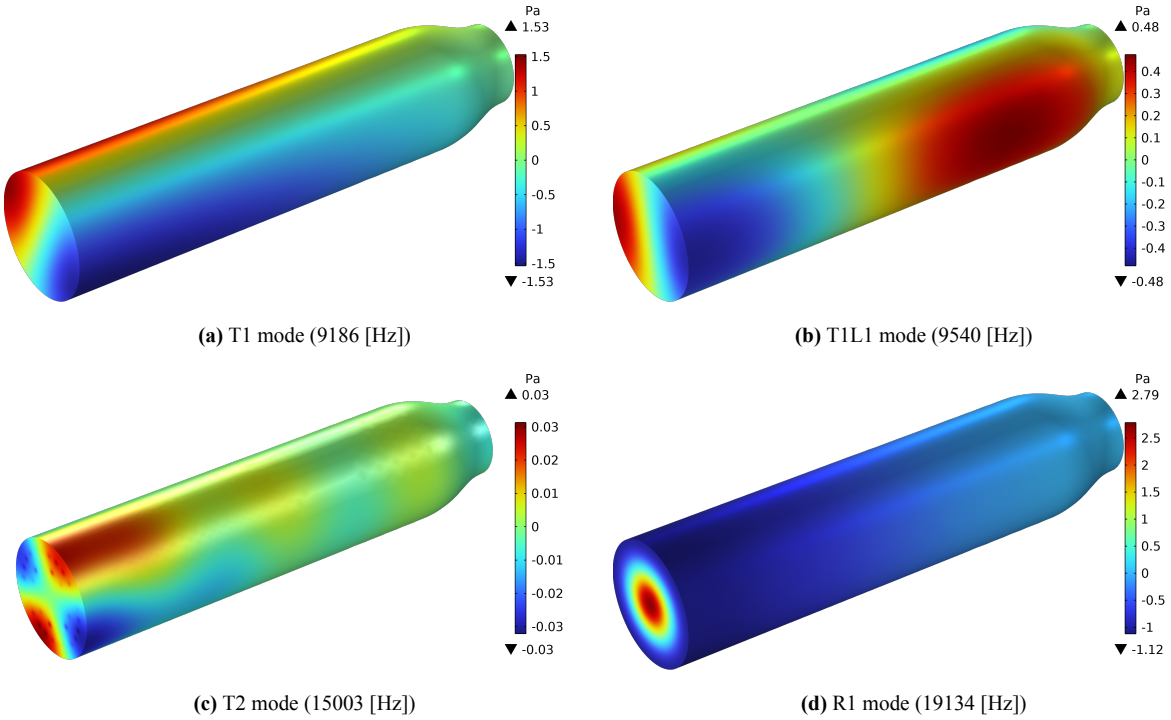

(a) T1 mode (9186 [Hz])

(b) T1L1 mode (9540 [Hz])

(c) T2 mode (15003 [Hz])

(d) R1 mode (19134 [Hz])

Figure 4.6: Transverse and combined mode shape results obtained from the Helmholtz simulation using constant CEA values

Table 4.5: Eigenfrequency solutions obtained from the Helmholtz simulation using constant CEA values

	L1	L2	T1	T1L1	T2	R1
Frequency	1934 [Hz]	3846 [Hz]	9186 [Hz]	9540 [Hz]	15003 [Hz]	19134 [Hz]

4.2 State-of-the-art Flow Description

Although applicable for very preliminary design phases, due to not requiring elaborate analyses as input, the previously introduced Helmholtz and analytical solutions using CEA properties, can not account for how varying flow properties in the chamber influence the acoustic field. Given the large flow gradients occurring in rocket combustors, the applicability of the previous methods is seen to be limited to preliminary design phases where fundamental design parameters of the engines are still iterated quickly. For a detailed design phase, the modeling of the background flow is critical to allow for accurate predictions of the combustion chamber's acoustic mode shapes, and for that, the current section introduces the current state-of-the-art approach for hybrid CFD/CAA (Computational Aeroacoustic) analyses. Firstly, a walk-through of the process behind the modern standard of radially averaging CFD fields, and using the resulting 1D distribution of flow properties as input for the acoustic simulation, is introduced in Section 4.2.1. Here, the results for LUMEN are reported as well. Next, since the LUMEN CFD was not performed for the complete engine's injectors, in Section 4.2.2 the approach used to complete the radial-averaged background flow descriptions for the LUMEN test case is explained. Once the whole background flow could be described for the modeling geometry (shown in Figure 4.1) via a 1D distribution, the acoustic simulations were run. For that, the analytical solution and the Helmholtz simulation are updated, and, after that, the first LNS simulation is introduced in Section 4.2.5.

4.2.1 Radial averaging of the CFD field

Slicing a CFD flow field, taking the area average at each slice, and extracting a radially-averaged 1D profile are referred to in this report as taking the radial average of a given CFD field. Using this method to

describe the background flow field in rocket combustor has become the go-to method for Acoustic-based methods in recent years [17, 29, 30, 43, 98]. From the surveyed literature on the topic, in the rocket propulsion community, this approach found its first applications in 2010 and 2013, with the cooperation between Astrium Space Transportation (now part of ArianeGroup) and TUM [106, 107], and is nowadays the standard method used by TUM in their research conducted with the LEE solver [29, 30, 43, 66, 98]. In this report, the performance of LNS is first benchmarked with the Helmholtz solver using a radially-averaged CFD field as input, and then the accuracy of LNS is aimed to be ameliorated by improving the description of the background in the next chapter.

For the radial-averaging, use is made of the LUMEN CFD analysis conducted prior to this thesis by Schneider, kept, to the moment of writing of this report, internal to DLR. This simulation was run using DLR's developed CFD tool *TAU*, and for the analyses here presented the results were post-processed using Paraview and Python. As mentioned earlier in the introduction of this chapter, the analyses presented in this report were first performed for the combustion chamber geometry for which the CFD analyses were run. During the validation of the results, it was found that an unexplainable large error was returned by all analyses for the longitudinal modes only. After performing a root-cause analysis for the unexpected large error in longitudinal modes, from pictures of the test set-up it was discovered that during experiments an adapter ring was added at the injection plane of the chamber to introduce high-frequency pressure transducers. As a result, this adapter ring added 15.41 [mm] of length to the cylindrical section of the combustion chamber (for the same internal geometry). Given that re-running the CFD simulation of LUMEN was not an option, and that the combustion region of the chamber would not be altered by the addition of the measuring rig, the output 1D profiles from the radial average of the CFD field, together with the chamber geometry, were "lengthened" by the required amount. Prolonging the profile of the flow parameters at the end of the cylindrical section of the combustion chamber (i.e. before the start of the nozzle) was deemed to not have a significant influence on the acoustic results. As will be seen hereafter, values such as pressure, speed of sound, and density reach a plateau at the end of the combustion chamber where their variations can be assumed independent of chamber length. Furthermore, since the adapter ring that was added during experiments did not alter the diameter and internal geometry of the chamber, and because the combustion zone was seen to end around 140 [mm] before the start of the nozzle, the flame length could be assumed to be constant and independent of the chamber length.

To start, cross-sectional slices of LUMEN CFD's flow field were taken in Paraview at steps of 1 [mm] along its length. Then, for each slice, the area average was computed in Python, as formulated in Equation 4.1 for a given variable x. This process was applied for all variables returned by the LUMEN CFD analysis. The atomization and vaporization of the liquid propellants, as modeled by the CFD analysis of the chamber, are thus also averaged for the cross-sectional slices in which such phenomena appear. Even though it does not follow any fundamental conservation law, area averaging is a simple method that for cylindrical rocket combustors with smooth transitions at the nozzle can return highly accurate results for the eigenfrequencies, as was shown in Table 2.3. An improvement to area averaging for which the necessary information can still be straightforwardly retrieved from Paraview is the mass averaging approach. While this has the advantage of meeting the conservation of mass, a previous study at DLR found that it weighted too heavily the properties of the LOX core, thus leading to large underestimations for the speed of sound and temperatures in the chamber [92]. The mass averaging used in this study accounted for the presence of all fluids in the chamber (e.g. both liquid propellants being injected and combustion gases), and followed the formulation presented in Equation 4.2. In the study conducted at DLR [92], substituting the area-averaged profiles with the mass-averaged ones, as input for the LNS simulation, led to the initial 10 % error of the L1 mode and 7.8 % error of the T1 mode, of DLR's LOX/LH_2 BKH combustor, to respectively increase to 21.7 % and 47.8 %.

$$\bar{x}^A = \frac{1}{A}\int_A x dA \qquad (4.1) \qquad\qquad \bar{x}^M = \frac{1}{\dot{m}}\int_m x d\dot{m} \qquad (4.2)$$

The LUMEN radially-averaged profiles are given in Figure 4.7 for the static pressure, density, speed

of sound, and static temperature, for both the short and the long chamber configurations. The former refers to the original chamber length as used in the CFD simulation, while the latter indicates the chamber length corresponding to the ”real” combustor tested during experiments. Constant values of the flow properties are taken at the end of the cylindrical (short) chamber to lengthen it to obtain the long chamber results. In the figures, the origin of the axial distance is fixed at the injection plane, and the convergent section of the nozzle starts at a distance of 322.8 [mm] for the short chamber and at 338.2 [mm] for the long chamber case. It is worth noting that the profiles shown also include the whole diverging section of the nozzle from the CFD analysis of LUMEN.

Previously, in Figure 2.6, the radially-averaged speed of sound for the LOX/H_2 BKD combustor was shown. This combustor, while operating at a pressure higher than LUMEN's by around 6.5 [bar], has the same number of injection elements, uses the same injector geometry as LUMEN's configuration studied in this report, and has an identical chamber diameter. Comparing its results with the speed of sound shown in Figure 4.7, two differences can be noted in the variation of the radially-averaged speed of sound that can be attributed to the difference in the fuel of the two combustors. Firstly, in Figure 2.6, for the test run having the lowest speed of sound at injections, the ratio between the maximum attained speed of sound value in the chamber to the minimum one is around 1.9, while for LUMEN it is equal to 2.6. This shows that larger axial variations in properties are encountered in methalox engines than in hydrolox engines, indicating that using constant CEA properties throughout the chamber is less applicable for the former. Secondly, the larger variation of the speed of sound for LUMEN also occurs over a longer section of the chamber. In Figure 2.6, plateauing can be estimated to occur around 72 [mm] downstream of the face plate of the injectors, while for LUMEN this does not occur before 200 [mm] after injection due to the slower kinetics of the chemistry. These results not only suggest that the variations of the background flow are more dominant for methalox engines, but also that these changes occur far deeper in the combustion chamber than for similar hydrolox engines, thus having an effect on the acoustic propagation over a larger region.

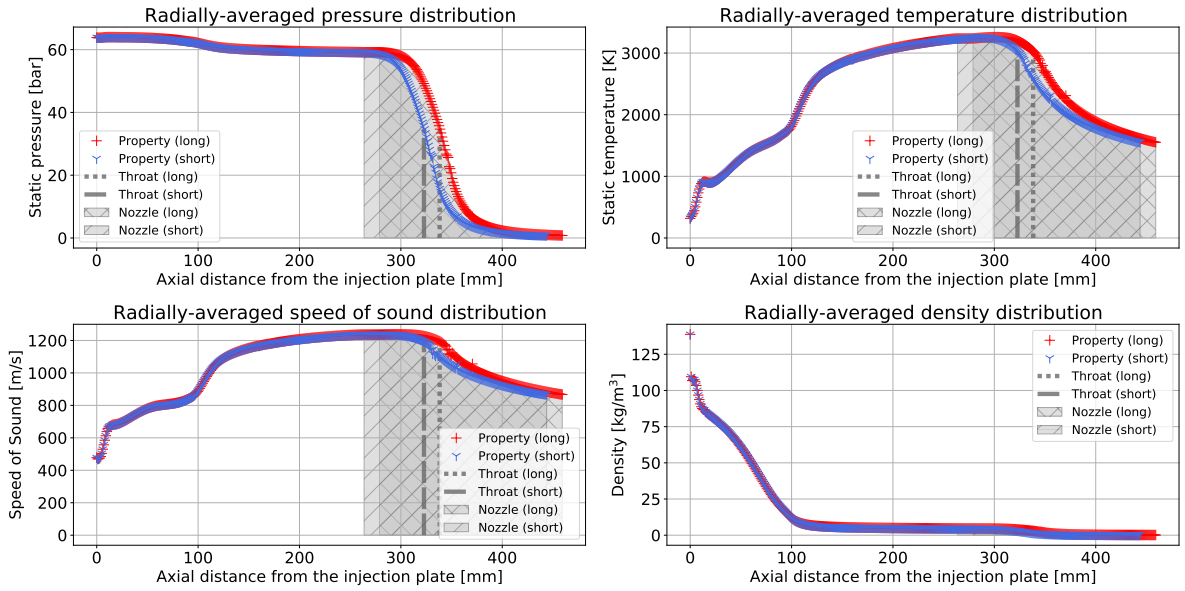

Figure 4.7: One-dimensional variation for the pressure, temperature, speed of sound, and density obtained by radially-averaging LUMEN's CFD field. Shown for the long chamber (in red) and short chamber (in blue)

To illustrate that the CEA values are only obtained at the end of the chamber and are not representative for most of the combustor, Figure 4.8 plots in the same graph the radially-averaged CFD results with the CEA values of Table 4.2 for the speed of sound, density, and Mach number.

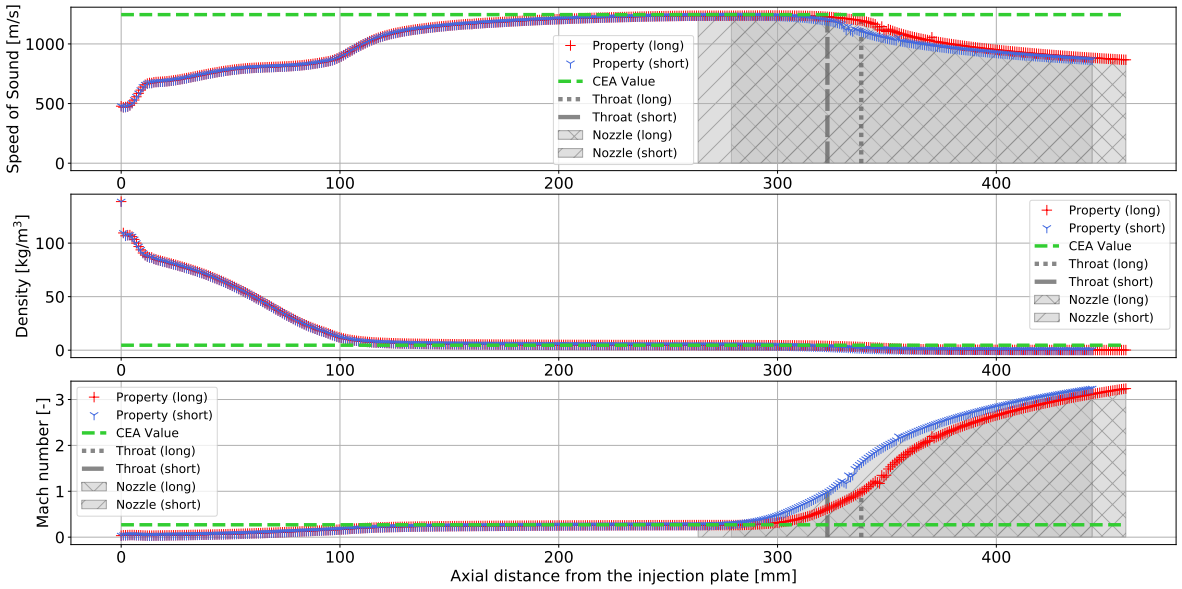

Figure 4.8: Comparison of the constant CEA values for the chamber with the radially-averaged profiles for the speed of sound, density, and Mach number

The CFD results that were radially averaged were based on the required input parameters from the LNS solver in COMSOL. For the interested reader, an overview of the various input parameters required by an LNS simulation in COMSOL is given in Figure G.1, where the background flow parameters are either used to describe the latter directly in the LNS equations or to retrieve the gas properties inside the combustion chamber or injectors. Figure G.1 also shows how these were computed in the present study but in short, the variables required as input to describe both fluid properties and background flow are pressure, temperature, velocity vector, density, viscosity, heat capacity at constant pressure, speed of sound, specific heat ratio and the thermal conductivity. Regarding the latter, this was obtained from RPA for the chamber gases, by extracting its value at the injection plane, at end of the combustion chamber (i.e. start of the nozzle), at the throat, and at the plane where the diverging nozzle was cut. Initially, as done in a previous study at DLR [92], it was tried to obtain the thermal conductivity by taking the mass fraction average of the thermal conductivities of the species returned by the CFD simulation, where the conductivities of the various species were retrieved from CoolProp. Trying to do so for LUMEN, led to the finding that for the pressure and temperature variations experienced in the chamber, CoolProp did not have data for most of the species of combustion gases.

4.2.2 Flow description of the injectors

To aim to accurately resolve the damping rates, profiles for the injectors also had to be computed. The CFD analysis previously introduced was only performed for the chamber and the last sections of the injection elements (as visible from Figure 3.5a), thus neglecting the presence of the injector domes. For that, an incompressible RANS simulation was run for the LOX injector in COMSOL and a one-dimensional compressible flow description was computed via the so-called *influence coefficient matrix* formulation from Greitzer, Tan & Graf [108] for the CH_4 injector. At first, it was tried to run a RANS simulation for the fuel injector in COMSOL as well, but given the un-physical results obtained and no direct way to improve them, it was decided to simplify the analysis and solve 1D compressible equations in Python. For the Methane RANS simulation that was tried, COMSOL's compressible flow module, that is the *High-mach Number Flow* physics, using a k-ϵ turbulence model was employed. Here, unrealistic velocities were obtained at the end of the injector regardless of whether the dome was included in the simulation or not. Given the requirement imposed by COMSOL to have to specify Dirichlet conditions for the pressure, velocity, and Mach number at the inlet and for the pressure at the outlet (not the case for

the incompressible simulation of the LOX injector) limited room for trying to improve the results was given. To try to do so, the mesh was refined in zones of large gradients, the injector geometry was further simplified, the isothermal versus adiabatic wall condition was tested, and changing the turbulence model and stabilization parameters of the solver were also examined. Also, the gaseous Methane fluid model was directly taken from the one built-in in COMSOL's material library. In the end, given the low flow gradients expected in the injector and that the LOX injector has a bigger influence on triggering high-frequency combustion instabilities in the chamber [12], partly due to its larger admittance, it was decided to model the background flow in the Methane injector by means of 1D compressible flow equations.

LOX injector: incompressible RANS simulation

Due to its liquid state, an incompressible simulation was run for the LOX injector. For this, the RANS k-ϵ turbulence model was employed together with the use of wall functions for the wall treatment. The steady-state simulation was run using linear discretizations for all variables, and the resulting unstructured mesh is shown in Figure 4.9. The mesh consists of $6{\cdot}10^5$ elements with an average quality for their skewness of 0.61.

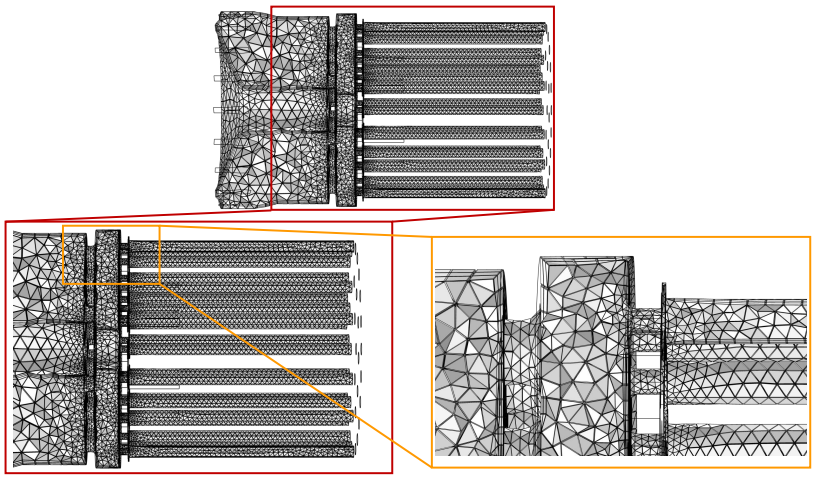

Figure 4.9: Cross-sectional view of the mesh used for the CFD simulation of the LOX injector

For the material properties, by comparing the density at the inlet of the injector obtained by COMSOL through its built-in material library with the one determined by CEA, it was found that the built-in material library for liquid Oxygen led to a large underestimation of the density for the given dome pressure and temperature (by around a factor of 2). Hence, all necessary input properties (namely density, dynamic viscosity, thermal conductivity, and specific heat) were overwritten with NIST data and made in function of the pressure attained. Besides that, boundary conditions were applied. Firstly, no-slip walls were defined. Secondly, the mass flow was specified at the inlet of the injector, and thirdly, the static pressure corresponding to the chamber pressure designated at the outlet of the injector (i.e. at the injection plane of the chamber). The surfaces corresponding to these conditions are shown in Figure 4.10. Next to that, due to difficulties in making the code converge when running COMSOL's default iterative solver (GMRES) for the problem considered, a more robust, yet more computationally-intensive, direct solver (PARDISO) was used together with COMSOL's standard convergence criteria set to 1e-3 for the residual.

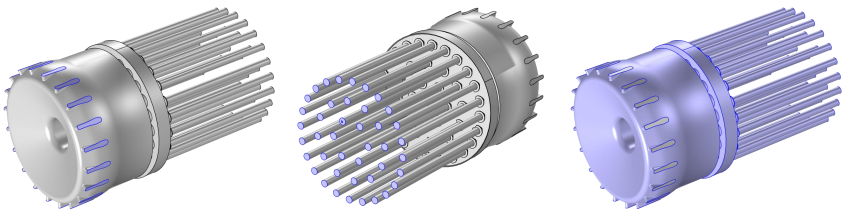

Figure 4.10: LOX injector boundary condition surfaces for CFD analysis

Running on a 6 cores and 32Gb RAM machine, the CFD simulation took around 30 hours to run, leading to the results shown in Figure 4.11 and Figure 4.12b for the streamlines and pressure, respectively. From the former, the injection velocity of LOX in its injector dome (at the radial area slots visible in Figure 4.11 causing the flow to swirl in the dome) is computed by the simulation to be 15.7 [m/s]. While from the mass flow equation, using Table 4.1 for the injection conditions and an injection area of a single slot of $3.116 \cdot 10^{-5}$ [m^2] (determined from the CAD file), an injection velocity of 9.2 [m/s] is obtained. The higher injection velocity obtained by the CFD is associated to the coarse mesh elements used at the injection locations of the injector. Discretizing the injector geometry with the coarse mesh used at the dome entrance reduces the injection area, causing an increase in velocity for a constant mass flow. This is not seen as a crucial difference since not only it occurs at the most upstream location from the faceplate of the engine, but also because this velocity over-estimation is only localized in the vicinity of the inlet planes and rapidly reduces due to the large area expansion of the dome. For the outlet velocity of the injector, that is, the velocity upon injection in the combustion chamber, an average value of 14.1 [m/s] is obtained, which compares well with the CFD simulation of the LUMEN combustor, where an injection velocity of 14.0 [m/s] was obtained at the exit of the LOX posts. The LOX injector results were also radially averaged to have a consistent representation of the background flow for the LUMEN engine, as for the CFD results of the chamber. For that, 23 slices along the injector's length with a higher concentration near the transition between the dome and the LOX posts (where higher gradients occur) were taken. The result of the averaging can be seen in Figure 4.12a for the case of the static pressure. Here, the same coordinate system for the radial averaging of the chamber is used, meaning that its origin is situated at the center of the injection plane of the engine. For the sake of clarity, the distances are kept positive in Figure 4.12a, which, for the depiction provided, uses the reference system indicated on the picture on its right (Figure 4.12b). A sudden reduction in pressure is visible in Figure 4.12a around 65 [mm] downstream of the inlet location of the LOX. The reason for this is the correspondingly rapid reduction in area at that location of the LOX injector, where the injector posts attain a minimum in diameter as was visible in Figure 3.4.

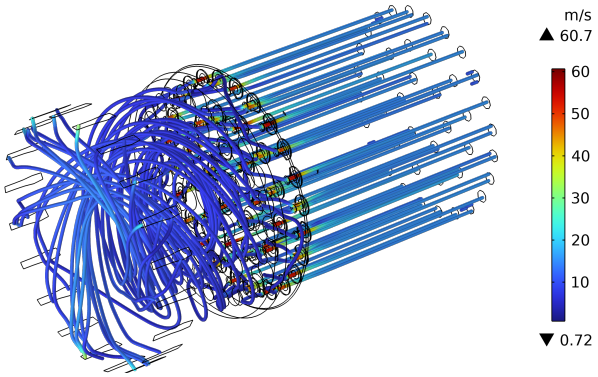

Figure 4.11: LOX Injector streamlines

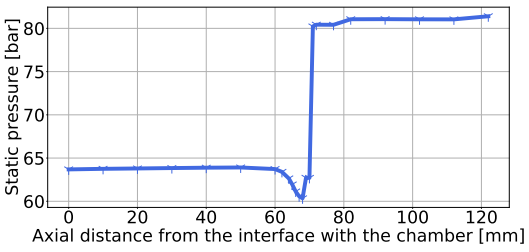

(a) One-dimensional static pressure profile of the radially-averaged LOX injector's CFD field

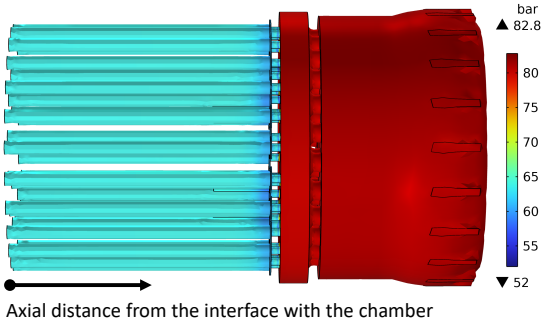

(b) CFD result of the LOX injector's static pressure

Figure 4.12: Inner chamber's volume and mesh used for the LUMEN CFD

From the pressure results it can be seen that a dome pressure of 82.8 [bar] is returned by the simulation, while in reality, based on the pressure recorded during the reference calorimetric experiment, the LOX injector inlet pressure is 69.8 [bar]. This 13 [bar] difference, corresponding to an 18.6 % absolute error, was mainly associated with neglecting the wall roughness (smooth walls were assumed) and due to disregarding heat transfer at the wall. The inclusion of the wall roughness increases losses at the wall, and for mass flow conditions prescribed at the inlets of the injector and the chamber pressure set at its outlet, a lower inlet pressure would be returned by the simulations in case roughness were to be included. Due to the LUMEN injectors being additively manufactured and information on their wall roughness lacking, the wall roughness in the simulation was omitted, and a pressure drop of 13 [bar] was kept. For future analyses, a sensitivity study on this shall be performed to see how it affects the results, especially the damping rates. Besides the pressure drop, the obtained CFD results were determined to be mesh converged given that running the simulation for meshes with $2.4{\cdot}10^5$ and $3.3{\cdot}10^5$ elements led to a deviation of the maximum dome pressure of 4.3% and 1.2% when compared to the results here presented (obtained with a mesh of $6{\cdot}10^5$ elements).

Lastly, for the variables that were not returned by the simulation but that would still be required to describe the background flow for the LNS simulation (i.e. the specific heat at constant pressure, speed of sound, and specific heat ratio), NIST was used to formulate them as a function of the static pressure attained, where the minimum and the maximum pressure from the simulation were used to set the range. Given their negligible variations between the inlet and outlet of the LOX injector (sub 3%), for simplicity, the latter variables can be assumed constant in future studies focusing on accurately predicting the eigenfrequencies of the chamber. If accurate damping rates of the system are of interest, besides accounting for the flame response in the chamber, as previously mentioned, a sensitivity analysis shall be performed to understand how errors in the injector properties influence the system damping.

CH_4 injector: 1D compressible flow analysis

After the analysis of the LOX injector, the flow description for the CH_4 injector was tackled using 1D compressible flow equations. These were based on the influence coefficient formulation presented by Greitzer, Tan & Graf [108], assuming constant specific heat and molecular weight of the gas, and accounting for the influence of area variations in the channel and of friction. The Methane conditions at the inlet of its injector were reported in Table 4.1, corresponding to a supercritical phase. Since the largest gradients are expected to occur within the posts of the injector leading up to the combustion chamber (due to area changes), only these posts are here modeled. A detailed view of one of the 42 (identical) injector elements is given in Figure 4.13. For the analysis here presented, the three slots that are visible in Figure 4.13 where the B-B cut was taken, were neglected. This led to that section of the injector elements being analyzed as a perfect cylinder tube without local reductions in area.

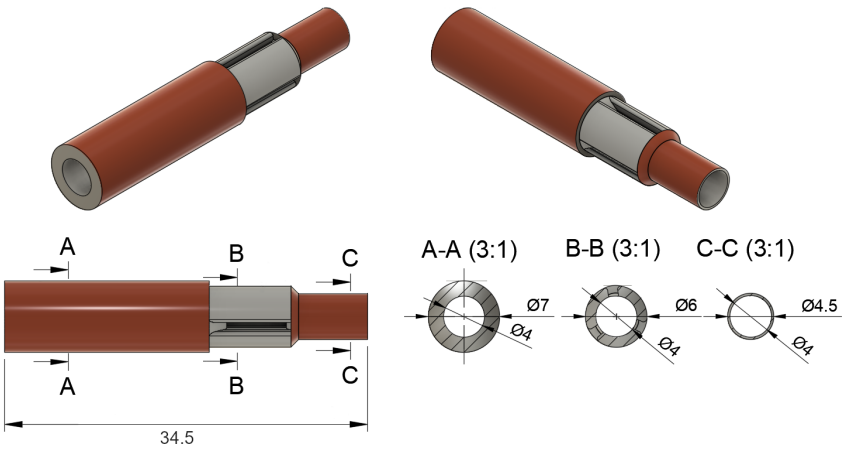

Figure 4.13: Dimensions of the CH4 injector posts

Regarding the approach used, while marching along the length of the injector element, the static temperature and static pressure at step *i* were respectively computed via Equation 4.3 and Equation 4.4, following the previously mentioned Greitzer approach. In these equations, x indicates the axial direction of the injector, f is the friction coefficient (explained in the next paragraph), and D_h is the hydraulic diameter of the tube. For circular tubes, the hydraulic diameter can be expressed in terms of the inner and outer radius as shown in Equation 4.5.

$$\frac{dT}{T} = \frac{(\gamma-1)M^2}{1-M^2}\frac{dA}{A} - \frac{\gamma(\gamma-1)M^4}{2\left(1-M^2\right)}4f\frac{dx}{D_h} \tag{4.3}$$

$$\frac{dp}{p} = \frac{\gamma M^2}{1-M^2}\frac{dA}{A} - \frac{\gamma M^2\left[1+(\gamma-1)M^2\right]}{2\left(1-M^2\right)}4f\frac{dx}{D_h} \tag{4.4}$$

$$D_h \equiv \frac{4A}{P_{wet}} = \frac{2\left(R_{out}^2 - R_{in}^2\right)}{R_{out}+R_{in}} \tag{4.5}$$

Once the thermodynamic state at step *i* was found, CoolProp was then used to retrieve the density, dynamic viscosity, specific heat, speed of sound, specific heat ratio, and thermal conductivity at that step. From that, the new axial velocity was determined via the mass flow condition $\dot{m}=\rho\ \mathrm{v}_x\ A$, and the Mach number at step *i* was calculated. Before using the newly computed properties to determine the static pressure and static temperature again at the next step, the friction coefficient at step *i* was obtained. For this, the explicit formulation proposed by Fang, Xu & Zhou [109] for Colebrook's equation was used. For the range of the Reynolds number between 3000 and 10^8, the latter equation leads to a maximum relative error of 0.5% when compared to the Colebrook solution for both smooth and rough pipes, leading to the method from Fang et al. being the simplest one for such a relative difference from the Colebrook equation and for such a large Reynolds number range [109]. The Fang et al. formulation for the friction coefficient is here presented in Equation 4.6, which is valid for Reynolds numbers between 3000 and 10^8, and relative roughness ($\frac{e}{D}$) below 0.05 [-]. For the roughness, based on the construction material used for the Methane injector (i.e. copper) an absolute value of 0.002 [mm] was taken [110]. It should be noted that the latter, together with the assumption of smooth walls for the LOX injector CFD simulations, is an underprediction of the real injector walls' roughness. The injectors are manufactured via additive manufacturing methods, which are known to provide rough surface finishes, with an active field of research dealing with how these affect the heat transfer to the wall [111]. Hence, to investigate how these assumptions influence the results, a future study shall perform a sensitivity analysis on how wall roughness and the inclusion of the three slit cavities (here neglected) influence the acoustic results of the chamber. For the assumptions made in this report, the calculations were started using the fluid properties determined prior to the entrance of the injector posts (i.e. in the dome) using the thermodynamic state presented in Table 4.1 as input. The injector elements were broken up into 4 sections, as shown in Figure 4.14, with 500 discretization points for each. Additionally, given the approach chosen, where the temperature and pressure at location *i* are calculated based on the information of location *i-1*, the fractions in Equation 4.3 and Equation 4.4 containing the Mach number and friction coefficient were assumed independent of temperature, pressure, area, and axial distance, allowing to find a closed form solution of the equations.

$$f = 1.613\left[\ln\left(0.234\left(\frac{e}{D}\right)^{1.1007} - \frac{60.525}{Re^{1.1105}} + \frac{56.291}{Re^{1.0712}}\right)\right]^{-2}, \tag{4.6}$$
$$if \quad 3\cdot 10^3 < Re < 10^8 \quad \& \quad 0 < \frac{e}{D} < 0.05$$

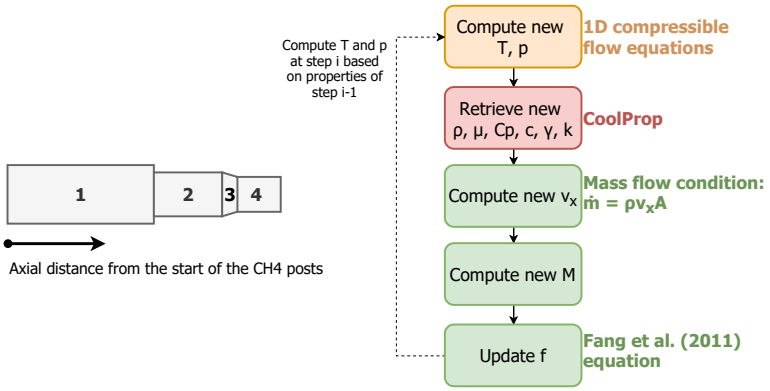

Figure 4.14: Modeling flowchart of the CH4 injector posts for their 1D compressible flow analysis

To have a smooth transition between the background flow in the Methane injector and the combustion chamber, once a solution was found at the end of the injector, the whole previously-explained process (which is summarized in a flowchart in Figure 4.14) was iterated starting from a lower guess for the initial static pressure at the entrance of the injector elements. The solutions presented hereafter were iterated until the exit pressure of the injector elements coincided with the chamber pressure of Table 4.1. The resulting flow profiles for the static pressure, temperature, speed of sound, and density in the CH_4 injector posts are shown in Figure 4.15. If the same process that was here presented for the injector posts is carried out after the latter's solution has been obtained, the values in the Methane dome can also be obtained. Carrying out the process in the reverse order, using the initial properties in the injector posts as the starting values at location *i-1*, leads to a pressure in the dome of 68.82 [bar], which is 2.2 [bar] lower than the CH_4 dome pressure measured during experiments. As a general takeaway for the injector analysis, in the future, it is recommended to perform a more accurate CFD analysis by means of dedicated software to investigate how the error in pressure drop influences the acoustic results, in particular the damping rate and hence the stability of the system.

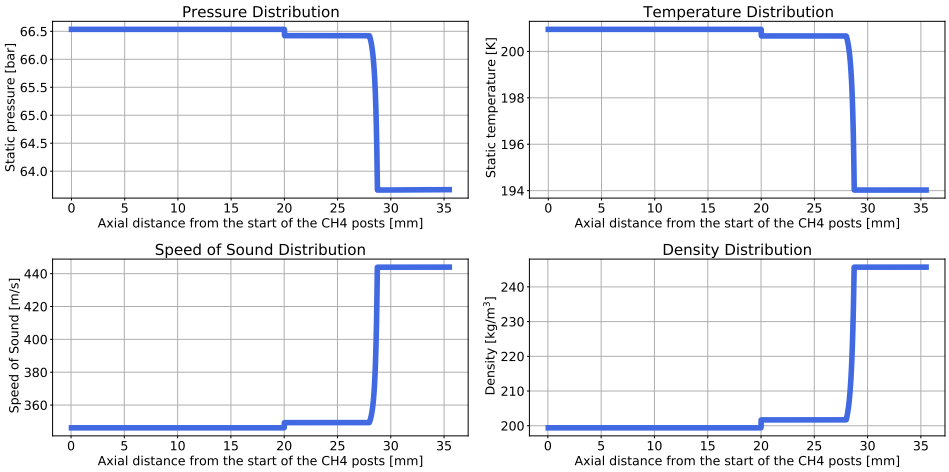

Figure 4.15: One-dimensional profiles for the pressure, temperature, speed of sound, and density distributions in the CH4 injector posts, stemming from compressible flow calculations

From the 1D profiles, a number of effects can be seen. Firstly, the reduction in area and the inclusion of friction, for the subsonic flow considered, reduce the static pressure and static temperature as expected. The same can be said for the velocity, which increases due to area contraction. With a reduction in temperature, considering the ideal gas formula for the speed of sound, $c = \sqrt{\gamma \frac{R}{MW} T}$, a reduction in speed of sound would be expected, while the opposite occurs in Figure 4.15. The reason for this behavior is attributed to the phase of the fluid, which is supercritical and does not meet the ideal gas assumptions.

Plotting the sound speed variation for given pressure and temperature values leads to Figure 4.16. The fluid properties in the figure were retrieved from CoolProp, and show that at low enough temperatures, a reduction of temperature leads to an increase in the speed of sound. For supercritical hydrocarbons, this behavior could also be seen in the work of Cheng, Fan & Yang [112]. At the critical point, by lowering the temperature, the fluid will tend more to its liquid phase (supercritical liquid) which is associated with a higher density and speed of sound. In Figure 4.16, three reference points are given in green, which refer to the thermodynamical states at the inlet of the Methane injector (circular marker), and at the outlet of the injector, that is, upon injection in the combustion chamber. For the latter, the plus-shape marker indicates the conditions obtained by the 1D analysis explained above, while the cross-shape marker represents the physical conditions retrieved from the CFD results of the LUMEN combustor. Compared to the values obtained by the LUMEN CFD simulation, the 1D analysis returns an exit pressure and temperature of the Methane injector that are respectively 0.8 % and 2.8 % lower. Albeit small, the difference in temperature obtained via the 1D analysis is enough to lead to an opposite behavior for the speed of sound variation in the Methane injector than obtained at the end of the injector element by the CFD analysis, showing the high sensitivity for the speed of sound in terms of static pressure and static temperature the closer one gets to the critical point. The same behavior as the speed of sound was also observed for the density. The sensitivity of the speed of sound on the static temperature computed by the 1D analysis supports the previously mentioned recommendation of conducting a sensitivity study on the fluidic analysis of the injector to assess its influence on the acoustic results of the combustion chamber. Regarding the output Methane velocity (i.e. chamber injection speed of the fluid), through the 1D analysis, a value of 50.7 [m/s] was found while a Methane injection velocity of 82.4 [m/s] was returned by CFD simulation of the LUMEN combustor. The reason for this lower velocity was mainly associated with the neglected cross-sectional area decrease in the injector element at its intermediate location (i.e. section 2 as shown on the left of Figure 4.14).

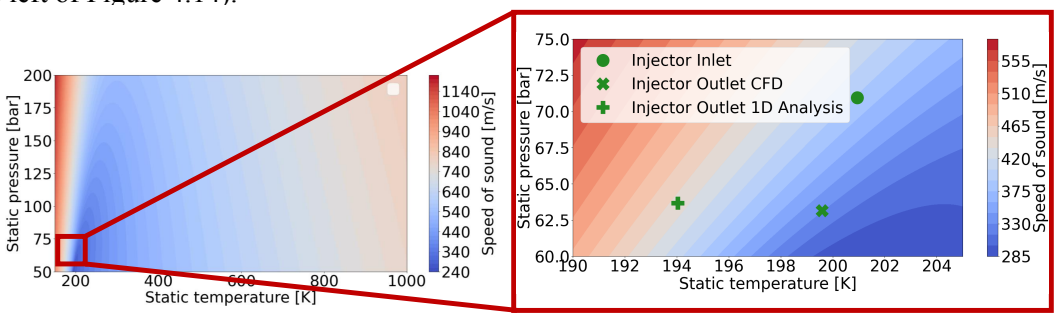

Figure 4.16: Pressure-temperature plot of Methane's speed of sound variation

4.2.3 Corrected analytical solution

Before presenting the results of the updated Helmholtz and LNS simulations, the corrected analytical results are first introduced. Given the availability now of one-dimensional profiles computed from a CFD simulation, a better estimate for the speed of sound can be used in the analytical results. Here, the improved speed of sound description takes the form of correction factors in Equation 2.26. For the 1D profiles obtained in Figure 4.7 for LUMEN, a longitudinal coefficient (accounting for the flow field up to the nozzle throat) of 0.85 [-] was found ($\bar{c} = 1046.73$ [m/s] and $c_{max} = 1237.88$ [m/s]) while for the transverse coefficient, first, the combustion zone had to be defined. To do so, from the CFD results, the mass fraction of CH_4 was analyzed together with the speed of the sound. Slices for such fields are shown in Figure 4.17, together with the axial distance from the injection face (the injection face can be seen as the left-most cross-sectional face of the two plots in Figure 4.17) to where the combustion zone was deemed to end. The combustion zone length was chosen as the distance from the point of injection where the majority of the methane has already reacted. Downstream of the cross-sectional slice delimiting the combustion zone in Figure 4.17a, only a mass fraction below 0.1 could be found. The speed of sound field shown in Figure 4.17b was then used to check that the majority of the axial and radial variations of this property would also occur within the combustion zone defined based on the CH_4 mass fraction,

verifying that the latter could be used to describe the region within which most of the speed of sound (radial) stratification would occur. Based on this, the end of the combustion zone was set at a distance of 106.8 [mm] from the injection plane. Taking the average of the speed of sound within this region, and normalizing it by the maximum value in the chamber, led to a transverse coefficient for LUMEN of 0.61 [-] ($\bar{c_{cz}} = 757.24$ [m/s]). This suggests that if a background flow correction is not applied, and constant CEA properties are used, then the T1 mode frequency will be more than 60% higher than the one computed via this corrected analytical method.

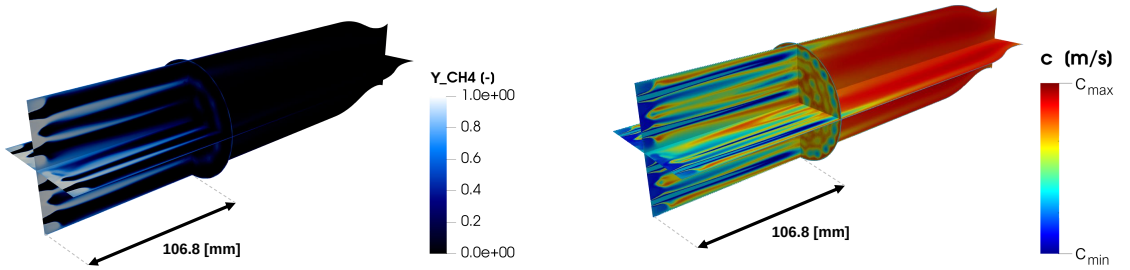

(a) Combustion zone shown for the CH4 mass fraction

(b) Combustion zone shown for the speed of sound distribution

Figure 4.17: Depiction of the chosen combustion zone

Using the previous correction factors of $k_l = 0.85$ [-] and $k_t = 0.61$ [-] together with Equation 2.26, gives the frequency results presented in Table 4.6. Compared to the results of Table 4.4 and Table 4.5, the corrected analytical solution generally leads to lower frequencies, with a reduction of about 15% and 62% when respectively compared to the longitudinal and transverse modes of the simple analytical solution given by Equation 2.24, and of around 15% and 69% when comparing the closest corrected analytical solution (i.e. Natanzon-1/3) to the Helmholtz simulation using CEA values. Concerning the sensitivity of the results, by decreasing and increasing the end of the combustion zone by 10 %, leading to a length and k_t correction factor of 96.3 [mm] and 0.6 [-] for the -10 % case and of 117.5 [mm] and 0.63 [-] for the +10 % case, absolute T1 frequency differences of 1.6 % and 3.3 % are found. Based on the approach used in this report, where the combustion zone limit is based on the Methane mass fraction downstream of this boundary not being higher than 0.1 [-], the eigenfrequencies are not considered to be very sensitive to the length of the combustion zone chosen. Even though changing the latter's length by around 10.8 [mm] leads to frequency changes between 0.6-3.3 %, following the method used for describing the combustion region for methalox systems, deviations in combustion zone length higher than 10 % (in magnitude) are not expected to occur. Reducing this length by 10 % leads to values of the Methane mass fractions of 0.3-0.4 [-] falling outside of the combustion region. Given that these magnitudes are considered to be too high to assume the majority of the reaction to have occurred within the described combustion region, reductions of more than 10 % in the chosen combustion zone length are not foreseen to occur.

Table 4.6: Solution of the analytical solution of the convective Helmholtz equation corrected for the speed of sound

	L1	L2	T1	T1L1	T2	R1
Natanzon-1/3 (L = 298.2 [mm])	1678 [Hz]	3357 [Hz]	5412 [Hz]	5666 [Hz]	8977 [Hz]	11267 [Hz]
Natanzon-1/2 (L = 308.2 [mm])	1624 [Hz]	3248 [Hz]	5412 [Hz]	5650 [Hz]	8977 [Hz]	11267 [Hz]
Analytical solution (with nozzle, L = 338.2 [mm])	1480 [Hz]	2960 [Hz]	5412 [Hz]	5611 [Hz]	8977 [Hz]	11267 [Hz]

4.2.4 Helmholtz with radially-averaged and axially varying properties

In addition to the analytical solution being corrected for the variation in speed of sound, also the Helmholtz results were updated to account for a better description of the background flow. The same boundary conditions, solver setting, and mesh as used in Section 4.1.3 for the Helmholtz run with constant CEA properties were here utilized. The only difference between the simulation described hereafter and the one

introduced in Section 4.1.3 is how the background flow is modeled. A description of the settings used in COMSOL to input the radially-averaged profiles and link them to the fluid properties and to the physical model is given in Appendix F. Here, the one-dimensional profiles for the speed of sound and density of the combustion chamber, LOX injector, and CH4 injector were input in COMSOL. Even though the Helmholtz equation does not account for mean flow gradients, describing the variation of the speed of sound and density as a function of axial coordinates provides an indirect way of including the effects that the background flow has on the acoustic field. The mode shape results for this Helmholtz simulation using the state-of-the-art method of radially averaging along the longitudinal axis an engine's detailed three-dimensional CFD field, are shown in Figure 4.18, while their respective frequencies are given in Table 4.7. Running on a computer with 128 Gb of RAM and 16 cores, all of the solutions presented in Figure 4.18 took 11 minutes to solve.

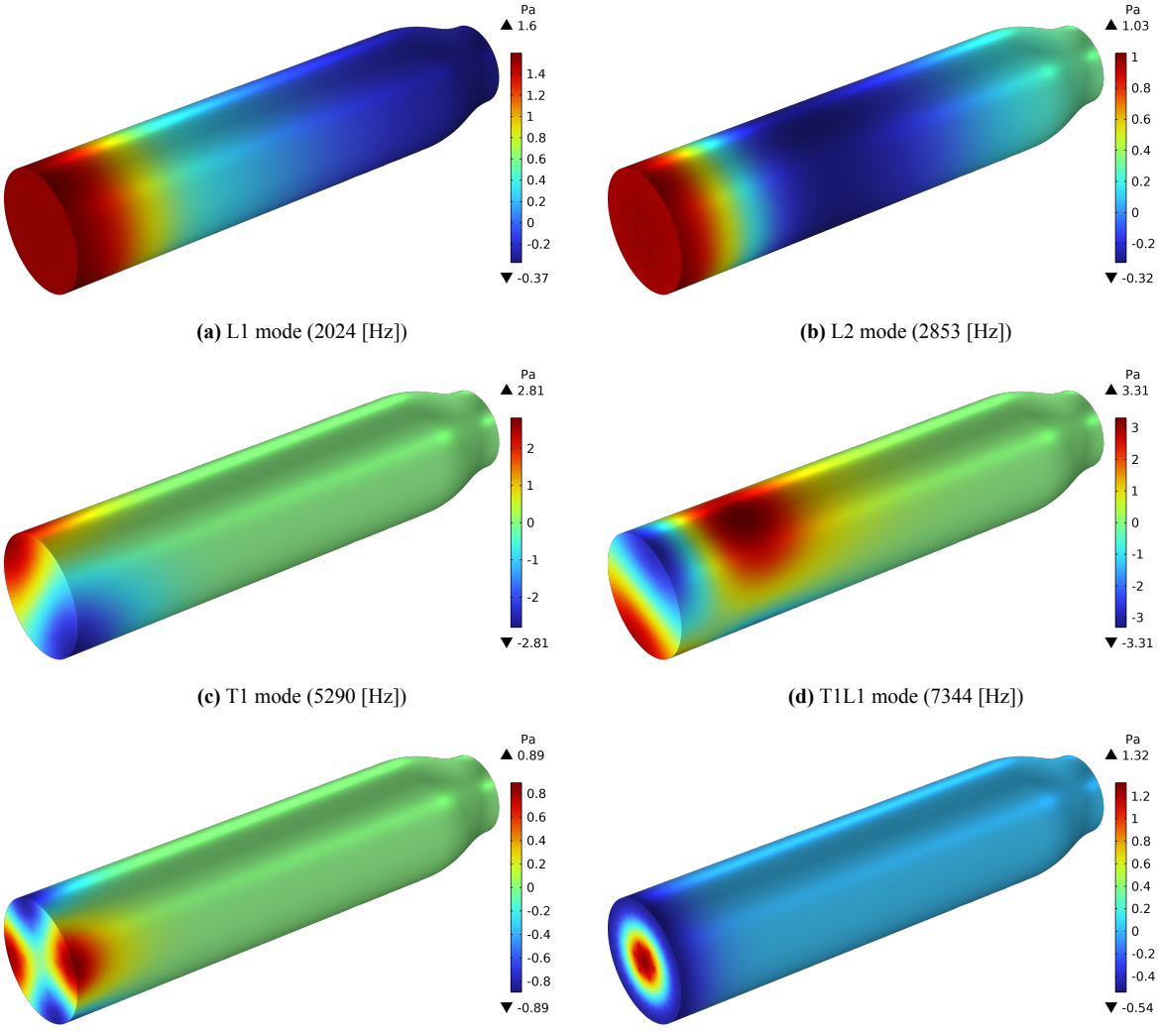

(a) L1 mode (2024 [Hz])

(b) L2 mode (2853 [Hz])

(c) T1 mode (5290 [Hz])

(d) T1L1 mode (7344 [Hz])

(e) T2 mode (7752 [Hz])

(f) R1 mode (9416 [Hz])

Figure 4.18: Mode shape results for the Helmholtz simulation with radially-averaged and axially varying properties

Table 4.7: Eigenfrequency solutions obtained from the Helmholtz simulation with radially-averaged and axially varying properties

	L1	L2	T1	T1L1	T2	R1
Frequency	2024 [Hz]	2853 [Hz]	5290 [Hz]	7344 [Hz]	7752 [Hz]	9416 [Hz]

From the mode shapes of Figure 4.18, it can be seen that by just accounting for axial variations in the speed of sound and the density, the mode shapes for the acoustic pressure are more heavily concentrated

towards the face plate of the engine; an effect that is more pronounced the higher the Mach number in the chamber is (as was visible from Figure 2.7). By comparing Figure 4.5 and Figure 4.6 with Figure 4.18, it can be seen that by accounting for varying background properties, all the modes that previously extended up to the nozzle (Figure 4.5 and Figure 4.6) are now more focused in the initial part of the combustor, with this effect being more visible for transverse modes. Confronting the regions where due to the varying flow properties, in Figure 4.18, the modes are more concentrated, with the previously identified combustion region (Figure 4.17), it can be seen that now the largest gradients in the pressure oscillation arise in the region where the background flow is dominated by the radial flame stratification. Putting the accuracy of the eigenfrequencies aside (discussed later in Chapter 5), this suggests the need to account for radial background flow variations in the combustion zone since as a consequence of being more localized in the flame region, pressure fluctuations would interact with the flame. For the input properties of the Helmholtz simulation, besides the speed of sound and the density, also the background flow pressure and temperature can be specified as model input. Contrary to the LNS simulations, background flow gradients are not used in the wave equation, however the option is provided to describe speed of sound and density variations in function of pressure and temperature, for example in case one of COMSOL's built-in materials is used. Since in the current analysis the variation of speed of sound and density were prescribed based on the radially averaged profiles, adding the pressure and temperature as model input will not affect the results.

Next to verifying the mode shapes, a mesh independence study for the Helmholtz simulation was performed. The original mesh, consisting of $2.13 \cdot 10^6$ elements, which was presented in Figure 4.2, was mostly refined/coarsened in the chamber and at the end of the injector elements interfacing with the combustor. This resulted in four meshes consisting of $1.43 \cdot 10^6$, $1.57 \cdot 10^6$, $1.82 \cdot 10^6$ and $2.86 \cdot 10^6$ unstructured elements. Running the Helmholtz simulation with radially averaged CFD input and using the T1 frequency as a case study, led to a difference in frequency compared to the results presented previously of less than 0.2 [Hz], corresponding to a $3.8 \cdot 10^{-3}$ percentage difference. In addition to showing that the results presented in Figure 4.18 and Table 4.7 are independent of the mesh size used for the simulation, the mesh independence study also showed that a coarser mesh, for example, the coarsest one used ($1.43 \cdot 10^6$), could have been used to obtain the same results in a more computationally efficient way. In their Acoustics User Manual [113], COMSOL recommends using 20 mesh elements per maximum wavelength wished to be solved for acoustic simulations using linear elements. As described in Appendix B, for the problem at hand, this leads to a very coarse discretization for which the results can not be considered mesh independent. To improve that, based on the mesh refinement study conducted in this subsection, the element size of the coarsest mesh used is recommended as an initial step towards obtaining frequency results independent of the mesh. For this, the finest elements in the chamber are found near the faceplate, with a minimum element size of 3.4 [mm], while the coarsest ones are found at the end of the cylindrical section of the combustor, with a maximum size of 27.9 [mm].

4.2.5 Linearized Navier-Stokes with radially averaged and axially varying properties

The previous analyses provided the results for the analytical solutions and Helmholtz equation, both performed with and without the assumption of constant background flow. In Section 4.1, the first modeling step to predict the eigenfrequencies in liquid rocket engines was taken. This set the basis to verify subsequent analyses and, in the next chapter, will provide insight into whether using constant CEA properties for the study of rocket engines could potentially be a valid alternative, during preliminary design phases, to forecast the frequencies of acoustic modes inside combustors subject to various design iterations. To compare, the same analyses were updated with a more detailed background flow description, in Section 4.2.1. With the goal of assessing the performance and accuracy of the LNS solver for predicting the eigenfrequencies of a LOX/CH_4 engine, the following subsection takes an additional step with respect to modeling complexity by changing the solver in COMSOL from Helmholtz to LNS while still retaining the 1D radially averaged profiles as input for the simulations. To start, a discussion on the numerical stabilization needed to remove spurious solutions in convection-dominated problems solved with FEM is given. This is followed by a description of the meshing strategy since the mesh used for the Helmholtz

simulations in Section 4.1.3 and Section 4.2.4 was based on the approach used for the LNS mesh. Next, this subsection is concluded by providing the boundary conditions for the LNS simulations and its results.

Numerical stabilization

As seen in Section 2.3, contrary to Helmholtz, where the transport equations are restated into a single pressure wave propagation formula, Aeroacoustic methods such as LNS employ the original formulation of the governing Navier-Stokes equations. This allows the latter to account for convection terms, having the advantage of directly including the influence of background flow gradients on the acoustic field. By using FEM software like COMSOL, based on the standard Galerkin formulation, accounting for the convection also adds a disadvantage in terms of stabilization. In cases dominated by convection, as in fluid problems, the respective convection operator (stemming from the Galerkin formulation) is non-symmetric. This leads to spurious solutions being returned by the Galerkin method [114]. Since the booming of FEM in the early seventies, a number of approaches exist nowadays to get rid of such spurious solutions, with the most efficient one characterized by the use of stabilized FEM (sFEM).

To assess the relation between convection and diffusion properties of a considered flow field, the Peclet number can be investigated. This dimensionless number is reported in Equation 4.7, where $\overline{u}$ indicates the average flow velocity, h the mesh size, and ν_{dif} a diffusion coefficient. For $Pe > 1$, spurious solutions are returned, while for $Pe < 1$ numerically stable solutions are obtained, i.e. absent from spurious oscillations [66, 114]. To avoid spurious solutions, thus reducing the Peclet number, from Equation 4.7 it can be seen that either the mesh size is reduced or additional diffusion is added to the system. The latter leads to stabilized FEM methods, for which various stabilization techniques exist [114]. In general, these prove to be the preferred approaches to get rid of spurious solutions, since they lead to higher order schemes than the first order one represented by reducing the mesh size, and to a lower computational cost.

$$Pe = \frac{\overline{u}h}{2\nu_{dif}} \tag{4.7}$$

For the research activities presented in this report, GLS (Galerkin Least-Squares method) was selected as the stabilization approach for the LNS simulations, with the reason being twofold. Firslty, it is the most efficient and the recommended method by COMSOL for their aeroacoustic solvers, as described in the latter's user manual for its Acoustic Module [113]. Secondly, GLS leads to a higher-order scheme than SUPG (Streamline Upwind Petrov-Galerkin method), a stabilization technique widely used by the TUM research group. Albeit neglecting the impact on entropy fluctuations, a recent study conducted by Hofmeister, Hummel & Sattelmayer [66] has shown that the degree of stabilization chosen strongly influences the dissipation of vortical structures, while barely affecting the acoustic velocity and pressure fluctuations even when using a stabilization coefficient of 100 for SUPG. Furthermore, the numerical stabilization impacts more heavily regions dominated by vorticity (e.g. in regions with sudden increases in area, as is the case at the injection plane), with excessive SUPG stabilization coefficients leading to the unphysical dissipation of vortical structures which in turn affects the acoustic damping rate. A similar study conducted by Hofmeister et al. [82] also showed that the SUPG stabilization can greatly influence the damping rates, with deviations around 30 % for a 3D analysis of a swirl-stabilized gas-generator when increasing the stabilization coefficient from 0.5 to 1. The study from Hofmeister, Hummel & Sattelmayer [66], also showed that the dependencies of the damping rate on the stabilization coefficient increase for coarser meshes. The authors showed that a constant error of around 18%, independent of the stabilization coefficient chosen, could be obtained for a fine mesh, while for a 10 times coarser mesh, an error of 250%, dependent on the stabilization coefficient chosen, was attained [66]. At the moment of writing of this report, a similar study for the GLS stabilization was found to be missing, and it is unknown whether this stabilization technique influences the damping rates more or less than SUPG. A discussion on the available stabilization methods in COMSOL is provided for the interested reader in Appendix E. In a previous study conducted at DLR, aimed at assessing the performance of COMSOL aeroacoustic solvers for frequency predictions inside rocket combustors [92], it was found that based on COMSOL v.5.6's user manual [115], typical values for the GLS stabilization coefficient are found in the range 0.001-1, with the

default value set to 1 in COMSOL v.6. From the previous DLR study, a GLS coefficient of 1 accurately returned the L1, T1 and T1L1 modes for a LOX/LH2 combustor in the presence of a radially averaged background flow within an accuracy of 10% for their frequencies. With this value of the stabilization coefficient, only one clear solution was returned per expected eigenmode. If the coefficient was lowered, it was found that more mode shapes were returned looking similar to the expected mode that was solved for, which varied slightly in frequency from each other in frequency. Therefore, for the following research study, COMSOL v.6's default stabilization constant of 1 was chosen for GLS.

Mesh

Regarding the mesh refinement and how it lowers the influence of the damping rates on the stabilization coefficient chosen, the analysis from Hofmeister, Hummel & Sattelmayer [66] also revealed that the influence of the numerical diffusion on the results is minimized if the mesh is refined at the origin of the mean shear layer. For a geometry with a backward-facing step, this is located at the corner where the sudden increase in the cross-sectional area occurs [99], which is the case at the transition between injectors and combustion chamber. Hence, a local mesh refinement in the chamber in the vicinity of the injector elements was applied (up to 5 [mm] downstream of the injection plane). The final mesh used for the LNS simulation is shown in Figure 4.19, where such a refinement region can be seen. The refinement was also required to retrieve the pure longitudinal modes solved for in this study (i.e. L1, L2), else unphysical high-amplitude peaks localized at the transition between injector elements and the combustion chamber were returned by COMSOL.

Furthermore, within the combustion chamber six further refinement regions were defined. The mesh in these partitions was based on the axial rate of change of the radially averaged speed of sound, which for convenience was calculated via a forward difference scheme from the available CFD results of LUMEN's combustor. Since the largest gradients occur in the initial section of the chamber, for practical purposes, the finest mesh in the chamber was defined to be the one attained in the first partition, that is within the first 5[mm] after the injection plane. The other regions were then based on the gradients of the speed of sound, which were calculated in Python via forward Euler using a 1 [mm] step size. Lastly, because the LNS equations now conserve the formulation of the governing equations and account for viscous terms, gradients at the wall needed to be resolved. Hence, in contrast to the mesh used for the Helmholtz simulations, a boundary layer refinement was added to the LNS mesh, as visible in Figure 4.19. The final three-dimensional mesh consisted of $2.73 \cdot 10^6$ unstructured elements with an average element of quality of 0.65. This led the smallest mesh element size in the chamber (just downstream of the the faceplate) being 0.85 [mm], and the maximum chamber element size (just before the start of the nozzle) being 11 [mm].

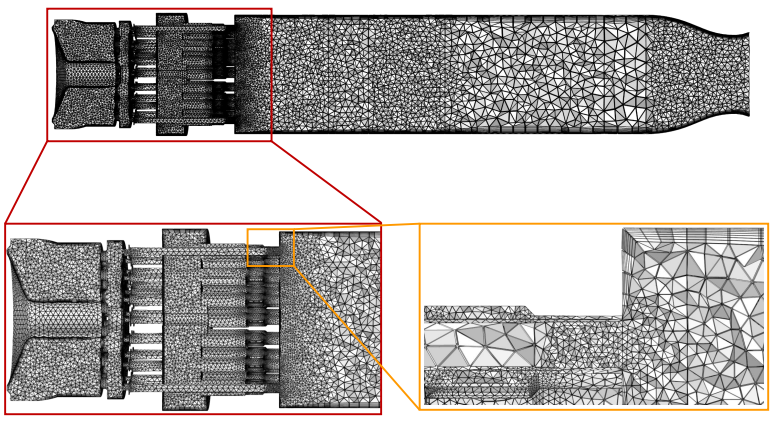

Figure 4.19: Cross-sectional view of the mesh used for the LNS simulation with radially-averaged background flow

Boundary conditions and results

Regarding the boundary conditions, these remained the same as the ones used for the Helmholtz simulations, with an exception of the wall conditions. Now that five equations are solved for the LNS (continuity equation, momentum equations, and energy equation), in addition to the pressure oscillation (the dependent variable solved for the Helmholtz case) also the velocity components and the temperature oscillations are solved for LNS, thus requiring respective boundary conditions. For a well-posed problem, when compared to the boundary conditions already prescribed for the Helmholtz runs, additional conditions for the temperature and velocity at the walls of the geometry had to be specified. For that, a no-slip and isothermal wall were specified for the velocity and temperature, respectively. With the isothermal condition, the total temperature fluctuation at the wall is set to zero.

With the boundary conditions set, and the same solver settings as described in Section 4.1.3, the LNS simulation could be solved. Since it is expected that by accounting for convective terms the presence of the background flow would lower the frequency predictions when compared to the Helmholtz simulation using constant CEA properties, the results of the corrected analytical solution were used as input to center the frequency search, instead of the results from Equation 2.24. The resulting eigenfrequencies are given in Table 4.8 , while the respective mode shapes from the LNS simulation are shown in Figure 4.20 and Figure 4.21. One of the main advantages of LNS over the Helmholtz equation is that by formulating the former in the frequency domain, the damping rate information per mode shape is directly an output of the analysis. This was not the case for the Helmholtz simulation, which would require a time-domain simulation to be performed to obtain the temporal variation of the pressure oscillation from which the same post-processing as done in the next chapter for the experimental results would have to be carried out to retrieve the damping rates. However, this comes at the cost of the added computational time of having to solve five equations instead of one using a finer mesh. Running on a 64 Gb machine with 6 cores, it took around 2 hours to perform 5 frequency searches with LNS, leading to the solution of one eigenmode, which is a drastic increase when compared to the 11 minutes of runtime to find the solution of all six modes for the Helmholtz run presented in Section 4.2.4.

Table 4.8: Eigenfrequency solutions obtained from the LNS simulation with radially-averaged and axially varying properties

	L1	L2	T1	T1L1	T2	R1
Frequency	1588 [Hz]	3307 [Hz]	5717 [Hz]	7437 [Hz]	9013 [Hz]	11119 [Hz]
Damping Rate	94.8 [1/s]	98.9 [1/s]	137.2 [1/s]	232.0 [1/s]	113.9 [1/s]	103.4 [1/s]

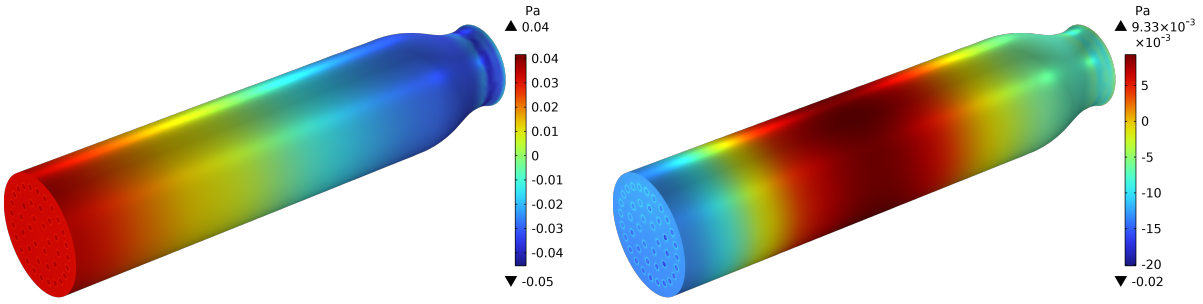

(a) L1 mode (1588 [Hz]) **(b)** L2 mode (3307 [Hz])

Figure 4.20: Longitudinal mode shape results for the LNS simulation with radially-averaged and axially varying properties

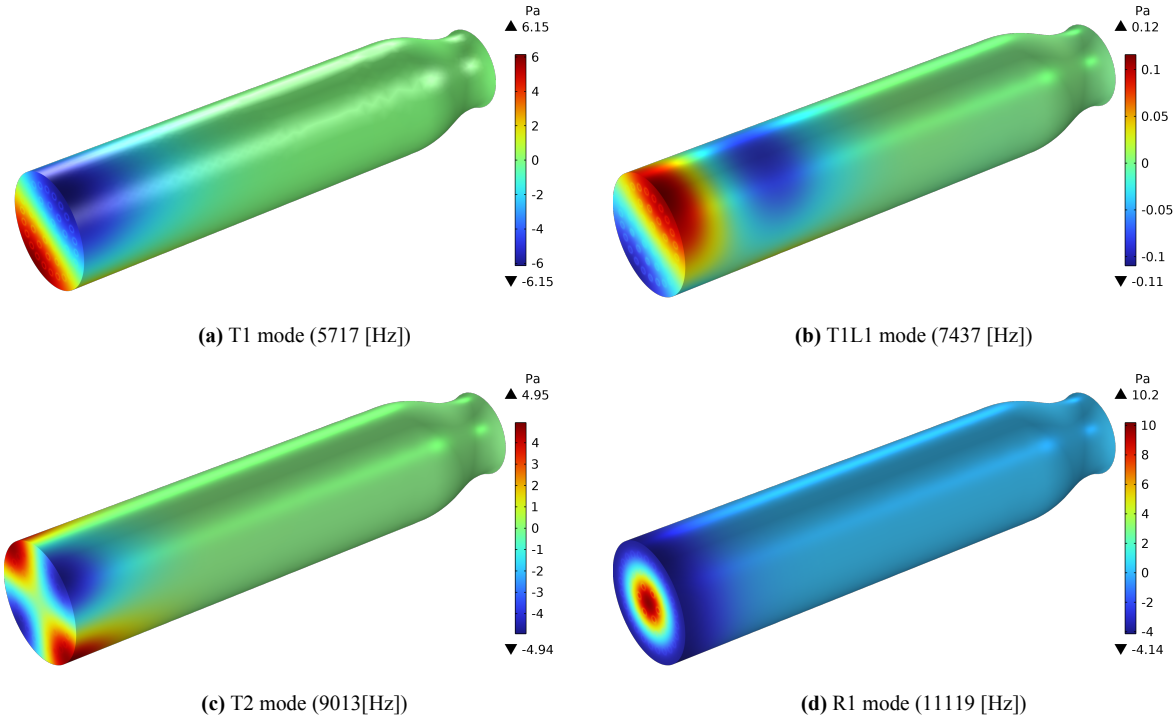

(a) T1 mode (5717 [Hz])

(b) T1L1 mode (7437 [Hz])

(c) T2 mode (9013[Hz])

(d) R1 mode (11119 [Hz])

Figure 4.21: Transverse and combined mode shape results for the LNS simulation with radially-averaged and axially varying properties

By comparing the results above with the ones from Section 4.1 it can be seen that accounting for the presence of a varying background flow along the longitude of the engine greatly reduces the frequencies of the modes. The reduction is more pronounced for tangential modes, with around a 9% lower difference than what the Helmholtz results using radially averaged input (Section 4.2.4) had with the results from Section 4.1. In addition, as was the case for the Helmholtz simulation from Section 4.2.4, the mode shapes for LNS show the same behavior as the ones presented in Gröning [62] in the presence of a moving background flow, namely with the transverse modes concentrated at the injection plane and not spreading along the whole chamber's length. Similarly to the Helmholtz simulation from Section 4.2.4, a mesh independence study was also performed for the LNS simulation here presented. For that, the change in frequency and damping rate of the T1 mode was studied for three additional mesh sizes, these having: $2.34{\cdot}10^6$, $2.49{\cdot}10^6$, and $2.85{\cdot}10^6$ elements. Albeit close in the number of elements, the refinement in the chamber at the previously mentioned seven partitions was modified, while keeping the same mesh for the injectors, which, due to their small dimensions, accounts for approximately 53% of the elements of the overall mesh. The difference in T1 frequency and damping rate results for the coarsest mesh was calculated to be 0.1% and 16%, respectively, while for the finest mesh, these differences corresponded to 0.1% and 1.4%. These results show that the frequency converges faster than the damping rates and that for properly assessing the mesh independence the latter should be used as a metric. The results presented earlier in Table 4.8, for the eigenfrequencies, and in Figure 4.20 and Figure 4.21, for the mode shapes, can be deemed independent of the mesh since the mesh used is closer to the finest one than the coarsest tested. Also, the T1 damping rate difference of Table 4.8 with the intermediate mesh of $2.49{\cdot}10^6$ elements leading a 6.4 % difference.

4.3 Detailed three-dimensional flow description

With the results obtained for the LNS simulation using radially averaged profiles as input for the background flow, the final modeling step consists in solving the LNS equations using a three-dimensional flow field as input. Using radially averaged CFD results to describe the background flow inside rocket combustors indicates the current standard for assessing the combustion stability of an engine using

an acoustic-based approach. As described in Section 3.1, by using radially averaged profiles as input, in-plane variations of flow properties are neglected, leading to acoustic simulation not returning physical distributions of flow fluctuations in radial directions (apart from the pressure). Therefore, besides aiming to ameliorate eigenfrequency accuracy, a natural next step to address this issue is to input a detailed three-dimensional field for the acoustic simulations, which in this section is done for the LNS equations.

This section is structured as follows. Firstly, the way in which the three-dimensional background flow field is accounted for in the LNS simulation is described in Section 4.3.1. This is then followed in Section 4.3.2 by reporting the LNS set-up. Here, the mesh used for this last simulation is introduced, and given that the boundary conditions and solver settings remained the same as the ones used in Section 4.2.5, the results presented. The following section also concludes the chapter, which is then followed by a discussion of the results, where the analysis of the experimental data is explained and all of the acoustic simulations and analyses, presented in the current chapter, are validated.

4.3.1 CFD mesh to acoustic mesh mapping

Applied to the field of liquid rocket propulsion, the publication that was found to described in most depth the influence that a 3D varying background flow has on the acoustic results' accuracy was the work of Chemnitz & Sattelmayer [98], as described in Section 3.1. To improve upon the background flow description of the authors, a detailed CFD field accounting for all flame structures is here mapped to the acoustic mesh to be used by the aeroacoustic analysis. To map the CFD results to the acoustic mesh, three options were identified. In the past, a researcher at DLR tried to perform a similar study applied to a Helmholtz solver in COMSOL and developed a Python tool internal to DLR (named *interp2comsol*) to carry out a nearest-neighbor interpolation using as input the original output results from DLR's CFD code TAU, its CFD mesh, and the acoustic mesh to be used for the analyses in COMSOL. Over the years issues related to the interpolated outcome were discovered by the research group at DLR, and, recently, efforts were invested in debugging the code. Using this Python tool to map the results represented the first option that was tried. Unfortunately, while attempting to make the tool work for the LUMEN analysis, two issues were found. Firstly, given the size of the CFD mesh and how the code was set up, even if a coarse acoustic mesh was used (e.g. of around 10^6 elements) it took the code 8 hours to identify the locations of the nearest neighbors, making the code unpractical considering that in the meanwhile three eigenmodes could have been solved using the LNS simulation from Section 4.2.5. Secondly, the code could only be run on Linux, and errors preventing the code from delivering the intended output were discovered. Their cause was found to be related to the Python version used. The Python tool was written in Python 2.6 and even if Python was downgraded to the right version and the IDE modified, the error still persisted. Given the non-existent documentation about this tool, that its developer no longer worked at DLR, and that two other options were identified to perform the mapping, it was decided to drop the above-mentioned approach.

The second option tested was to perform the mapping in Paraview, which was the software used, together with Python, to post-process the CFD results. Albeit eight times faster than the Python tool approach, this option also turned out to be inconclusive. Loading the COMSOL mesh together with the CFD results to Paraview and using the *Resample With Dataset* filter to map the CFD results onto the acoustic mesh led negative and null values of the speed of sound at the wall of the geometry, causing COMSOL to crash when trying to solve the LNS simulation. The reason for this was found to be that the Paraview mapping filter is not able to map results onto curved surfaces if the nodes between the two meshes do not match at the wall. To solve this, the nodes at the wall of the acoustic mesh would have had to be orthogonally projected onto the wall of the CFD mesh before sampling them for the mapping. Since this would defeat the purpose of the simplicity of using the latter filter operation in Paraview, and given one last option to try for the mapping, it was also decided to not proceed with fixing this approach.

The third and last option that was tested ended up being the one used in the current work for performing

the mapping, with the latter being directly performed in COMSOL. It should be noted that DLR only had the acoustic license for COMSOL and that the CFD simulation of the LOX injector was performed in COMSOL using TU Delft's license. If both CFD and acoustic licenses are available, then COMSOL allows the use of the so-called *Background Fluid Flow Coupling*, a multiphysics coupling, where the mapping from the CFD results obtained in COMSOL to an acoustic mesh is automatically performed. Since a method had to be devised that DLR could use in the future without requiring additional licenses, the previous multiphysics coupling option could not be used and a manual version of it had to be set up from scratch. An overview of how to do so is provided in the user manual of COMSOL's Acoustic module [113].

For the manual mapping in COMSOL a *Weak Form PDE* study had to be run prior to the LNS study. The former makes use of the built-in Mathematics module of COMSOL and thus could be used by DLR. To start the file containing all the CFD variables to be mapped had to be input in COMSOL via the *Interpolation* definition. For this, it is important to set up the file such that the first three columns contain the x, y, and z coordinates of the data, and all the subsequent columns have the magnitude of the data at those points. Furthermore, linear interpolation were used. Note, that screenshots of the settings used to do so are included in Appendix F.

Once the data from the LUMEN CFD analysis was added in COMSOL, this could then be used in the mapping study to solve for the mapped values. This study made use of the *Weak Form PDE* physics that can be found under the *Mathematics* library. With this physics, an arbitrary number of variables can be solved for an equivalent number of equations that have to be defined by the user. Of the eleven input variables required by LNS, ten were obtained via the mapping study, and only the thermal conductivity was obtained using the same method used in Section 4.2. The partial differential equations solved by the mapping study all had the same form, and the one for the speed of sound is provided in Equation 4.8 as an example. To obtain the equation for another variable, this only has to be substituted to the speed of sound in Equation 4.8. In this equation, $c_{0,LNS}$ indicates the desired (mapped) speed of sound output, $c_{0,CFD}$ is the input CFD result at a given point, δ is a diffusion coefficient that can be used to obtain smoother results and h is the mesh size. The right-hand-side of Equation 4.8 represents the source term stabilization term and relates to the divergence of the gradient of the desired output. The value that COMSOL recommends for the diffusion coefficient for aeroacoustic problems is 0.01 [-] [113]. Additionally, zero flux conditions on all surfaces of the domain were specified as boundary conditions. Then, to map the CFD results to the acoustic mesh, the latter had to be selected as the mesh for the stationary study used for solving all equations of the form of Equation 4.8.

$$c_{0,LNS} - c_{0,CFD} = \delta \cdot h^2 \nabla \cdot (\nabla c_{0,LNS}) \tag{4.8}$$

Solving the ten mapping equations using a machine with 128 Gb of RAM and 16 cores took around 30 minutes for an acoustic mesh composed of $1.43 \cdot 10^6$ unstructured elements. A more detailed description of the mesh used is provided in Section 4.3.2. While trying to run the LNS simulation presented in this section, it was found that COMSOL is a "graphics-intensive" software. For the computer used to run the mapping, the default COMSOL settings had to be changed, or else the simulation would keep crashing. To prevent the mapping from crashing, the *Graphics and Plot Windows* settings had to be optimized for performance, *Detail* set to wireframe, and *Rendering* changed to *Software*. Once solved, the output variables could then be linked as input for the LNS study. All necessary details are also provided in Appendix F.

In addition, it was discovered that for the problem studied, the recommended value of 0.01 [-] for the diffusion coefficient could not be used. In Figure 4.22 two figures are shown that explain why. Figure 4.22a shows a longitudinal slice of the speed of sound field as obtained directly by the CFD results (i.e. prior to mapping it), while Figure 4.22b depicts this same slice for the mapped speed of sound using the diffusion coefficient's value as recommended in COMSOL's user manual [113]. Although a sharp distribution can be obtained, using a value of δ=0.01 for the diffusion coefficient leads to no physical solutions to be found by the LNS solver, where the only returned solutions show local peaks in the pressure oscillation,

suggesting that entropy and vortical modes coupled with the acoustics via flow non-uniformities. A longitudinal slice of one of the returned un-physical solutions is shown for reference in Figure 4.23.

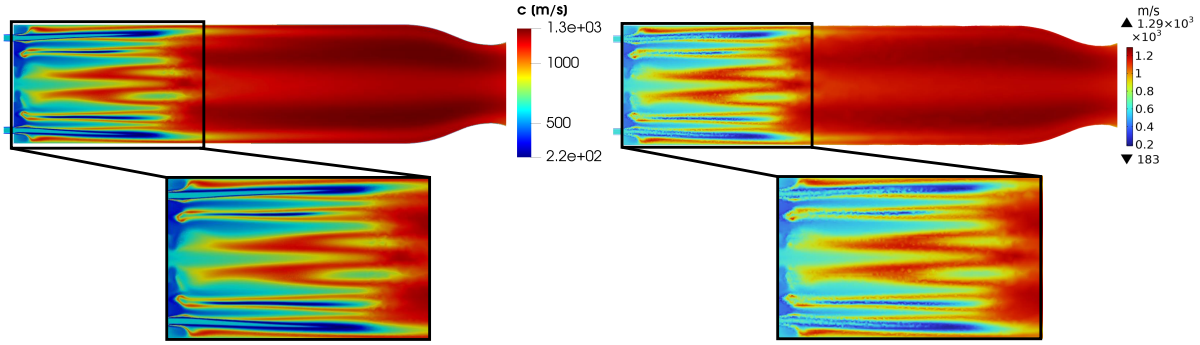

(a) Original speed of sound field from the CFD

(b) Mapped speed of sound with δ=0.01

Figure 4.22: Comparison of the original speed of sound field (a) with the mapped one (b) using COMSOL's recommended diffusion coefficient

Figure 4.23: Unphysical LNS result using a diffusion coefficient of δ=0.01 for the mapping

If a closer look is taken at the flame region of Figure 4.22b, "rough" and "noisy" parts of the mapped output field can be discerned which were not originally there (Figure 4.22a). This suggests that with a diffusion coefficient of 0.01, a too-coarse and un-regular representation of the mapped field is obtained, leading to a deformed background flow field description that over-constraints the problem and results in no physical acoustic disturbance to be found by the solver. A remedy for this is either refining the acoustic mesh or increasing the smoothing factor during the mapping. It has to be noted that, initially, finer meshes with $4.55 \cdot 10^6$ and $2.13 \cdot 10^6$ elements wanted to be used for the current LNS analysis, but, unfortunately, the memory limit of the computer would not allow it. Hence, the mesh size had to be reduced to run the simulation with the given computational resources, and therefore refining the mesh further to smoothen the mapping result was not an option. Instead, a parametric sweep was performed to determine one of the lowest values of the diffusion coefficient that would return physical results with LNS. The final value chosen was δ=0.1 [-], and the corresponding mapped speed of sound slice is shown in Figure 4.24.

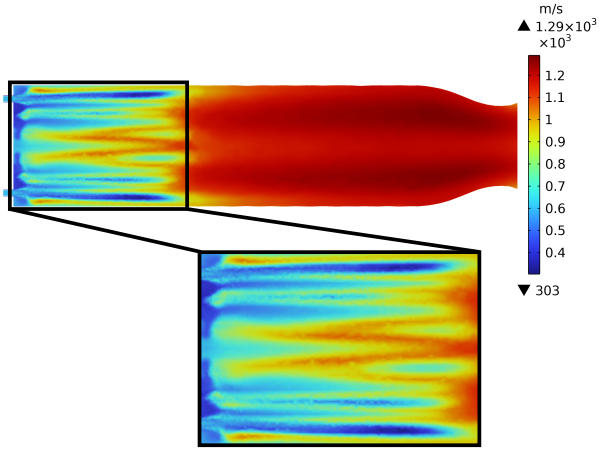

Figure 4.24: Mapped speed of sound distribution using a diffusion coefficient of δ=0.1

In addition to increasing the diffusion coefficients to 0.1 [-], the diffusion coefficient for the density required a further increase for the simulation to not crash. This time, because of null and negative values returned in the mapped density result if a coefficient of 0.1 [-] was used. The density represents an exception that required a higher diffusion coefficient than the other values, due to its very sharp gradients attained across only a few millimeters in the flame regions. This can be seen from Figure 4.25a, where the same slice as in Figure 4.22 is taken but this time showing the density field from the CFD results. To prevent negative or null values to be returned by the mapping, the diffusion coefficient for the density was increased until a positive minimum value was reached. This led to a value of the smoothing coefficient of δ=0.23 [-] to be chosen, with its result shown in Figure 4.25b. For reference, the difference in the maximum and minimum density shown in Figure 4.25b with respect to the maximum and minimum of Figure 4.25a are respectively 50 % and 2 % higher.

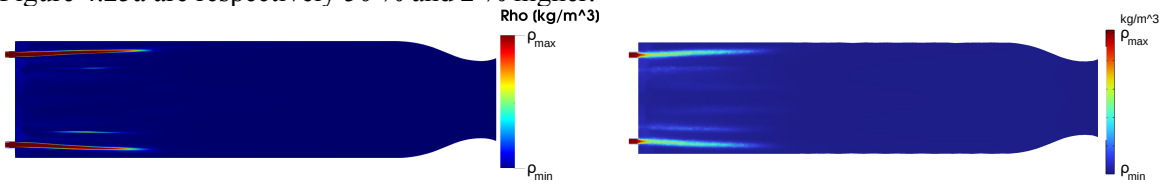

(a) Original density field from the CFD

(b) Mapped density with δ=0.23

Figure 4.25: Qualitative comparison of the original density field (a) with the mapped one (b) using δ=0.23 [-]

4.3.2 Linearized Navier-Stokes with detailed flow descriptions

In the following subsection, the mesh and the results of the LNS simulation with mapped 3D input are discussed. For the sake of clarity, in Section 4.3.1 the availability of an acoustic mesh was assumed, while in reality, to arrive at the final mesh used, which is presented hereafter, an iterative process had to be employed. On one hand, a finer mesh would allow for a lower diffusion coefficient to be used during the mapping process while still leading to a smooth mapping result. On the other hand, a finer mesh requires more computational resources to solve the LNS simulation. Given that the LNS simulation presented in this section required close to the maximum available RAM from the computer used, the initial meshes had to be coarsened iteratively until one could be run based on the RAM requirement of the computer. Initially, the mapping of Section 4.3.1 was tested using a very coarse mesh, and after that, included in the LNS routine.

All the meshes that were tried were based on the same meshing strategy here described. Firstly, it should be noted that mapping the CFD results for the LNS analysis required the latter to also make use of the short version of the LUMEN chamber, namely the one used during the CFD analysis of LUMEN's combustor. While this means that longitudinal modes stemming from this analysis will have a large error in frequency when validated against experimental data, the method still applies to purely transverse modes. The reason for this is that due to the presence of the background flow, as already seen from the results in Section 4.2.4 and Section 4.2.5, transverse modes propagate within the combustion zone, which can be assumed independent of whether 15 [mm] are added or not to the end of the combustion chamber. Also, the long and short version of the LUMEN chamber both have the same diameter, and injector configuration, and their flow field are not perturbed by any measuring devices, thus in-plane oscillation of these modes are not expected to vary between the latter two chambers. This can also be seen in the analytical solutions presented earlier in this work. The use of the short LUMEN chamber, as used by the CFD analysis, also implies that a comprehensive representation of the injectors, as done for example in Section 4.1.3, Section 4.2.4 and Section 4.2.5, can not be used. Instead, only the final 6.75 [mm] of the injector elements (upstream of the chamber) are included, as was visible from Figure 3.5a. Regarding the meshing strategy used, to allow for a higher refinement in all directions for the flame regions, cylindrical flame refinement regions were partitioned in the geometry. Each cylinder is centered around the central axis of its respective injector element, and its radius was chosen so as to encompass the speed of sound distribution of its flame structure. The radii of the flame refinements were chosen so

to maximize the included volume of the flame details while leaving around 2 [mm] of distance between neighboring cylindrical refinements to prevent intersection and low-quality mesh elements. The resulting radii for the flame refinement regions were chosen as 5 [mm] for the inner-most row of injectors, 3.8 [mm] for the outer-most row of injectors, and 4.2 [mm] for the middle injector row. Figure 4.26 shows these regions for a number of selected injector elements (shown highlighted in blue).

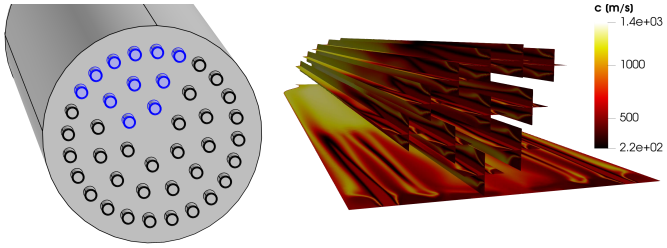

Figure 4.26: Cylindrical flame refinement diameters (right) centered at the highlighted injector elements (left)

Based on these additional refinement regions, the combustion chamber geometry was further partitioned, and the flame refinements were terminated at the end of the combustion zone region, as determined in Section 4.2.3. The resulting refinement domains, as implemented in COMSOL, are shown, together with the final mesh used, in Figure 4.27, while a close-up view of a longitudinal cut of this mesh is given in Figure 4.28. As mentioned earlier in Section 4.3.1, the final mesh used for the current LNS study is composed of $1.43 \cdot 10^6$ unstructured elements.

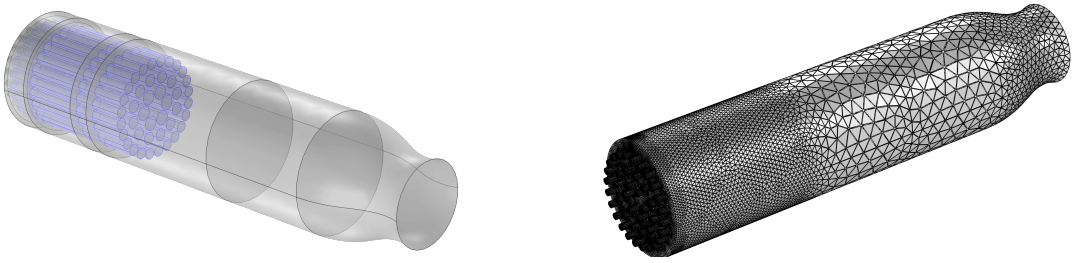

(a) View of the mesh flame refinement regions (highlighted in blue)

(b) View of the mesh used for the LNS simulation with 3D mapped CFD input

Figure 4.27: View of the flame refinement region (a) and of the resulting three-dimensional mesh (b)

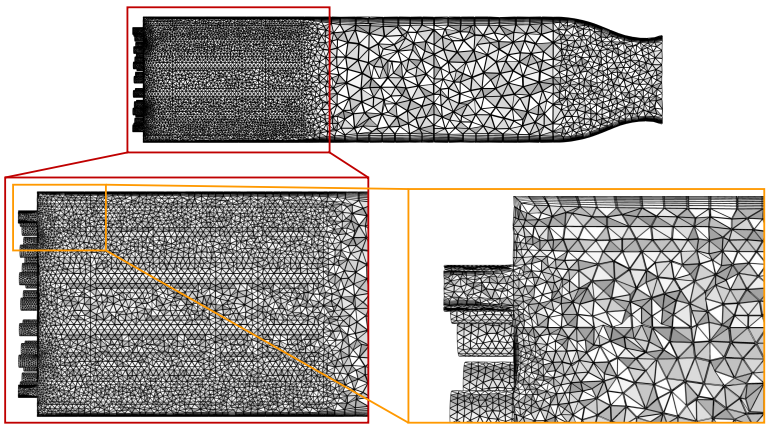

Figure 4.28: Cross-sectional view of the mesh used for the LNS simulation with 3D mapped CFD input

Before solving the LNS equations, when linking the output of the mapping study to the input of the LNS study, care should be taken in making sure that the former's use as input is enabled under the *Values of Dependent Variables* in LNS' eigenfrequency settings. Besides using the 3D mapped field as input, the solver settings and boundary conditions for the LNS simulation with 3D background flow description were kept the same as for the previous LNS with radially averaged input. For the current case, acoustically open conditions were set at the start of the injector elements' surface. To solve the equations, as done

for the aforementioned simulations, a parametric sweep for the search frequency is specified in the LNS study settings. By inputting the flame region with its LOX core in detail, the results of the LNS simulation with 3D mapped CFD input are expected to have lower frequencies than the ones of the LNS study from Section 4.2.5. Thus, if the frequency results of Section 4.2.5 are taken as search values for the current LNS study, additional lower values had to be added to the auxiliary sweep search to capture the lower expected frequencies of the eigenmodes. A distance of 300 [Hz] between search frequencies was chosen and four search frequencies were used per mode to be solved. Given the shorter chamber length than used in the experiments, only purely transverse modes were solved. To solve one mode, this LNS simulation took considerably longer to solve than for the previous LNS simulation, with an average run-time-per-mode of around 37 hours. The modes shape results are given in Figure 4.29 and their respective eigenfrequencies are provided in Table 4.9. Again, only the purely transverse modes were solved due to the discrepancy between the chamber length used for the LUMEN CFD simulation and the one used in the experiments.

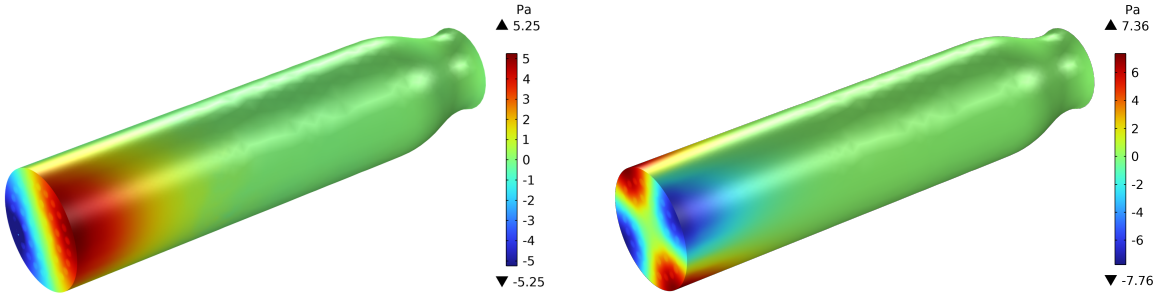

(a) T1 mode (5208 [Hz])

(b) T2 mode (8063 [Hz])

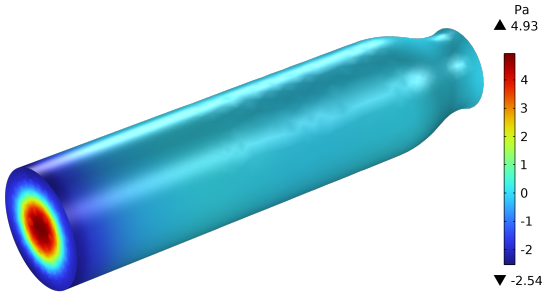

(c) R1 mode (9196 [Hz])

Figure 4.29: Mode shape results for the LNS simulation with detailed flow description

Table 4.9: Eigenfrequency solutions obtained from the LNS simulation with three-dimensional mapped CFD input

	T1	**T2**	**R1**
Frequency	5208 [Hz]	8063 [Hz]	9196 [Hz]
Damping Rate	104.3 [1/s]	112.3 [1/s]	70.9 [1/s]

Lastly, before getting to Chapter 5, where the experimental results are analyzed and the simulations validated, a comparison of the velocity mode shape is provided between the LNS simulation with radially averaged input and 3D mapped input. It was mentioned at the start of this section that in addition to aiming to attain more accurate frequency results, the 3D-mapped LNS simulation also had the advantage of returning a three-dimensional description of mode shapes other than that of the pressure fluctuation. This could in turn be used as a more representative input for the flame transfer function in case parameters other than pressure oscillations are accounted for. From the work of Lieuwen [40] an extensive discussion on the heat release dynamics from the flame response can be obtained for both premixed and non-premixed flames. By integrating the heat release of a flamelet over its surface, the author shows that this is in function of the burning rate mass flow ($\dot{m}_b$), the heat of reaction (H_R), and the flamelet area (A), as reported in Equation 4.9.

$$\dot{Q}(t) = \int_A \dot{m_b}' \Delta H_R dA \tag{4.9}$$

This shows that fluctuations in these three quantities lead to oscillations in the heat release rate of the flame. From Lieuwen, it can further be learned that three main mechanisms can be identified that influence the variables leading to heat rate fluctuations, namely: the velocity mechanism, the oxidizer-to-fuel-ratio mechanism, and the pressure mechanism. Therefore, fluctuations in the latter quantities will lead to oscillations in the heat release rate. Turning to the first mechanism as an example, disturbances in the velocity can directly lead to fluctuations in the mass burning rate and the flame area which in turn modify the heat release rate. From these, in non-premixed flames, the heat release is principally controlled by mass burning rate fluctuations and to a smaller degree by burning area fluctuations [40]. If radially-averaged profiles are used to describe the background flow field for LNS analyses, then ideal planar velocity modes are obtained by the solver. These are solely driven by where the nodes of the pressure modes are located. Meanwhile, if a detailed three-dimensional field is used to describe both the axial variation of the background flow, as well as the radial one, then the non-uniform properties in the radial direction of the engine are expected to return more complex planar velocity oscillations. Which will then interact differently with the flame. To compare how the velocity disturbance profiles differ between simulations using radially averaged profiles as input and LNS using the 3D mapping as input, Figure 4.30 compares the velocity slice of the latter with one of the LNS simulations from Section 4.2.5. The slices were all taken at the same axial distance, namely 30 [mm] downstream of the faceplate, and are depicted for the T2 mode since this clearly shows how for uniform planar profiles the maximum velocity disturbances are attained at the pressure nodes (Figure 4.30c). Figure 4.30a and Figure 4.30b present the pressure mode at the chosen slice for the LNS simulation from Section 4.2.5 and for the LNS simulation from the following section, respectively. Similarly, for that same slice, Figure 4.30c and Figure 4.30d depicts the corresponding velocity oscillation.

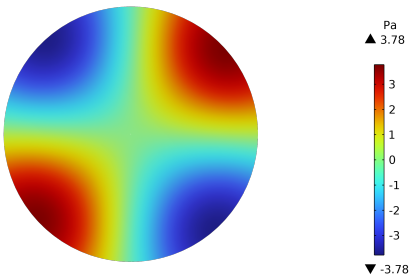

(a) Radially averaged background flow LNS pressure slice

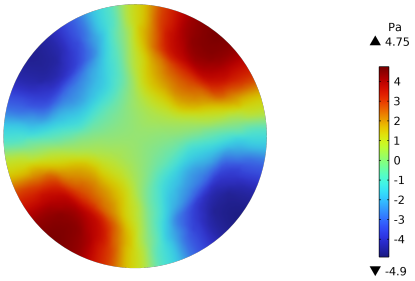

(b) 3D mapped background flow LNS pressure slice

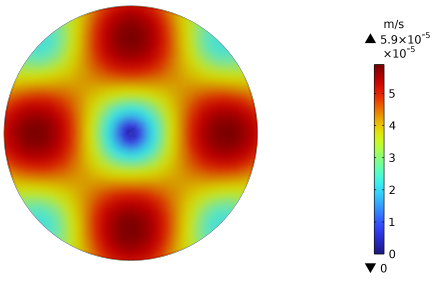

(c) Radially averaged background flow LNS velocity slice

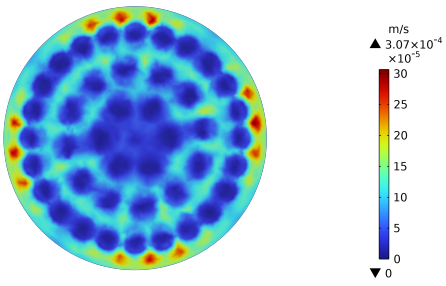

(d) 3D mapped background flow LNS velocity slice

Figure 4.30: Comparison of the pressure and velocity fluctuations for the LNS simulation with radially averaged flow input (a,c) and the LNS case with 3D mapped input (b,d)

Figure 4.30 shows that while the pressure modes of the LNS simulation with radially averaged and of the LNS simulation with mapped 3D input are almost identical to each other, the velocity oscillations are remarkably different. The only similarity in the velocity plots is that both attain their maximum velocity amplitude at the node line of the pressure oscillations. More precisely, in Figure 4.30c, the velocity maximum is obtained at the pressure node almost between the middle and outer-most injector

rows, while in Figure 4.30d the maximum is obtained between the outer-most row of injectors and the wall. Furthermore, in Figure 4.30d regions of null velocity fluctuations are visible in the core of the injected propellants, and low-velocity regions are apparent between injector rows.

Additionally, to show how the distribution of the velocity changes between the two simulations, Figure 4.31 was generated. Here, the direction of the planar velocity fluctuations is plotted over the corresponding pressure disturbance with a logarithmic scale. The latter is visualized on a black-to-white scale for ease of distinguishing the velocity arrows. Also, a logarithmic scale was used to clearly delineate the pressure node line where the velocity maxima are attained. The velocity arrow plot is colored based on the acoustic velocity magnitude reached. Besides the complex swirling motion of the flow in Figure 4.31b, it can be seen that compared to Figure 4.31a the magnitude of the maximum velocity amplitude also greatly changes. Namely, compared to the maximum of Figure 4.31a, the maximum velocity fluctuation stemming from the LNS simulation with 3D mapped input is larger by more than a factor of 4. The velocity disturbance finding its way around the injected propellant cores can be understood in the following way. Upon injection, and while traveling in the core of the flame before reacting, the propellants have a greatly lower speed of sound than that of the surrounding combustion gases. This leads to an increase in the impedance that is perceived when crossing the flame cores, which for the hypothetical limit case where a null speed of sound is achieved at the propellant core would lead to an infinite impedance, which is associated with a solid wall. Therefore, the disturbance more easily travels across regions filled by combustion gases where the speed of sound is greater.

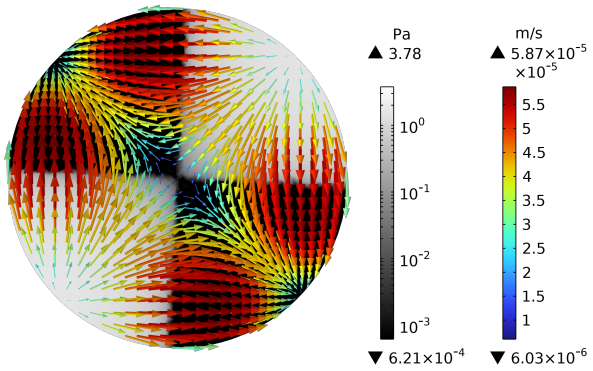

(a) Velocity distribution for the radially averaged LNS simulation

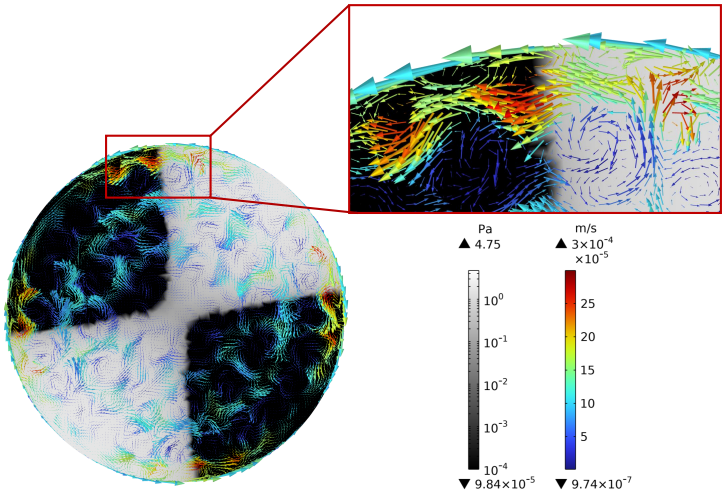

(b) Velocity distribution for the 3D mapped LNS simulation

Figure 4.31: T2 velocity fluctuating direction plotted over the (logarithmic) pressure fluctuation, for the LNS simulation with radially averaged input (a) and with 3D mapped input (b)

5 Discussion of the results

The previous chapter showed that different approaches, with respect to the equations solved and how the background flow is modeled, led to significant differences in the eigenfrequencies. Following from these acoustic analyses, in this chapter the results are validated to see which approach returns the most accurate results. Firstly, the results need to be validated against experimental data. For that, in Section 5.1, two hot-fire test runs of LUMEN are analyzed. Here, through available high-frequency pressure sensor data, the power spectral densities of these runs are analyzed, and by combining the knowledge obtained by the previous simulations and the phase differences of the sensors the various mode shapes are identified. This is then followed by an analysis aimed at retrieving the damping rates of the respective modes.

Once the experimental results are obtained, the absolute percentage error for the different modes of the previous analyses are assessed in Section 5.2. The accuracy and performance of the various methods are compared to each other, and a recommendation regarding what approaches are best suited for given applications is provided. Lastly, Section 5.3 concludes the chapter by proposing a hypotheses aimed at explaining the deviation from the simulations through possible flame lift-off in the experiments and averaging technique used.

5.1 Experimental analysis

To start, the validation data is extracted from the raw data of LUMEN hot-fire runs. These two test runs were made available by DLR and are the second and sixth runs of the BKL-CALO 2020 campaign. Throughout the remainder of this chapter, to distinguish between these two runs, the respective results are either denominated as *run2* or *run6* results. In Section 5.1.1, the measuring instrumentation from which the data was recorded is explained. After that, from the test profiles, the windows of interest for the analyses conducted in this report are identified. With clarity on what data can be post-processed, in Section 5.1.2 a first step is taken towards identifying the modes of interest employing Power Spectral Density diagrams and by examining the filtered phase difference of the pressure transducers. Next, by knowing where to look to detect the desired modes, Section 5.1.3 concludes the section by retrieving the eigenfrequency and damping rates of the modes, via a Lorentz-profile fitting strategy.

5.1.1 Hot-fire test runs

The results used in this report stemmed from a calorimetric test campaign of LUMEN. Here, the data of interest was acquired by a measuring ring that during experiments is attached between the start of the combustion chamber and the faceplate, which is shown in Figure 5.1. Figure 5.1a depicts a frontal cut-out view of this system, where in the middle the old porous injector of LUMEN is visible. From the visible slots of the measuring devices, three are highlighted in blue, green, and orange. These are the three dynamic pressure sensors on which the data analysis hereafter will be based. The filtered output of these sensors will also be used to gain insight into which mode is identified. Other than the three high-frequency pressure sensors (labeled as DYN1, DYN2, and DYN3), the measurement ring also contains two static pressure transducers to sense the chamber pressure at lower frequencies at the start of the combustor. In addition, not shown in the picture, two sensors for capturing the temperature and two for measuring the pressure of the LOX and CH_4 injectors are found radially-inserted in their domes. Besides these sensors, an additional one measuring the ROF at the chamber inlet was also present. To show the extra chamber length that is added by assembling the measurement ring in the propulsion system during testing, Figure 5.1b, taken from Losco [116], depicts the BKD-equivalent of LUMEN's measurement ring, in three dimensions. Even though the gauging system from DLR's BKD engine contains more

high-frequency pressure sensors, its depth, and inner diameter are the same as LUMEN's. In Figure 5.1b the approximate location of the dynamic pressure sensors, as found in the LUMEN set-up, are highlighted to give the reader an impression of Figure 5.1a in three-dimensional space.

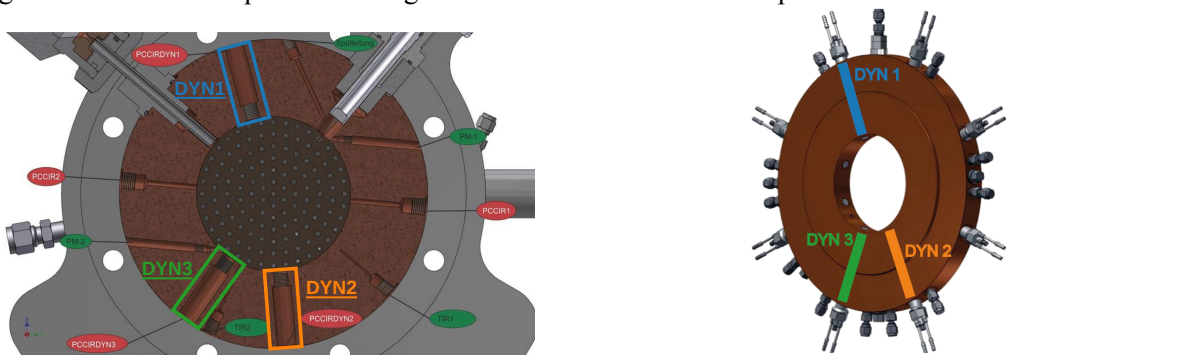

(a) Front-view of the LUMEN measurement ring with the high-frequency pressure sensors indicated (DYN1, DYN2, DYN3)

(b) Three-dimensional view of the measurement ring used during BKD test campaigns. Adapted from Losco [116]

Figure 5.1: View of the measurement rings' set-up as used by DLR

Next, the chamber pressure and the ROF of the two test runs were plotted for the whole test duration, to identify the time windows where the operating condition corresponding to p_c=63.7 [bar] and ROF=3.4 [-] would be reached. Figure 5.2 shows the complete operational profile of the experiments for the pressure and ROF, with Figure 5.2a and Figure 5.2b corresponding to run2 and run6, respectively. Note, that while the data of two transducers measuring the chamber pressure were available for each run, their average is shown in Figure 5.2 given the negligible difference that was seen between their outputs. The operating window of interest in the plots of Figure 5.2 is highlighted in green, with this being between 34.0 [s] and 41.0 [s] for run2 and between 64.0 [s] and 68.6 [s] for run6. The green regions for the window of interest were chosen for validating the data because there the operating conditions simulated by the CFD of the LUMEN combustor were attained. For the other operating windows no CFD analysis was conducted. Hence, these could not be used for validation due to the different flow properties in the chamber that would occur at different chamber pressure and ROF.

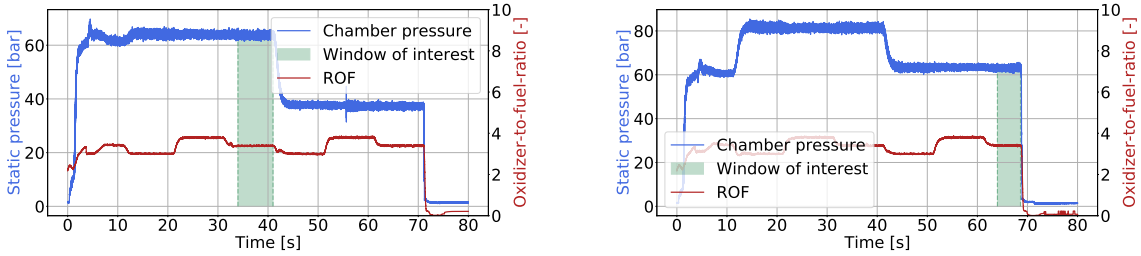

(a) Test-run 2

(b) Test-run 6

Figure 5.2: Identified windows of interest from the hot-fires of test-run 2 (a) and test-run 6 (b)

Lastly, before starting to identify the modes from the experimental results, a summary of the Mean Absolute Error (MEA) of the input parameters used by the CFD simulation of LUMEN's combustion chamber (Table 3.1) with respect to the experimental values, and the Standard Deviation (SD) of the latter, were computed. For all variables other than the ROF, provided that sets of data from at least two sensors were available, the standard deviation assumes random errors and uncorrelated errors, allowing it to be computed via Equation 5.1. Here, the subscripts on the right-hand side indicate the two sensors. The resulting mean errors and SD for the experiments are shown in Table 5.1.

$$\bar{\sigma} = \sqrt{\sigma_A^2 + \sigma_B^2} \tag{5.1}$$

Table 5.1: Mean Absolute Error (MEA) of the CFD input parameters and Standard Deviation (SD) of the measured fluid properties during experiments

	run2		run6	
Property	**CFD MEA**	**SD**	**CFD MEA**	**SD**
p_c	0.59 %	0.98 [bar]	0.83 %	1.00 [bar]
ROF	0.01 %	0.02 [-]	0.25 %	0.02 [-]
T_{CH4}	4.39 %	0.25 [K]	5.89 %	0.23 [K]
T_{LOX}	3.07 %	0.47 [K]	1.37 %	0.42 [K]
p_{CH4}	1.66 %	0.35 [bar]	1.83 %	0.34 [bar]
p_{LOX}	2.24 %	0.22 [bar]	1.71 %	0.22 [bar]

5.1.2 Mode identification

With the time window of interest identified, the next step was to determine the various modes in the chamber so that their frequencies and damping rates could be retrieved. For analyzing the data, a Power Spectral Density (PSD) function was used to display the power content of the signal decomposed over the frequency range of interest. With this, the PSD normalizes the magnitude content of the signal by the frequency resolution so that different signals can be compared to each other. The advantage of using the PSD is that acoustic modes become easily discernible, where each eigenmode is characterized by a peak in normalized magnitude. For the PSD analysis, the use is made of DLR's *RASPy* Python git library, which is a data-processing library written to standardize the processing of test data across various test stands of the institute.

For each run, the three high-frequency pressure sensors are imported, the last 1 [s] of the identified window of interest (as found in Section 5.1.1) kept, and the PSD performed with RASPy. For the latter, SciPy's *Signal* module is used, and Welch's method is employed, leading to a smoother power spectrum thanks to averaging the power spectrum of overlapping windows across the whole considered signal. For the frequency resolution used, values around 20 [Hz] were used. A low resolution will lead to a rougher PSD result since it will average more segments of the original signal for the spectrogram (following Welch's method), while a higher value will lead to a smoother signal. In general, based on the approach described later in Section 5.1.3 to retrieve the damping rates, this value led to a good trade-off between accounting for more sections of the signal to generate the PSD and a smooth enough result that would lead to a good curve-fit for the Lorentz profiles used to obtain the damping rates. For a given test run, the PSD of each of the high-frequency pressure sensors was performed and their output averaged. This led to a PSD for run2 and run6 as shown in Figure 5.3a and Figure 5.3b, respectively, using a frequency resolution of 20 [Hz]. The two PSD plots show dominant peaks at the same frequency locations, except for the peak at 2000 [Hz] in Figure 5.3a. Since this peak is only visible in the run2 data and is missing in run6, because the natural acoustic modes have to be identifiable from both runs given the same operating conditions, measuring equipment and stable runs, the 2000 [Hz] peak of run2 was determined to be a sensor artifact.

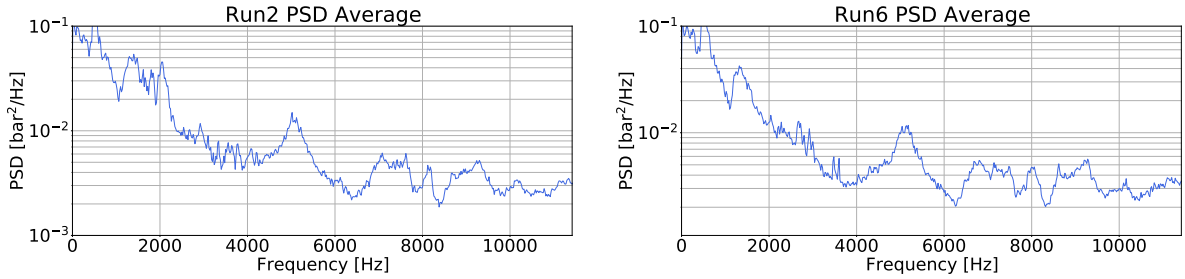

(a) Run2

(b) Run 6

Figure 5.3: Power Spectral Density (PSD) plots for test-run2 (a) and test-run 6 (b)

With the PSD available for both test runs, the modes were identified by combining the knowledge obtained from the simulations of where each mode is expected to be found, and by examining the phase difference of the three dynamic pressure sensors. For this, the latter's signal was filtered through two Butterworth bandpass filters using the RASPy module based on Scipy's *Signal* library. The bandpass filter has a filter order twice that of the original signal, and filters out the signal having frequencies below and above a provided low and upper bound. This bound is to be set manually for each frequency peak so that it filters out the regions outside the "base" of the peak. As an example, if the large peak between 4000 [Hz] and 6000 [Hz] from Figure 5.3 is considered, then the lower and upper bounds for the filtering operation should be taken around 4872 [Hz] and 5329 [Hz]. Once filtered, the three pressure sensors were plotted over three temporal ranges, namely: at the start of the window of interest from Figure 5.2, at the middle of this time range, and at the end. Furthermore, to provide enough resolution in the plots to compare the oscillations, each signal was plotted for 10 periods after the given start time, using the frequencies at the center of the peaks from Figure 5.3. A result of this analysis is shown for the L1 mode of run2 in Figure 5.4a for the intermediate time windows chosen for these phase plots. Moreover, as a further example, Figure 5.4b shows the phase difference of run2's T1 mode for the intermediate time window as well. All the other phase difference plots can be found in Appendix H. The plots use the same color coding for the high-frequency pressure sensors as used previously in the measurement ring figures (Figure 5.1).

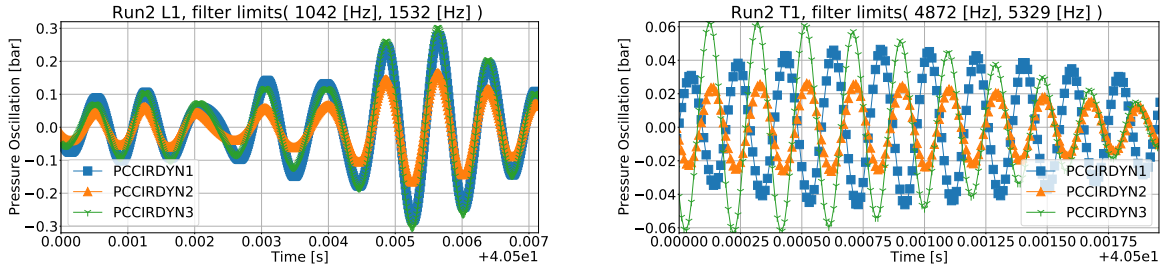

(a) L1 mode

(b) T1 mode

Figure 5.4: Filtered dynamic pressure data for test-run 2 L1 mode (a) and T1 mode (b) for the intermediate range

From the above figures, the oscillatory behavior of the L1 mode is visible. Considering the layout of the dynamic pressure sensors in Figure 5.1a, with all three sampling at the same axial location in the engine, for an ideal L1 mode signal it is expected that all three sensors show the same phase and same amplitude across the considered timeframe. While no phase difference is visible in Figure 5.4a, the slight amplitude difference is associated with either damage to the sensors, since these get re-used for numerous engine tests in DLR, or due to calibration issues. If the peak around 1350 [Hz] from Figure 5.3 is considered (for which Figure 5.4a was generated), it can be seen that the peak prior that (below 1000 [Hz]) is attained at a frequency too low for it to be an L1 mode, given that all simulations, including the corrected analytical solution, do not estimate the L1 mode to occur far below 1480 [Hz]. Hence, the peak around 1350 [Hz] was associated with the L1 mode. The same approach was then carried out for all subsequent peaks, starting first with the peaks closest to the frequencies obtained by the last few simulations. Similarly, a T1 behavior can be seen from Figure 5.4b. Here, a dominant amplitude peak is expected between either sensor DYN1 or one between DYN3 and DYN2. Then, almost a perfectly out-of-phase difference is expected between DYN1 and DYN2, and a similar phase between DYN2 and DYN3.

Following from the approach mentioned earlier, the PSD peaks were associated with the various modes, and the result is shown in Figure 5.5. In this figure, the depicted PSD corresponds to the average between the one from run2 and the one from run6 and is shown with a 4 [Hz] frequency resolution. Based on the difficulties encountered in verifying the T2 and R1 modes with the phase difference of their pressure sensors, it is recommended to consider re-designing the LUMEN high-frequency measurement ring to allow more dynamic pressure sensors to be used. This could not only enable a higher resolution in the phase differences but could also allow more data points to be gathered to assess whether one of the sensors

is damaged or if its calibration is off.

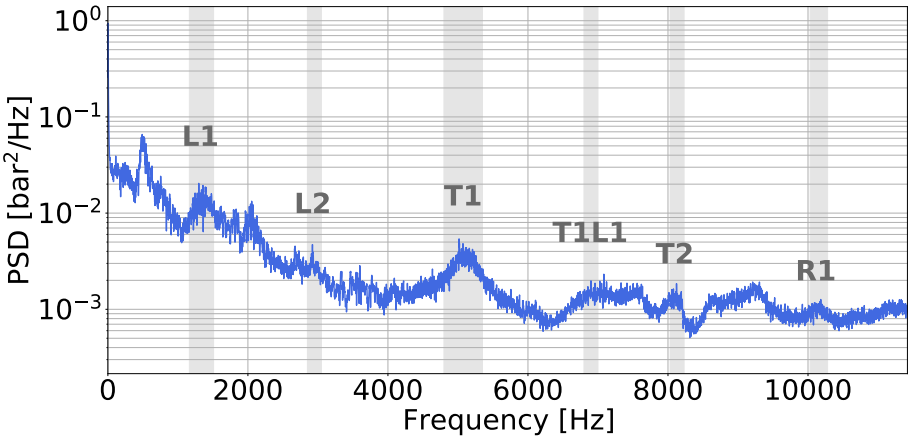

Figure 5.5: Average Power Spectral Density (PSD) plot of test-run 2 and test-run 6 showing all identified acoustic modes

5.1.3 Eigenfrequencies and damping rates

With the peaks from the PSD diagrams linked to the eigenmodes of interest, the next step, characterized by extracting the damping rate information for each of these oscillatory cases, is here presented. From the NASA report by Casiano [117], an overview of practical approaches to derive damping rate information of dynamic systems is provided. Here, six methods are given for extracting the damping from available data, five separate techniques to estimate the damping rate for simplified physical models given, as well as the FEM approach using COMSOL. From the data analysis methodologies proposed, a curve-fitting approach is recommended if a PSD function of the data is available. From the journal and conference publications, mentioned throughout this report, where damping rate data from experiments was retrieved, no clear understanding could be obtained regarding the method used to do so [29, 33, 82, 94, 99]. Turning to the Ph.D. theses of Webster and Schulze [24, 118] provided more insight into how the fitting procedure described by Casiano can be used in practice to obtain the damping rates from dynamical data of propulsion systems.

In the work of Schulze [118], the approach of retrieving the damping rates of DLR's BKD combustor by performing a curve-fitting of the PSD peaks via a Lorentzian function is validated. While in his thesis, Webster [24], expands this approach by allowing similar functions to be used, namely an asymmetric Lorentzian profile and a Fano function. Based on the good agreement between fitted function and data [24, 118], the use of Lorentzian profiles is here used to extract the damping rate information of LUMEN from its run2 and run6 PSD profiles. The Lorentzian function results from the Fourier transform of an exponentially decaying profile and is commonly used in planetary sciences to study the decay of emission and absorption lines of planetary atmospheres [119]. The Lorentzian is provided below in Equation 5.2, where PSD_L indicates the PSD output of this function, f_c is the central frequency of the considered peak, A_{fc} is the amplitude of the PSD diagram at this central frequency and W_{fc} is the width at half maximum of the peak [24]. Even though with this method the fitting has to be performed for each mode, a main advantage is that the damping rate follows straightforwardly from the W_{fc} fitting parameter.

$$PSD_L(f) = \frac{A_{fc} \cdot W_{fc}^2}{(f - f_c)^2 + W_{fc}^2} \quad , \quad with \quad W_{fc} = 2\pi\nu \tag{5.2}$$

For a given mode to be studied, a lower and upper bound for the data of the peak used for the fitting was set and the corresponding frequencies and PSD amplitudes falling within this range fitted to the Lorentzian profile via non-linear least squares following SciPy's *curve_fit* routine. For that, the initial

guesses for the fitting parameters f_c, A_{fc} and W_{fc} were estimated graphically from the PSD plots in Figure 5.3a and Figure 5.3b. A comprehensive table indicating exactly what the chosen input variables and the obtained output parameters of the fitting procedures were, is given in Appendix I. Furthermore, to allow for a better fitting of non-perfectly symmetric peaks, in addition to the (symmetric) Lorentzian profile of Equation 5.2, its asymmetric version, as well as the Fano profile, were also fitted to the data. The asymmetric Lorentzian function and the Fano profile are respectively given in Equation 5.3 and Equation 5.4. In Equation 5.3, B is the coefficient of asymmetry (a further fitting parameter) that leads to the symmetric case if B=0, and accounts for high asymmetry if its magnitude equals unity. As an initial guess, B was always set to zero. While in Equation 5.4, q_f refers to the asymmetry coefficient of the Fano profile, which, similarly to B for the asymmetric Lorentzian profile, is an additional fitting parameter, and is here denoted for simplicity as the Fano asymmetry coefficient. Values around q_f=1 indicate high asymmetry, and if q_f>100, then the Fano profile can be approximated by a symmetric Lorentzian function [24]. For illustration, the fit of the three functions is shown in Figure 5.6 for the T1 peak of run2.

$$PSD_{AL}(f) = A_{fc}\frac{1 + B\left(\frac{f-f_c}{\frac{W_{fc}}{2}}\right)^2 + B^2}{1 + \left(\frac{f-f_c}{\frac{W_{fc}}{2}}\right)^2} \tag{5.3}$$

$$PSD_F(f) = A_{fc}\frac{\left(q_f + \frac{2(f-f_c)}{W_{fc}}\right)^2}{1 + \frac{2(f-f_c)}{W_{fc}}^2} \tag{5.4}$$

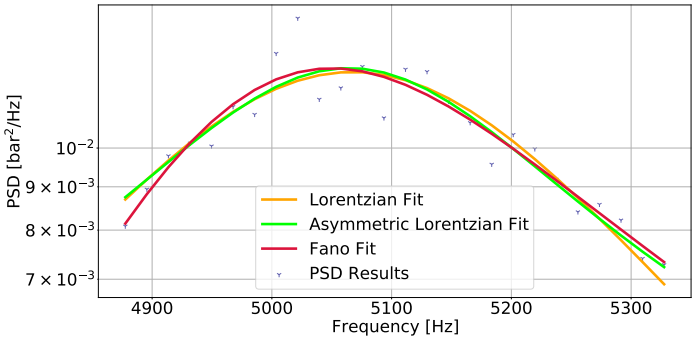

Figure 5.6: Curve fitting of the run2's T1 peak for a Lorentzian profile (orange line), Asymmetric Lorentzian function (green line) and Fano curve (red line)

The results of the curve fitting study are presented below in Table 5.2 for both of LUMEN's test runs. For most of the modes, a symmetric Lorentzian function led to the best results. The information related to which profile was used to generate the results of Table 5.2, is given for each mode in Appendix I. Regarding the parameters used to assess the quality of the fit, a threshold of 0.8 was set for R^2 for the lowest acceptable coefficient of determination. The results of Table 5.2, represent the data that will be used in the subsequent section to validate the simulations, which also include one standard deviation error in the parentheses. Table 5.2 shows that all the frequencies of test-run 6 are slightly lower than the ones of run 2 and that this is also the case for most damping rates except for the two tangential modes, where run 6's values are higher. On average, the difference in results of run 2 compared to run 6 is considerably larger for the damping rates than for the frequencies, with a difference of 3.4 % for the frequencies and of 19.9 % for the damping rates.

Table 5.2: Eigenfrequency and damping rate results of LUMEN's hot-fire test-run2 and 6 of the CALO-20 campaign

		L1	L2	T1	T1L1	T2	R1
Run 2	**f [Hz]**	1374	2910	5068	7062	8175	10171
	(± SD [Hz])	(± 7)	(± 6)	(± 7)	(± 8)	(± 29)	(± 11)
	ν [1/s]	130.3	106.9	143.8	243.9	163.3	279.3
	(± SD [1/s])	(± 7.4)	(± 8.4)	(± 8.5)	(± 26.3)	(± 12.3)	(± 18.3)
Run 6	**f [Hz]**	1336	2667	5024	6938	7783	9865
	(± SD [Hz])	(± 6)	(± 27)	(± 9)	(± 12)	(± 5)	(± 9)
	ν [1/s]	115.8	92.4	192.8	200.7	226.0	240.4
	(± SD [1/s])	(± 6.8)	(± 11.1)	(± 8.8)	(± 19.1)	(± 27.3)	(± 17.0)

It is important to note that while the modes of Figure 5.4 were straightforward to identify via their phase difference plots, not the same can be said for higher order modes such as T2 and R1. For such modes, the use of the results from Chapter 4 was mainly used for identification. Based on the limits of where the T2 and R1 modes are expected from the calculations presented earlier, and verified by the preliminary analysis of the LUMEN chamber's modes conducted by Hardi et al. (with T2 at 8360 [Hz] and R1 at 10490 [Hz]) [77], the T2 and R1 modes were expected to be found between 7700-9000 [Hz] and 9500-11000 [Hz], respectively. As visible from the PSD plot presented in the work of Schulze for DLR's BKD chamber [43] (same diameter as LUMEN but around 70 [mm] shorter), for a similar engine geometry various mixed modes can occur between T1 and T2 and R2, with some of them having peaks close to the T2 and R1 modes. In reality, all modes are superimposed on each other, and if two modes occur close enough that the bandpass filter is not able to filter one of them out, then a combination of them could be visible from the temporal evolutions of the high-frequency pressure sensor plots. Additionally, the LUMEN engine is known to be a stable engine, with combustion roughness below 2.5% of the chamber pressure [77], which in itself can make the identification of modes tedious given their low amplitudes. Also, only three high-pressure sensors were available to identify the eigenmodes, and even though no optimum number and distribution of transducers can be set to identify all transverse modes [8], with more transducers, cross-checking of sensor data could have been carried out. For the BKD case, eight of such sensors were available during experiments [120], enabling a better resolution for identifying transverse modes and allowing to verify the sensor data with each other, so as to identify damaged, wrongly installed or poorly calibrated sensors.

5.2 Comparison of simulation results with experimental results

In this section the results from Chapter 4 are validated against the experimental findings from Table 5.2. The corresponding mean percentage errors for mode previously computed mode, are reported for the frequency in Table 5.3 for both run 2 and run 6.

Table 5.3: Absolute percentage error of the predicted eigenfrequencies versus experiments

		Analytical CEA	Helmholtz CEA	Analytical Corrected	Helmholtz radial-averaging	LNS radial-averaging	LNS 3D-mapping
Run 2	**L1**	24.5 %	40.8 %	7.7%	47.3 %	15.6 %	N.A.
	L2	17.5 %	32.2%	1.7 %	2.0 %	13.6 %	N.A.
	T1	73.4 %	81.3 %	6.8 %	4.4 %	12.8 %	2.8 %
	T1L1	26.8 %	35.1 %	20.5 %	4.0 %	5.3 %	N.A.
	T2	78.3 %	82.5 %	9.8 %	5.2 %	10.3 %	1.4 %
	R1	79.9 %	88.1 %	10.8 %	7.4 %	9.3 %	9.6 %
Run 6	**L1**	27.9 %	44.8 %	10.8 %	51.5 %	18.9 %	N.A.
	L2	28.2 %	44.2 %	11.0 %	7.0 %	24.0 %	N.A.
	T1	75.0 %	82.8 %	7.7 %	5.3 %	13.8 %	3.7 %
	T1L1	29.1 %	37.5 %	19.1 %	5.9 %	7.2 %	N.A.
	T2	87.3 %	92.8 %	15.3 %	0.4 %	15.8 %	3.6 %
	R1	85.5 %	94.0 %	14.2 %	4.6 %	12.7 %	6.8 %

To obtain a general comparison of the performance of the various analysis methods used, the average error per mode per numerical approach is given in Table 5.4 together with the average run-time to solve for one eigenmode for the respective tabulated methods. Note, that data for the modes with longitudinal components for the LNS simulation with 3D-mapped input is missing in the tables below for the reason described earlier in Section 4.2.1.

Table 5.4: Average eigenfrequency error of the conducted analyses and average computational time per mode

	Analytical CEA	**Helmholtz CEA**	**Analytical Corrected**	**Helmholtz radial-averaging**	**LNS radial-averaging**	**LNS 3D-mapping**
L1	26.2 %	42.8 %	9.3 %	49.4 %	17.3 %	N.A.
L2	22.9 %	38.2 %	6.4 %	4.5 %	18.8 %	N.A.
T1	74.2 %	82.1 %	7.3 %	4.9 %	13.3 %	3.3 %
T1L1	28.0 %	36.3 %	19.8 %	5.0 %	6.3 %	N.A.
T2	82.8 %	87.7 %	12.6 %	2.8 %	13.1 %	2.5 %
R1	82.7 %	91.1 %	12.5 %	6.0 %	11.0 %	8.2 %
Run-time/mode (RAM used)	$\ll 1$ [min] (64 Gb)	2 [min] (128 Gb)	$\ll 1$ [min] (64 Gb)	2 [min] (128 Gb)	2 [hrs] (64 Gb)	37 [hrs] (128 Gb)

Throughout this section, use is made of the term *CEA* to denote the analysis performed that made use of constant CEA background flow properties. Similarly, *Corrected* indicates the corrected analytical solution of Section 4.2.3, *radial-averaging* refers to the approaches using the radially averaged 1D profiles as input, and *3D-Mapped* describes the LNS simulation with the detailed three-dimensional CFD field as input. From the results, several findings follow and are classified per topic in the subsections presented hereafter.

5.2.1 Low Order Model's accuracies and the influence of a varying background flow

Firstly, the initial approaches, namely the ones described in Section 4.1 using constant CEA properties, were used to set the ground to verify the simulations from Section 4.1.3, Section 4.2.5, and Section 4.3.2. These analyses led errors above 30 % for almost all modes. Even though these methods have the advantage of being computationally cheap and do not require any input obtained from CFD, with an average error in their overall predictions above 50%, these methods can not be used in practice since their prediction could as well lead to the same accuracy as an informed guess. Hence, even during preliminary design phases, it is required to account for the variation in the background flow to better represent the flow field in the combustor, which, from Table 5.3, can be seen to greatly influence the accuracy of the mode frequencies.

Secondly, a computationally-cheap improvement of the latter can be found in the corrected analytical solution. Note, that while in Chapter 4 different lengths were used to determine the results for the analytical solutions, the percentage errors here presented were calculated using the results that account for the full length of the nozzle (i.e. total length of the cylinder of 338.2 [mm]), since this approach was found to be the most accurate for the LUMEN chamber. By correcting the CEA-obtained speed of sound value to account for its variation across the whole chamber length (for longitudinal modes) and within the combustion zone (for transverse modes), the corrected analytical solution greatly improves upon the constant-CEA results. Both analytical solutions assumed a uniformly convecting background flow, with the difference between these two analyses being a more representative description of the speed of sound variation in the chamber. The importance that accounting for variation in flow properties plays for an accurate description of the acoustic field inside combustors can also be understood from the results of the Helmholtz solver. The formulation of the latter in COMSOL does not account for convective effects (a homogenous non-convective form is used by the software, and no monopole nor dipole source terms were added), and by simply accounting for the variation of the speed of sound and density across the chamber via the radially averaged 1D profiles, the frequency accuracy for its constant-CEA-value counterpart could be improved. The Helmholtz run using constant CEA values achieved an overall average error for its prediction that was around 10% higher than one of the analytical solutions using constant CEA

properties. In comparison, for the same chamber length modeled by the corrected analytical solution, the Helmholtz simulation using radially averaged profiles had only a 0.8% higher average total error. This shows that even though a moving background flow significantly reduces the eigenfrequencies, one of the major parameters that influence the prediction accuracy in real rocket engines with non-uniform background flow is due to the variation of flow properties.

Going back to the corrected analytical equation, its T1-frequency accuracy is comparable to the one obtained by Kobayashi et al. (Table 2.3). All in all, when compared in Table 5.4 to the accuracy of the other approaches, the corrected analytical equation provides one of the most accurate results for the L1, L2, and T1 modes, while also requiring minimal computational resources. This makes this method attractive for use during early design phases, where the system characteristics undergo various iterations, possibly leading to variation in the combustion chamber geometry or background flow properties. The only issue during such early design phases is the computation of the correction coefficients k_l and k_t. In the present analysis, these were obtained from the CFD results of the LUMEN combustion chamber, but for preliminary design phases, such analyses are not expected to be performed. Even though applicable ranges have been reported for hydrolox systems [77], a lack of data for methalox engines has been noticed. Hence, for a given engine manufacturer, for the corrected analytical equation to have more general applicability, either resources are allocated to set up a databank based on prior experience and literature to determine such correction coefficients for a variety of propulsive systems, or the latter has to be computed via other means. An option could be to use CEA to retrieve the speed of sound at different locations in the engine (i.e. chamber inlet, chamber end, and nozzle throat) and perform a curve-fit for obtaining a smooth variation along the chamber's longitudinal axis. The main shortcoming of this approach is foreseen to be the neglection of the variations within the combustion zone, thus leading to a higher k_t estimate than obtained through more detailed methods, therefore over-predicting the frequency of the transverse modes.

5.2.2 A need to investigate various modes simultaneously

In general, the results presented in Table 5.4 and Table 5.3 show that assessing the performance of a given method by only validating one mode can be misleading. For example, if the results from Kobayashi et al. [87] were to be used to investigate what accuracy LOM approaches using the analytical solution could provide for a methalox system, one would only consider the accuracy that the authors provide for the T1 mode. While Table 5.4 suggests that more modes should be studied for a proper assessment of the accuracy of a given numerical methodology. For the example of a low-order model like the corrected analytical solution, this can return an error that is off by a factor of two depending on whether a T1L1 mode or a T1 mode is investigated. To get a better sense of the accuracy spread from Table 5.3, a box-and-whisker plot was generated based on its information. This is shown in Figure 5.7, and led the mean overall frequency error to be 52.8 % for the analytical CEA equation, of 63 % for the Helmholtz solver with CEA input, of 11.3 % for the corrected analytical solution, of 12.1 % and 13.3 % for the Helmholtz and LNS simulations using radially averaged input, respectively, and finally, of 4.7% for the LNS simulation using 3D-mapped input.

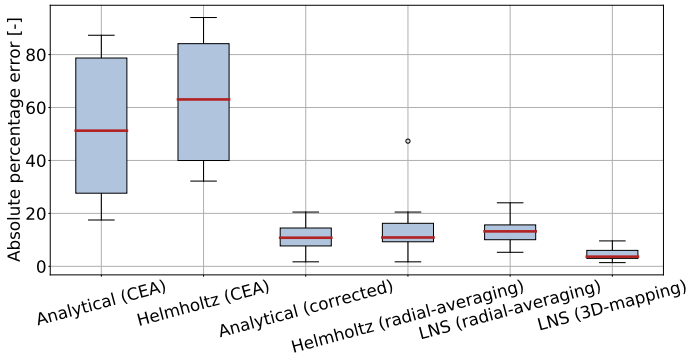

Figure 5.7: Box-and-whisker plot showing an overview of the error of the different analyses conducted

Per computation time, the corrected analytical equation and the Helmholtz solver with radially-averaged input, represent the most accurate methods. While overall, the LNS simulation using the detailed 3D CFD field as input leads to the highest accuracy. Before continuing the discussion of the results, it is worth noting that based on the literature it is unknown what can be considered to be an acceptable accuracy for the eigenfrequencies prediction in rocket engines. At the time of writing, no clear guideline regarding the minimum tolerable accuracy (for both frequency and damping rates) that would still lead to a correct prediction of the stability of an engine, could be found. Also, due to the complexity of the problem studied, it can also not be estimated at this point to what extent an instability can be accepted during design phases. This directly links to the increase in wall heat flux and pressure amplitude stemming from the instability, and what safety margins are used for these remains a choice that engine designers have to take.

5.2.3 Linearized Navier-Stokes solver's accuracy using a detailed background flow

For the current study, based on the surveyed literature, errors below 5% were aimed at for the frequency predictions of the LNS solver, since these represent what the current state-of-the-art of Acoustic-based methods and CFD-based methods are able to achieve. From the work conducted, this threshold, falling within the research question **RQ.2**, was obtained for the LNS simulation using a detailed 3D background flow description mapped from the LUMEN CFD results. From the analyses conducted, this simulation led to the most accurate results for the T1 and T2 frequencies, even though it achieved an average error of 8.2 % for the R1 mode. Based on Table 5.4 the R1 error consistently ranks amongst the highest ones returned by the various analyses. Unfortunately, from the literature, only the work of Urbano et al. [121] provided an accuracy for the R1 mode. The authors obtained an error between 4.4 % and 6.3 % depending on whether an LES analysis was used to solve for the acoustics or a Helmholtz solver; slightly higher than the one of their T1 mode predictions. Given that no other reference for the R1 accuracy was found, there is not enough data to support the hypothesis that the R1 mode is associated with an inherently higher error than the other modes presented in this report. Thus, for future studies on the topic, it is recommended to investigate if and how the error of the predicted frequencies varies for higher-order modes.

5.2.4 Frequency results of the radially averaged Helmholtz and Linearized Navier-Stokes

Besides demonstrating that sub-5 % errors are attainable with LNS by using a mapped 3D CFD field to describe its background flow, the results from Table 5.4 also show that if the radially averaged profiles are used as input to the LNS simulation instead of the 3D-mapped field, then more than a four-fold increase in error is attained in the frequency of the transverse modes. For this case, the radially averaged Helmholtz approach then leads to more accurate results than the radially averaged LNS simulation, even though they do not return damping rates as output and thus not providing information about whether a mode is stable or not in case the equation is not solver in the time domain and its results post-processed. Since Helmholtz only models the propagation of an acoustic wave neglecting the influence of the background flow on the acoustic, while LNS solves for the transport equations accounting for flow gradient effects and interaction of the acoustic disturbances with vortical and entropy modes, a possible error could be introduced in the LNS solution via the background flow description. The LNS equations relax the modeling assumptions made by the Helmholtz equation regarding having a homogenous flow, quiescent and inviscid flow, and by also further accounting for the presence of vortical and entropy modes, and their interaction with the acoustic perturbations. LNS models the physics of the problem more accurately and is thus expected to return better results than the Helmholtz equation. If the LNS equations from Equation 2.8, Equation 2.9 and Equation 2.10 are compared to the simplified linearized governing equations used to derive the wave equation (which can be converted to the frequency domain to obtain the Helmholtz equation), it can be seen that the main difference between the two resides in the terms involving gradients of the background flow. Since the simplified linearized governing equations of the wave equations were not reported in Chapter 2, these are shown below in Equation 5.5 for the continuity equation, in Equation 5.6 for the momentum equation and Equation 5.7 for the isentropic relation.

$$\frac{\partial \rho'}{\partial t} + \rho_0 \nabla \cdot \mathbf{u}' = 0 \qquad (5.5) \qquad \rho_0 \frac{\partial \mathbf{u}'}{\partial t} + \nabla p' = 0 \qquad (5.6) \qquad p' = c_0^2 \rho' \qquad (5.7)$$

Since the LNS equations account for gradients of the background flow field, while the Helmholtz equation neglects them, if an error in the background flow description exists, then this is anticipated to affect the frequency results of the former more. From the background flow description, the Helmholtz solver uses the speed of sound and density as input. Possible reasons for errors in the radially averaged flow description are proposed hereafter. Starting with the averaging technique used, even though the area average method does not meet any conservation law, as mentioned in Section 4.2.1, a mass average technique was compared in a past study at DLR with the area average one for a cryogenic LOX/LH_2 system. By more heavily weighing the LOX core's properties, leading to a largely lower speed of sound magnitude within the combustion zone, the profiles obtained via mass-averaging led to a considerable reduction in predicted frequency, resulting in a twofold increase in L1 error and an increase by a factor of 6 in the T1 error when compared to the results obtained via area-averaging [92]. Hence, the source of the error in the background flow description is not foreseen to be due to the area-averaging technique used. Also, by using the same approach, Schulze & Sattelmayer [43] achieved the most accurate T1-frequency prediction found in the literature using LEE (as seen in Table 2.3). If a future study aims at removing this averaging factor from the possible causes, then a Helmholtz simulation using the 3D-mapped CFD input shall be run so to compare its results with one of the respective LNS simulations presented earlier. Other than the averaging technique used, shortcomings in the CFD results could be the source of errors. At the time of writing of this document, an investigation was ongoing at DLR to understand whether or not lifted flames were occurring during LUMEN hot fires. As an hypothesis aiming to describe the reason for why the input profiles could lead to errors in the predicted frequencies, Section 5.3.1 will describe this flame lift-off problem and how accounting for it could lead to more accurate results. Furthermore, modeling aspects of the radially averaged profiles and LNS equations are further discussed in Section 5.3.2, where a further hypothesis is advanced to explain possible sources of errors leading the radially averaged LNS frequency results to be less accurate than for the corresponding Helmholtz case.

5.2.5 Natural damping rates and requirements for their accurate prediction

Lastly, contrary to the Helmholtz equation, the LNS solver returned the damping rate results of the modes directly as one of its primary outputs. The errors obtained for this parameter when compared to experiments, are shown below in Table 5.5 and in Table 5.6 for their average error per mode.

Table 5.5: Absolute percentage error of the predicted damping rates versus experiments

		LNS radial-averaging	LNS 3D-mapping
Run 2	**L1**	27.2 %	N.A.
	L2	7.5 %	N.A.
	T1	4.6 %	27.5 %
	T1L1	4.9 %	N.A.
	T2	30.3 %	31.2 %
	R1	64.0 %	74.6 %
Run 6	**L1**	18.1 %	N.A.
	L2	7.0 %	N.A.
	T1	28.8 %	45.9 %
	T1L1	15.6 %	N.A.
	T2	49.6 %	50.3 %
	R1	57.0 %	70.5 %

Table 5.6: Absolute percentage error of the predicted damping rates versus experiments averaged over the two test runs

	LNS radial-averaging	LNS 3D-mapping
L1	22.7 %	N.A.
L2	7.3 %	N.A.
T1	16.7 %	36.7 %
T1L1	10.3 %	N.A.
T2	40.0 %	40.8 %
R1	60.5 %	72.6 %

The above damping rate results show a better agreement to experimental data than the ones found in literature and reported in Table 2.3 (research sub-question **RQ.3.S.2**). While promising for future LNS

applications, more analyses shall be conducted in the future to assess its damping results. The LUMEN test runs studied were stable and the flame response was neglected in the analyses. Hence, it can not be concluded whether the lower damping errors of Table 5.6 are due to the natural damping rates representing a good approximation of the combustor damping under stable conditions, or if their errors will increase or decrease if flame forcing is added. Also, by not including the flame forcing in the equations, it could not be investigated whether this would increase the damping of the system or reduce it. Thus, from the present study, conclusions can not be drawn on whether including the heat release rate source term and utilizing transfer functions, will improve or worsen the accuracy of the damping rates presented above. Nevertheless, some observations can be made, and the research question **RQ.3** answered. Firstly, the influence of including the detailed CFD field as input for the LNS study (research sub-question **RQ.3.S.1**) could not properly be analyzed. The reason for that is that the latter's simulation did not include the presence of the injector domes, which are known to influence the damping behavior of the chamber [29]. Based on the investigation run by Schulze & Sattelmayer [29], the inclusion of the domes leads to an increase in the system's damping. For the LNS with 3D-mapping this would lead to damping rates magnitude becoming closer to the values of the LNS simulation with radially averaged input.

Secondly, the modeling requirements necessary for an accurate description of the eigenfrequency were found to be less critical than the ones for the damping rates. It was already mentioned before the need to include the injector domes to allow modeling of the damping of the chamber plus injector system. For the frequencies, this is not necessary, since these are solely governed by the geometry inside the combustion chamber, by the flow field inside of it, and by the acoustic boundary conditions at the interface of the combustor. Furthermore, as noticed in Section 4.2.5, the eigenfrequencies converge faster than the damping rates. This allows a coarser mesh to be used in case only the former are of interest, allowing to save considerable computational time due to not only not requiring the whole injector domes to be meshed but also due to the less number of elements needed in the chamber. Finally, for determining the eigenfrequencies, the flame response can be omitted (for low amplitude oscillations), while this is necessary to be included for an accurate description of the system's damping because the flame forcing can further dampen or amplify the natural acoustic modes in the chamber, as described in Section 2.5.

5.3 Potential sources of error

In this section, two hypotheses are outlined to propose why the frequency results of the radially averaged LNS simulation were found to be less accurate (except for the L1 mode) than the ones of its Helmholtz counterpart and of the LEE results from Table 2.3; currently the most accurate (frequency-wise) method available. The first explanation is given in Section 5.3.1, where the case of a possible flame lift-off is described. Secondly, in Section 5.3.2, the sensitivity of LNS to errors in the input background flow is discussed, and a higher error from the radially averaging technique is proposed for methalox systems when compared to hydrolox engines.

5.3.1 Flame Lift-Off

Earlier, in Section 5.2.4, flame lift-off was mentioned as a possible reason why the radially-averaged LNS frequency results deviate more from the experiment than the ones of the Helmholtz counterpart. It was discussed that in addition to requiring more input parameters than Helmholtz, the LNS equations directly account for background flow gradients in their formulation, while, through the quiescent flow assumption, Helmholtz neglects such terms. This suggests that errors in the background flow description could become more prominent in the LNS solver than in the Helmholtz case.

In a recent publication by Börner et al. [122], the authors investigate the possibility of lifted flames occurring in the LUMEN engine, by analyzing two test-runs. Use is made of the momentum flux ratio J also called the J-number and given in Equation 5.8, to characterize the flame anchoring process in the

combustor. The J-number is seen to govern the primary breakup of the LOX jet in coaxial injectors [122]. In the equation, v indicates the velocity upon injection in the chamber, and the subscripts o and f refer to the oxidizer and fuel, respectively.

$$J = \frac{\rho_f v_f^2}{\rho_o v_o^2} \tag{5.8}$$

By associating variations in the J-number to measured oscillations in OH* radiation, via an optical probe, and fluctuations in the wall temperature, the authors concluded for the given LUMEN experiments, that a J-number-threshold of $J > 7.5 \sim 10$ would lead to anchored flames. If the two test runs used by the authors are analyzed, J-numbers of 4.9 [-] and 2.8 [-] can be retrieved for similar operating conditions to the one used for the simulations in this report (i.e. p_c=58 [bar], ROF=3.4 [-]), and if the LUMEN CFD results are analyzed, a J-number of $J = 5.4$ [-] is found. Due to the dependency of this process on the state of the injected propellants [39, 122] and the lack of a study analyzing a large number of test-runs, conclusions on whether flame lift-off occurred during the LUMEN hot-fires analyzed in this report can not be drawn. If flame lift-off occurred during the test-runs that were here used to validate the analyses of Chapter 4, then a higher accuracy of the simulation results is to be expected. If the flame is lifted, then the anchoring at the injector is missing, leading to the reaction of the products taking place downstream of the face plate. In turn, this means the cold propellants enter a given initial section of the chamber without combusting and thus lower the average speed of sound of the flow. Taking the corrected analytical solution as a reference, the result of flame lift-off is therefore a reduction in the correction coefficient.

The possibility of lifted flames occurring during the hot-fire runs analyzed in this report is further supported by the similar correction factors obtained by Martin et al. [39] for the BKD combustor running on LOX/LNG. With the same injector configuration as LUMEN and a similar chamber pressure of 60 [bar] (although with ROF of around 2) the authors obtained $k_l = 0.84$ [-] and $k_t = 0.59$ while observing flame lift-off behaviors from their experiments [39]. Even though it could represent a source of error, flame anchoring and detachment can occur throughout the experiment and there is no certainty that it occurred at all during the analyzed test runs. The examination of flame lift-off behaviours for LUMEN remains an open topic in DLR which at the moment of writing of this document was still being investigated at the institute.

5.3.2 Chemical kinetics and averaging technique

If the flame lift-off hypothesis is tested in the future and stable anchored flames are concluded to occur within LUMEN's combustor under the considered operating conditions, then further hypotheses shall be tested. Hereafter two are given, with the first one related to the averaging of hydrocarbon-based flames versus Hydrogen-based flames. If equal operating conditions, engine geometry and injection system are considered, then what differentiates the flame length inside the combustor between these two cases is the vaporization and atomization of the propellants and the chemical kinetics. Hydrolox combustion has a faster reaction rate than methalox, suggesting that LOX/CH_4 flames travel further into the chamber than comparative LOX/LH_2 ones. If errors are introduced by the radial averaging method at each slice where an average is taken, then, if regions of large gradients extend further into the chamber, a higher error could be accumulated by the averaging procedure for a LOX/CH_4 case than for a LOX/LH_2 system. If flame lift-off is found to not have occurred for the operating conditions of test-run 2 and test-run 6, then the error introduced by averaging could explain why for the 3D-mapped LNS the frequency results are more accurate and why for a similar combustion chamber running on LOX/LH_2, such as the BKD case studied by Schulze [43], lower errors are obtained using an aeroacoustic solver with radially averaged input. At the same time, the faster chemical kinetics of hydrolox systems could allow more compact chambers to be designed than for methalox systems, possibly leading to a flame-length-to-chamber-length comparable to that of a similar methalox system. Furthermore, elements such as the turbulence in the

chamber and vaporization rates can also limit how far into the chamber combustion still occurs, and so the above hypothesis regarding methalox flames travelling deeper into a combustion chamber than hydrolox cases, can not be generalized to all liquid engines. In general, to test this hypothesis, an hydrolox system shall be investigated using an LNS solver with radial averaged input.

The second hypothesis concerning the averaging technique relates to the gradients in the radial direction of the engine, more specifically at the wall. In the LNS equations (Equation 2.8, Equation 2.9 and Equation 2.10) terms such as $\mathbf{u}' \cdot \nabla \mathbf{u_0}$ can be distinguished. In the latter's case, this represents a convection term where the background flow convects a velocity disturbance. Through radially averaging, gradients along the axial direction are represented, while constant values are taken at each cross-sectional slice of the engine. While the variation of the background flow is represented in one dimension, LNS will still solve the problem in 3D, falsely taking zero gradients in the radial direction as input from the radially average background flow. This means that wrong background flow gradients are also used by LNS when solving the acoustic boundary layer at the wall, where large errors in the background flow gradients at the wall are used. While the LNS sensitivity to errors in the input flow field will have to be investigated in the future, this could explain why more accurate frequency results can be obtained with a Helmholtz and LEE solver, as seen in Table 2.3, if radially averaged inputs are used. Being inviscid could suggest why these solvers return lower errors, since they do not solve for the acoustic boundary layer at the wall and hence are not influenced in that respect by wrong background flow gradients at the wall.

6 Recommendations and Conclusion

In this chapter, the research work is ended by proposing recommendations for future work and by providing a conclusion of the work described in the aforementioned chapters. To do so, Section 6.1 systematically addresses how the LNS results can be ameliorated in the future, and what steps lie ahead before combustion instabilities can reliably be predicted by Acoustic-based numerical tools. After that, Section 6.2 finalizes the report, summarizing the key outcomes and linking the results back to the research questions.

6.1 Recommendations

Based on the findings from the previous chapters, several recommendations are devised hereafter. These are grouped per topic, where each set either suggests ways to improve the results obtained, aims at answering questions that arose at the end of the research activities, or proposes a way forward to recommend the next steps required to be taken by DLR to work towards achieving their goal of reliably predicting thermoacoustic instabilities numerically. For this, the following section is divided into three parts. In Section 6.1.1, recommendations are provided that are aimed at reducing the LNS errors obtained in this report and describing the resources needed to do so. Next, Section 6.1.2 introduces recommendations regarding the measurement ring for LUMEN focused on the set-up for the dynamic pressure sensors, to allow for better identification of higher order modes such as T2 and R1. Lastly, Section 6.1.3 deals with future longer-term steps required to be taken by DLR to work towards achieving their goal of numerically predicting high-frequency combustion instabilities in liquid rocket engines.

6.1.1 Improving the current Linearized Navier-Stokes results

Starting with the recommendations related to LNS, firstly, it is advised to perform a subsequent study with this solver for a hydrolox system. This would allow the general applicability of LNS to be studied across different propellants, and learn how the errors in frequency and damping rates would compare using the same solver and methodology while changing the propellants. In case this follow-up research activity is to be performed at DLR, and if a CFD analysis of the whole chamber has already been performed at the institute, then it would be ideal to perform the hydrolox study for the BKD combustor. Not only are the modes of this engine well known [39, 43], for which the data of eight dynamic pressure transducers are available, but, by also studying the BKD combustor, a direct benchmark of the LNS results with Schulze's LEE results [43] would be possible. The latter represents the most accurate eigenfrequency results obtained via an aeroacoustic solver for rocket propulsion applications. Furthermore, by comparing the LNS results with the LEE analysis from Schulze, a better understanding can be obtained of whether higher errors are attained for higher-frequency modes or not, since the authors only presented results for the T1 mode of the BKD engine. If CFD results for the BKD combustor are not available, then the BKH chamber could be used instead, allowing a direct comparison with Beinke's results (obtained using a Helmholtz solver) [17].

Secondly, besides conducting studies using different test cases, some recommendations can also be named for the LUMEN study here presented. To begin with, the outcome of the data analysis investigation for assessing the flame anchoring characteristics of the LUMEN combustor, which at the time of writing was being conducted at DLR, shall be studied. If for the operating conditions used here the flame anchoring investigation further supports the possibility from Section 5.3.1 of lifted flames, then a new CFD simulation shall be conducted to either account for this, or to model a new redesign of LUMEN. In the opposite case, then the reason for the higher errors from the radially averaged LNS simulation compared to the radially averaged Helmholtz run shall be further investigated. For that, a Helmholtz simulation with mapped 3D

CFD input could be performed, so to allow a direct comparison with the accurate 3D-mapped LNS results, or the applicability of the area averaging technique shall be questioned. Even though the area-averaged approach has also been used by Schulze [43] and the mass-averaged approach was found to lead to higher errors for a hydrolox system [92], a third option could be tested, namely a mixed-out average at constant pressure [108]. This third type of averaging technique meets the conservation equations and has the added advantage of accounting for mixing losses. However, it also represents the most complex method of the three, and no straightforward approach to perform such an average in Paraview could be found.

Thirdly, set aside how the background flow was calculated, to obtain a more accurate description of the natural damping rates for the 3D-mapped LNS simulation, the LUMEN injector domes shall be included. For this, 3D CFD analyses of the LOX injector and CH_4 injector are required. Even though the former was already performed for the work presented in this document, it is further recommended to perform all CFD analyses externally to COMSOL. First of all, for DLR this represents a necessity given that they do not possess the COMSOL license for the CFD module. But besides that, the CFD module from COMSOL was found to provide less freedom to the user regarding numerical schemes and turbulence models than in other ad-hoc CFD software such as Ansys Fluent or OpenFoam. Also, issues were encountered with the compressible CFD module when trying to run the simulation for the CH_4 injector, and performing the CFD analyses for both injectors externally, would represent an opportunity to try to ameliorate their pressure drop loss (e.g. by accounting for a wall roughness) and compare the LNS results with the ones presented by this work to quantify the influence of this on the predicted frequencies and damping rates. In addition, once 3D CFD results are obtained for the injectors, before running an updated version of the 3D-mapped LNS simulation, more computational resources shall be made available than the ones of the 128Gb Linux machine used for this study. This requirement arises from the fact that to run the LNS simulation from Section 4.3.2, the acoustic mesh had to be coarsened to meet the RAM constraint of the hardware used. Because adding the injector domes will lead to a considerable increase in mesh size, more computational resources will be needed.

The need for more powerful hardware results also from the following recommendation. From Section 4.3.2 it was found that the mapping coefficient greatly influences whether or not acoustically-meaningful results are returned by the simulation. Its value was calibrated once for the flow variables and once for the density separately, and the two resulting values were used. The two diffusion coefficients were so chosen to have the lowest possible coefficient that would return the expected mode shapes for LUMEN. This minimization problem was based on the results obtained for discrete values of the diffusion coefficient, procured through a parametric sweep. This means that lower values for the diffusion coefficients that would still return physical results are possible. On top of attempting to find better values for these coefficients, it is also advised to perform a sensitivity analysis for this parameter to see how sensitive the frequency and damping rate results are to it. Moreover, having more RAM available would allow using a finer mesh in the combustion zone of the engine thus allowing to lower the dependency of the results on the chosen diffusion coefficients.

In addition, based on the promising accuracy of the frequency results of the 3D-mapped LNS simulation, it is recommended to apply this method to another combustor using CFD results that were obtained for the same chamber length as tested during experiments. For example, if the above recommendation of analyzing a hydrolox engine is followed, then the accuracy of additional modes shall be assessed. Here only transverse modes were solved for LUMEN, but for a more thorough evaluation of the accuracy of this LNS approach, at least the first longitudinal and first combined longitudinal-tangential modes shall also be added.

6.1.2 Experimental analysis

Following is a suggestion to consider re-designing the measurement ring of LUMEN if the budget and workforce at DLR allow it. For the phase difference of the dynamic pressure sensors of LUMEN, in Figure 5.4a it was seen how the sensor *DYN2* attained lower amplitudes than the other two transducers

despite expecting all of them to attain the same amplitudes for a longitudinal mode. This difference could be associated with this sensor either being damaged or possibly its calibration being off. Given the little room for redundancy, if only three sensors are used, it is recommended to add further dynamic pressure sensors along the perimeter of the measurement ring, as is for example the case for the instrumentation of the BKD chamber (Figure 5.1b). More sensors would also make it easier to identify modes; a difficulty encountered for the T2 and R1 modes of LUMEN, where the expected frequencies for these modes from Chapter 4 were required to verify experiments.

6.1.3 Outlook

Lastly, the section about recommendations for future work is closed out by the subsequent outlook on longer-term activities needed to construct from the aforementioned LNS analysis an Acoustic-based stability prediction tool. By mapping a three-dimensional CFD field to the input of LNS, for describing its background flow field, not only could more accurate results be obtained for the eigenfrequencies, but also more representative velocity oscillation distributions were retrieved. Although the highest accuracy of other Acoustic-based methods from literature is comparable to the one obtained in this work for the 3D-mapped LNS simulation, the former has the downside of retrieving a more uniform velocity disturbance distribution in the chamber which neglects the presence of the flame structures. This suggests that if the velocity oscillations want to be included as influence parameters for the flame transfer functions (to describe the source term for Acoustic-based instability prediction tools), the resulting heat release rate is expected to be different between the 3D-mapped LNS and in the case, a radially averaged aeroacoustic solver is used; with the former foreseen to return more physical results. For this reason, the 3D-mapped LNS approach not only provides high accuracy for the prediction of eigenfrequencies but also allows the flexibility of allowing more complex flame responses to be included for the prediction of thermoacoustic instabilities.

For this reason, as a next step required towards building an Acoustic-based prediction tool with the 3D-mapped LNS, a source term for the flame response shall be implemented, where this can straightforwardly be added via the *Domain Sources* condition in COMSOL. To derive such a flame response, an initial step can be taken to obtain an FTF from a transient CFD simulation of one flame. Once the LNS with source term is solved in COMSOL, whether a mode is unstable can be assessed via the sign of the damping rate. If this attains a negative value, then it becomes a growth rate, amplifying the amplitude of the respective mode. Once the flame response is added in COMSOL for LNS, further steps can be taken in increasing the complexity of the FTF (e.g. by accounting for the velocity as a driving parameter as well). Before getting to the point of incorporating source terms into LNS, in chronological order, the recommendations from Section 6.1.1 shall be tackled first.

Testing other approaches than LNS in this report also showed that while the 3D-mapped LNS can be used for future stability prediction analysis, based on its computation time and CFD input requirement, it is not seen as a useful method to be used in phases other than the detailed design phase of an engine. Only frequency results are mostly sought after in preliminary design phases, where care must be taken to not have the modes of the injector element lines match the ones of the chamber. For this, the corrected analytical solution provided accurate-enough results, while the use of constant CEA values in the analyses was found to return too high errors to be practical. The radially averaged Helmholtz solver in COMSOL also returned high accuracy for use in early design phases, considering the assumptions made, and has a runtime 60 times lower than its LNS counterpart, making it a useful tool allowing to study complex geometries over quick design iterations, if accurate results are still obtained in case the background flow profiles are attained via other 1D flow analyses.

6.2 Conclusion

In this report, the extent to which the Linearized Navier-Stokes (LNS) solver can be used to model the acoustic eigenmodes in a LOX/CH_4 rocket engine for future high-frequency combustion instability prediction analyses, was examined. The research work was conducted at the Space Propulsion Institute of the DLR (German Aerospace Center) as part of a Master's thesis at the Aerospace Engineering faculty of the Delft University of Technology. From DLR, the use of the finite element analysis software COMSOL was required, and their LUMEN (Liquid Upper-stage Demonstrator Engine) methalox engine was used as a test case for which the analyses were validated. From the surveyed literature, a knowledge gap was discovered regarding the need for a numerical framework to accurately predict the onset of thermoacoustic instabilities in liquid rocket engines. Following a thorough review of the literature about numerical methods to predict thermoacoustic combustion instabilities, three parameters driving the accurate prediction of the instabilities were identified. These were the frequency and the damping rate of the modes of the considered instabilities, and how the feedback between the heat release rate of the flames and the acoustic field is modeled. Based on the lack of data about broad ranges of eigenmode predictions, and the time requirement imposed by the Master's thesis, it was decided to contribute towards closing the identified knowledge gap by validating a computationally efficient Acoustic-based method for the modeling of acoustic modes inside a rocket combustor, to address the prediction accuracy of acoustic eigenfrequencies and damping rates. Regarding Acoustic-based prediction methods, from a study conducted by the author, preceding the research work here discussed, COMSOL's LNS solver was found to not only be more stable than its Linearized Euler Equations (LEE) counterpart but also able to account for viscous effects; having the potential of returning more accurate frequency and damping rate results. Hence, based on this experience and since at the moment of writing no LNS applications were found for combustion instability studies in liquid rocket engines, it was decided to investigate the LNS solver in the current research work.

The research aimed to determine whether the LNS solver could return physical results for the acoustic mode shapes within a cryogenic rocket combustion chamber under nominal operating conditions and if the associated eigenfrequencies of these modes could be predicted with sub-5% error (comparable to the error achieved by literature's state-of-the-art Acoustic-based methods aimed at predicting combustion instabilities). Furthermore, the effect on the estimated frequencies of accounting for the background flow in the acoustic simulations was evaluated through three approaches. Firstly, by using constant CEA (Chemical Equilibrium with Applications) properties, secondly, by using one-dimensional (1D) profiles obtained by radially averaging a three-dimensional (3D) CFD field describing the flow inside the chamber, and, thirdly, by mapping the latter CFD results to the acoustic mesh used in the simulations. While for low-amplitude instabilities the natural frequencies correspond to the frequencies of the unstable modes, the damping rate of the combustor during an instability is driven by the feedback of the flame forcing. Due to the fact of omitting such flame feedback in this research work, conversely to the eigenfrequencies, no aimed accuracy was targeted for LNS' damping rate predictions. Instead, an additional objective of this research was to assess how accurately the natural damping rates predicted by the LNS analysis, in the absence of the flame feedback, are to the ones of the real system. To validate the results, two hot-fire runs of LUMEN were analyzed for which data from three dynamic pressure sensors were made available by DLR.

Given the lack of literature regarding LNS simulations applied to complex propulsive systems such as the LUMEN demonstrator rocket engine, to answer the research aims, a modeling strategy based on gradually increasing the complexity of the problem to be solved was employed. For this, to verify the more complex simulations, use of the analytical solution of the wave equation for a cylindrical geometry was used together with the established Helmholtz solver in COMSOL. Besides benchmarking LNS against other numerical approaches, the modeling of the background flow in the chamber was also gradually modified. Firstly, constant CEA properties in the combustion chamber were used for the analytical solution of the wave equation and the Helmholtz solver. Secondly, 1D flow profiles were imposed as input for a renewed

version of the analytical equation and Helmholtz analysis, and the LNS simulation. Such profiles were radially averaged from the results of a CFD analysis of LUMEN's chamber, a CFD simulation of its LOX injector, and by using a 1D compressible flow description of its CH_4 injector. Lastly, the detailed CFD simulation of LUMEN was mapped in 3D to the acoustic mesh of the LNS simulation.

Based on the analyses conducted for a number of acoustic eigenmodes and the validation with two LUMEN hot-fire test runs, three main outcomes of the research activities can be outlined. Firstly, for LOX/Hydrocarbon rocket engines, depending on how the distribution of the flow field inside the combustion chamber is modeled, vastly different eigenfrequency results are obtained. The analysis showed that assuming chemical equilibrium in the whole chamber leads to more than 50% errors in the eigenfrequencies, thus requiring accounting for variation in the acoustic properties across the combustion chamber. Secondly, different modeling requirements could be distinguished based on whether an accurate estimation of the eigenfrequencies or the damping rates was sought. With respect to the mesh size, frequency results were found to converge faster than damping rate ones. Furthermore, although the frequency accuracies improved by going from a radially averaged background flow description to a detailed 3D one, the same can not be said for the damping rates, which, due to not accounting for the injector domes in the latter simulation, had higher errors. Hence, besides requiring a finer mesh than the frequencies, including the effect of the injector domes is also necessary for improving the accuracy of the damping rates. Additionally, given that the flame response can act as a forcing term for the acoustics, future studies shall investigate whether the accuracy of the damping rate results from literature can be improved by using an LNS solver with a Flame Transfer Function as the source term.

Lastly, choosing which method is best depends on the requirements of the modeling capabilities, since all of the models tested have their advantages and disadvantages based on their modeling complexity. If the primary goal of the analysis is to predict only the resonance frequency of given modes of a rocket engine, then the use of the analytical solution of the convective wave equation corrected for speed of sound variations in the chamber can be sufficient. Of the methods tested, this one was the most computationally efficient if a steady-state CFD solution of the chamber or literature about the necessary correction factors are available. With an average frequency error of 11.4% and the minimal computational resources it requires for its almost instant results, this method could represent the best modeling approach for an engine that is early in the development phase and will likely undergo several design iterations, if the risk of injection-coupled instabilities is to be assessed. Conversely, if a reliable and accurate combustion stability prediction shall be performed for an engine, the most accurate numerical approach was found to be LNS using a detailed 3D background flow description as input. Albeit being the most computationally expensive method in this report, its frequency accuracy is on average three times higher than the one of LNS using the current state-of-the-art standard for the background flow description. The LNS simulation with a detailed 3D background flow description led to an average frequency error of 4.7%, achieving the most accurate eigenfrequency results ever published for a methalox engine, in addition to returning a more representative distribution of the velocity fluctuations when compared to the current state-of-the-art Acoustic-based methods investigated in the literature.

References

[1] Deutsches Zentrum für Luft- und Raumfahrt e.V. "DLR Lampoldshausen." (), [Online]. Available: https://www.dlr.de/content/en/articles/sites/lampholdshausen/about-lampoldhausen.html.

[2] G. P. Sutton and O. Biblarz, *Rocket propulsion elements*. John Wiley & Sons, 2016.

[3] D. K. Huzel and D. H. Huang, "Modern engineering for design of liquid-propellant rocket engines (revised and enlarged edition)," *Progress in astronautics and aeronautics*, vol. 147, 1992.

[4] B.T.C. Zandbergen, *Thermal Rocket Propulsion (version 2.08)*. Delft: Delft University of Technology - Faculty of Aerospace Engineering, 2020.

[5] J. S. Hardi, M. Oschwald, and B. Dally, "Acoustic characterisation of a rectangular rocket combustor with liquid oxygen and hydrogen propellants," *Proceedings of the Institution of Mechanical Engineers, Part G: Journal of Aerospace Engineering*, vol. 227, no. 3, pp. 436–446, 2013.

[6] W. Armbruster, J. S. Hardi, Y. Miene, D. Suslov, and M. Oschwald, "Damping device to reduce the risk of injection-coupled combustion instabilities in liquid propellant rocket engines," *Acta Astronautica*, vol. 169, pp. 170–179, 2020.

[7] V. Young, *Liquid rocket engine combustion instability*. AIAA, 1995, vol. 169.

[8] D. T. Harrje and F. H. Reardon, *Liquid propellant rocket combustion instability*. Scientific, Technical Information Office, National Aeronautics, and Space …, 1972, vol. 1.

[9] D. Watanabe, H. Manako, and K. Ikeda, "Combustion Stability Improvement of LE-9 Engine for Booster Stage of H3 Launch Vehicle TADAOKI ONGA *2 TAKASHI TAMURA *2," Tech. Rep. 4, 2016.

[10] H. Asakawa *et al.*, "The Status of the Research and Development of LNG Rocket Engines in Japan," in *Springer Aerospace Technology*, Springer Nature, 2017, pp. 463–487. DOI: 10.1007/978-3-319-27748-6{_}19.

[11] T. Poinsot, "Prediction and control of combustion instabilities in real engines," *Proceedings of the Combustion Institute*, vol. 36, no. 1, pp. 1–28, 2017.

[12] J. Martin, W. Armbruster, J. S. Hardi, D. Suslov, and M. Oschwald, "Experimental investigation of self-excited combustion instabilities in a LOX/LNG rocket combustor," *Journal of Propulsion and Power*, vol. 37, no. 6, pp. 944–951, 2021, ISSN: 15333876. DOI: 10.2514/1.B38289.

[13] F. Zhuang *et al.*, "At A A Liquid Rocket Combustion Instability Analysis Methodology-Methods and Representative Examples LIQUID ROCKET COMBUSTION INSTABILITY ANALYSIS METHODOLOGY-METHODS AND REPRESENTATIVE EXAMPLES," Tech. Rep.

[14] Y. Wang, C. H. Sohn, J. Bae, and Y. Yoon, "Prediction of combustion instability by combining transfer functions in a model rocket combustor," *Aerospace Science and Technology*, vol. 119, Dec. 2021, ISSN: 12709638. DOI: 10.1016/j.ast.2021.107202.

[15] S. Clark. "Blue Origin encounters setback in BE-4 engine testing." Accessed: 28-06-2022. (), [Online]. Available: %7Bhttps://spaceflightnow.com/2017/05/15/blue-origin-encounters-setback-in-be-4-engine-testing/%7D.

[16] A. Young, *The Saturn V F-1 engine: powering Apollo into history*. Springer Science & Business Media, 2008.

[17] S. K. Beinke, "Analyses of flame response to acoustic forcing in a rocket combustor," Ph.D. dissertation, 2017.

[18] J. C. Oefelein and V. Yang, "Comprehensive review of liquid-propellant combustion instabilities in f-1 engines," *Journal of Propulsion and Power*, vol. 9, no. 5, pp. 657–677, 1993.

[19] heroicrelics.org. "F-1 ENGINE INJECTOR BAFFLES." (), [Online]. Available: http://heroicrelics.org/info/f-1/f-1-injector-baffles.html.

[20] NOVA. "Combustion Instability [Video]. YouTube." 02-02-2022. (), [Online]. Available: https://www.youtube.com/watch?v=DjWiuMIGVEs.

[21] J. S. Hardi *et al.*, "High frequency combustion instabilities in liquid propellant rocket engines: Research programme at dlr lampoldshausen," in *Proc. Int. Symp. Thermoacoustic Instab. Ind. meets Acad*, 2016, pp. 1–11.

[22] R. Kaess, S. Koeglmeier, R. Behr, J.-P. Rocchi, C. Cruz, and O. Knab, "Liquid propellant rocket combustion stability evaluation using singe flame calculations for combustion dynamics," Tech. Rep.

[23] M. L. Dranovsky, *Combustion instabilities in liquid rocket engines: testing and development practices in Russia*. American Institute of Aeronautics and Astronautics, 2007.

[24] S. Webster, "Analysis of pressure dynamics, forced excitation and damping in a high pressure lox/h2 comustor," Ph.D. dissertation, RWTH Aachen, 2016.

[25] F. Culick and P. Kuentzmann, "Unsteady motions in combustion chambers for propulsion systems," NATO Research and Technology Organization Neuilly-Sur-Seine (France), Tech. Rep., 2006.

[26] J. O'Connor, V. Acharya, and T. Lieuwen, "Transverse combustion instabilities: Acoustic, fluid mechanic, and flame processes," *Progress in Energy and Combustion Science*, vol. 49, pp. 1–39, 2015.

[27] Y. Mery, S. Ducruix, P. Scouflaire, and S. Candel, *Injection coupling with high amplitude transverse modes: Experimentation and simulation*, Jun. 2009. DOI: 10.1016/j.crme.2009.06.009.

[28] Y. Méry, L. Hakim, P. Scouflaire, L. Vingert, S. Ducruix, and S. Candel, *Experimental investigation of cryogenic flame dynamics under transverse acoustic modulations*, Jan. 2013. DOI: 10.1016/j.crme.2012.10.013.

[29] M. Schulze and T. Sattelmayer, "A comparison of time and frequency domain descriptions of high frequency acoustics in rocket engines with focus on dome coupling," *Aerospace Science and Technology*, vol. 45, pp. 165–173, Sep. 2015, ISSN: 12709638. DOI: 10.1016/j.ast.2015.05.007.

[30] A. Chemnitz and T. Sattelmayer, "Calculation of the Thermoacoustic Stability of a Main Stage Thrust Chamber Demonstrator," in *Notes on Numerical Fluid Mechanics and Multidisciplinary Design*, vol. 146, Springer Science and Business Media Deutschland GmbH, 2021, pp. 235–247. DOI: 10.1007/978-3-030-53847-7{_}15.

[31] M. Schulze, T. Hummel, N. Klarmann, F. Berger, B. Schuermans, and T. Sattelmayer, "Linearized euler equations for the prediction of linear high-frequency stability in gas turbine combustors," in *Turbo Expo: Power for Land, Sea, and Air*, American Society of Mechanical Engineers, vol. 49767, 2016, V04BT04A045.

[32] M. Schulze, M. Schmid, D. Morgenweck, S. Köglmeier, and T. Sattelmayer, "A conceptional approach for the prediction of thermoacoustic stability in rocket engines," in *49th AIAA/ASME/SAE/ASEE Joint PropulsionConference*, 2013, p. 3779.

[33] L. Selle, R. Blouquin, M. Théron, L. H. Dorey, M. Schmid, and W. Anderson, "Prediction and analysis of combustion instabilities in a model rocket engine," *Journal of Propulsion and Power*, vol. 30, no. 4, pp. 978–990, 2014, ISSN: 15333876. DOI: 10.2514/1.B35146.

[34] G. M. R. Tamanampudi, S. Sardeshmukh, W. Anderson, and C. Huang, "Combustion instability modeling using multi-mode flame transfer functions and a nonlinear Euler solver," *International Journal of Spray and Combustion Dynamics*, vol. 12, 2020, ISSN: 17568285. DOI: 10.1177/1756827720950320.

[35] T. Poinsot and D. Veynante, *Theoretical and numerical combustion*. RT Edwards, Inc., 2005.

[36] D. C. Giancoli, *Physics for scientists & engineers with modern physics*. Pearson, 2014.

[37] G. Heilmann and T. Sattelmayer, "On the convective wave equation for the investigation of combustor stability using FEM-methods," *International Journal of Spray and Combustion Dynamics*, p. 175 682 772 210 844, Mar. 2022, ISSN: 1756-8277. DOI: 10.1177/17568277221084470.

[38] J. W. S. B. Rayleigh, *The theory of sound*. Macmillan & Company, 1896, vol. 2.

[39] J. Martin, W. Armbruster, J. S. Hardi, D. Suslov, and M. Oschwald, "Experimental investigation of self-excited combustion instabilities in a lox/lng rocket combustor," *Journal of Propulsion and Power*, vol. 37, no. 6, pp. 944–951, 2021.

[40] T. C. Lieuwen, *Unsteady combustor physics*. Cambridge University Press, 2021.

[41] J. Delfs, "Grundlagen der aeroakustik (basics of aeroacoustics)," *Technische Universität Braunschweig, Braunschweig*, 2014.

[42] S. Glegg and W. Devenport, *Aeroacoustics of low Mach number flows: fundamentals, analysis, and measurement*. Academic Press, 2017.

[43] M. Schulze and T. Sattelmayer, "Linear stability assessment of a cryogenic rocket engine," *International Journal of Spray and Combustion Dynamics*, vol. 9, no. 4, pp. 277–298, Dec. 2017, ISSN: 17568285. DOI: 10.1177/1756827717695281.

[44] J. Hardi *et al.*, "Lumen thrust chamber-injector performance and stability," in *Space Propulsion Conference 2020*, vol. 1, 2020.

[45] Aerojet Rocketdyne. "RS-25 ENGINE." (), [Online]. Available: https://www.rocket.com/space/liquid-engines/rs-25-engine.

[46] Spaceflight101. "SpaceX Raptor." (), [Online]. Available: https://spaceflight101.com/spx/spacex-raptor/.

[47] F. Marble and S. Candel, "Acoustic disturbance from gas non-uniformities convected through a nozzle," *Journal of sound and vibration*, vol. 55, no. 2, pp. 225–243, 1977.

[48] J. Portillo, J. Sisco, Y. Yu, V. Sankaran, and W. Anderson, "Application of a generalized instability model to a longitudinal mode combustion instability," in *43rd AIAA/ASME/SAE/ASEE Joint Propulsion Conference & Exhibit*, 2007, p. 5651.

[49] H. Krediet, W. Krebs, J. E. Portillo, and J. Kok, "Prediction of thermoacoustic limit cycles during premixed combustion using the modified galerkin approach," in *46th AIAA/ASME/SAE/ASEE Joint Propulsion Conference & Exhibit*, 2010, p. 7150.

[50] A. H. Nayfeh and D. T. Mook, *Nonlinear oscillations*. John Wiley & Sons, 2008.

[51] P. Doak, "Fundamentals of aerodynamic sound theory and flow duct acoustics," *Journal of Sound and Vibration*, vol. 28, no. 3, pp. 527–561, 1973.

[52] A. D. Pierce, *Acoustics: an introduction to its physical principles and applications*. Springer, 2019.

[53] H. Tsien, "The transfer functions of rocket nozzles," *Journal of the American Rocket Society*, vol. 22, no. 3, pp. 139–143, 1952.

[54] L. Crocco, R. Monti, and J. Grey, "Verification of nozzle admittance theory by direct measurement of the admittance parameter," *ARS Journal*, vol. 31, no. 6, pp. 771–775, 1961.

[55] L. Crocco and W. A. Sirignano, "Behavior of supercritical nozzles under three-dimensional oscillatory conditions," ADVISORY GROUP FOR AEROSPACE RESEARCH and DEVELOPMENT NEUILLY-SUR-SEINE (FRANCE), Tech. Rep., 1967.

[56] W. Bell, B. Daniel, and B. Zinn, "Experimental and theoretical determination of the admittances of a family of nozzles subjected to axial instabilities," *Journal of Sound and Vibration*, vol. 30, no. 2, pp. 179–190, 1973.

[57] S. Candel, "Acoustic conservation principles and an application to plane and modal propagation in nozzles and diffusers," *Journal of Sound and Vibration*, vol. 41, no. 2, pp. 207–232, 1975.

[58] F. Vuillot, "Acoustic mode determination in solid rocket motor stability analysis," *Journal of Propulsion and Power*, vol. 3, no. 4, pp. 381–384, 1987.

[59] I. 10534-1, *Acoustics — determination of sound absorption coefficient and impedance in impedance tubes — part 1: Method using standing wave ratio*, 1996.

[60] I. 10534-2, *Acoustics—determination of sound absorption coefficient and impedance in impedance tubes—part 2: Transfer-function method*, 1998.

[61] L. Trotta, "AE4020 Literature Study, Numerical modeling of the acoustic eigenmodes of a LOX/CH4 rocket combustion chamber via CAA solvers," Delft University of Technology, Tech. Rep., 2022.

[62] S. Gröning, "Untersuchung selbsterregter verbrennungsinstabilitäten in einer raketenbrennkammer," Ph.D. dissertation, RWTH Aachen, 2017.

[63] B. Ivancic and W. Mayer, "Time-and length scales of combustion in liquid rocket thrust chambers," *Journal of propulsion and power*, vol. 18, no. 2, pp. 247–253, 2002.

[64] R. Kaess, S. Koeglmeier, R. Behr, B. Kniesner, and T. Sattelmayer, "5 TH EUROPEAN CONFERENCE FOR AEROSPACE SCIENCES (EUCASS 2013) Impact of Axial Gradients on Combustion Chamber Acoustics," Tech. Rep.

[65] J. Peiringer, T. Sattelmayer, and F. Fassl, "Simulation of combustion instabilities in liquid rocket engines with acoustic perturbation equations," *Journal of Propulsion and Power*, vol. 25, no. 5, pp. 1020–1031, 2009, ISSN: 15333876. DOI: 10.2514/1.38782.

[66] T. Hofmeister, T. Hummel, and T. Sattelmayer, "Impact of the stabilized finite element method on acoustic and vortical perturbations in thermoacoustic systems," *Journal of Engineering for Gas Turbines and Power*, vol. 143, no. 6, Jun. 2021, ISSN: 15288919. DOI: 10.1115/1.4049349.

[67] G. Jourdain and L. Eriksson, "Combustor stability analysis based on linearized flow solvers and arnoldi-based eigenmode extraction techniques," in *16th AIAA/CEAS Aeroacoustics Conference*, 2010, p. 3866.

[68] J.-F. Parmentier, P. Salas, P. Wolf, G. Staffelbach, F. Nicoud, and T. Poinsot, "A simple analytical model to study and control azimuthal instabilities in annular combustion chambers," *Combustion and Flame*, vol. 159, no. 7, pp. 2374–2387, 2012.

[69] T. Emmert, S. Jaensch, C. Sovardi, and W. Polifke, "Tax—a flexible tool for low-order duct acoustic simulation in time and frequency domain," in *Forum Acusticum, Krakow, Poland, Sept*, 2014, pp. 7–12.

[70] S. D'Alessandro, B. Favini, and F. Nasuti, "A low order modeling approach to transverse combustion instability," in *AIAA Propulsion and Energy 2019 Forum*, 2019, p. 4374.

[71] M. Son, W. Armbruster, F. Tonti, and J. Hardi, "Numerical study of acoustic resonance in a LOX injector induced by orifice flow," in *AIAA Propulsion and Energy Forum, 2021*, American Institute of Aeronautics and Astronautics Inc, AIAA, 2021, ISBN: 9781624106118. DOI: 10.2514/6.2021-3568.

[72] T. Emmert and W. Polifke. “Low Order Modeling of Thermoacoustic Systems.” 05-08-2022. (), [Online]. Available: https://www.epc.ed.tum.de/tfd/forschung/low-order-modeling-of-thermoacoustic-systems/.

[73] N. Noiray, D. Durox, T. Schuller, and S. Candel, “A unified framework for nonlinear combustion instability analysis based on the flame describing function,” *Journal of Fluid Mechanics*, vol. 615, pp. 139–167, 2008.

[74] A. Cuquel, D. Durox, and T. Schuller, “Impact of flame base dynamics on the non-linear frequency response of conical flames,” *Comptes Rendus Mécanique*, vol. 341, no. 1-2, pp. 171–180, 2013.

[75] S. Candel, D. Durox, S. Ducruix, A.-L. Birbaud, N. Noiray, and T. Schuller, “Flame dynamics and combustion noise: Progress and challenges,” *International Journal of Aeroacoustics*, vol. 8, no. 1, pp. 1–56, 2009.

[76] K. Kedia, H. Altay, and A. Ghoniem, “Impact of flame-wall interaction on premixed flame dynamics and transfer function characteristics,” *Proceedings of the Combustion Institute*, vol. 33, no. 1, pp. 1113–1120, 2011.

[77] J. Hardi *et al.*, “Lumen thrust chamber-injector design and stability analysis,” in *32nd International Symposium on Space Technology and Science*, 2019.

[78] G. Heilmann, C. Hirsch, and T. Sattelmayer, “Energetically consistent computation of combustor stability with a model consisting of a helmholtz finite element method domain and a low-order network,” *Journal of Engineering for Gas Turbines and Power*, vol. 143, no. 5, May 2021, ISSN: 15288919. DOI: 10.1115/1.4050024.

[79] S. Camporeale, A. Forte, B. Fortunato, M. Mastrovito, and A. Ferrante, “Numerical simulation of the acoustic pressure field in an annular combustion chamber with helmholtz resonators,” in *Turbo Expo: Power for Land, Sea, and Air*, vol. 41669, 2004, pp. 713–724.

[80] A. Innocenti, A. Andreini, and B. Facchini, “Numerical identification of a premixed flame transfer function and stability analysis of a lean burn combustor,” *Energy Procedia*, vol. 82, pp. 358–365, 2015.

[81] J. R. Hulka and G. W. Jones, “Performance and stability analyses of rocket thrust chambers with oxygen/methane propellants,” in *46th AIAA/ASME/SAE/ASEE Joint Propulsion Conference*, 2010.

[82] T. Hofmeister, T. Hummel, F. Berger, N. Klarmann, and T. Sattelmayer, “Elimination of Numerical Damping in the Stability Analysis of Noncompact Thermoacoustic Systems with Linearized Euler Equations,” *Journal of Engineering for Gas Turbines and Power*, vol. 143, no. 3, Mar. 2021, ISSN: 15288919. DOI: 10.1115/1.4049651.

[83] R. Kaess, S. Koeglmeier, M. Schmid, and T. Sattelmayer, “Linearized euler calculation of acoustics of a rocket combustion chamber,” in *2nd REST Modeling Workshop*, 2010.

[84] R. Kaess, S. Koeglmeier, T. Sattelmayer, M. Schulze, M. Oschwald, and J. Hardi, “SP2016_3124816 HF Combustion Stability-Research Activities in Germany,” Tech. Rep.

[85] A. B. S. Chemnitz, “Analysis and improvement of rocket engine combustion stability simulations,” Ph.D. dissertation, Technische Universität München, 2022.

[86] L. Crocco and S.-I. Cheng, “Theory of combustion instability in liquid propellant rocket motors,” Princeton Univ Nj, Tech. Rep., 1956.

[87] K. Kobayashi, Y. Daimon, N. Iizuka, H. Tamura, T. Mitani, and T. Onodera, “Studies on Combustion Instability for Liquid Propellant Rocket Engines,” Tech. Rep., 2011.

[88] J. J. Hutt and M. Rocker, “High-frequency injection-coupled combustion instability,” *Progress in Astronautics and Aeronautics*, vol. 169, pp. 345–356, 1995.

[89] M. S. Natanzon, *Combustion instability*. American Institute of Aeronautics and Astronautics, 2008.

[90] R. Jensen, H. Dodson, and S. Claflin, "Lox/hydrocarbon combustion instability investigation," Tech. Rep., 1989.

[91] J. S. Hardi, "Experimental investigation of high frequency combustion instability in cryogenic oxygen-hydrogen rocket engines.," Ph.D. dissertation, 2012.

[92] L. Trotta, "Numerical Investigation of COMSOL's Aeroacoustic Solvers for the Analysis of Thermoacoustic Combustion Instabilities in Cryogenic Bi-propellant Rocket Combustors," Deutsches Zentrum für Luft- und Raumfahrt e.V., Tech. Rep., 2022.

[93] A. Urbano *et al.*, "Exploration of combustion instability triggering using Large Eddy Simulation of a multiple injector liquid rocket engine," *Combustion and Flame*, vol. 169, pp. 129–140, Jul. 2016, ISSN: 15562921. DOI: 10.1016/j.combustflame.2016.03.020.

[94] G. Kangkang, X. Boqi, R. Yongjie, T. Yiheng, and N. Wansheng, "Three-Dimensional Numerical Analysis of Longitudinal Thermoacoustic Instability in a Single-Element Rocket Combustor," *Frontiers in Energy Research*, vol. 10, Feb. 2022, ISSN: 2296598X. DOI: 10.3389/fenrg.2022.835977.

[95] V. R. Hasti and R. Ranjan, "Computational study of longitudinal combustion instability in a high-pressure combustor," in *AIAA Science and Technology Forum and Exposition, AIAA SciTech Forum 2022*, American Institute of Aeronautics and Astronautics Inc, AIAA, 2022, ISBN: 9781624106316. DOI: 10.2514/6.2022-2087.

[96] S. Srinivasan, R. Ranjan, and S. Menon, "Flame dynamics during combustion instability in a high-pressure, shear-coaxial injector combustor," *Flow, Turbulence and Combustion*, vol. 94, no. 1, pp. 237–262, 2015.

[97] R. Kaess, J. Braun, and R. Behr, "Calculation of hf eigenmodes in liquid rocket combustion chambers,"

[98] A. Chemnitz and T. Sattelmayer, "Influence of radial stratification on eigenfrequency computations in rocket combustion chambers," *8th EUCASS*, 2019.

[99] T. Hofmeister, T. Hummel, B. Schuermans, and T. Sattelmayer, "Modeling and Quantification of Acoustic Damping Induced by Vortex Shedding in Noncompact Thermoacoustic Systems," *Journal of Engineering for Gas Turbines and Power*, vol. 142, no. 3, Mar. 2020, ISSN: 15288919. DOI: 10.1115/1.4044936.

[100] J. C. Deeken, G. Waxenegger-Wilfing, M. Oschwald, and S. Schlechtriem, "Lumen demonstrator-project overview," 2021.

[101] J. Deeken. "Technology demonstrator for the development of innovative engine concepts." (), [Online]. Available: https://event.dlr.de/en/ila2022/lumen/#:~:text=Video$%5C%$20Player-,00$%5C%$3A00,-01$%5C%$3A40.

[102] D. T. Banuti, V. Hannemann, K. Hannemann, and B. Weigand, "An efficient multi-fluid-mixing model for real gas reacting flows in liquid propellant rocket engines," *Combustion and Flame*, vol. 168, pp. 98–112, 2016.

[103] N. Perakis *et al.*, "Qualitative and quantitative comparison of rans simulation results for a 7-element gox/gch4 rocket combustor," in *2018 Joint Propulsion Conference*, 2018, p. 4556.

[104] RP Software+Engineering UG. "Rocket Propulsion Analysis Version 2.3." (), [Online]. Available: http://www.rocket-propulsion.com/downloads/2/docs/RPA_2_User_Manual.pdf.

[105] I. H. Bell, J. Wronski, S. Quoilin, and V. Lemort, "Pure and pseudo-pure fluid thermophysical property evaluation and the open-source thermophysical property library coolprop," *Industrial & Engineering Chemistry Research*, vol. 53, no. 6, pp. 2498–2508, 2014. DOI: 10.1021/ie4033999. eprint: http://pubs.acs.org/doi/pdf/10.1021/ie4033999. [Online]. Available: http://pubs.acs.org/doi/abs/10.1021/ie4033999.

[106] R. Kaess, S. Koeglmeier, M. Schmid, and T. Sattelmayer, "Linearized Euler Calculation of Acoustics of a Rocket Combustion Chamber," Tech. Rep. 1.

[107] R. Kaess, S. Koeglmeier, R. Behr, B. Kniesner, and T. Sattelmayer, "Impact of axial gradients on combustion chamber acoustics," in *5th European Conference for Aerospace Sciences (EUCASS)*, 2013.

[108] E. M. Greitzer, C. S. Tan, and M. B. Graf, *Internal flow: concepts and applications*. Cambridge University Press, 2007, vol. 3.

[109] X. Fang, Y. Xu, and Z. Zhou, "New correlations of single-phase friction factor for turbulent pipe flow and evaluation of existing single-phase friction factor correlations," *Nuclear Engineering and Design*, vol. 241, no. 3, pp. 897–902, 2011.

[110] Hydraulic Institute (Cleveland), *Engineering Data Book*. Hydraulic Institute, 1990.

[111] L. Hernandez *et al.*, "The effect of surface roughness on lch4 boiling heat transfer performance of conventionally and additively manufactured rocket engine regenerative cooling channels," in *AIAA Propulsion and Energy 2019 Forum*, 2019, p. 4363.

[112] D. Cheng, X. Fan, and M. Yang, "Quasi-1d compressible flow of hydrocarbon fuel," in *48th AIAA/ASME/SAE/ASEE Joint Propulsion Conference & Exhibit*, 2012, p. 4090.

[113] COMSOL Multiphysics, "Acoustics module user's guide version 6.0," *User's manual*, 2021.

[114] J. Donea and A. Huerta, *Finite element methods for flow problems*. John Wiley & Sons, 2003.

[115] COMSOL Multiphysics, "Acoustics Module User's Guide Version 5.6," *User's manual*, 2020.

[116] P. L. Losco, L. d'Agostino, and F. Paganucci, "Analysis of the first tangential mode in a cylindrical rocket engine combustion chamber equipped with an absorber," Master's thesis, Universitá Degli Studi di Pisa, Pisa, Tech. Rep., 2015.

[117] M. Casiano, "Extracting damping ratio from dynamic data and numerical solutions," National Aeronautics and Space Administration (NASA), Tech. Rep., 2016.

[118] M. Schulze, "Linear stability assessment of cryogenic rocket engines," Ph.D. dissertation, Technische Universitöt München, 2016.

[119] J. J. Lissauer and I. De Pater, *Fundamental planetary science: physics, chemistry and habitability*. Cambridge University Press, 2013.

[120] W. Armbruster, J. S. Hardi, D. Suslov, and M. Oschwald, "Injector-driven flame dynamics in a high-pressure multi-element oxygen–hydrogen rocket thrust chamber," *Journal of propulsion and power*, vol. 35, no. 3, pp. 632–644, 2019.

[121] A. Urbano *et al.*, "Exploration of combustion instability triggering using Large Eddy Simulation of a multiple injector Liquid Rocket Engine," Tech. Rep.

[122] M. Börner, J. Martin, J. Hardi, D. Suslov, J. C. Deeken, and M. Oschwald, "Lumen thrust chamber-flame anchoring for shear coaxial injectors," 2021.

[123] R. Ewert and W. Schröder, "Acoustic perturbation equations based on flow decomposition via source filtering," *Journal of Computational Physics*, vol. 188, no. 2, pp. 365–398, 2003.

[124] C. O. Zienkiewicz, L. R. Taylore, and P. Nithiarasu, *The Finite Element Method for Fluid Dynamics*. Butterworth-Heinemann publications, 2014.

[125] J. Gikadi, "Prediction of acoustic modes in combustors using linearized navier-stokes equations in frequency space," Ph.D. dissertation, Technische Universität München, 2014.

[126] T. Hughes and A. Brooks, "A multi-dimensioal upwind scheme with no crosswind diffusion, vol. 34," ASME, 1979.

[127] T. J. Hughes, M. Mallet, and M. Akira, "A new finite element formulation for computational fluid dynamics: Ii. beyond supg," *Computer methods in applied mechanics and engineering*, vol. 54, no. 3, pp. 341–355, 1986.

[128] J. Gikadi, W. C. Ullrich, T. Sattelmayer, and F. Turrini AVIO SpA, “PREDICTION OF THE ACOUSTIC LOSSES OF A SWIRL ATOMIZER NOZZLE UNDER NON-REACTIVE CONDITIONS,” Tech. Rep., 2013. [Online]. Available: `http://www.asme.org/about-asme/terms-of-use`.

[129] T. J. Hughes, L. P. Franca, and G. M. Hulbert, “A new finite element formulation for computational fluid dynamics: Viii. the galerkin/least-squares method for advective-diffusive equations,” *Computer methods in applied mechanics and engineering*, vol. 73, no. 2, pp. 173–189, 1989.

A Description of additional Acoustic-based models

In this appendix, further details are provided on the additional Acoustic-based models that were mentioned in Table 2.2 but not presented in Chapter 2. The following detailed overview was not included in Chapter 2 because the solver described were not applied to the research conducted, and hence their detailed description was deemed out of the scope of the report. Nevertheless, the remaining Acoustic-based models are here described for two reasons. Firstly, even though an expanded version of the information contained in this appendix was included in the literature study preceding this report, for DLR employees, using this report as reference for the LNS study, under an information-management point-of-view, it might be of interest to have all information contained in one single document. Secondly, while researching about Acoustic-based methods, no single go-to publication was found that provided an extensive overview of the latter. Thus, this appendix can also be of help for the readers accessing the public version of this report, wishing to obtain a condensed view of what other Acoustic-based methods are available.

To start, Section A.1 describes the inhomogenous convective Helmholtz equation (iCHE). As a bridge between pressure acoustic (e.g. Helmholtz) and aeroacoustic methods (e.g. LEE and LNS), this is followed by Section A.2, where the Acoustic Perturbation Equations are introduced (APE). Lastly, this appendix is concluded with the Linearized Euler Equations (LEE) in Section A.3.

A.1 Inhomogeneous convective Helmholtz equation (iCHE)

The Helmholtz equation can be further expanded to account for the presence of heat release rate source term, for the influence that a non-uniform background flow would have on the acoustic, and for the interaction of the acoustic with entropy and vortical modes. Doing so leads to the inhomogeneous Convective Helmholtz Equations (iCHE), derived for the first time in recent years by Heilmann & Sattelmayer [37]. The time-domain representation of the iCHE is given in Equation A.1, while its frequency-domain formulation is given in Equation A.2. In these equations, the term $\mathbf{S}_{\mathbf{u}}^{v,s,\nabla p_0=0}$ represents the source term for the entropy and vortical modes, which can be included if the latter is driving for the problem at hand. Furthermore, the left-hand side of Equation A.1 and Equation A.2 represents the wave operator of the homogeneous convective Helmholtz equation for the case where all the source terms, which are found on the right-hand side of Equation A.1 and Equation A.2, are neglected.

$$\frac{\partial^2 p'}{\partial t^2} + 2\mathbf{u_0}\cdot\nabla\frac{\partial p'}{\partial t} + \mathbf{u_0}\cdot\nabla\left(\mathbf{u_0}\cdot\nabla p'\right) - \rho_0 c_0^2\nabla\cdot\left(\frac{1}{\rho_0}\nabla p'\right) = -\gamma\frac{\partial p'}{\partial t}\nabla\cdot\mathbf{u_0} - \mathbf{u_0}\cdot\nabla\left(\gamma p'\nabla\cdot\mathbf{u_0}\right)$$
$$-\gamma p_0(\mathbf{u_0}\cdot\nabla)\left(\nabla\cdot\mathbf{u'}\right) + \gamma p_0\Delta\left(\mathbf{u_0}\cdot\mathbf{u'}\right) - \gamma p_0\nabla\cdot\mathbf{S}_{\mathbf{u}}^{v,s,\nabla p_0=0} + (\gamma-1)\frac{\partial\dot{q}'}{\partial t} + (\gamma-1)\mathbf{u_0}\cdot\nabla\dot{q}' \tag{A.1}$$

$$\omega^2\hat{p} - 2\mathrm{i}\omega\mathbf{u_0}\cdot\nabla\hat{p} - \mathbf{u_0}\cdot\nabla(\mathbf{u_0}\cdot\nabla\hat{p}) + \rho_0 c_0^2\nabla\cdot\left(\frac{1}{\rho_0}\nabla\hat{p}\right) = \mathrm{i}\omega\gamma\hat{p}\nabla\cdot\mathbf{u_0} + \mathbf{u_0}\cdot\nabla(\gamma\hat{p}\nabla\cdot\mathbf{u_0})$$
$$+\gamma p_0(\mathbf{u_0}\cdot\nabla)(\nabla\cdot\hat{u_0}) - \gamma p_0\Delta(\mathbf{u_0}\cdot\hat{\mathbf{u}}) + \gamma p_0\nabla\cdot\hat{\mathbf{S}}_{\mathbf{u}}^{v,s,\nabla p_0=0} - \mathrm{i}\omega(\gamma-1)\hat{\dot{q}} - (\gamma-1)\mathbf{u_0}\cdot\nabla\hat{\dot{q}} \tag{A.2}$$

The iCHE method was for the first time applied in 2022 for predicting the combustion stability of a gas turbine's combustor but has not been validated yet against experimental data [37]. The iCHE was derived to take advantage of the single equation stemming from the wave equation and hence to cut costs while being able to account for source terms and acoustic-flow field interactions. However, a few downsides of

the equation should be mentioned. Firstly, when testing the equation, the authors had to neglect the third and fourth terms on the right-hand side of Equation A.1 and Equation A.2 due to difficulties in closing the equation. The results obtained by the authors for the iCHE with the latter two terms neglected, showed considerable deviation in the obtained damping rates of the acoustic modes when compared to the ones resulting from an APE's simulation (Acoustic Perturbation Equations), showing that these terms do not have a negligible effect on the results. Secondly, difficulties in prescribing the boundary conditions for the velocity oscillations were encountered by the authors, resulting in a null Mach number having to be enforced [37].

A.2 Acoustic Perturbation Equations (APE)

All variations of the Helmholtz equation described in this report, fell under the pressure acoustic approach. Starting with this section, now the most computationally economical of the aeroacoustic approaches are described. The Acoustic Perturbation Equations (APE) were first employed by Pieringer, Sattelmayer & Fassl in 2009 to study the combustion stability of liquid rocket engine [65], despite lacking validation against experimental results. A derivation of these equations can be found in the work of Ewert & Schröder [123], and their time-domain formulation is reported in this report by Equation A.3 for the continuity equation and by Equation A.4 for the momentum equation. The right-hand side of the APE's momentum equation represents the source term due to heat release rate fluctuations from the flame.

$$\frac{\partial \mathbf{u}'}{\partial t} + \nabla \left(\mathbf{u_0} \cdot \mathbf{u}' \right) + \nabla \left(\frac{p'}{\rho_0} \right) = 0 \tag{A.3}$$

$$\frac{\partial p'}{\partial t} + c_0^2 \nabla \cdot \left(\rho_0 u' + \mathbf{u_0} \frac{p'}{c_0^2} \right) = (\gamma - 1)\dot{q}' \tag{A.4}$$

In short, the APE can be derived by taking the LNS equations, assuming inviscid flow, thus obtaining the Linearized Euler Equations (LEE), and then using source filtering to only retain the fluctuations due to the acoustic mode [123]. As for the previous cases, the frequency-domain formulation of the APE can also be obtained by assuming harmonical oscillations and is given by Equation A.5 and Equation A.6.

$$i\omega \hat{\mathbf{u}} + \nabla \left(\mathbf{u_0} \cdot \hat{\mathbf{u}} \right) + \nabla \left(\frac{\hat{p}}{\rho_0} \right) = 0 \tag{A.5}$$

$$i\omega \hat{p} + c_0^2 \nabla \cdot \left(\rho_0 \hat{\mathbf{u}} + \mathbf{u_0} \frac{\hat{p}}{c_0^2} \right) = (\gamma - 1)\hat{\dot{q}} \tag{A.6}$$

Over the pressure acoustic approaches, the APE shares the same advantage related to the nozzle boundary condition as the rest of the aeroacoustic solvers. Namely, the boundary condition at the sonic throat of the nozzle can automatically be obtained by aeroacoustic solvers if a small section of the supersonic part of the nozzle is still considered (so to make sure that the transition between subsonic and supersonic flow is captured in the problem). Moreover, compared to the rest of the aeroacoustic solvers, the APE is cheaper to compute since it makes use of two equations that neglect the entropy and vortical modes' fluctuations terms.

A.3 Linearized Euler Equations (LEE)

Not applying source filtering during the derivation of the APE leads to the Linearized Euler Equations (LEE), reported in the time-domain below in Equation A.7, Equation A.8 and Equation A.9, with S_c and S_m indicating source terms.

$$\frac{\partial \rho_\mathrm{t}}{\partial t} + \nabla \cdot \left(\rho' \mathbf{u}_0 + \rho_0 \mathbf{u}' \right) = S_\mathrm{c} \tag{A.7}$$

$$\frac{\partial \mathbf{u}'}{\partial t} + \left(\left[\mathbf{u}' + \frac{\rho'}{\rho_0} \mathbf{u}_0 \right] \cdot \nabla \right) \mathbf{u}_0 + (\mathbf{u}_0 \cdot \nabla)\, \mathbf{u}' + \frac{1}{\rho_0} \nabla p' = \mathbf{S}_\mathrm{m} \tag{A.8}$$

$$\frac{\partial p'}{\partial t} + \mathbf{u}' \cdot \nabla p_0 + p' \gamma\, (\nabla \cdot \mathbf{u}_0) + \mathbf{u}_0 \cdot \nabla p' + \gamma p_0 \left(\nabla \cdot \mathbf{u}' \right) = S_\mathrm{e} \tag{A.9}$$

Compared to LNS, the LEE as well as the APE neglect viscous terms, hence not requiring a boundary layer to be refined by the mesh and thus allowing a coarser mesh to be used. In turn, the lack of viscous terms, which leads to the term representing viscous stresses, viscous dissipation, and perturbation of heat conduction being neglected, negatively affects the stability of the solver. When solving fluid simulations with FEM numerical instabilities are known to arise if the method is not stabilized by artificial means [124]. In a previous study conducted at DLR, it was found that due to the lack of ”physical” viscosity, the LEE solver was found to be numerically unstable even when stabilized via a Galerkin Least-Squares (GLS) method, while the LNS, for the same amount of stabilization, was found to be stable [92].

Regarding its applications, in recent years an increased interest in using LEE for rocket stability applications could be seen [29, 30, 33, 43, 64, 83–85], thanks also to the developments made in the field of CFD for combustion applications which allow for a detailed and efficient description of the flame response [22]. Besides rocket propulsion applications, LEE solvers have also been applied for the study of combustion instabilities in gas turbines and cylindrical research combustors with conical flame holders [66, 67, 82, 99].

B Initial simulations for the shorter LUMEN chamber

In the following appendix a brief discussion on the acoustic simulations that were run prior to the ones presented before in this report, is provided. Given the difference the shorter chamber length used during these simulations, validation of the longitudinal modes with experimental data would have led to large errors no representative for the solvers's performance. Furthermore, by comparing the results of the transverse modes of the shorter chamber simulations with the aforementioned ones in the report, it could be observed that the latter led to non-negligible differences. Based on the main difference being the mesh density between these two sets of simulations, and given that from the mesh independence study conducted for the LNS simulation it was seen that a coarser mesh led to a lower predicted frequency, it is concluded that the simulations presented in this appendix are not mesh-independent, and thus make use of a too coarse mesh for accurate predictions. Nevertheless, their results are presented here since they show an interesting behavior of the damping rate with respect to the mesh size, namely that even though the frequency is seen to slightly change with finer meshes, the damping rate can still greatly vary in magnitude.

This appendix is divided into two sections. Firstly, the various "short chamber" simulations are presented in Section B.1, where mainly the geometrical models simulated are discussed and their meshes, since the boundary conditions and solver settings are the same as the ones used by previous simulations. Secondly, and lastly, the results of the short chamber simulations are presented in Section B.2 together with a brief discussion of the results.

B.1 Set of short chamber simulations

The first simulation presented, named for simplicity as the "Helmholtz without injectors" run, as the name suggests, is a Helmholtz simulation of the LUMEN chamber without the presence of any injector elements. Its mesh was set up using maximum element sizes set to 20 mesh elements per maximum wavelength expected to be solved, as given by Equation B.1. Here, $n_{elements}$ refers to the number of elements per wavelength, while c is the reference speed of sound and f_{max} is the maximum frequency expected to be solved. For the analyses described in this appendix, the latter was set to 10 [kHz]. The 20 elements per maximum wavelength are based on the suggested settings from the COMSOL user manual for the acoustic library. This number of elements is suggested to be used if a linear discretization is employed, while the use of 10 elements per wavelength is suggested if a second-order discretization is applied [113]. The resulting mesh, made up of $3.65 \cdot 10^5$ elements, for the Helmholtz run without injectors is shown in Figure B.1a. For the boundary conditions for this test-run, acoustically closed conditions were set on all faces of the domain, meaning at the nozzle outlet and faceplate as well.

$$h_{max} = \frac{n_{elements} \cdot c}{f_{max}} \tag{B.1}$$

Following a similar approach, the next simulation increased the modelling complexity by accounting for the presence of the injector elements. The geometry considered for this was the one used for the CFD analysis of LUMEN, which was shown in Figure 3.5a, and using the constant CEA properties from Table 4.2 Table 4.3 for the background flow description. For the mesh of this simulation, denoted as the *Helmholtz CFD geometry CEA* run, 20 elements per maximum wavelength were still used in the chamber, while 50 and 60 elements were used for the Methane and LOX injectors, respectively. For the injectors, their respective CEA speed of sound was used to retrieve the maximum mesh element size to be described.

The resulting mesh is shown in Figure B.1b, which is composed of $6.70 \cdot 10^5$ elements. For the acoustic boundary conditions, the nozzle outlet was kept closed, while the inlet of the modeled injector elements was set to be open.

(a) Mesh of the Helmholtz run without injectors of the (short) LUMEN chamber using constant CEA properties

(b) Mesh of the Helmholtz run using the LUMEN combustor CFD geometry using constant CEA properties

Figure B.1: Meshes of the Helmholtz runs for the short chamber geometry using constant CEA properties for the combustor only (a) and for the LUMEN CFD geometry

For the next modelling step, an additional Helmholtz simulation was run using constant CEA properties in the chamber (as for the previously introduced one) including for the whole LUMEN injector elements and domes, as done in Chapter 4. The same boundary conditions as used for the Helmholtz runs of Chapter 4 were also used for this step. Given the larger computational domain, for the Helmholtz simulation using constant CEA properties and modelling the whole LUMEN geometry (referred to as the *Helmholtz full-geometry CEA* simulation), 20 mesh elements per maximum wavelength were used everywhere to save on computational resources, with its mesh of $8.41 \cdot 10^5$ elements shown in Figure B.2. Next, the same geometry and mesh as the *Helmholtz full-geometry CEA* run was used to perform an Helmholtz simulation with radially averaged input, using the same methodology as described in Section 4.2. For the remainder of this appendix, the latter is addressed as the *Helmholtz full-geometry radially averaged* simulation.

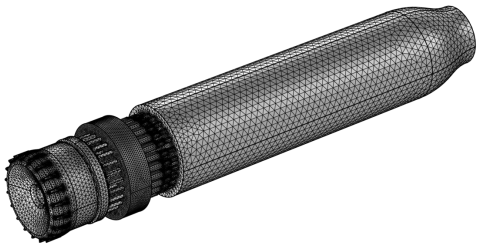

Figure B.2: Mesh of the Helmholtz run of the complete (short) LUMEN geometry using constant CEA properties

Following the Helmholtz runs with increasing complexity for the geometry modelled and for the background flow, the last short chamber simulation runs were performed for the LNS solver using radially averaged input and for the whole LUMEN geometry, in other words, for the same set-up described in Section 4.2.5. The first of these LNS runs was carried out for on a corse mesh, while the second one refined such mesh to investigate how the results would change. Both meshes are shown below in Figure B.3, with the coarse mesh having $3.88 \cdot 10^5$ elements and the fine mesh with $1.52 \cdot 10^6$ elements. For the coarse mesh, refinement zones were used while still basing its size on a prescirbed numer of mesh elements per maximum wavelength to be solved. In the chamber, 20 and 10 mesh elements per wavelength were used for the region just downstream of the faceplate and for the remaining of the chamber, respectively. For the Methane injector, 10 elements per wavelength were used for the CH_4 dome, 20 for CH_4 injector elements. Lastly, for the LOX injector, 10 elements per wavlength were used in its dome and 50 in its injector elements.

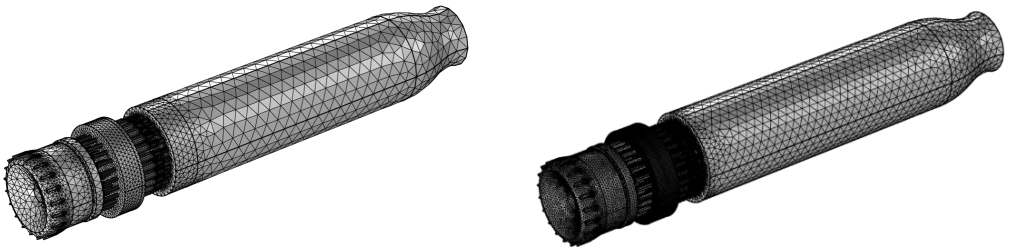

Figure B.3: Meshes of the LNS runs for the complete (short) LUMEN geometry using radially averaged properties. Left: coarse mesh, Right: fine version of the mesh

B.2 Results from short chamber simulations

For the test cases described in the previous section, the simulation were run, and their respective results are given in Table B.1 for the eigenfrequency and in Table B.2 for the damping rates of the LNS simulations. If not specified otherwise in the previous section, the same numerical set-up as used for their counterpart simulations in Chapter 4 was used. From the results it can be seen how accounting for the background flow reduces the frequency of the modes. This is especially visible for the transverse modes when going from the Helmholtz simulation with constant CEA values to the radially averaged one. Furthermore, using LNS, a solver that in its equations accounts for the effect of background flow gradients on the acoustics, a pronounced reduction in the longitudinal mode is visible. The results presented were computed for the L1, T1 and T1L1 since these were the first tested during LUMEN analyses.

Given the coarser meshes of the simulations presented in this appendix and the difference in results when compared to the ones of Chapter 4, it can be concluded that the results in this chapter are not mesh independent. Nonetheless, from Table B.1 and Table B.2 it can be learned that the frequencies converge faster than the damping rates when refining the mesh. Looking at the LNS results, refining the mesh, as described earlier, changes the frequencies by maximum 2.4% for the modes investigated. However, for the damping rates differences up to 27.4 % are visible. This shows how an accurate description of the damping rates requires a finer mesh to be used, and is thus more computationally expensive than for the eigenfrequencies.

Table B.1: Eigenfrequency results for the shorter LUMEN chamber acoustic simulations (mesh-dependent results)

	Helmholtz without injectors CEA	**Helmholtz CFD geometry CEA**	**Helmholtz full-geometry CEA**	**Helmholtz full-geometry radially averaged**	**LNS full-geometry radially averaged (coarse)**	**LNS full-geometry radially averaged (fine)**
L1	2031	2044	2034	2080	1607	1647
T1	9181	9184	9203	5300	5113	5141
T1L1	9548	9551	9553	7330	6786	6811

Table B.2: Damping rate results for the shorter LUMEN chamber LNS simulations (mesh-dependent results)

	LNS full-geometry radially averaged (coarse)	**LNS full-geometry radially averaged (fine)**
L1	261.3	258.6
T1	228.4	179.3
T1L1	555.7	446.6

C Original RPA input and output parameters

C.1 Input parameters used

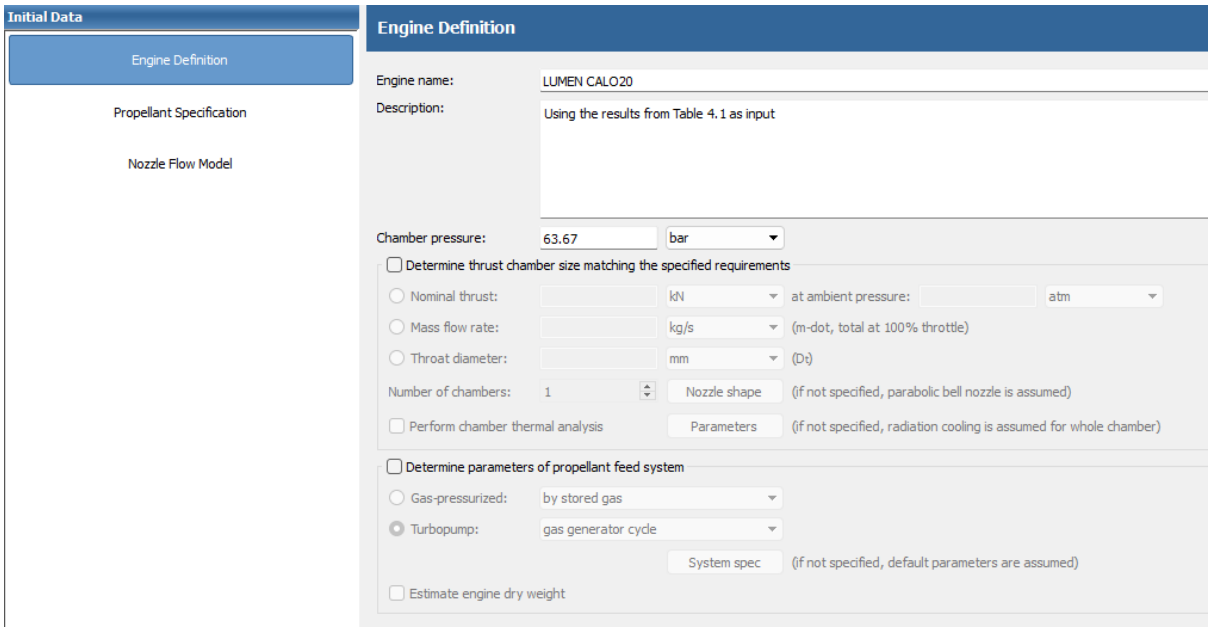

Figure C.1: Engine definition input

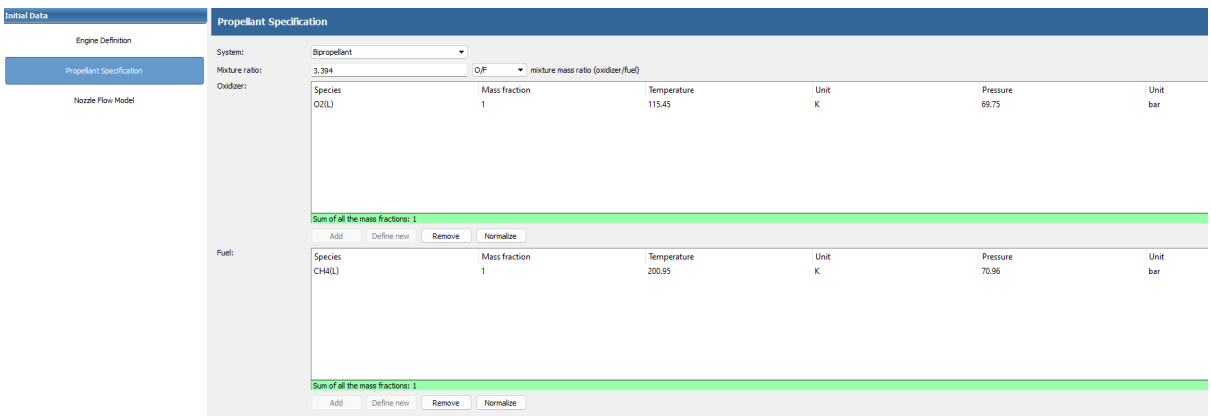

Figure C.2: Propellant specification input

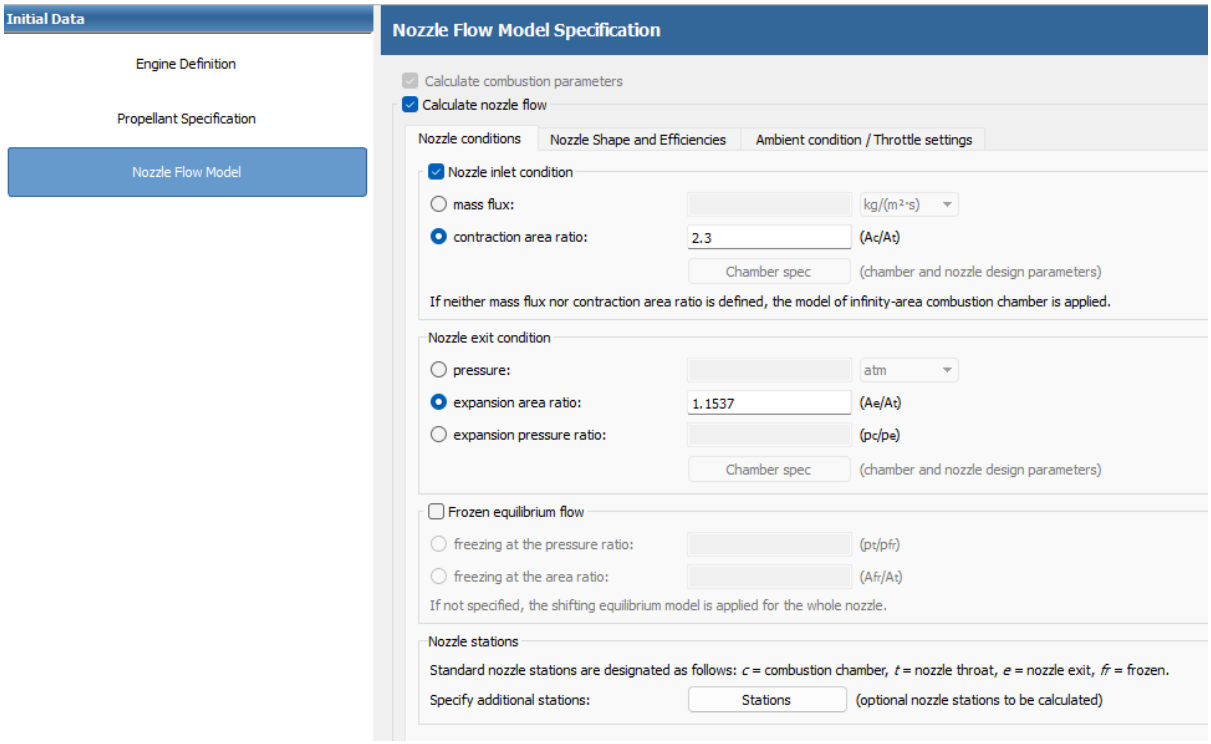

Figure C.3: Nozzle flow model input

C.2 Output parameters obtained

Thermodynamic properties (O/F=3.394)

Parameter	Injector	Nozzle inlet	Nozzle throat	Nozzle exit	Unit
Pressure	6.3670	5.8883	3.5511	2.1044	MPa
Temperature	3556.5838	3538.5019	3381.6458	3228.8005	K
Enthalpy	-1445.6635	-1501.1384	-2171.6760	-2826.3539	kJ/kg
Entropy	12.2566	12.2711	12.2711	12.2711	kJ/(kg·K)
Internal energy	-2818.0066	-2865.8076	-3459.9203	-4041.4223	kJ/kg
Specific heat (p=const)	7.2809	7.3102	7.1538	6.9007	kJ/(kg·K)
Specific heat (V=const)	6.1910	6.2192	6.1281	5.9506	kJ/(kg·K)
Gamma	1.1760	1.1754	1.1674	1.1597	
Isentropic exponent	1.1307	1.1302	1.1271	1.1246	
Gas constant	0.3859	0.3857	0.3810	0.3763	kJ/(kg·K)
Molecular weight (M)	21.5479	21.5589	21.8255	22.0940	
Molecular weight (MW)	0.02155	0.02156	0.02183	0.02209	
Density	4.6395	4.3148	2.7565	1.7319	kg/m³
Sonic velocity	1245.6529	1241.9168	1205.0016	1168.9829	m/s
Velocity	0.0000	333.0913	1205.0016	1661.7403	m/s
Mach number	0.0000	0.2682	1.0000	1.4215	
Area ratio	2.3000	2.3000	1.0000	1.1537	
Mass flux	1437.2181	1437.2181	3321.6417	2877.9560	kg/(m²·s)
Mass flux (relative)	2.257e-04	2.441e-04			kg/(N·s)
Viscosity	0.0001132	0.0001128	0.0001096	0.0001064	kg/(m·s)
Conductivity, frozen	0.3913	0.3896	0.374	0.3586	W/(m·K)
Specific heat (p=const), frozen	2.332	2.331	2.32	2.309	kJ/(kg·K)
Prandtl number, frozen	0.6746	0.6748	0.6797	0.6848	
Conductivity, effective	1.553	1.554	1.457	1.343	W/(m·K)
Specific heat (p=const), effective	7.281	7.31	7.154	6.901	kJ/(kg·K)
Prandtl number, effective	0.5308	0.5306	0.5381	0.5466	

Figure C.4: Thermodynamic output properties

Fractions of the combustion products

Species	Injector mass fractions	Injector mole fractions	Nozzle inlet mass fractions	Nozzle inlet mole fractions	Nozzle throat mass fractions	Nozzle throat mole fractions	Nozzle exit mass fractions	Nozzle exit mole fractions
CO	0.2359746	0.1815330	0.2354206	0.1811993	0.2251673	0.1754508	0.2144986	0.1691940
CO2	0.2535077	0.1241223	0.2543823	0.1246141	0.2705153	0.1341560	0.2872922	0.1442290
COOH	0.0000288	0.0000138	0.0000269	0.0000129	0.0000165	0.0000080	0.0000098	0.0000048
H	0.0011394	0.0243584	0.0011372	0.0243241	0.0009846	0.0213197	0.0008391	0.0183932
H2	0.0078514	0.0839245	0.0078381	0.0838245	0.0074245	0.0803840	0.0070282	0.0770286
H2O	0.4011467	0.4798077	0.4015419	0.4805256	0.4107833	0.4976641	0.4197007	0.5147233
H2O2	0.0000335	0.0000212	0.0000315	0.0000200	0.0000196	0.0000126	0.0000117	0.0000076
HCHO,formaldehy	0.0000006	0.0000004	0.0000005	0.0000004	0.0000003	0.0000002	0.0000002	0.0000001
HCO	0.0000178	0.0000132	0.0000166	0.0000124	0.0000095	0.0000071	0.0000053	0.0000040
HCOOH	0.0000046	0.0000022	0.0000042	0.0000020	0.0000025	0.0000012	0.0000014	0.0000007
HO2	0.0001915	0.0001250	0.0001830	0.0001195	0.0001182	0.0000781	0.0000728	0.0000487
O	0.0082238	0.0110758	0.0081611	0.0109970	0.0064692	0.0088250	0.0049406	0.0068226
O2	0.0360635	0.0242851	0.0359160	0.0241981	0.0309899	0.0211373	0.0257569	0.0177843
O3	0.0000003	0.0000001	0.0000003	0.0000001				
OH	0.0558157	0.0707172	0.0553397	0.0701499	0.0474993	0.0609558	0.0398426	0.0517591

Figure C.5: Ouput fraction of the combustion products

D Additional radially-averaged results

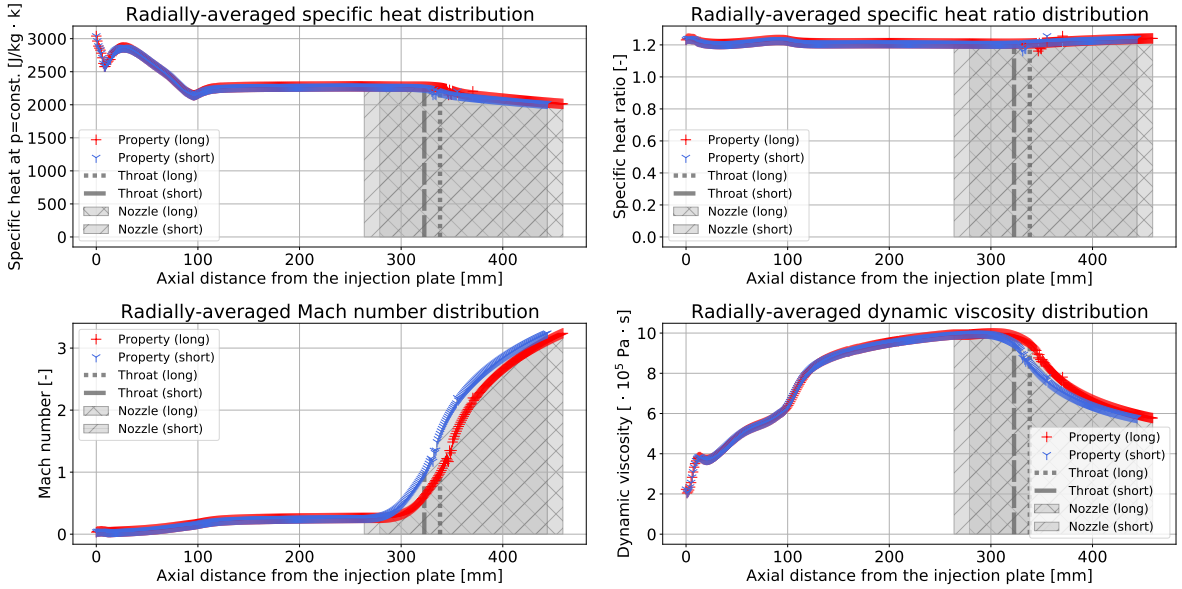

Figure D.1: One-dimensional variation for the specific heat, specific heat ratio, Mach number and dynamic viscosity obtained by radially-averaging LUMEN's CFD field. Shown for the long chamber in red and short chamber in blue

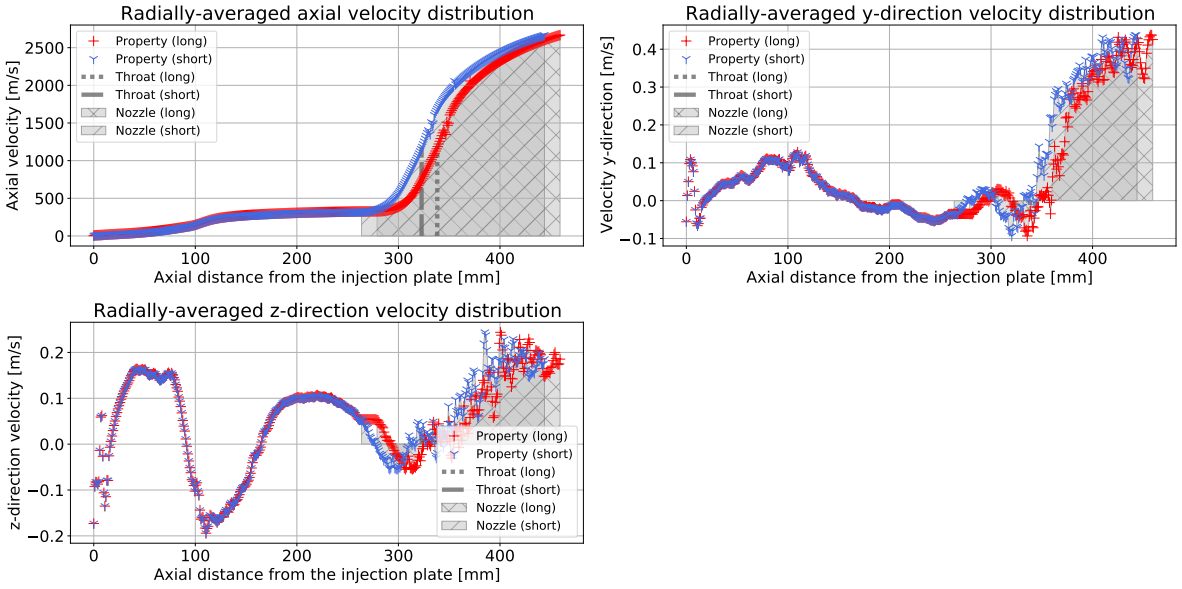

Figure D.2: One-dimensional variation for the velocities obtained by radially-averaging LUMEN's CFD field. Shown for the long chamber in red and short chamber in blue

For the sake of clarity, in Figure D.3 only the mass fractions for the most predominant species are shown. For all the other species, their maximum mass fractions were found to be below 0.01 [-].

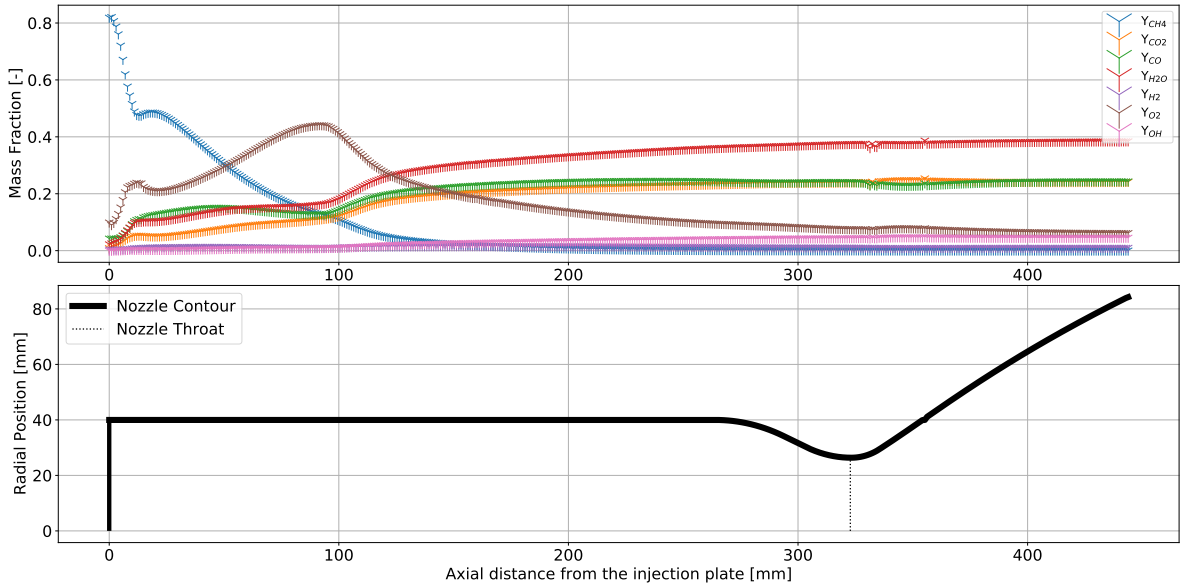

Figure D.3: One-dimensional variation for the short chamber of the species mass fractions obtained by radially-averaging LUMEN's CFD field

E Available numerical stabilization in COMSOL

Section 4.2 referred to stabilization techniques needed to solve convection dominated problems in COMSOL, and that the Garlekin least-squares (GLS) method was chosen for the simulations due to its efficiency and providing promising results for LNS in studies preceding this work. In this appendix, the various stabilization techniques available in COMSOL for aeroacoustic problems are discussed.

Recent stabilization techniques share a similar form, where an additional operator is added to the weighting function of the standard Galerkin method. This extra term is a function of the residual of the equations and can be tweaked via a stabilization coefficient [125]. In COMSOL, three stabilization methods are made available, these being: Streamline diffusion, Streamline upwind Petrov-Galerkin (SUPG) stabilization, and Galerkin least-squares (GLS) stabilization. A detailed description and comparison of these methods can be found in Gikadi's Ph.D. thesis [125]. Streamline diffusion represents a legacy method from COMSOL that compared to the other two is deemed outdated. The Streamline diffusion approach, introduced by Hughes & Brooks in the late seventies [126], adds artificial diffusion along the streamline direction while restricting it along the cross-wind direction, but contrary to the SUPG and GLS approaches, it does not act on the residual of the equations and has an order $\mathcal{O}(h)$.

A more consistent formulation of the Streamline diffusion method was then proposed by Hughes et al. [127], with the SUPG technique. Here, the operator used in the previous method is extended to be also applied to the residual of the equations. For convection-dominated problems, as studied by the current research, the SUPG method is of order $\mathcal{O}\left(h^{p+1/2}\right)$, where p indicates the order of the discretization used, which in this report is always equal to 1 given the use of the linear elements. Albeit containing the word "upwind" in its name, in contrast to this classical scheme, the SUPG approach does not trade lower accuracy for higher stability [125]. In the field of aerospace propulsion systems, the SUPG stabilization approach is heavily used as the go-to method by the research group at TUM when utilizing the LEE solver to predict the stability of rocket engines and gas turbines [29, 31, 43, 66, 82, 99, 128].

The last stabilization method available in COMSOL is GLS. This is the one recommended by COMSOL in their user manual for aeroacoustic applications [113] and in COMSOL v.6 also the default one for LNS. Note, that in earlier releases of COMSOL, as was the case with COMSOL v.5.6 which was used in a previous DLR study to assess the extent to which aeroacoustic solvers can be used for combustion instability prediction analyses, the stabilization was by default turned off and had to be manually activated. The GLS technique, developed by Hughes et al. [129] in the late eighties, aims to minimize the least-square error of the residual of the governing equations. This method is of order $\mathcal{O}\left(h^{2p+1}\right)$ [113, 125], and has the added advantage over SUPG that it also stabilizes the reactive terms of the equation where gradients of the background flow are present.

F COMSOL settings input: radially-averaged profiles and three-dimensional mapping

In the following appendix, a brief description is provided of how one-dimensional profiles and three-dimensional data can be input in COMSOL and linked to model properties and material properties. The case of inputting 1D profiles and using them directly for the simulation is described in Section F.1, while the 3D field case is shown in Section F.2. For the latter, the settings for the mapping are also explained. The description provided in this appendix makes use of screenshots taken from the LNS simulations presented in this report.

F.1 One-dimensional profiles

Starting with how one-dimensional profiles can be input in COMSOL, Figure F.1 shows how the speed of sound was imported for the LNS run with radially averaged input described in Chapter 4. Here, *int1* represents the name in COMSOL that refers to the interpolated data, which can be imported via the *Load from file* option just above the *Interpolation and Extrapolation* section shown in Figure F.1. From this, a piecewise cubic interpolation function was chosen since from the available options it returned the smoothest results without sudden overshoot or undershoot regions (which would have been obtained if a cubic spline interpolation were to be chosen). Note, that since in this report, the simulations use the 1D profiles from three different domains (i.e. combustion chamber, LOX, and Methane injector) to describe the background flow, care should be paid to defining a consistent coordinate system in COMSOL and inputting the data formatted for this coordinate system into COMSOL for the interpolation. Otherwise, unphysical results will be returned by the acoustic simulation due to the wrong provided inputs. For the simulations presented in Chapter 4, the origin of the coordinate system was set at the longitudinal centerline of the combustor on the faceplate, with the positive axis pointing towards the nozzle exit, and negative axial distances for the injectors. For the extrapolation, this can be set to *None* given that the profiles were computed for the whole domains considered. Nevertheless, to prevent the simulation from crashing in case the start/end location was rounded up to a different decimal point than the position COMSOL would retrieve from the geometry, an *constant* extrapolation was here set for safety.

The interpolation in Figure F.1 is shown for the speed of sound distribution of the combustor only (for the sake of clarity), but in reality, a separate interpolation had to be performed for each input parameter of the injectors and combustor required by the simulations. In COMSOL, the interpolation option can be found under the *Definitions* tab. Next, the interpolated properties have to be linked to model input either to the material properties or to the physics. Figure F.2 shows the case of linking the speed of sound interpolation of Figure F.1 to the material properties of the combustion gases. In Figure F.2, *comp1.int1(...)* represents the name of the interpolation function shown in Figure F.2 including its root component. Similarly, *comp1.sys2.x* indicates the coordinate system that was defined under *Definitions* as a *Base Vector System*, so as to have a consistent axial axis reference for all radially averaged profiles of the combustor, LOX and Methane injectors.

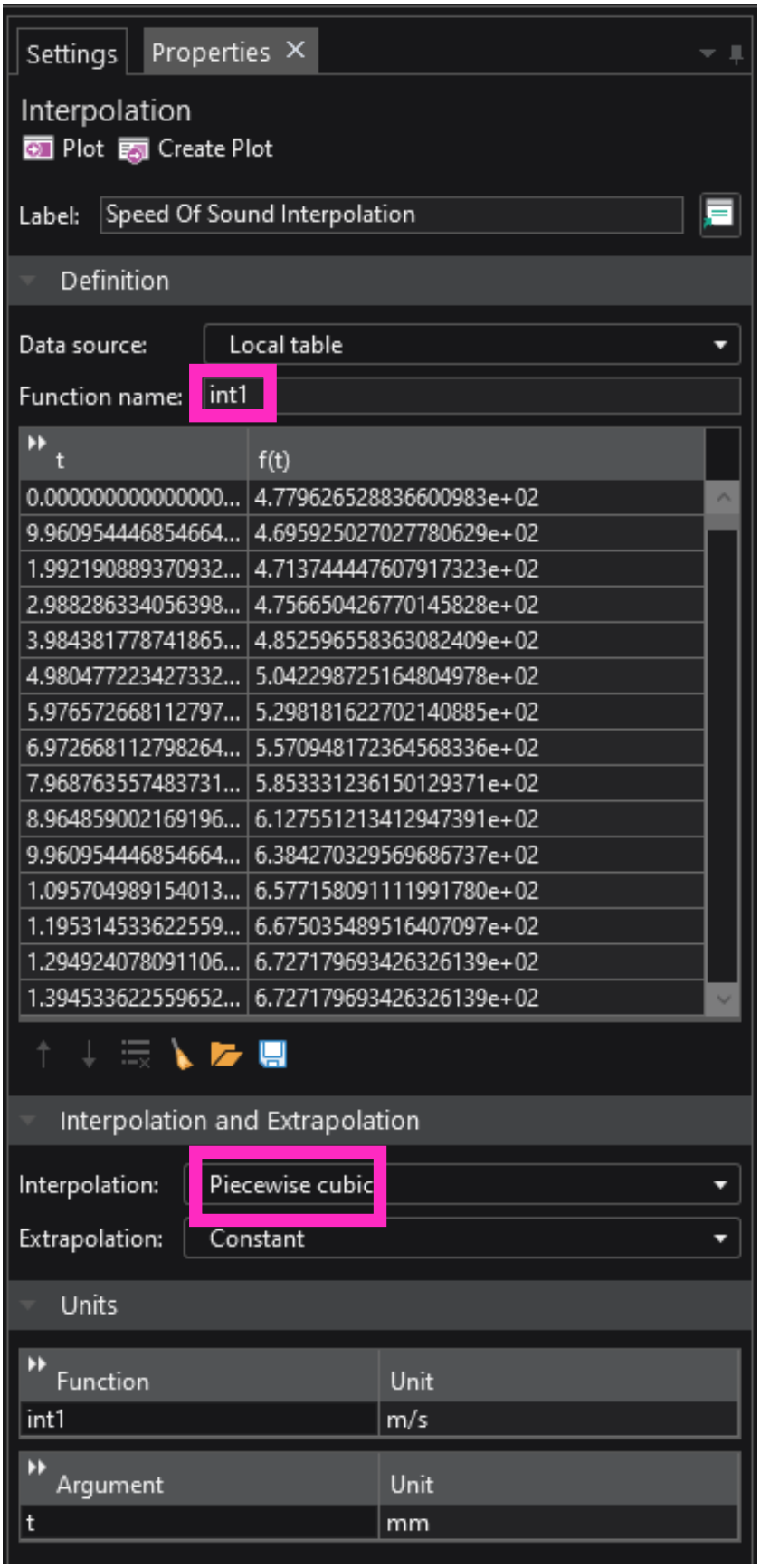

Figure F.1: Interpolation of one-dimensional profiles in COMSOL

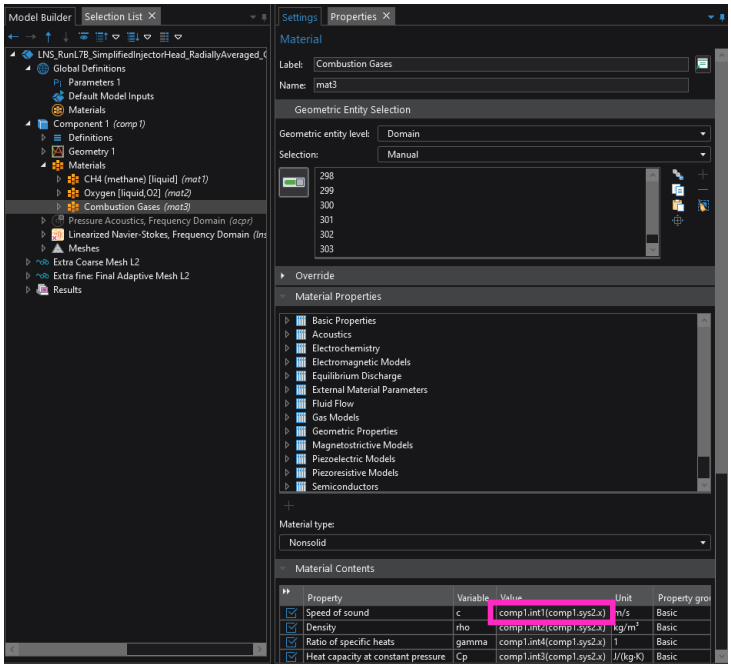

Figure F.2: Linking one-dimensional profiles as input for material properties

Once linked to all necessary material properties, some interpolations also have to be linked to the model input, as shown in Figure F.3 for the background pressure field (with interpolation function named *int16*). For describing profiles as input for the physics, so-called *model inputs* have to be created (as shown in Figure F.3). For the problem studied, for each background flow property, three model inputs had to be created, one per each of the combustor, LOX injector, and Methane injector domains. In Figure F.3, the case for the combustor domain is shown. In general, it is always recommended to plot the 3D result of the input interpolations once the first simulation is run. This allows us to verify whether the profiles were input as expected and to discover a possible source of issues for the simulation results. If the reader wishes to obtain more information about how to use interpolated data as input for simulations in COMSOL, the latter software company makes publicly available (if the reader is in possession of an active COMSOl license) solved test cases that can be downloaded from their website, where 1D profiles are used as input. After this, the *Weak Form PDE* model can be solved via a single stationary study.

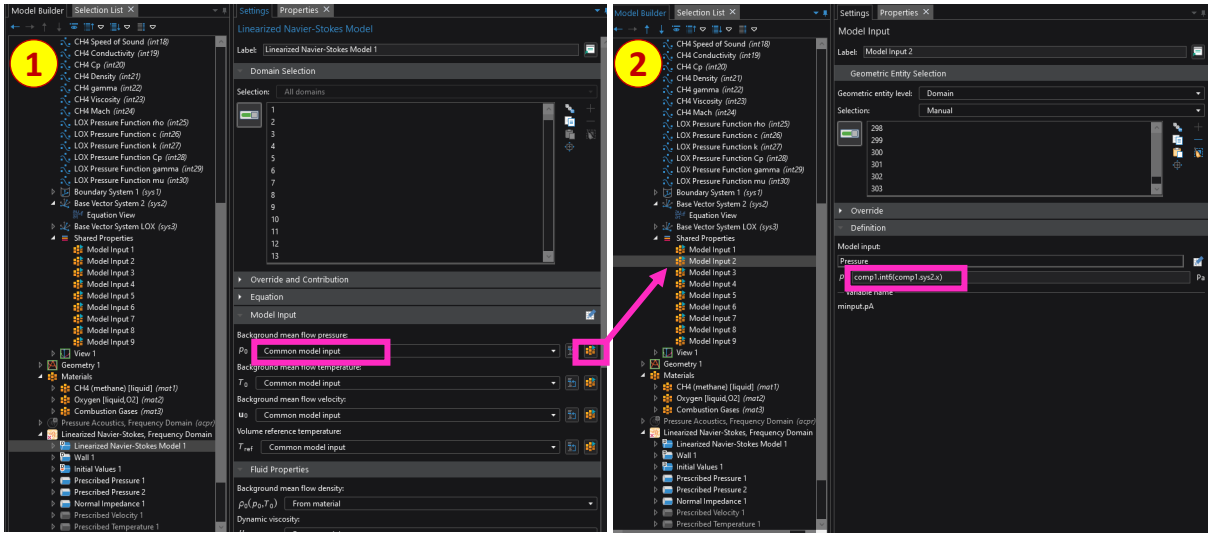

Figure F.3: Linking one-dimensional profiles as input for the Lineraized Navier-Stokes model

F.2 Three-dimensional field and mapping

Besides the one-dimensional interpolations, performing a three-dimensional mapping of data in COMSOL is here also described. Starting with importing 3D data, Figure F.4 shows how to import this data in COMSOL and how the field is reconstructed via linear interpolation. Note, this step will return the CFD data of the LUMEN combustor obtained for the CFD mesh described in Table 3.2. To map this data to the acoustic mesh, and thus using it as input for the simulations, requires an additional mapping study to do so. To import 3D data, contrary to Figure F.1, *file* has to be chosen as a data source. For this, it is most convenient to have a text or data file ready that has as the first three columns the x,y, and z coordinates of the data, and as the additional columns the values of the desired quantities at those coordinates. In Figure F.4, *Number of arguments* indicates whether the data is 1D, 2D, or 3D, while the *Position in file* under the *Functions* tab of Figure F.4, indicates the column position **after** the coordinate columns for which the desired data can be found. As an example, the position of 1 for the *get_c* function (the name given here for the speed of sound data) means that COMSOL will take the first column after the coordinate columns for the data of *get_c*. Regarding the coordinate columns, if 3 is chosen as a number of arguments, it means that the data for a 3D field is given. For the given input file, COMSOL will then automatically take the first three columns of the files as the x, y, and z coordinates respectively. This means that if the speed of sound data is provided in the fourth column of the input file, and if a 3D field is considered, a *Position in file* of 1 has to be prescribed. In case a 2D field would have been considered instead, with say the speed of sound at the third column of the file, then a *Number of arguments* of 2 should be used, while still having a *Position in file* of 1 for the speed of sound function. Next to this COMSOL standard, for 3D interpolations, the choice between *Nearest Neighbour* and *Linear* interpolation is made available. In contrast to the method shown in Section F.1 for the 1D profiles, for the 3D case of Figure F.4, all necessary parameters can be imported into COMSOL for their interpolation under a single interpolation command.

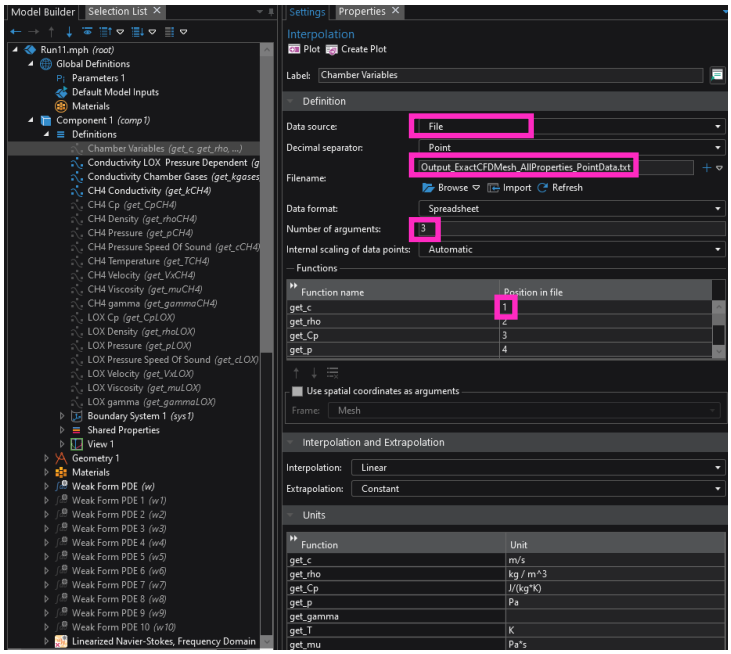

Figure F.4: Inputting three-dimensional data for interpolation

With the 3D data interpolations set, a *Weak Form PDE* study had to be solved to map the 3D CFD data to the acoustic mesh to be used as input for the acoustic analyses. This was explained in Section 4.3.2, and here only the screenshots of the COMSOL implementation are shown. For a discussion on the methodology, the reader is referred back to Section 4.3.2. The *Weak Form PDE* implementation in COMSOL is shown in Figure F.5. Here, the dependent variable (i.e. the ones to be used as input for

the acoustic simulations) have to be defined, and the equations to be solved are given under the *Weak Expressions* tab of the Weak Form PDE Model settings. If necessary, for example for the diffusion coefficient, additional input values required by the *Weak Expressions* can be specified a priori in the *Parameters* table in the *Global Definition* of the COMSOL file.

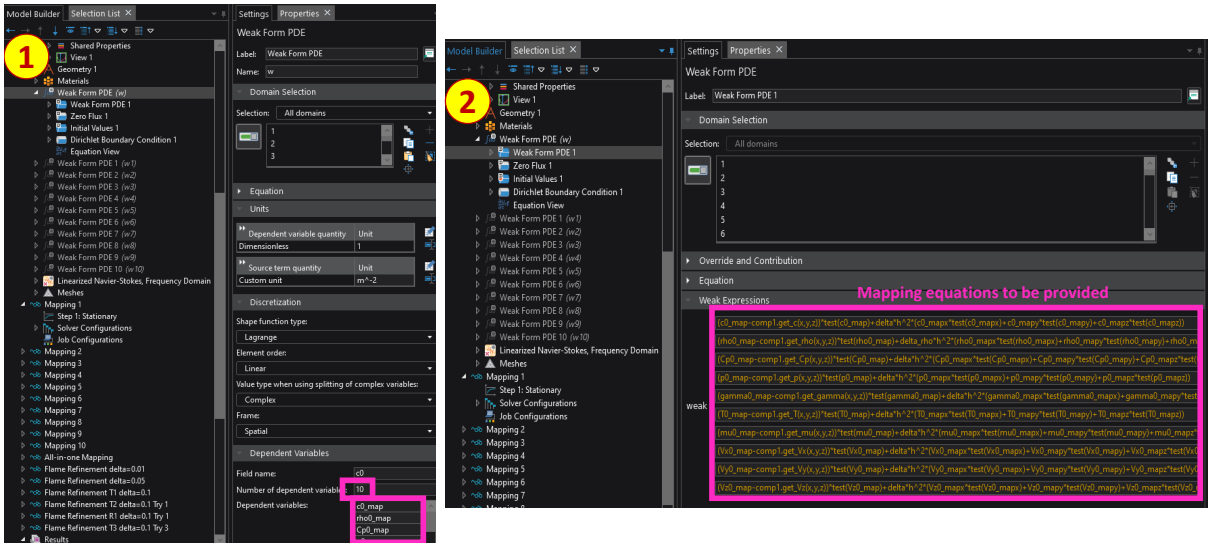

Figure F.5: Mapping three-dimensional input data to the acoustic mesh used by the simulations

Once solved, the same approach as described above in Section F.1 can be used to link the results of the mapping to the necessary material and model inputs (using the names defined in Figure F.5. Lastly, for inputting the three-dimensional field to LNS, when setting up the study of the latter, attention should be paid to defining the output of the Weak Form study as a constant input (not to be solved) for the LNS. This can be done by setting the *Values of Dependent Variables* options as shown in Figure F.6

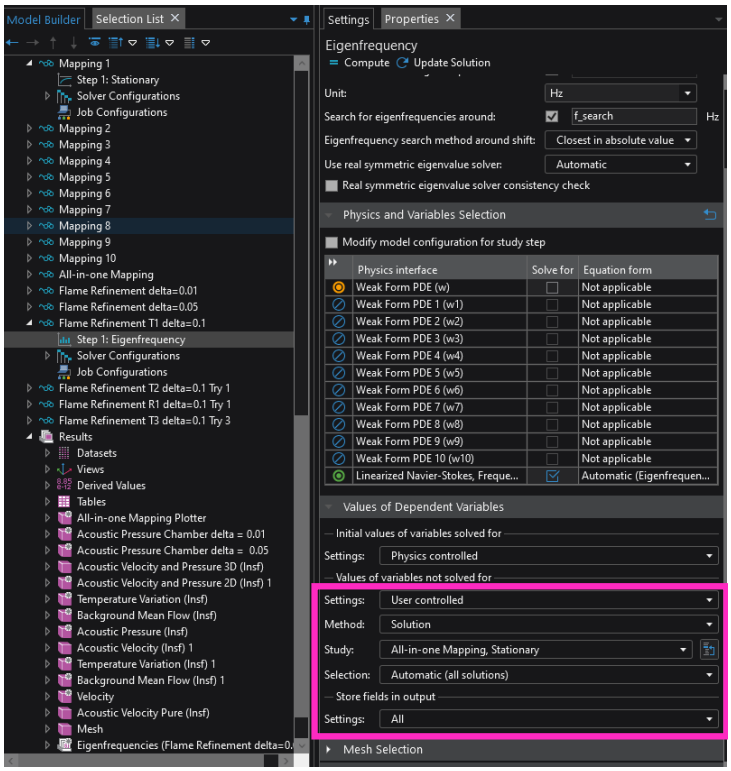

Figure F.6: Defining the solution of the Weak Form mapping as input for the Linearized Navier-Stokes simulation

G Linearized Navier-Stokes input fluid properties flowchart

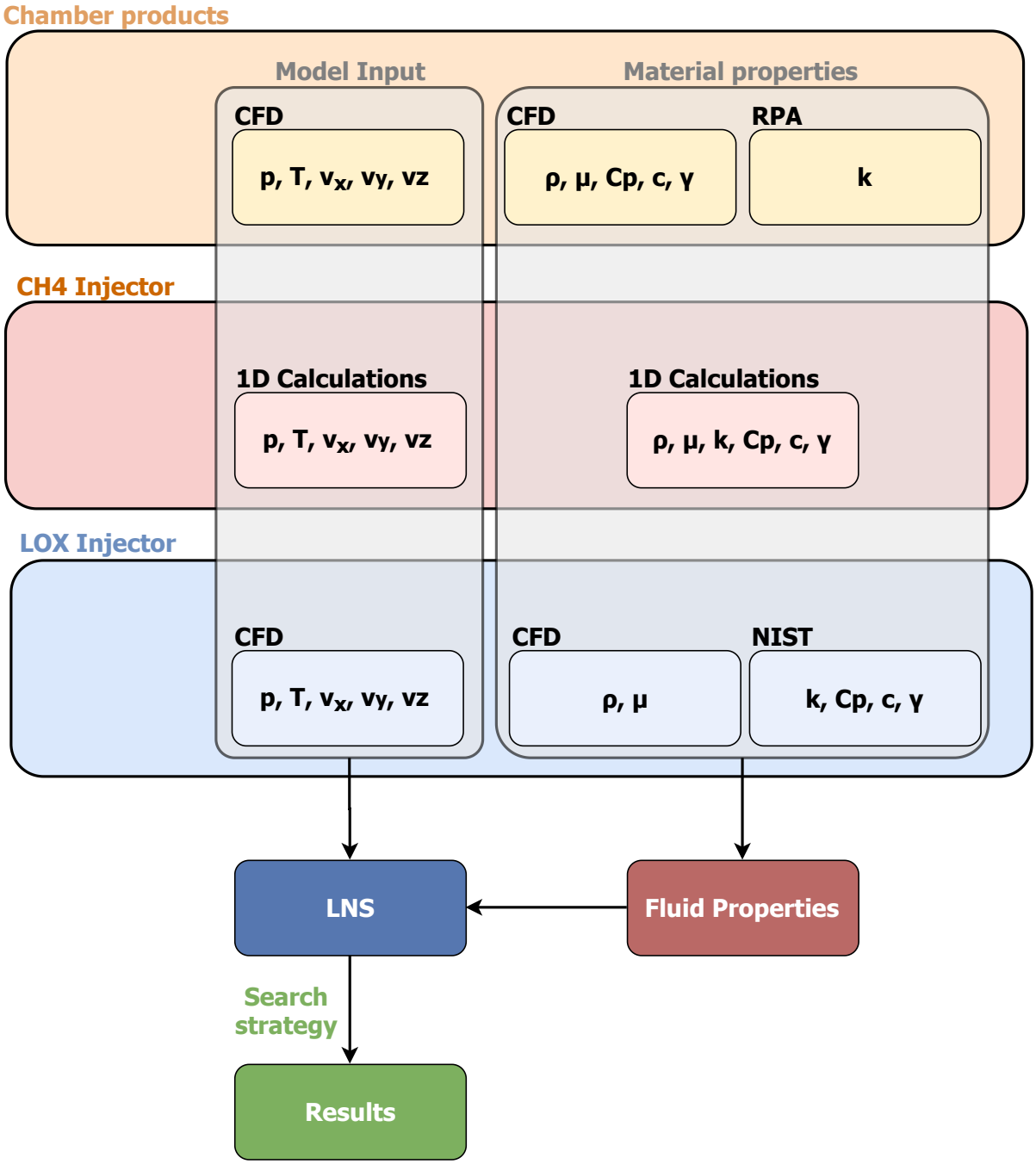

Figure G.1: Flowchart of the input flow properties required by the LNS simulation

H Additional Dynamic Pressure Sensors Temporal Evolutions

H.0.1 Test-run 2

L1 Mode

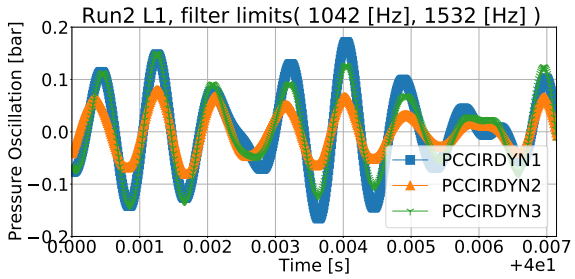

(a) Initial temporal range

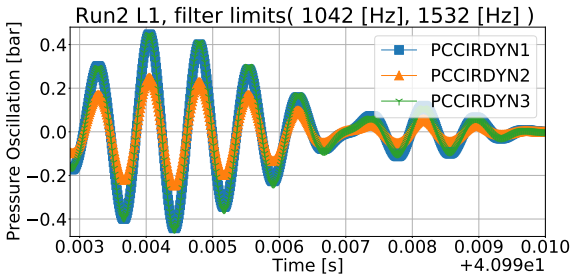

(b) Final temporal range

Figure H.1: Filtered dynamic pressure data for test-run 2 L1 mode for the initial temporal range (a), intermediate range (b), and final range (c)

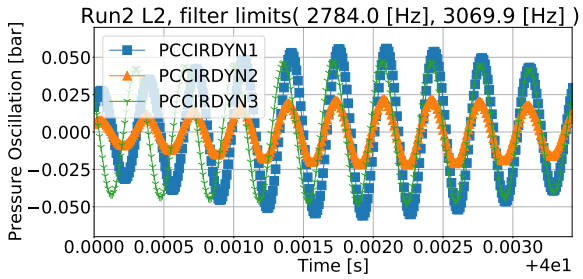

(a) Initial temporal range

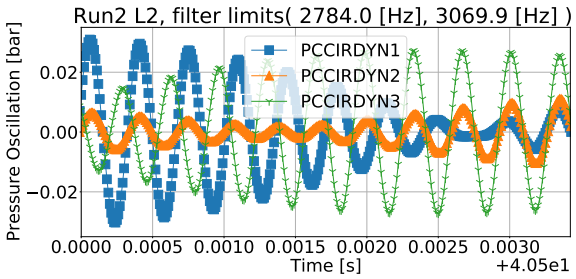

(b) Intermediate temporal range

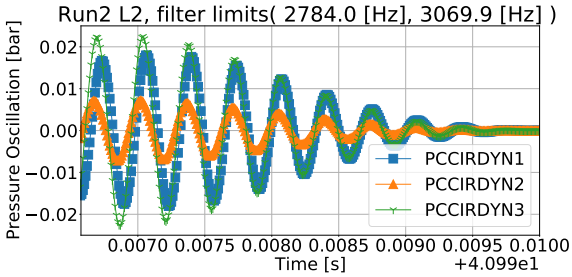

(c) Final temporal range

Figure H.2: Filtered dynamic pressure data for test-run 2 L2 mode for an initial temporal range (a), intermediate range (b), and final range (c)

T1 Mode

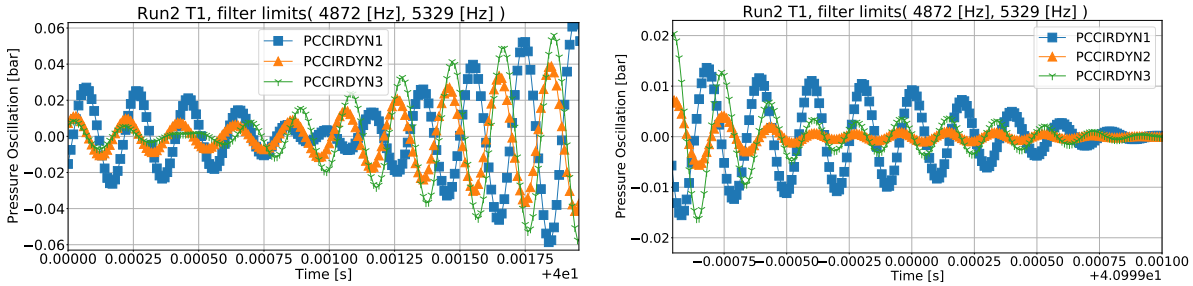

(a) Initial temporal range

(b) Final temporal range

Figure H.3: Filtered dynamic pressure data for test-run 2 T1 mode for an initial temporal range (a) and final range (c)

T1L1 Mode

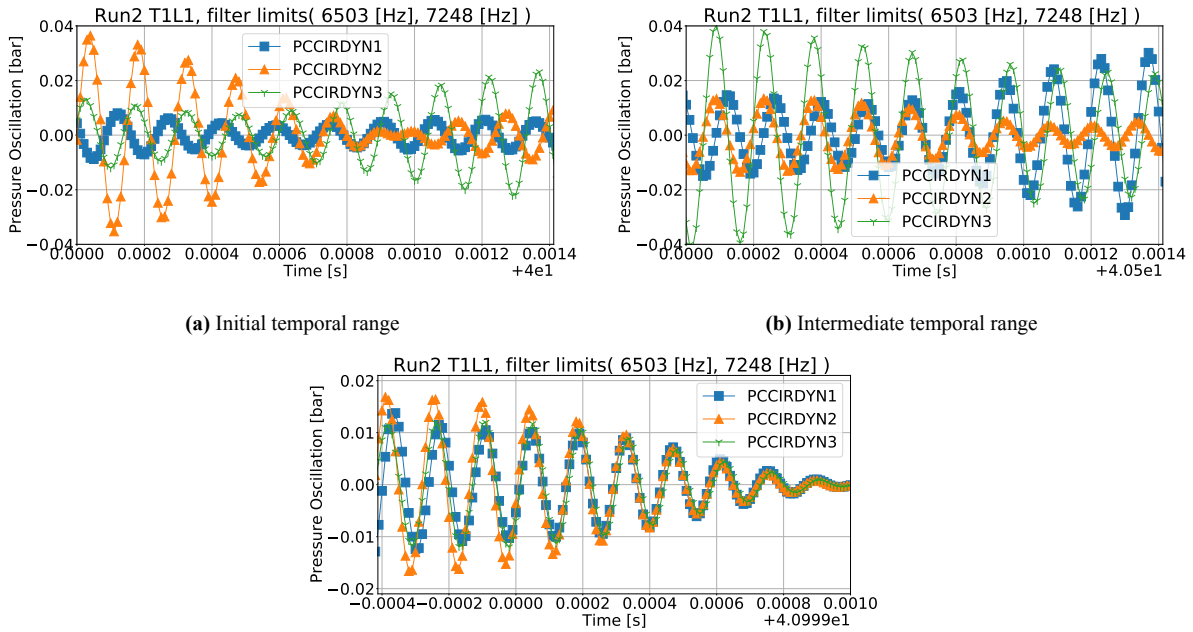

(a) Initial temporal range

(b) Intermediate temporal range

(c) Final temporal range

Figure H.4: Filtered dynamic pressure data for test-run 2 T1L1 mode for an initial temporal range (a), intermediate range (b), and final range (c)

T2 Mode

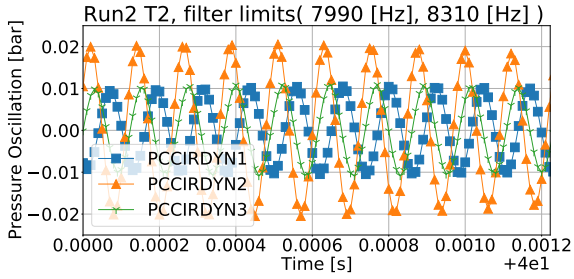

(a) Initial temporal range

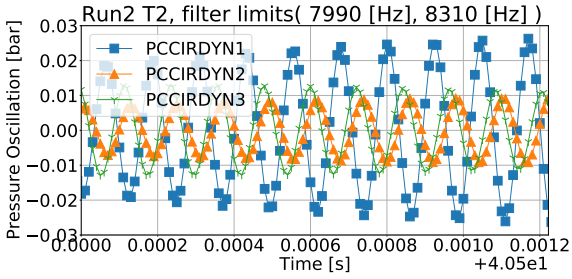

(b) Intermediate temporal range

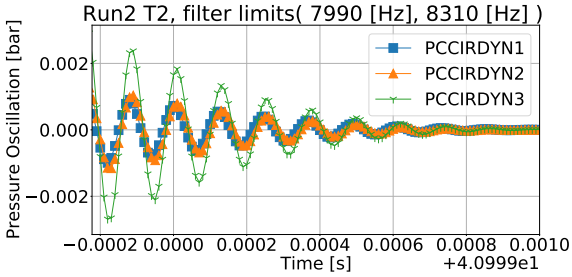

(c) Final temporal range

Figure H.5: Filtered dynamic pressure data for test-run 2 T2 mode for an initial temporal range (a), intermediate range (b), and final range (c)

R1 Mode

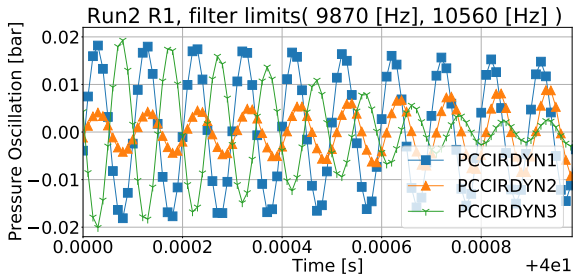

(a) Initial temporal range

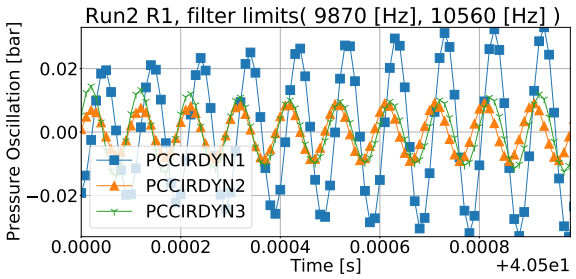

(b) Intermediate temporal range

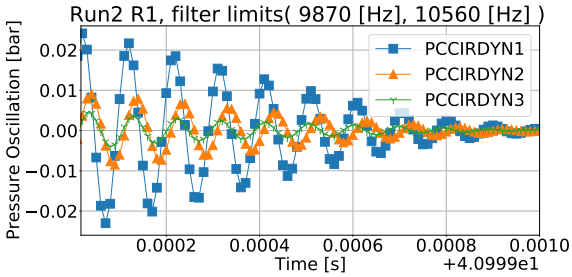

(c) Final temporal range

Figure H.6: Filtered dynamic pressure data for test-run 2 R1 mode for an initial temporal range (a), intermediate range (b), and final range (c)

H.0.2 Test-run 6

L1 Mode

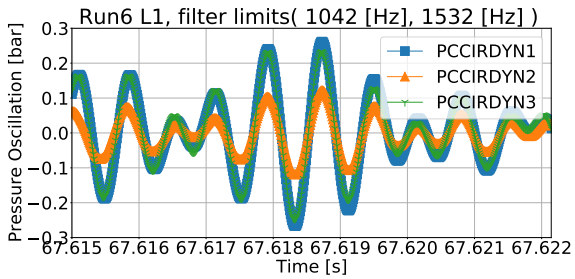

(a) Initial temporal range

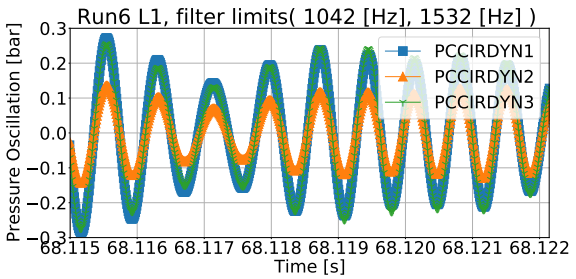

(b) Intermediate temporal range

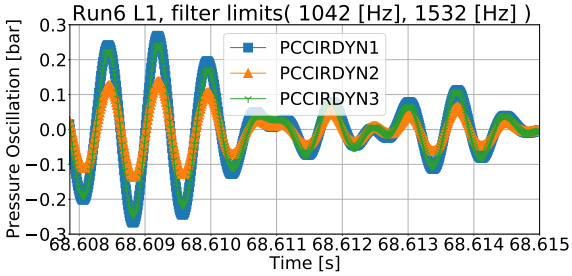

(c) Final temporal range

Figure H.7: Filtered dynamic pressure data for test-run 6 L1 mode for an initial temporal range (a), intermediate range (b), and final range (c)

L2 Mode

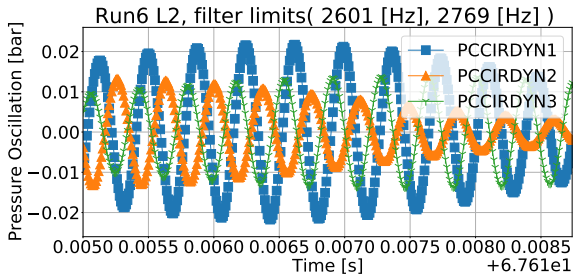

(a) Initial temporal range

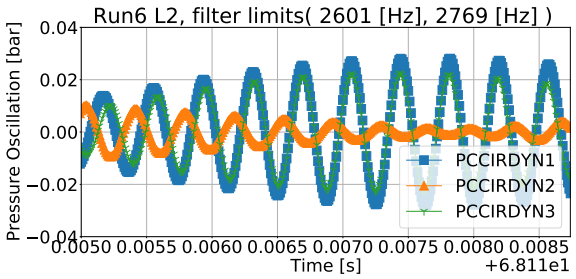

(b) Intermediate temporal range

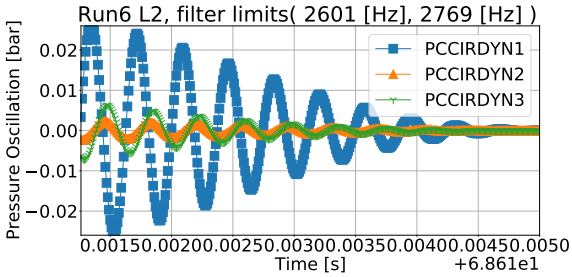

(c) Final temporal range

Figure H.8: Filtered dynamic pressure data for test-run 6 L2 mode for an initial temporal range (a), intermediate range (b), and final range (c)

T1 Mode

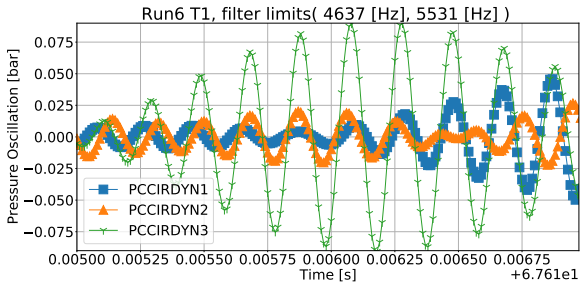

(a) Initial temporal range

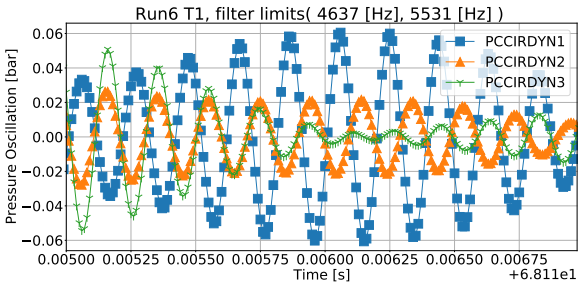

(b) Intermediate temporal range

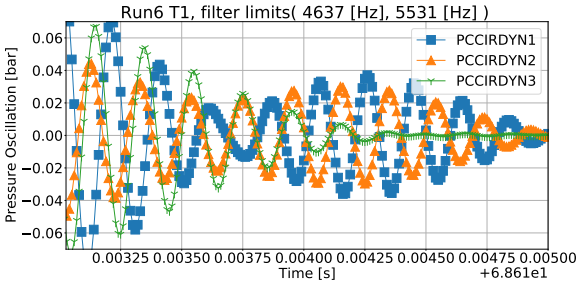

(c) Final temporal range

Figure H.9: Filtered dynamic pressure data for test-run 6 T1 mode for an initial temporal range (a), intermediate range (b), and final range (c)

T1L1 Mode

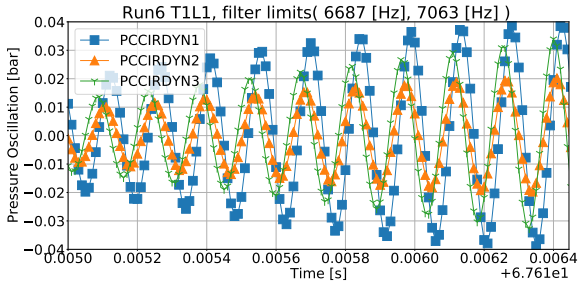

(a) Initial temporal range

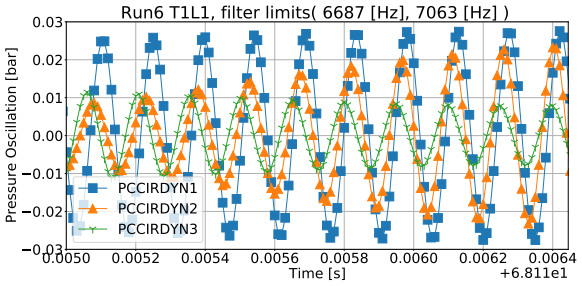

(b) Intermediate temporal range

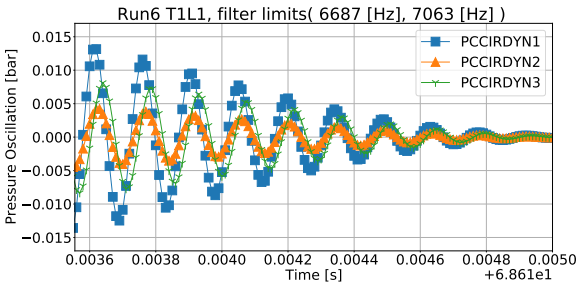

(c) Final temporal range

Figure H.10: Filtered dynamic pressure data for test-run 6 T1L1 mode for an initial temporal range (a), intermediate range (b), and final range (c)

T2 Mode

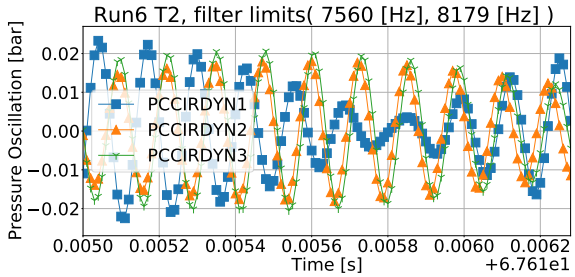

(a) Initial temporal range

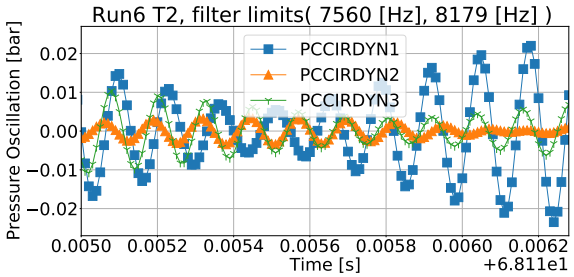

(b) Intermediate temporal range

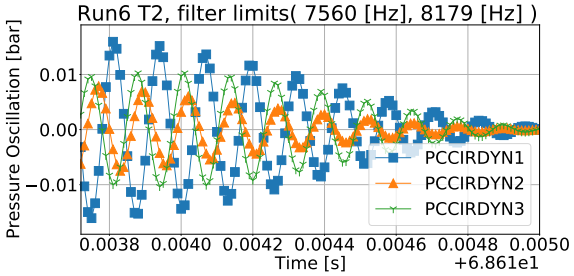

(c) Final temporal range

Figure H.11: Filtered dynamic pressure data for test-run 6 T2 mode for an initial temporal range (a), intermediate range (b), and final range (c)

R1 Mode

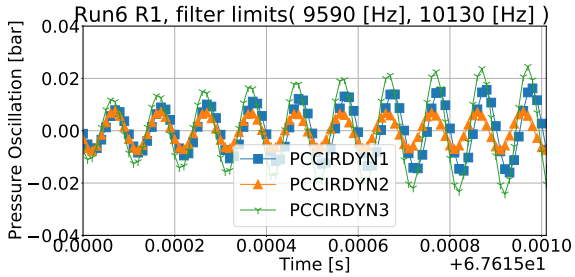

(a) Initial temporal range

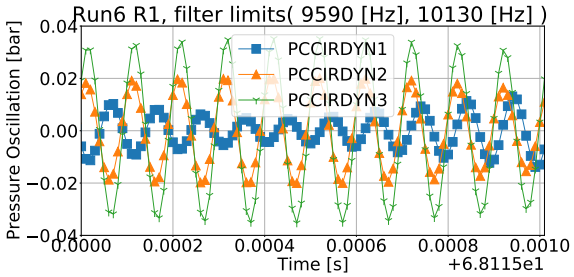

(b) Intermediate temporal range

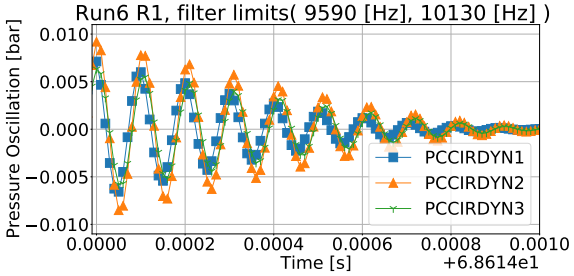

(c) Final temporal range

Figure H.12: Filtered dynamic pressure data for test-run 6 R1 mode for an initial temporal range (a), intermediate range (b), and final range (c)

I Experimental data fitting input and output parameters

In Table I.1 and Table I.2 below, further information are provided for the input and output data of the curve fitting performed for the test-run 2 and 6, respectively, of the LUMEN-CALO20's hot-fire campaign from DLR. In the tables, wherever necessary, values of B=0 and q_f=50 were used as initial guesses for the additional fitting parameters of the Asymmetric Lorentzian profile and Fano profile.

Table I.1: Extra curve fitting information for test-run 2

		Input						Output	
Mode	**Fitting profile**	**f_c [Hz]**	**$f_{lowerbound}$ [Hz]**	**$f_{upperbound}$ [Hz]**	**W_{fc} [1/s]**	**A_{fc} [bar^2/Hz]**	**Frequency resolution [-]**	**$A_{peak,output}$ [bar^2/Hz]**	**R^2 [-]**
L1	Lorentzian	1340	1042	1532	148	0.05390	20	0.05096	0.93
L2	Lorentzian	2920	2784	3070	19	0.00629	14	0.00827	0.80
T1	Lorentzian	5016	4677	5376	88	0.01312	20	0.01452	0.89
T1L1	Asymmetric Lorentzian	7080	6503	7248	118	0.005113	12	0.00368	0.90
T2	Fano	8180	7990	8310	45	0.003875	20	0.000176	0.90
R1	Asymmetric Lorentzian	10176	9870	10560	115	0.00275	30	0.003897	0.80

Table I.2: Extra curve fitting information for test-run 6

		Input						Output	
Mode	**Fitting profile**	**f_c [Hz]**	**$f_{lowerbound}$ [Hz]**	**$f_{upperbound}$ [Hz]**	**W_{fc} [1/s]**	**A_{fc} [bar^2/Hz]**	**Frequency resolution [-]**	**$A_{peak,output}$ [bar^2/Hz]**	**R^2 [-]**
L1	Lorentzian	1400	1042	1532	148	0.05390	20	0.040326	0.90
L2	Fano	2675	2601	2769	50.5	0.00786	14	0.000305	0.83
T1	Lorentzian	5067	4637	5531	215	0.006405	20	0.00586	0.86
T1L1	Lorentzian	6922	6687	7063	101	0.002628	20	0.002681	0.81
T2	Asymmetric Lorentzian	8180	7990	8310	45	0.003875	30	0.005093	0.94
R1	Asymmetric Lorentzian	9901	9590	10130	110	0.002677	20	0.002548	0.81